Web Crippling Behaviour of Pultruded Glass Fibre Reinforced Polymer Wide Flange-Section Profiles with Web Perforations

A thesis submitted for the degree of

Doctor of Philosophy

by

Jyotirmoy Haloi

Department of Civil Engineering

Indian Institute of Technology Guwahati

Guwahati – 781039, India

This page is intentionally left blank.

To the Lord

To my lovely wife:

Nabanita Medhi

To my dearest parents:

Ramesh Haloi (Deuta)

Manju Haloi (Maa)

This page is intentionally left blank.

ABSTRACT

An increasing use of Glass Fibre Reinforced Polymer (GFRP) pultruded structural profiles has been seen in the recent past as an alternative option to traditional structural members, made of materials such as steel, concrete, aluminium etc. owing to their numerous advantages such as high strength to weight ratio, corrosion resistance, lower maintenance cost, easy installation process etc. However, limited research has been seen in GFRP structural members when subjected to web crippling load for both unperforated and perforated GFRP profiles. Additionally, in the Indian context, limited technical test data of the GFRP materials are available in the public domain and there are no Indian standards for recommending design or test procedures for these GFRP materials or members. Hence, in this thesis, an attempt has been made to characterize a type of GFRP manufactured in India, followed by investigations into the web crippling behaviour of GFRP wide flange (WF)–section profile for both perforated and unperforated cases.

Initially, an investigation on the mechanical properties has been assessed for six different GFRP profile shapes and sizes by conducting tensile, compression, interlaminar shear and in-plane shear tests that are performed on coupons obtained from the flanges and webs of the profiles, and their characteristic material properties are evaluated. Following this, a comparative study has been performed on the material partial safety factors and conversion factors and subsequent design values by considering four design guidelines (Italian guideline, 2007; ASCE, 2010; EUROCOMP, 1996; and Ascione *et al*., 2016).

Second, an investigation on the web crippling behaviour of unperforated GFRP profile has been performed by utilising a GFRP wide flange (WF)–section profile. The study investigates systematically the effects of bearing lengths and plate thickness on the web crippling behaviour of the GFRP profile. Both experimental and numerical investigations have been performed by considering two loading configurations such as end-two-flange (ETF) and interior-two-flange

(ITF) loadings. Bearing length is found to have direct influence on the web crippling strength and behavior of the GFRP profile. Based on the combined test data from the current experimental campaign and data from literature, new design equations have been proposed for both ETF and ITF loading configurations.

Finally, the effects of centred circular web perforations of different sizes on the web crippling behaviour of GFRP WF-section profile, under ETF and ITF loadings, have been studied experimentally and numerically. Based on parametric study, it has been observed that the ultimate crippling strength of the GFRP profile is significantly influenced by the bearing plate length to web height ratio and the perforation diameter to web height ratios. Further, on the basis of both experimental and numerical results, reliable web crippling strength reduction factor equations are proposed.

DECLARATION

I, JYOTIRMOY HALOI, a PhD Scholar of Indian Institute of Technology Guwahati declare that the content of this thesis entitled 'Web Crippling Behaviour of Pultruded Glass Fibre Reinforced Polymer Wide Flange-Section Profiles with Web Perforations' submitted here is a partial fulfilment for the requirement of awarding the Degree for **Doctor of Philosophy** and submitted in Indian Institute of Technology Guwahati, India. This thesis is the documentation of the research work carried out by me at the institute in a period of January, 2016 to March, 2021 under the supervision of ***Dr. Konjengbam Darunkumar Singh***, Professor, Department of Civil Engineering and ***Dr. Arun Chandra Borsaikia***, Technical Officer (Grade I), Department of Civil Engineering, Indian Institute of Technology Guwahati. I certify that the content of this thesis is the original one and has not been used for awarding any other degree. Moreover the thesis content has not been published by any other person.

Jyotirmoy Haloi

Date: 26-03-2021

Place: IIT Guwahati

(Mr. Jyotirmoy Haloi)

Reg. No: 156104044

This page is intentionally left blank.

CERTIFICATE

This is to certify that the work content in the thesis entitled by '***Web Crippling Behaviour of Pultruded Glass Fibre Reinforced Polymer Wide Flange-Section Profiles with Web Perforations***' being submitted here by **Mr. Jyotirmoy Haloi** to Indian Institute of Technology Guwahati, India for the award of degree of **Doctor of Philosophy** is a record of genuine research work carried out by the aspirant being a PhD scholar under our supervision and guidance.

The Thesis work, being shown is creditable of considering for the award of degree of **Doctor of Philosophy** in accordance with the regulation of the Institute.

(**Dr. Konjengbam Darunkumar Singh**)
Professor
Department of Civil Engineering
Indian Institute of Technology Guwahati

(**Dr. Arun Chandra Borsaikia**)
Technical Officer (Grade I)
Department of Civil Engineering
Indian Institute of Technology Guwahati

Date:

Place: IIT Guwahati

Date:

Place: IIT Guwahati

This page is intentionally left blank.

ACKNOWLEDGEMENT

My acknowledgement goes to all the persons who helped me out in the course of my research work. Their company, advices and knowledge enabled me to complete my work. I shall ever remain indebted to all of them. First of all, I would to thank IIT Guwahti, Department of Civil Engineering, Central Instruments Facility and Mechanical Engineering Department for providing the required facilities to complete my research work. I will be grateful to Bajrang Agencies, Guwahati for providing me the materials required for carrying out the experimental programme.

I would like to express my sincere gratitude to my supervisors **Prof. *Konjengbam Darunkumar Singh*** and **Dr. *Arun Chandra Borsaikia*,** Department of Civil Engineering, IIT Guwahati for their constant effort, invaluable guidance, encouragement and kind help throughout the course of my research work. They always give me the inspiration and motivation for my research work that help me in completing my thesis. I have experienced and learnt many things from their way of working, which will have a great impact in my future life.

I shall also be thankful to Prof. Sudip Talukdar, Dr. Tadikonda Venkata Bharat and Prof. P. S. Robi, my doctoral committee members, who have enlightened me giving valuable suggestion and remarks from time to time, which help me in getting the final touch of my research work.

I want to express my special thanks to Prof. Chandan Mahanta for constantly supporting me throughout my PhD life.

I would like to express my sincere thanks to my dearest friend Suman Kr. Mushahary for extending his support whenever necessary. Also, I would like to express my special thanks to my seniors Maharshi da, Narendra Babu, Patil sir, Sukumar da and my friends Vipej, Sabnam, Arunabh, Gishan, Prashant, Saroj for giving me their companion and cherish during my stay in IIT Guwahati.

I am also thankful to all my family members – Nabanita Medhi (wife), Ramesh Haloi (Father), Manju Haloi (Mother), Bandita Haloi (Sister) and Maitreyee Haloi (Sister). Their motivation and inspiration during my hard time shall be my unforgettable moments in my entire life. Their blessing has enabled me to reach this stage of my life.

Last but not the least, I express my thanks to Almighty God for his constant guidance and blessing and giving me the strength to complete my thesis work.

Jyotirmoy Haloi

CONTENTS

LIST OF FIGURES

This page is intentionally left blank.

LIST OF TABLES

NOTATIONS

AISC	American Institute of Steel Construction
AISI	American Iron and Steel Institute
AS	Australian Standard
ASCE	American Society for Civil Engineers
ASTM	American Society for Testing and Materials
A_{shear}	Shear area under the loading plate
A_{eqv}	Equivalent rectangular area
B	Plate width
B_{eff}	Effective length of the web at mid height
COV	Coefficient of variation
C	Overall web crippling coefficient
C_h	Web slenderness coefficient
C_M	Moisture condition factor
C_N	Bearing length coefficient
C_p	Correction factor
C_R	Inside bend radius coefficient
C_T	Temperature factor
C_χ	Coefficient used to address the web buckling effect
CF	Carbon Fibre

CFRP	Carbon Fibre Reinforced Polymer
C3D8R	Eight-node solid elements with reduced integration
DL	Dead Load
E	Young's modulus
E_T	Transverse elastic modulus
EG	End bearing load with ground support
EN	European standard
EOF	End-one-flange
ETF	End-two-flange
F^{sbs}	Short-beam strength
$\mathrm{F_m}$	Mean value of fabrication factor
FE	Finite element
FRP	Fibre Reinforced Polymer
G_{fc}	Longitudinal compressive fracture energy
G_{ft}	Longitudinal tensile fracture energy
G_{mc}	Transverse compressive fracture energy
G_{mt}	Transverse tensile fracture energy
GF	Glass Fibre
GFRP	Glass Fibre Reinforced Polymer
H	Profile depth
I_F	Tsai–Hill failure index
IG	Interior bearing load with ground support
IOF	Interior-one-flange
ITF	Interior-two-flange

L	Length of the specimen
LRFD	Load Resistance Factor Design
LL	Live load
M_m	Mean value of material factor
N	Length of bearing plate
NAS	North American Specification
P_{EXP}	Experimental web crippling strength
P_m	Mean value of load ratio
P_{mi}	Maximum load in interlaminar shear test
P_n	Nominal web crippling strength
P_{Num}	Numerical web crippling strength
P_u	Ultimate load
R	Strength reduction factor
R_P	Proposed strength reduction factor
R_i	Inside bend radius
RP	Reference Point
RH	Rectangular Hollow Section
SD	Standard deviation
SEM	Scanning electron microscopy
S4R	Four noded reduced integration conventional shell element having six degrees of freedom per node
SC8R	Eight noded continuum shell element having three degrees of freedom per node with reduced integration
S_{12}	In-plane shear strength
S_{23}	Transverse shear strength

$S_{t,i}$	Tensile strength in direction *i*
$S_{c,i}$	Compressive strength in direction *i*
S_s	Bearing length
UTM	Universal testing machine
V_F	Coefficient of variation of fabrication factor
V_M	Coefficient of variation of material factor
V_P	Coefficient of variation of load ratio
V_x	Coefficient of variation
WF	Wide flange material design values
X_d	Material design value
X_k,	Characteristic value
X_m	Mean value
X_{SD}	Standard deviation
a	Perforation size or diameter
b_{plate}	Bearing plate width
b	Specimen width in interlaminar shear test
d	Overall depth of member
d_{shear}	height of equivalent rectangular area
e	Depth of impression in units of 0.002 mm in Rockwell Hardness test
f_s	Interlaminar shear strength
$f_{cu,T}$	Transverse compression strength of GFRP member
$f_{u,L}$	Longitudinal strength
$f_{u,T}$	Transverse strength
f_y	Longitudinal tensile strength of the web

h	Depth of the web or web height
h_w	Depth of the web or web height
k	Distance from top of flange to the web toe of the fillet
k_e	Effective length factor
k_n	Characteristic fractile factor
r	Inside bend radius
s	Measured specimen thickness in interlaminar shear test
t	Thickness of section
t_f	Thickness of flange
t_p	Thickness of bearing plate
t_{plate}	Thickness of bearing plate
t_w	Thickness of web
x	Distance of the perforation from the edge of the bearing plate
α_b	Member section constant
α_c	Member slenderness reduction factor
α_d	Load dispersion angle
α_i	Parameter that takes into account the effect of shear stress to the fibre tension index in the Hashin damage criterion
α_k	Correction factor
β	Reliability Index
β_d	Load dispersion angle
β_o	Target reliability Index
γ_{12}	Shear strain
γ_{f1}	Sub-factor related to the uncertainty level of determining the properties of GFRP

γ_{f1}	Sub-factor relating the fragile behaviour of the GFRP
γ_M	Material partial safety factor
$\gamma_{M,1}$	Sub factor associated with the uncertainty level in obtaining the GFRP properties
$\gamma_{M,2}$	Sub factor associated with the production process and curing of the GFRP profiles
γ_m	Material partial safety factor
$\gamma_{m,1}$	Partial safety coefficient associated with the uncertainty level in obtaining the GFRP properties
$\gamma_{m,2}$	Partial safety coefficient associated with the production process and curing of the GFRP profiles
$\gamma_{m,3}$	Partial safety coefficient associated with the environmental effects and duration of loading on the structure
ε	Strain
ε_1	Strain obtained from the strain gauge $1(0^o)$ in 10^o off-axis test
ε_2	Strain obtained from the strain gauge $2(45^o)$ in 10^o off-axis test
ε_3	Strain obtained from the strain gauge $3(90^o)$ in 10^o off-axis test
η	Conversion factor
η_c	Conversion factor
η_{ct}	Conversion sub-factors for temperature effect
η_{cm}	Conversion sub-factors for humidity effect
η_a	Conversion factor associated with environmental effects
η_l	Conversion factor associated with long term effects
θ	Angle between the plane of web and plane of bearing surface
λ	Non-dimensional slenderness ratio

λ_n	Modified member slenderness
σ_i	Stress in direction *i*
σ_L	longitudinal stress
σ_T	Transverse stress
σ_{xx}	Stress value in the loading direction
τ_{12}	In-plane shear stress
τ_{in}	Interlaminar shear strength
τ_{LT}	Shear stress
$\tau_{u,LT}$	Shear strength
Φ	Resistance factor
χ_F	Buckling reduction factor

This page is intentionally left blank.

CHAPTER 1

INTRODUCTION

1.1 BACKGROUND

Use of Fibre Reinforced Polymer (FRP) composite materials such as Glass Fibre Reinforced Polymer (GFRP) in the construction industry has gained significant popularity in the last few decades. Several new buildings and bridges have been constructed and numerous existing structures are strengthened and retrofitted with these materials. Fibre reinforced polymer composites are manufactured by embedding fibres in a matrix of polyester, epoxy, vinylester, or phenolic thermosetting resins where fibre concentrations are usually greater than 30% by volume (e.g. Bank, 2006). Different types of fibres are available e.g. glass, carbon, aramid etc. which can be used for different purposes. A comparison of the properties of different fibre materials is given in Table 1.1. FRP composites are used in the construction industry mainly in three different forms such as a) strips and sheets for external strengthening of concrete and steel; b) internal reinforcing bars for concrete members; and c) full section structural profiles (see Figures 1.1a–c and Figures 1.2a–d). These materials are supplied by the manufacturer in different forms or components such as reinforcing bars, full section profiles and as dry fibre/fibre mats with liquid polymer resin that can be formed and cured at the site for achieving the required sizes of structural components. The main advantages of the FRP materials over other traditional materials such as concrete and steel; are their high strength-to-weight ratio, corrosion resistance, resistance to frost and de-icing salt, electromagnetic transparency, good electrical insulation, lower maintenance cost and their quick and easy transportation and installation at the site etc. In contrast, some disadvantages such as lack of ductility, low fire resistance and a lack of consensus design standards have restricted their widespread use. However, researchers are constantly putting their efforts to overcome the disadvantages and improve the quality of these materials. Various manufacturing methods (e.g. pultrusion, hand layup, filament winding, resin transfer molding and vacuum assisted resin transfer molding) are employed to produce the FRP section profiles (e.g. Bank, 2006). However, in the last three decades, the pultrusion method has gained significant popularity as this method on industry scale, can manufacture good-quality uniform cross-section FRP structural profile shapes at moderately low cost (e.g. Bank, 2006). Pultrusion is a process (Figure 1.3), where fibres are impregnated with a resin matrix material and are continuously being pulled through the heated equipment and cured for the required geometry, and subsequently cut into required lengths. The pultruded materials used in the pultrusion process mostly consist of different fibre reinforcements such as glass fibre or carbon fibre and thermosetting resins such as polyester, vinylester, and epoxy polymers. In some cases, in order to improve the mechanical or physical properties of the pultruded profiles, woven fabrics, fibre mats are also used along with the unidirectional roving layers. Manufacturers also use different chemical catalysts and promoters, inorganic fillers, ultraviolet retardants, release agents, fire retardants, pigments and surfacing veils etc. for improving the properties of pultruded materials.

1.2 USES OF PULTRUDED FRP PROFILES

Over the past decades, various braced framed structures and truss structures have been built using the pultruded FRP members including building frames, pedestrian bridges, stair towers, vehicular bridges, cooling towers, and walkways and platforms (e.g. Bank, 2006; Potyrala, 2011 etc.). The first FRP pultruded structure was a single-story gable frame structure and was used for Electromagnetic Interference (EMI) test laboratories (Figure 1.4a) (Bank, 2006). These buildings required electromagnetic transparency above the foundation level and the FRP profiles provided the benefit. Ceramic Cooling Tower (CCT) was developed with these profiles in the 1980s by Composite Technology Inc. (Figure 1.4b) that consisted of numerous unique FRP beams, columns, and panels. Large numbers of long and short span pedestrian footbridges of lengths 9 to 27 m have been designed and constructed worldwide using pultruded FRP profiles (Potyrala, 2011). A typical FRP pedestrian bridge designed and constructed by ApATeCh is shown in

Figure 1.5a. Figure 1.5b depicts an image of the Russian first FRP Bridge during installation which was completed with an installation period of only one hour. Other than buildings and bridges, FRPs are also being widely used for other purposes such as electric fencing (good insulation to electricity), as drain covers (good corrosion resistance) etc. in different parts of the world (see Figures 1.6a–b).

1.3 STRUCTURAL BEHAVIOUR OF FRP PROFILES

Though the shapes of the FRP materials are similar to structural steel but the mechanical properties of FRP are not the same. The FRPs are brittle and the strength (tension or compression) in the longitudinal direction or pultrusion direction can be in the range of 200 MPa to 500 MPa (e.g. Correia, 2012; Fernandes *et al*., 2015) which is comparable to structural graded steel. But the elastic modulus of these materials in the longitudinal direction varies between 20 GPa and 35 GPa which is only about 1/6 to 1/10th of steel (e.g. Correia, 2012; Fernandes *et al*., 2015). A comparison of the properties of different construction materials is given in Table 1.2. Presently, different pultrusion manufacturers are producing these pultruded shapes for commercial and structural applications worldwide. However, there are no standard geometries and standard mechanical and physical properties for the FRP profiles to be adopted for structural applications. Their properties may vary depending upon the different strategies adopted for embedding the different fibre layers and mats in the resin with different stacking sequences. Though the manufacturers supply these data but many a times, incomplete property data are provided. Also, the FRP members are non homogeneous and anisotropic in nature, hence, the strength and stiffness properties can change within the cross section on the fibre, lamina, and laminate levels (Bank, 2006). Therefore, it is always recommended to have an independent estimation and verification of the material properties of FRPs prior to their structural applications (Bank, 2006).

Because of the low stiffness-to-strength ratio of the FRP members, their structural behaviour is dominated by excessive deformations in the service limit states (SLS) and global and/or local buckling behaviour in the ultimate limit states (ULS) (e.g. Clarke, 1996; Chambers, 1997; Correia, 2012). The FRP profiles when used as column members fail due to the lower axial stiffness and the buckling behaviour (global or local) that prevent the members to attain their ultimate strengths. These members while subjected to transverse loading, are very much susceptible to lateral torsional buckling (e.g. Turvey, 1996; Razzaq *et al*., 1996; Shan and Qiao, 2005; Correia, 2012; and Nguyen *et al.*, 2014), local buckling phenomenon in the webs and flanges and material crushing under transverse concentrated loading (e.g. Borowicz and Bank, 2011; Fernandes *et al*., 2015; Wu *et al.*, 2019) etc. Lack of consensus design standards has prompted the researchers to extensively investigate the material behaviour and local and global buckling phenomenon of these profiles by employing experimental, analytical and numerical studies. Significant numbers of studies have been performed and new design equations and procedures have been established for predicting the load carrying capacity, failure pattern and enhancing the performance of these members. But there are still several technical requirements and questions that need be addressed before FRP profiles can be extensively used.

1.4 GAP AREAS AND OBJECTIVES

In the last few years, several Indian FRP manufacturers have started producing pultruded GFRP profiles and their uses have rapidly increased. On the other hand, limited technical test data of the GFRP materials manufactured in India are available in the public domain (e.g. Singh and Chawla, 2018; Singh and Chawla, 2019; Sirajudeen and Sekar, 2020) which can be used for research or development of design codes for GFRP structures. Also, to the best of authors' knowledge, no Indian standards/guidelines are available for suggesting the test procedures for these materials. Henceforth, extensive investigations and proper comparisons are required in order to establish reliable design guidelines.

Due to lower mechanical properties in their transverse direction than the pultruded or longitudinal direction, GFRP sections are very much susceptible to web crippling failure when loaded in the transverse direction (when used as rafters, purlins etc.) (e.g. Borowicz and Bank, 2011; Fernandes *et al.*, 2015; Wu and Bai, 2014; Chen and Wang, 2015; Wu *et al.*, 2019). The web crippling failure in GFRP profiles mainly involves web buckling, web-flange junction separation, crushing of web or web shearing (e.g. Borowicz and Bank, 2011; Fernandes *et al*., 2015 and Wu *et al*., 2019). However, very limited research (e.g. Borowicz and Bank, 2011; Fernandes *et al.*, 2015; Wu and Bai, 2014; Chen and Wang, 2015; Wu *et al.*, 2019; Zhang and Chen, 2017) on the web crippling behaviour of GFRP profiles has been reported. Researchers have mostly focused on the effects of bearing length (Borowicz and Bank, 2010; Chen and Wang, 2015; Fernandes *et al*., 2015; Chen and Wang, 2015; Zhang and Chen, 2017), bearing plate thickness (Borowicz and Bank, 2010), slenderness ratio (Borowicz and Bank, 2010; Wu and Bai, 2014; Fernandes *et al*., 2015; Wu *et al*., 2019) and loading (e.g. end two flanges (ETF) and interior two flanges (ITF)) and support boundary conditions (specimens seated on bearing plate or on the ground) (Wu and Bai, 2014; Chen and Wang, 2015; Fernandes *et al*., 2015; Chen and Wang, 2015; Zhang and Chen, 2017; Wu *et al*., 2019), on the web crippling phenomena of GFRP profiles. However, contradictory findings have been reported in case of bearing length effect on web crippling behaviour of GFRP profiles. Borowicz and Bank (2010) and Fernandes *et al*. (2015) reported an enhancement in the ultimate crippling strength with increasing bearing length, whereas, Chen and Wang (2015), Chen and Wang (2015) and Zhang and Chen (2017) reported that increasing the bearing length did not increase the ultimate capacity of the GFRP profiles. Therefore, considering the availability of limited experimental data and inconsistency in the effect of plate bearing length, it is assumed that, addition of more experimental data would be useful in gaining further insight into the web crippling behavior of GFRP profiles. Additionally, it can be said that previous web crippling design equations were developed based on the experimental test data on GFRP I–sections of various sizes e.g. overall section depth of 152.4 to 304.8 mm (Borowicz and Bank, 2010); 100 to 400 mm (Fernandes *et al*., 2015); 99.50 mm (Chen and Wang, 2015). In this context, their suitability can be assessed with additional test data for other section sizes. Further, to the author's knowledge, the effect of web perforations (or openings) on the web crippling behaviour of GFRP section profiles has been rarely investigated till date. Moreover, perforations in the web are required for various purposes such as to pass services (plumbing and electrical services) through the web, for ease of connections in built-up members or when the GFRP profiles are used as wall studs or floor joists etc. (Figures 1.7a–b). To the best of authors' knowledge, Gand *et al*. (2020) investigated web crippling behaviour of GFRP I–beams considering rectangular and circular web perforation under various loading conditions. The study reported a reduction of around 20% and 25% in the load-carrying capacity with circular (a/h = 0.72; a being the perforation size and h being the web height) and rectangular web perforation (a/h = 0.54), respectively. However, the investigation considered only a particular perforation size (a/h = 0.72) and did not include the effect of varying perforation sizes.

Henceforth, highlighting the aforementioned gap areas, and to include additional data to the current database on GFRP materials and share the test data for GFRPs manufactured in India for potential development of Indian standards for GFRP structural members, an experimental test programme has been conducted for various GFRP structural profiles produced by an Indian pultruder (Bajrang Agencies, Guwahati). In addition, an attempt has been made in order to study the web crippling behaviour of GFRP wide flange (WF) sections with and without perforations. The goal of the research program will be to develop design equations that will govern the web crippling behaviour of GFRP WF-section profile with and without perforations subjected to transverse web crippling load. The main objectives of the present study are itemised below:

1) To study the mechanical properties of GFRP profiles produced by an Indian manufacturer.
2) To investigate the effect of bearing lengths and thickness on the web crippling behaviour of GFRP WF-sections.
3) To assess the effect of perforation diameter on the web crippling behaviour of GFRP WF-sections with web perforations.

1.5 THESIS OUTLINE

The content of the thesis is split into six chapters.

A brief background on the present research work is introduced in **Chapter 1,** as well as the main objectives of the research effort followed by thesis outlines. In **Chapter 1**, the main focus is given on the behaviour of a fairly new and promising material Glass Fibre Reinforced Polymer (GFRP) under different loading configurations, particularly on its web crippling behaviour with and without perforation.

In **Chapter 2,** discussions on the various literature pertaining to the current work is presented. The literature review has been roughly arranged into different sub-headings *viz.*, structural behaviour of GFRP profiles, web crippling behaviour of unperforated and perforated GFRP profiles, and design rules for web crippling of GFRPs. Also, reviews on literature related to FE modelling of GFRP profiles have also been discussed.

In **Chapter 3,** a comprehensive study on the mechanical properties and behaviour of GFRP pultruded profiles of various shapes and sizes has been presented. Based on the experimental data, design stresses and moduli values have been obtained considering four design guidelines.

Chapter 4 investigates systematically the effects of bearing lengths and plate thickness on the web crippling behaviour of unperforated GFRP wide flange (WF) –section profile, under ITF and ETF loading conditions. FE models have also developed and validated with the experimental results. Applicability of existing design rules for web crippling of GFRP profiles have been verified with the experimental data and improved design equations have been proposed.

In **Chapter 5, t**he work summarised in Chapter 4 on the web crippling of unperforated GFRP WF–section profile, is further extended for sections with circular web perforation. In **Chapter 5**, the investigation on the effect of perforation diameter on the web crippling behaviour of GFRP WF-section profiles have been presented.

In **Chapter 6,** the key findings obtained from the present research effort on unperforated and perforated GFRP WF–section profiles have been summarised. Also, some of the possible future works that can be extended from present study have been highlighted in **Chapter 6**.

Sample design calculations for web crippling strength of GFRP wide flange profile sections with and without perforation have been presented in **Appendices A-B**.

Table 1.1: Typical properties of glass, aramid and carbon fibres (Potyrala, 2011).

Typical properties	Fibres					
	Glass		Aramid		Carbon	
	E-glass	S-glass	Kevlar-29	Kevlar-49	HS (High strength)	HM (High modulus)
Density (g/cm^3)	2.6	2.5	1.44	1.44	1.8	1.9
Young's Modulus (Gpa)	72	87	100	124	230	370
Tensile strength (Mpa)	1.72	2.53	2.27	2.27	2.48	1.79
Extension (%)	2.4	2.9	2.8	1.8	11	0.5

Table 1.2: Comparison of properties of different construction materials to various FRP composites (Potyrala, 2011).

Typical properties	Materials					
	Duralu minium	Titan TiA 16Va4	Steel St52	GFRP	CFRP quasiisotr. vol. fraction	CFRP orthotropic vol. fraction 80%
Density (g/cm^3)	2.8	4.5	7.8	2.1	1.5	1.7
Young's Modulus (Gpa)	75	11	210	30	88	235
Tensile strength (Mpa)	350	800	510	720	900	3400

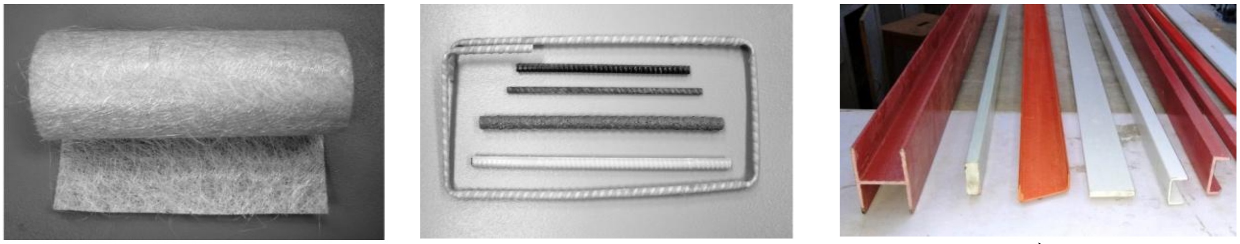

a) b) c)

Figure 1.1: a) E-glass continuous filament mat (Bank, 2006); b) FRP reinforcing bars (Bank, 2006); and c) FRP pultruded profiles.

a) b)

Figure 1.2: a) FRP wrapping of highway bridge columns (Bank, 2006), b) bridge deck construction using FRP reinforcing bars (owenscorning.com).

c) d)

Figure 1.2: c) Footbridge in Poland (grotteart.pl; Potyrala, 2011); d) FRP shelter house (karmod.eu).

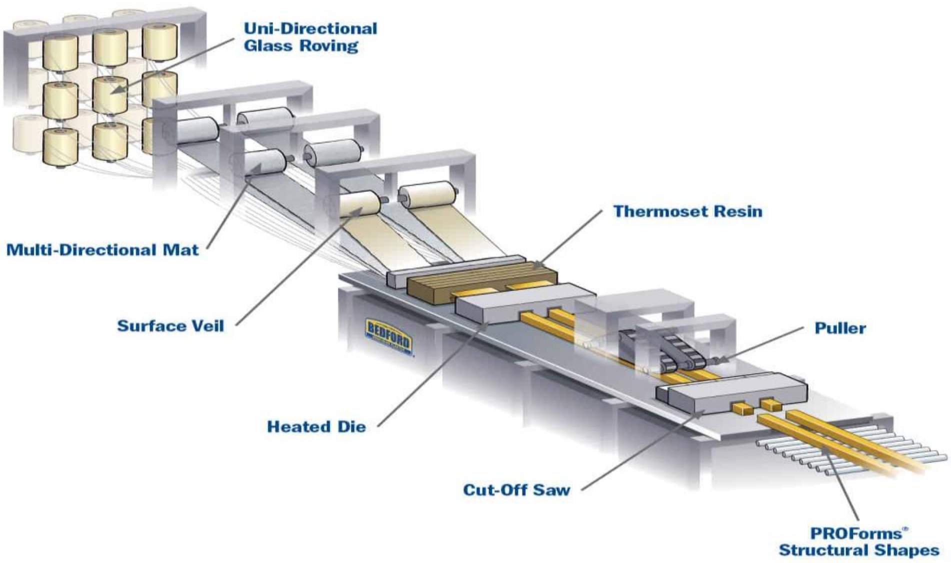

Figure 1.3: Pultrusion process (bedfordreinforced.com).


a)


b)

Figure 1.4: a) FRP Gable frame structure (courtesy: Strongwell; Bank, 2006); b) FRP cooling tower (Bank, 2006).


a)


b)

Figure 1.5: a) FRP arch footbridge; b) Railway pedestrian bridge (apatech.ru; Potyrala, 2011).

a) b)

Figure 1.6: a) FRPs used for fencing purpose surrounding electric transformer; and b) FRP drain covers used in Guwahati city, India.

Figure 1.7: a) Cellular beams (newsteelconstruction.com); and b) Floor joist with perforation (weland.com).

This page is intentionally left blank.

CHAPTER 2

LITERATURE REVIEW

2.1 INTRODUCTION

The use of Fibre Reinforced Polymer (FRP) pultruded profiles, as structural beam and column members, as the replacement of conventional steel and concrete structural members in various structures has been increased rapidly due to their high durability and lightweight properties. However, their structural behaviour is driven by excessive deformations and global and/or local buckling behaviour (e.g. Corria, 2012). For many years, researchers are extensively investigating the material behaviour; and local and global buckling phenomenon of these profiles under various loading conditions etc. by employing experimental, analytical and numerical studies. As mentioned before in Chapter 1, FRP structural members can be obtained by several processes such as pultrusion, hand layup, filament winding, resin transfer molding and vacuum assisted resin transfer molding etc. Amongst the different types, pultruded sections are the most popular types, used worldwide for construction purposes (e.g. Bank, 2006; Potyrala, 2011). In this chapter, a detailed review on the works performed by various researchers on pultruded FRP profiles is presented. Brief introduction on the uses of FRP profiles in the construction industry, by keeping a particular attention to the work related to pultruded Glass Fibre Reinforced Polymer (GFRP) profiles is presented. Although, not related to the present work (web crippling behaviour of GFRP wide flange profile), a brief review on the literature relating to the compression and flexural performance of GFRP profiles are also presented, to provide an overview of the research work on the structural behaviour of GFRP profiles. Following this, a detailed review on the research work relating to web crippling behaviour of GFRP profiles with and without perforation is presented. A summary of the previously proposed design rules for web crippling of GFRP profiles is also presented along with design recommendations for steel sections with perforation. Further, discussion on the key finite element (FE) modelling parameters such as material models and failure criteria, element type, imperfections etc. for carrying out FE analysis (nonlinear imperfect analysis) of GFRP profiles, is also highlighted. At the end, a brief summary of the literature review is presented.

2.2 GFRP AS STRUCTURAL MEMBERS

In the civil construction industry, structural engineers have been utilizing various pultruded GFRP open (I-, channel, angle etc.) and closed (circular, square, rectangular hollow) section types (e.g. Bank, 2006; Potyrala, 2011; Guades *et al.*, 2014; Cardoso and Togashi, 2018; Turvey and Zhang, 2018) for construction of various structures such as pedestrian bridges, building frames, vehicular bridges, cooling towers, and walkways and platforms etc. (e.g. Bank, 2006; Potyrala, 2011). The GFRP profile shapes are similar to the shapes of the steel sections. However, the mechanical properties of the GFRP profiles are not the same as that of steel as GFRP materials are brittle and anisotropic. The tensile or compressive strength of the GFRPs in the pultrusion direction is in the range of 200–500 MPa (e.g. Correia, 2012; Fernandes *et al.*, 2015) which is comparable to the structural steel. However, the elastic modulus values in the longitudinal or pultrusion direction varies between 20–35 GPa (around 1/6 to 1/10th of steel's Young's modulus) (e.g. Correia, 2012; Fernandes *et al.*, 2015). As GFRPs are anisotropic material, it is important for the designers to identify the mechanical and physical properties of the GFRP materials in each direction for design purpose. In this regard, a number of studies can be found on the mechanical behaviour (e.g. tensile, compression, in plane shear) of GFRP profiles (e.g. Guades *et al*., 2014; Zhang *et al*., 2018; Quadrino *et al*., 2018).

2.2.1 Behaviour of GFRP profiles under compression

The use of GFRP pultruded profiles as column members have increased manifold due to their better compressive performance, as, the fibres in the pultruded GFRP sections are oriented either fully or mostly towards the axial or pultruded direction. Significant numbers of studies (e.g. Hashem and Yuan, 2001; Correia *et al*., 2012; Nunes *et al*., 2013; Nunes *et al*., 2016; Nunes *et al*., 2016; Sirajudeen and Sekar, 2020) have been reported in this regard and new design equations/procedures have been established for predicting the load carrying capacity, failure patterns and enhancing the axial performance of the GFRP members.

Hashem and Yuan (2001) carried out both analytical and experimental studies to establish a distinguishing criterion between short and long column behaviors for GFRP columns with universal and box sections. It was concluded that Euler's formula provided accurate results in predicting the critical buckling load of GFRP columns and serviceability criteria prevailed over the strength criteria in their design. Correia *et al*. (2012) studied the buckling behavior and strength of short columns considering GFRP I-section profile and Carbon Fibre Reinforced Polymer (CFRP) strengthened GFRP I-section profile (hybrid column). The study concluded that failure in both cases occurred at the web-flange junction with clear separation between the flanges and the web. Further, improvement in the critical load, ultimate load, and the axial stiffness were reported in case of CFRP strengthened GFRP profiles. Nunes *et al*. (2016) assessed the buckling behaviour of hybrid (GFRP and CFRP) FRP I-section columns and the delamination phenomena at the interface between GFRP and CFRP layers under compression. It was reported that the axial stiffness of GFRP members was increased by hybridization and resulted in higher global buckling critical load. According to Nunes *et al*. (2016), delamination was a major issue in the structural performance of hybrid (GFRP and CFRP) FRP I-section columns. The study also discussed applicability of the existing design procedures for evaluating the ultimate loads of the FRP columns. Nunes *et al*. (2013) concluded that small eccentricities in GFRP I-section members were significant in the behavior of GFRP members under compression. Sirajudeen and Sekar (2020) reported that the main failure modes in the GFRP angle sections under compression were the web flange junction separation and the ultimate load was directly related to cross sectional slenderness of the profiles.

2.2.2 Behaviour of GFRP profiles under flexure

Pultruded GFRP profiles have been used as members in vertical braced frame or horizontal unbraced grid structures, as well as plate or T-girders in bridge deck systems since they can be swiftly connected using the traditional mechanical connectors (e.g. Potyrala, 2011). However, their widespread use has been hampered by the lack of consensus design procedure (e.g. Correia *et al*., 2012; Nunes *et al*., 2016).

GFRP members (open sections such as I or channel sections) under flexure are very much susceptible to lateral torsional buckling, local buckling phenomenon in the webs and flanges and material crushing etc. Studies regarding the flexural performance of GFRP profiles have been reported and new design equations have been developed (e.g. Nunes *et al*., 2016; Correia, 2012; Insausti *et al*., 2009; Correia *et al*., 2011; Singh and Chawla, 2018; Singh and Chawla, 2019; Chawla and Singh, 2019). Nunes *et al*. (2016) reported the flexural performance of hybrid FRP I-shaped beams made of glass fibres (GF) and carbon fibres (CF). Four-point bending tests were performed and was seen that the hybrid beams exhibited higher bending stiffness than the reference GFRP beams. It was concluded that the failure was governed mainly by the in-plane shear strength, and the CF reinforcement was ineffective in improving the ultimate behavior of the beams. The Hashin damage criterion (Hashin, 1980) was found to be accurate in modeling the delamination and progressive collapse of hybrid FRP pultruded flexural members. Insausti *et al*. (2009) investigated the interaction between lateral and local buckling on GFRP I-beams and proposed new design equation to evaluate the lateral buckling bending moments. Correia *et al*. (2011) reported that the instability phenomena such as local or global buckling always prevailed over the strength criteria of GFRP I-beams. Correia (2012) investigated flexural performance of GFRP I-beams and found that the beam material failed before local buckling could occur in the GFRP profiles. Singh and Chawla (2019) studied the effect of stiffening elements in the flexural performance of GFRP I-beams considering various stiffening elements such as GFRP cover plates, bearing stiffeners, cover angles and carbon fibre layers with adhesive etc. It was concluded that beams strengthened with short bearing stiffeners exhibited higher strength than those strengthened using other stiffening elements. In a companion paper, Chawla and Singh (2019) reported that stability, failure loads and service loads of the GFRP beams were enhanced by the use of stiffening elements. However, it was observed that stiffening elements such as cover angle, bearing stiffeners and carbon fibre layers were more effective in increasing the ultimate strength than using cover plate.

2.3 WEB CRIPPLING BEHAVIOUR OF GFRP PROFILES

As discussed previously, GFRP members are highly orthotropic and have lower mechanical properties in their transverse direction than the pultruded direction (e.g. Guades *et al*., 2014; Fernandes *et al*., 2015; Bank, 2006). The webs of the GFRP profiles often comes under transverse in-plane loading when used as floor joist members, purlins and rafters etc. and may fail by a phenomenon termed as "*web-crippling*". In case of metallic sections, the web-crippling failure behaviour primarily involves web yielding and web buckling (e.g. Packer, 1984; Young and Hancock, 2001; Wu *et al*., 2011). However, in case of GFRP profiles, the web crippling failure behaviour mostly comprises web-flange junction separation, crushing of web or web shearing and web buckling (e.g. Borowicz and Bank, 2011; Fernandes *et al*., 2015; Wu *et al*., 2019). NAS (2007) identified four main loading configurations for investigating the web crippling phenomenon: a) end-one-flange (EOF), b) end-two-flange (ETF) c) interior-one-flange (IOF), and d) interior-two-flange (ITF) loadings. These loading configurations differ in the location of the cross-section subjected to web crippling loading (End or Interior) and also in the number of flanges (One or Two) that comes under concentrated load. The web crippling failure in GFRP profiles is a key concern for the engineers and designers due to their weaker mechanical properties in the transverse direction than the pultrusion direction. In the literature, limited research work on the web-crippling phenomenon of GFRP profiles have been reported (e.g. Borowicz and Bank, 2011; Fernandes *et al*., 2015; Wu and Bai, 2014; Chen and Wang, 2015; Wu *et al*., 2019). In the following sections, a review on the literature available for web-crippling of unperforated and perforated GFRP profiles is presented. Detailed discussion on the existing design equations will be provided in the subsequent section (Section 2.4).

2.3.1 Web crippling of GFRP profiles without perforation

Borowicz and Bank (2010) studied the structural performance of FRP I–beams under web crippling load. Both experimental and numerical investigation was carried out. In the test program, the depths of the sections were varied from 152.4 to 304.8 mm and experiments were performed with and without bearing plates of different thicknesses and widths. It was found that the use of bearing plates increased the beam capacity by around 35% and the web crippling capacity of the beams were influenced by the bearing plate width and thickness. The failure exhibited by the test specimens were in a wedge-like shear failure pattern at the upper web-flange junction. Finite element analysis results were in good agreement with the experimental findings from strain gauge and digital image correlation data. Finally, design equation was developed based on AISC (2005) and NAS (2007) design rules to predict the web crippling capacity of GFRP I–beams as function of different parameters such as interlaminar shear strength, length of bearing, member depth, bearing plate width and thickness etc.

Wu and Bai (2014) experimentally studied the web crippling behaviour of GFRP square hollow sections (depths of sections ranging from 50.2 mm to 102.7 mm) subjected to web crippling load. The study considered four loading conditions such as end-two-flange (ETF), interior-two-flange (ITF), end bearing load with ground support (EG) and interior bearing load with ground support (IG). The effects of loading and support conditions on the web crippling behaviour of the GFRP members were discussed. In all specimens, initial failure started at the web–flange junctions and later on was followed by buckling or crushing in the webs. It was observed that both elastic limit load and ultimate load were greatly enhanced when the loading position was shifted from end loading to interior loading position. In contrast, it was seen that the elastic limit load was not influenced by the support conditions; rather it was governed by the web–flange junction failure mechanism. Finally, an effective web area in the pultrusion direction was established to describe the load transfer path within the web and a new design equation for determining the web crippling strength of GFRP sections was proposed based on the experimental findings.

An experimental study was carried out by Fernandes *et al*. (2015) on the web-crippling behaviour of GFRP I-beams. The experimental programme included web-crippling tests on four different I-section profiles with depth of the sections ranging from 100.0 mm to 400.0 mm. Two load configurations such as interior two flanges (ITF) and end two flanges (ETF) were considered for the web-crippling experiments considering different bearing lengths (15 mm, 50 mm, and 100 mm). Influence of bearing lengths on the web-crippling phenomenon was found to be significant, specifically in the ultimate capacity and the stiffness of the I-profiles. It was found that when the bearing length was increased from 15 mm to 100 mm, the web-crippling strength was increased by +139% and +230%, for the ITF and ETF load configurations, respectively. Similarly, the stiffness of the test specimens increased by up to +129% and +224%, respectively for the two loading configurations.

Fernandes *et al*. (2015) conducted numerical study on the web-crippling behavior of GFRP I-beams for validating with their previous study (Fernandes *et al*., 2015). It was reported that the increasing the bearing lengths increased the sensitivity of the GFRP profiles from web crushing to web buckling failure. From the stress component analysis, it was found that shear stresses had higher influence over other stresses in the failure of the GFRPs. A new design equation was developed based on the formulations given in NAS (2007) and Eurocode EC3: 1–5 (2006) to predict the web-crippling strength of GFRP profiles.

Chen and Wang (2015) investigated the effects of loading positions, support conditions and bearing lengths on the web crippling behaviour of GFRP rectangular hollow section (depth of section = 100.28 mm). The GFRP specimens exhibited two different failure modes after the initial web-flange junction failure: web bending and web crushing. It was reported that change in bearing length had no effect in increasing the web crippling capacity of the GFRP specimens. Also, it was reported that specimens tested with interior loading exhibited larger ultimate strengths than those tested with end bearing load. The study proposed design equations based on Eurocode3 (2005) for predicting the web crippling strengths of GFRP rectangular hollow sections under various loading and boundary conditions for depth of sections ranging from 100 mm to 400 mm.

Wu *et al*. (2019) studied the effects of length of specimen, cross sectional dimensions and transverse loading conditions on the web crippling behavior of pultruded GFRP channel sections. In the experimental program, 4 channel sections with different dimensions (depth of sections ranging from 102.0 mm to 203.0 mm) were considered and specimens were tested under ETF and ITF loading conditions adopting two specimen lengths for each section. It was observed that the web slenderness ratio, loading condition and specimen length greatly influenced the failure modes of the specimens, as well as the ultimate capacities. It was observed that failure mode changed from web-flange junction failure to web buckling failure when web slenderness ratio or specimen length was increased, or the loading condition was shifted from ITF to ETF. It was seen that all GFRP specimens failed owing to web-flange separation at the junction or web buckling at peak load. Design equations for web crippling of GFRP channel sections were proposed pertaining to different failure mechanisms such as initial web-flange junction failure and initial web buckling failure (based on the formulations in AS4100, 1998).

Zhang and Chen (2017) investigated the effects of loading positions, support conditions and bearing lengths on the web crippling behaviour of GFRP channel section (with section depth = 99.0 mm). The main failure mode of the specimens reported in the study was the web bending failure. It was reported that specimens with interior bearing loading had exhibited higher crippling capacity. The study also concluded that the web crippling strengths of the channel sections were not influenced by the bearing lengths. Design equations were proposed (based on Eurocode3, 2005) for predicting the ultimate crippling load of GFRP channel sections for four different loading configurations (ETF, ITF, EG, IG).

Chen and Wang (2015) studied the web crippling behaviour of GFRP I-sections (section depth = 99.5 mm) considering the effects of various loading conditions and bearing lengths. The main failure modes observed in the GFRP specimens were web bending crack, bending wrinkling cracks and shear cracks. Specimens with interior bearing load were found to exhibit higher web crippling capacities than the specimens with end bearing load. It was also seen that increasing the bearing length decreased the ultimate strengths of the specimens. The study proposed web crippling design rules for GFRP I-sections under ETF, ITF, EG and IG loading and boundary conditions.

Nunes *et al*. (2017) reported progressive damage analysis of GFRP I-sections under web crippling load. The numerical models developed in the study used continuum shell elements and implemented the Hashin damage model for progressive damage analysis. It was reported that the Hashin based analysis resulted in more accurate prediction of the ultimate loads than the Tsai-Hill criterion based analysis. It was found that increasing bearing lengths increased the ultimate load and stiffness of the GFRP specimens. It was also concluded that the Initiation of failure was governed by the in-plane shear stress and strength, whereas, the ultimate behaviour was determined by the transverse compressive stress and strength of the GFRP.

An investigation was carried out by Borowicz and Bank (2013) on the failure mode and ultimate crippling capacity of FRP beams that were stiffened using full-depth web bearing stiffeners, ‘‘doubler’’ plates attached to the web and stiffening elements applied to the upper (loaded) web-flange junction. From the experimental results it was concluded that the development of a shear wedge failure in the upper web-flange junction could not be restricted by using the full-depth bearing stiffeners and the ‘‘doubler” plates. It was reported that formation of shear wedge-like failure in the upper web-flange junction could be prevented by strengthening the upper web-flange junction, however, the failure transferred to the bottom flange of the beam. It was reported that the junction stiffeners, bearing stiffeners, and ‘‘doubler’’ plates increased the ultimate capacity of the beams. It was also observed that the beam with bolted and bonded plates failed at a load 27.7% higher than a similar beam with plates that were only bolted to the web.

2.3.2 Web crippling of GFRP profiles with perforation

Very limited research is available on the effect of perforation on GFRP profiles (e.g. Gand *et al*., 2020). According to author’s knowledge, only Gand *et al*. (2020) reported the web crippling behaviour of I–beams considering rectangular and circular web perforation. The study also considered various loading conditions such as end bearing with solid base (EB), interior bearing with solid base (IB), ITF and ETF loadings. The study reported a reduction in the load-carrying capacity of around 20% for specimens with circular web perforation and 25% for specimens with rectangular web perforation, respectively. Furthermore, it was also concluded that specimens with ITF and IB load configurations showed higher nonlinear behaviour and deformability than the specimens tested with ETF and EB loading configurations.

As research on the web-crippling behaviour of GFRP profiles with web perforations is limited, hence, literatures relating to web crippling of metallic sections with web perforations are reviewed, to get an insight into the behaviour of thin walled structures such as GFRPs in general; as also, many design equations related to the GFRP profiles were based on steel design equations (see Section 2.3.1). Effect of web perforations on the web crippling behaviour of various steel sections has been studied in the recent past (e.g. Lian *et al*., 2016; Uzzaman *et al*., 2012, Uzzaman *et al*., 2013; Yousefi *et al*., 2018). In the following paragraphs, a review on the web crippling behaviour of steel members is presented.

Lian *et al*. (2016) carried out experimental and numerical investigations on the web crippling behaviour of cold-formed steel channel sections with circular web perforation subjected to end-one-flange (EOF) loading configuration. The web perforations considered for the experiments were positioned either at the mid-depth of the web and centred above the bearing plates and with a clear distance to the close end of bearing plates. The web slenderness values of the specimens were varied in the range of 111.7–157.8. The diameter of the web perforation was also varied in the range of 0.2*h*–0.6*h* (*h* is the web height) to study the effect of the web perforations on the web crippling phenomenon. Further, Lian *et al*. (2016) proposed web crippling strength reduction factor equations for cold-formed steel channel sections with circular web perforation.

Experimental and numerical investigations were carried out by Lian *et al*. (2017) on the web crippling behaviour of cold-formed steel lipped channel sections with circular web perforations under interior-one-flange (IOF) loading condition. The perforation sizes were varied in the range of 0.2*h*–0.6*h* and were positioned either at the mid-depth of the web and centred above the bearing plates and with a clear horizontal distance to the close end of bearing plates. The web slenderness values considered were varied in the range of 109–157.8. In a companion paper

(Lian *et al*., 2017), web crippling strength reduction factor equations were proposed for cold-formed steel lipped channel sections with circular web perforations.

Uzzaman *et al*. (2012) investigated the web crippling behaviour of lipped channel sections with circular web perforations with perforation diameter ranging from 0.2*h*–0.8*h* (*h* is the web height). The web slenderness ratios of the test specimens were varied in the range of 116–176. In the study, web crippling strength reduction factor equations were proposed for both cases of flanges fastened and unfastened to bearing plates.

Experimental and the numerical investigations were carried out by Uzzaman *et al*. (2013) on the web crippling behaviour of lipped channel sections with offset web perforations. The perforation diameters and the web slenderness ratios of the test specimens were varied in the range of 0.2*h*–0.8*h* and 112–170, respectively. The study also proposed web crippling strength reduction factor equations for lipped channel sections with offset web perforations.

Uzzaman et al. (2012) performed experimental and numerical investigation on the web crippling behaviour of cold-formed steel channel sections with web perforations under ITF and ETF loading conditions. Web perforation diameters and the web slenderness ratios of the test specimens were varied in the range of 0.2*h*–0.8*h* and 116–176, respectively. The study proposed web crippling strength reduction factor equations for both cases of flanges unfastened and fastened to the bearing plates.

Yousefi *et al*. (2017) investigated the web crippling behaviour of cold-formed ferritic stainless steel unlipped channel sections with circular web perforations subjected to ITF loading. The test programme comprised unlipped channel sections with web perforations located either at the centre or offset to the bearing plates and the flanges were either fastened or unfastened to the bearing plates. In the study, the ratio of the diameter of the web perforation to the web depth (*a/h*) was kept constant at 0.4. The web slenderness (*h/t*) values of the specimens were ranged from 154.25 to 251.75. Based on the study, web crippling strength reduction factor equations were proposed for both offset and centred web perforation.

Yousefi *et al*. (2018) reported a study on the web crippling behaviour of cold-formed ferritic stainless steel unlipped channels with web perforations under IOF and EOF loading configurations. In the study, the web perforation diameters and the web slenderness ratios of the specimens were varied in the range of 0.2*h*–0.8*h* and 148.9–232.6, respectively. Further, web crippling capacity reduction factor equations were proposed for both IOF and EOF loading conditions.

2.4 DESIGN CONSIDERATIONS OF GFRP SECTIONS UNDER WEB CRIPPLING

As discussed in the previous section (Section 2.3), limited research has been carried out on the web crippling behaviour of GFRP profiles. Design formulae for GFRP profiles without perforation have been proposed in the literature by Borowicz and Bank (2011), Wu and Bai (2014), Fernandes *et al*. (2015), Wu *et al*. (2019) and Chen and Wang (2015) based on the design formulations for steel structures (e.g. AS4100, 1998; AISC, 2005; Eurocode3, 2006 and NAS, 2007). In the following subsections, discussion on the design formulations for GFRP section profiles is summarised.

Borowicz and Bank (2010) proposed design equation based on AISC (2005) and NAS (2007) design equations for metallic sections. The equation directly relates the web crippling capacity to the interlaminar shear failure of the web-flange junction and is given by:

$$P_n = 0.7 d t_w f_s \left(1 + \frac{2k + 6t_{plate} + b_{plate}}{d}\right) \tag{2.1}$$

Here, P_n, d, t_w, f_s, k, t_{plate} and b_{plate} are the nominal web crippling strength; overall depth of member; web thickness; interlaminar shear strength of the material in web; distance from top of flange to the web toe of the fillet; bearing plate thickness; and bearing plate width, respectively. According to this equation, the web crippling capacity of a GFRP profile is obtained by adding the initial capacity of the section with the capacity contributed by the bearing plate. The first term in Equation 2.1 is related to the initial web crippling capacity and is a function of the interlaminar shear strength and bearing area of the section. The second term considers the effect of a geometric section property (k) to the initial web crippling strength. The third and fourth terms in Equation 2.1, takes into account the additional capacity contributed by the bearing plate.

The design equation (Equations 2.2 and 2.3) proposed by Wu and Bai (2014) considered that the nominal elastic limit load (P_n) at failure is a function of the interlaminar shear strength (f_s), the shear area under the loading plate (A_{shear}) and the shear stress distribution within the shear area under the bearing plate. In Equations 2.2 and 2.3, the value of a_e fitted for ETF loading condition is 0.58 and the value of a_i fitted for ITF loading is 1.07.

$$P_{ETF} = a_e f_s A_{shear} \tag{2.2}$$

$$P_{ITF} = a_i f_s A_{shear} \tag{2.3}$$

Wu *et al*. (2019) proposed design equations for based on two failure mechanisms observed in the GFRP profiles *viz.* web-flange junction failure and web buckling failure. The web crippling capacity (P_{WFJ}) of pultruded GFRP channel section with initial web-flange junction failure is given as follows:

$$P_{WFJ} = \alpha_k \frac{t_w}{\sin 45°} \tau_{in} K \left(1 - \frac{K^2}{3B_{eff}^2}\right) \tag{2.4}$$

For specimens with web buckling failure, the web crippling capacity (P_n) is given by the following equation which is based on the principles given in AS4100 (1998) for steel web buckling. The equation is given as:

$$P_n = \alpha_c \mathrm{A} f_{cu,T} \tag{2.5}$$

$$A = Kt_w \tag{2.6}$$

$$K = \min\left\{B_{eff}, L\right\} \tag{2.7}$$

$$B_{eff,ETF} = N + \frac{d}{2} + 1.5t_w \tag{2.8}$$

$$B_{eff,ITF} = N + d + 3t_w \tag{2.9}$$

Here, d, t_w, N, $f_{cu,T}$ and τ_{in} are the section depth; web thickness; bearing length; transverse compression strength of GFRP member; and interlaminar shear strength, respectively. α_k is a correction factor equals to 0.8 for ITF loading and 1.0 for ETF loading; and α_c is the member slenderness reduction factor as derived in Wu *et al*. (2019) from AS4100 (1998). B_{eff} denotes the effective length of the web at mid height upto which the transverse loading from the web-flange junction is assumed to be transferred. The value of α_c is given as:

$$\alpha_c = \xi\left(1-\sqrt{\left[1-\left(\frac{90}{\xi\lambda}\right)^2\right]}\right) \tag{2.10}$$

$$\xi = \frac{(\lambda/90)^2+1+\eta}{2(\lambda/90)^2} \tag{2.11}$$

$$\lambda = \lambda_n + \alpha_a\alpha_b \tag{2.12}$$

$$\eta = 0.00326(\lambda - 13.5) \geq 0 \tag{2.13}$$

$$\lambda_n = \frac{\sqrt{12}k_e(d-2t_w)}{t_w} \tag{2.14}$$

$$\alpha_a = \frac{2100(\lambda_n - 13.5)}{\lambda_n^2 - 15.3\lambda_n + 2050} \tag{2.15}$$

Here, α_b is the member section constant and taken to be 0.5, and k_e is effective length factor. For I-section, the value of $k_e = 1.0$ is adopted in AS 4100 (1998) for both ETF and ITF loading.

The equation proposed by Fernandes *et al*. (2015) addresses the occurrence of coupled effect of both web crushing and web buckling phenomena in GFRP I–profiles. The developed formula was a combination of the NAS (2007) and the EC3: 1–5 (2006) design formulae. Fernandes *et al*. (2015) modified the NAS (2007) equation by replacing the yield strength of steel (f_y) by the GFRP transverse strength ($f_{cu,T}$) and Young's modulus (E) by transverse elastic modulus (E_T) in formulating their equation. The equation is given as:

$$P_n = Cf_{cu,T}h_w^2\left(1-C_r\sqrt{\frac{r}{t_w}}\right)\left(1+C_{Lh}\frac{h_w^2N}{t_w^3}\right)\left(1-C_\chi\frac{h_w}{t_w}(1-\chi_F)\right) \tag{2.16}$$

Here, C, C_r, C_{Lh}, C_χ are empirical coefficients; χ_F is the buckling reduction factor; $f_{cu,T}$ is the transverse strength of GFRP member. The coefficient C_{Lh} was proposed to combine the coefficients C_N and C_h of the NAS (2007) equation (see Equation 2.21); and the coefficient C_χ was used to address the web buckling effect.

On the other hand, Chen and Wang (2015) proposed design formula (Equations 2.17 and 2.18) for GFRP I–profiles based on the design formulations given in Eurocode3 (2005) for cold-formed steel sections. The proposed design formulae are as follows:

$$P_{ETF} = \left[9 - \frac{(H - 2t_f)/t_w}{60}\right]\left[1 - 0.01 \times \frac{N}{t_w}\right] t_w^2 f_y \tag{2.17}$$

$$P_{ITF} = \left[12 - \frac{(H - 2t_f)/t_w}{60}\right]\left[1 - 0.01 \times \frac{N}{t_w}\right] t_w^2 f_y \tag{2.18}$$

In Equations 2.17 and 2.18, P_{ETF} and P_{ITF} are the web crippling ultimate capacities under ETF and ITF loading conditions, respectively. H, f_y, and N are the profile depth, longitudinal tensile strength of GFRP profile and bearing length, respectively.

In Eurocode3 (2006) and NAS (2007), the web crippling strength in steel members is the product between yield stress of material and a number of different non-dimensional geometrical ratios. In Eurocode3 (2006), the web crippling design strengths for cold formed steel sections are given as:

$$P_n = k_1 k_2 k_3 \left[6.66 - \frac{h_w/t}{64}\right]\left[1 + 0.01\frac{S_s}{t}\right] t^2 f_y \quad \text{(for ETF loading)} \tag{2.19}$$

$$P_n = k_3 k_4 k_5 \left[21.0 - \frac{h_w/t}{16.3}\right]\left[1 + 0.0013\frac{S_s}{t}\right] t^2 f_y \quad \text{(for ITF loading)} \tag{2.20}$$

Here, P_n, h_w, t, S_s and f_y are the web crippling strength; web height; web thickness; bearing length; and yield stress, respectively. The coefficients k_1 and k_4 take into account the effect of yield stress; k_2 and k_5 account for the ratio of internal radius of the corners to web thickness; and k_3 considers the effect of the angle of the web relative to the flanges.

The design equation proposed by the North American Specification (NAS, 2007) for cold formed steel structures is given as:

$$P_n = Ct^2 F_y \sin\theta \left(1 - C_R\sqrt{\frac{R_i}{t}}\right)\left(1 + C_N\sqrt{\frac{N}{t}}\right)\left(1 - C_h\sqrt{\frac{h}{t}}\right) \tag{2.21}$$

Here, P_n, C, t, F_y and θ are the nominal web crippling strength; overall web crippling coefficient; web thickness; design yield stress and angle between the plane of web and plane of bearing surface ($45° \leq \theta \leq 90°$), respectively. Also, C_R, C_h, C_N, N, R_i and h are the inside bend radius coefficient; web slenderness coefficient; bearing length coefficient; bearing length; inside bend radius and flat dimension of web measured in the plane of web, respectively.

2.5 FINITE ELEMENT MODELING OF GFRP MEMBERS

Finite element analysis is a tool which is often employed to understand the behaviour of structural members and researchers are using this technique to model various GFRP (e.g. Nunes *et al*., 2016; Fernandes *et al*., 2015, Nunes *et al*., 2017; Chen and Wang, 2015) structural members (beams, columns). FE analysis is a relatively cheaper technique and with validated FE models, large number of analysis can be carried out to generate data for facilitating parametric study, thereby covering a number of variables which may not be feasible with experiments. Researchers have used validated FE models to extract and analyse different parameters such as shear stresses, compressive stresses etc. in order to check their influences on the failure mechanism in GFRP profiles (e.g. Fernandes *et al*., 2015, Nunes *et al*., 2017). In FE analysis of GFRP members, numerous factors can influence the accuracy and reliability of the FE models which are primarily element type, material modeling, mesh, loading and boundary conditions, imperfection types etc., and are briefly discussed in the following sections.

2.5.1 GFRP material modeling

Precise material modelling plays significant role in predicting strength and behaviour of structural members. GFRPs are orthotropic in nature and have different strength and stiffness properties in different directions. In modeling GFRP members, the GFRP material is considered to be composite, laminated and elastic. Mainly three failure criteria *viz*. Maximum Stress criterion, Tsai–Hill criterion, Hashin damage criteria have been employed in order to predict the structural behaviour of GFRP members (e.g. Fernandes *et al*., 2015; Nunes *et al*., 2016; Nunes *et al*., 2017) and they are briefly discussed in the following paragraphs.

A) ***Maximum Stress criterion***

The Maximum Stress criterion (Jones, 1998) considers that there is no interaction between the stresses, and failure in a given composite lamina will initiate when any of the stresses (longitudinal, transverse or shear) reaches its maximum value. The stress criterion is defined by the following equations,

$$-S_{c,1} < \sigma_1 < S_{t,1} \tag{2.22}$$

$$-S_{c,2} < \sigma_2 < S_{t,2} \tag{2.23}$$

$$|\tau_{12}| < S_{12} \tag{2.24}$$

Here, σ_i is the stress in direction i (i = 1 for longitudinal, 2 for transverse); both stresses will be positive under tension and negative under compression; and τ_{12} is the in-plane shear stress.

B) *Tsai–Hill criterion*

In Tsai–Hill criterion (Jones, 1998; Tsai, 1968), interaction between the material strength components and acting stresses such as longitudinal, transverse and shear stresses of a composite layer, is considered. This criterion is presented in the form of a failure index known as Tsai–Hill failure index (I_F) and is given by the equation,

$$I_F = \frac{\sigma_L^2}{f_{u,L}^2} - \frac{\sigma_L \sigma_T}{f_{u,L}^2} + \frac{\sigma_T^2}{f_{u,T}^2} + \frac{\tau_{LT}^2}{\tau_{u,LT}^2} < 1.0 \tag{2.25}$$

In Equation 2.25, $f_{u,L}$, $f_{u,T}$ and $\tau_{u,LT}$ are the longitudinal, transverse and shear strengths; σ_L, σ_T and τ_{LT} are the longitudinal, transverse and shear stresses of the composite lamina. At a given node, if the failure index value reaches 1.0 then the node is said to be at the onset of failure. Though the Tsai–Hill failure criterion takes into account the stress interaction, it does not consider the material stiffness degradation when I_F > 1.0.

C) *Hashin damage criteria*

The Hashin damage failure criteria (Hashin and Rotem, 1973; Hashin, 1980; Barbero *et al.*, 2013) were exclusively developed for fibre reinforced composites. The failure criterion involves four independent damage initiation criteria which are: (a) fibre tension, F_f^t; (b) fibre compression, F_f^c; (c) matrix tension, F_m^t; and (d) matrix compression, F_m^c. These damage criteria are satisfied with the following conditions:

$$F_f^t = \frac{\sigma_1^2}{S_{t,1}^2} + \alpha_i \frac{\sigma_{12}^2}{S_{12}^2} < 1.0 \tag{2.26}$$

$$F_f^c = \frac{\sigma_1^2}{S_{c,1}^2} < 1.0 \tag{2.27}$$

$$F_m^t = \frac{\sigma_2^2}{S_{t,2}^2} + \frac{\sigma_{12}^2}{S_{12}^2} < 1.0 \tag{2.28}$$

$$F_m^c = \frac{\sigma_2^2}{4S_{23}^2} + \left(\frac{S_{c,2}^2}{4S_{23}^2} - 1\right)\frac{\sigma_2}{S_{c,2}} + \frac{\sigma_{12}^2}{S_{12}^2} < 1.0 \tag{2.29}$$

Here, σ_i is the load applied in direction i (i = 1 for longitudinal, 2 for transverse and 12 for in-plane shear); $S_{t,i}$ is the tensile strength in direction i; $S_{c,i}$ is the compressive strength in direction i; S_{12} is the in-plane shear strength; S_{23} is the transverse shear strength; and α is the parameter that takes into account the effect of shear stress to the fibre tension index, F_f^t. The version of this criteria proposed by Hashin and Rotem (1973) is obtained for α_i=0.0 and the criterion version proposed by Hashin (1980) is achieved if α_i=1.0.

Fernandes *et al*. (2015) reported that Tsai–Hill criterion based analyses provided conservative ultimate load values of the GFRP I–section profiles under web crippling loading. Further, Nunes *et al*. (2017) concluded that the Hashin damage criteria based analysis gave relatively closer prediction of the ultimate crippling loads of the GFRP I–beams than the Tsai–Hill criterion based analysis.

2.5.2 Element type

Several studies have employed various FE element types to model the GFRP profiles (e.g. Nunes *et al*., 2013; Nunes *et al*., 2016; Fernandes *et al*., 2015; Nunes *et al*., 2017; and Nunes *et al*., 2016; Singh and Chawla, 2018; Chawla and Singh, 2019). Generally shell FE elements are used for modeling the members where the thicknesses of the elements are comparatively smaller than other directions. Use of S4R element (four noded reduced integration conventional shell element having six degrees of freedom per node, three translations and three rotations) (available in Abaqus, 2009) in modelling the GFRP profiles have been reported (e.g. Fernandes *et al*., 2015 (crippling); Singh and Chawla, 2018; Chawla and Singh, 2019) and are found to simulate the experimental behaviour adequately. Use of continuum shell elements such as eight noded hexahedron continuum shell element with reduced integration having three degrees of freedom per node (three translations) (SC8R) in the analysis of GFRP members are also reported in Nunes *et al*. (2016), Nunes *et al*. (2017) and Nunes *et al*. (2016). It can be said that both continuum (SC8R) and conventional shell elements (S4R) used in those analyses (e.g. Fernandes *et al*., 2015; Nunes *et al*., 2016; Nunes *et al*., 2017; and Nunes *et al*., 2016; Singh and Chawla, 2018; Chawla and Singh, 2019) predicted the experimental ultimate loads accurately.

2.5.3 Initial imperfections

Presence of geometric imperfections in a GFRP member can considerably affect the structural behaviour in terms of load carrying capacity and deformed shapes etc. (Nunes *et al*., 2016). Geometric imperfections are the unevenness and undulations in a structural member that can occur during manufacturing, fabrication of specimens or transportation of materials to site etc. Initial imperfections are of two types: local and global. Local imperfections are the undulations developed in a surface and may be present in both inner and outer plate surfaces. In contrast, the global imperfections are caused by deformation of a member along its length in any direction (e.g. warping, twisting etc.). Initial imperfections in FE modeling are usually seeded by incorporating the first eigen mode (or lowest eigen mode) obtained from linear buckling analysis (e.g. Fernandes *et al*., 2015). Fernandes *et al*. (2015) considered an imperfection (local) magnitude of h/2000 (h is the web height). Nunes *et al*. (2016) adopted an imperfection amplitude of h/360 for hybrid (GFRP and CFRP) FRP I–beams.

2.6 SUMMARY

In this chapter, a detailed review on the research activities reported on the structural behaviour of GFRP pultruded profiles investigated by various researchers is presented. A brief introduction to the material properties, flexural and compression behaviour is also presented. Following this, a detailed review on the literature reported on web crippling behaviour of GFRP profiles with and without perforation is furnished. The design rules available for web crippling of GFRP and steel sections are also discussed in detail. Based on the literature review, following conclusions can be drawn:

1) The availability of technical test data of the pultruded GFRP profiles produced in India are limited in the public domain. Also, there is no Indian standard/guideline developed for the design of GFRP profiles till date.

2) Web crippling failure in GFRP profiles is a major issue for the designers due to their weak mechanical properties in the transverse direction and needs to be addressed properly. However, limited research has been reported on the web-crippling phenomenon of GFRP profiles.
3) Researchers have primarily investigated the effects of plate thickness, bearing length, slenderness ratio and loading and support boundary conditions on the web crippling behaviour of GFRP profiles. However, some literatures reported contradictory findings and inconsistency in the effect of plate bearing length which needs to be verified carefully with further studies.
4) Literature relating to the effect of varying web perforation on web crippling behaviour of GFRP is very limited and no design rule is available regarding this.
5) Numerical modeling techniques for finite element (FE) analysis of GFRP profiles are presented. The Hashin damage failure criteria are found to predict more accurately the experimental results than the other failure criteria.

This page is intentionally left blank.

CHAPTER 3

MECHANICAL CHARACTERIZATION OF PULTRUDED GFRP CHANNEL, WIDE FLANGE AND RECTANGULAR HOLLOW PROFILES

3.1 INTRODUCTION

In previous chapters, it has been highlighted that application of Glass Fibre Reinforced Polymer (GFRP) pultruded profiles have gained recognition in the construction industry owing to various advantages such as lightweight properties, resistance to corrosion, good insulation, electromagnetic properties and easy deployability etc. over traditional materials (steel and concrete) (e.g. Bank, 2006; Bakis *et al*., 2002; and Potyrala, 2011). However, their widespread uses have been restricted due to certain disadvantages such as low fire resistance; durability in harsh environment, especially in alkaline environment; proneness to buckling phenomena and lack of consensual design code etc. (e.g. Zaman *et al*., 2013; Guermazi *et al*., 2016; and Bank, 2006). Literatures have been reported on the buckling behaviour (e.g. Bank, 2006; Correia *et al*., 2012; Nunes *et al*., 2016; and Correia, 2012), compression behaviour (e.g. Hashem and Yuan, 2001; Correia *et al*., 2012; Nunes *et al*., 2013; Nunes *et al*., 2016; Nunes *et al*., 2016; Sirajudeen and Sekar, 2020), lateral torsional buckling (e.g. Nguyen, 2014), web crippling behaviour (e.g.

Borowicz and Bank, 2011; Fernandes *et al*., 2015; Wu *et al.*, 2019) of GFRP profiles. According to Bank (2006), GFRP members are anisotropic and inhomogeneous in nature. The strength and stiffness properties of GFRP profiles can vary in different directions and also within the cross-section on the fibre, lamina, and laminate levels (e.g. Bank, 2006; Fernandes *et al*., 2015; Turvey and Zhang, 2018). The variations in the material behaviour in different directions (e.g. longitudinal and transverse directions) are due to the fact that fibre rovings are oriented in the pultrusion direction which dominates their behaviour in the longitudinal direction. In transverse direction, their behaviour is mainly dominated by the existence of different fibre mats and resin matrix. Zhang *et al*. (2018) studied the effect of fibre orientation on the behaviour of GFRPs and reported that material properties decreased with the increase in *off-axis* fibre orientation. Quadrino *et al*. (2018) also reported that mechanical properties of the GFRP profiles were strongly influenced by the fibre orientations and the reduced strength in web-flange junction was mainly due to the existence of a weak rich core.

From the existing literature available, it can be understood that there are no recommended standardized geometries and minimum/maximum mechanical as well as physical properties for GFRP profiles. The properties of the GFRP profiles may differ based on the different strategies adopted by the manufacturers for embedding various fibre layers and mats in the polymer resin as well as with diverse stacking sequences. Although, manufacturers provide these data but often incomplete property data are provided. Therefore, it is always recommended to have an independent estimation and verification of the material properties of GFRPs prior to their structural applications (Bank, 2006). In recent years, many Indian GFRP manufacturers have started producing pultruded GFRP profiles and their uses have rapidly increased in the construction industry. However, limited technical test data of the GFRP materials produced in India are available in the public domain (e.g. Singh and Chawla, 2018; Singh and Chawla, 2019; Sirajudeen and Sekar, 2020) (for research or development of design codes etc.). To the best of authors' knowledge, there are no Indian standards available for recommending the test procedures for these materials. Nevertheless, in order to establish reliable design guidelines, extensive investigations and proper comparisons are required. Henceforth, underscoring these gap areas, and to add more data to the existing database on GFRP materials and share the test data for GFRPs produced in India for possible development of Indian standards for GFRP structural members, a series of experimental tests has been conducted for different GFRP profiles manufactured by an Indian pultruder (Bajrang Agencies, Guwahati). The experimental programme includes tensile, compression, interlaminar shear and in-plane shear tests that are performed on coupons obtained from the flanges and webs of the profiles. Based on 76 coupon test data, mean and characteristic material properties of the GFRP profiles are evaluated. Further, the design guidelines available internationally are assessed for their applicability to such India produced GFRPs, by performing a comparative study on the material partial safety factors and conversion factors and subsequent design values by considering four design guidelines owing to their differences on material reduction factors. The findings of this study are mainly arranged in five different sections: 1) physical properties of the GFRPs and their microstructure; 2) coupon tests; 3) data analysis; 4) determination of characteristic material properties and 5) comparison of design material values according to various design guidelines. At the end, a brief conclusion based on the whole investigation has been summarized.

3.2 DIMENSIONS AND PHYSICAL PROPERTIES OF THE GFRP PROFILES

Pultruded profiles of six sizes with three different shapes were produced by an Indian pultruder using 9800-tex E-glass continuous fibre rovings and fibre mats embedding in polyester resin. These profiles include three channels, one wide flange and two rectangular hollow sections (see Figure 3.1). Details of the GFRP profiles are presented in Table 3.1. Several tests *viz.*, burn-off tests, surface hardness test and scanning electron microscopy (SEM) were performed in order to characterise different physical properties of the profiles such as percentage of fibres used in producing each profile, their surface hardness and microstructure, and are described below.

3.2.1 Burn-off test

Burn-off test helps in determining the overall glass content and identifying the orientations of the different fibre architectures in GFRP materials. In the present study, burn-off tests were performed according to ASTM D2584. Specimen sizes of 25 mm × 25 mm were prepared from both webs and flanges of the profiles and burnt in a muffle furnace (see Figure 3.2) at 565 ± 28°C until all the carbonaceous or resin materials were disappeared. Following ASTM D2584, the specimens were kept in the muffle furnace for about 6 hours. Average glass content for each profile was determined by repeating the test for a minimum of three specimens and is detailed in Table 3.1.

From the burn-off tests, it was observed that the manufacturer used mainly three forms of E-glass fibre architectures; namely, combined mat, unidirectional roving and continuous strand mat (see Figures 3.3a–b). These three forms of fibre architectures were used in both flanges and webs of the profiles. In each case, the unidirectional roving layers were sandwiched between adjacent layers of combined mats and continuous strand mats.

3.2.2 Rockwell hardness test

Hardness tests for the GFRP profiles were performed according to ASTM D785 using a standard Rockwell hardness testing machine (make: Fuel Instruments & Engineers Pvt. Ltd., Maharashtra, India, see Figure 3.4a). Rockwell hardness test is generally preferred for harder polymer materials such as nylon, polycarbonate, polystyrene etc. (Kulkarni *et al*., 2011). The hardness values obtained by this test method can be used to gain some insight into the cure of a range of thermosetting materials at room temperature. Test samples were prepared from both longitudinal and transverse directions as well as from both flanges and webs at different locations. The load was applied through a ball indenter of diameter 0.25 inches with a maximum load of 60 kgf according to the standard *L-scale* of the tester. The Rockwell hardness numbers (HR) for the specimens were obtained from the relationship: $HR = 130 - e$, where, e is the depth of impression in units of 0.002 mm after the major load was removed. Hardness values for the GFRP profiles are shown in Figure 3.4b, where, higher number indicates harder material.

3.2.3 Microstructure investigation

In order to gain an insight into the internal structure of the GFRP profiles, microstructure study was carried out using a Gemini-300 Field Emission scanning electron microscopy (make: ZEISS). The study was mainly aimed at capturing various aspects such as fibre distribution pattern in the polymer matrix and identifying voids and cracks present due to imperfections in the manufacturing process. For this purpose, specimens were prepared with sizes of 5 mm × 5 mm × 3 mm from the profiles in both longitudinal and cross-sectional direction. For getting better quality images, specimen surfaces were first polished by using sand papers of various grit sizes, followed by a cleaning process. Prior to scanning, specimens were kept in an oven for 24 hours at 60^{o}C for removing any moisture present in the samples. An air blower was then used to clean the samples properly. As the GFRPs are non conductive, samples were being coated with gold films before SEM analysis.

SEM imaging was performed at different magnification levels ranging from 80x to 5000x. For each profile, minimum of two samples were investigated and analyses were performed to capture both longitudinal and cross-sectional images of the profiles (Figures 3.5a–c). All GFRPs showed disconnected voids or defects distributed randomly (see Figure 3.5b−c). The width of a discontinuous defect was around 146 micron meter (see Figure 3.5b). The defects observed in the GFRP profiles can adversely impact their durability in aggressive environment. According to Wan *et al*. (2006), hygrothermal environment can degrade and damage the fibre-matrix interface which in turn reduces the strength and modulus properties of the composites. On the other hand, moisture absorption can lead to reduction in strength properties of composites by softening the matrix, subsequently lowering their stress transfer function (Tsai *et al*., 2009; and Zhong and Joshi, 2015). Improvement in the microstructure with reduced defects can be achieved by precise quality control and maintaining appropriate pultrusion speed and dye temperature, as well as proper time of curing.

3.3 COUPON TEST DETAILS

For obtaining mechanical properties of the GFRP profiles, coupon specimens were prepared to conduct tensile, compression, interlaminar shear and 10° *off-axis* tensile tests. Coupon specimens were cut out from both webs and flanges of the profiles using a diamond edged circular cutting saw. After cutting the specimens, surfaces and edges were smoothened by polishing using sand papers of appropriate sizes. All the tensile and compression coupons were cut in the lengthwise direction from the webs and flanges of the profiles. However, coupons in the transverse direction could not be prepared (except for the wide flange or H1 profile) due to unavailability of required lengths in transverse direction. Specimens were obtained from the central portion of the webs and flanges in such a way that the specimen edges were at least 10 mm distant from the edges of the flanges or the web-flange junction.

3.3.1 Tensile test

The in-plane tensile properties of the GFRP profiles were determined according to the methods given in ASTM D3039. Specimens were prepared with standard plane dimensions of 250 mm × 25 mm with grip length 70 mm and gauge length 110 mm (see Figure 3.6a). The gauge length was selected in such a way that a uniform tensile stress can be applied across the central cross-section of the coupon. To prevent gripping damage and to introduce force into the specimen successfully, aluminium tabs of thickness 2 mm were bonded to the grips using an epoxy adhesive. An extensometer of 50 mm gauge length was used to measure the tensile moduli of the specimens. For measuring strains in both direction, two unidirectional strain gauges of 350 Ω resistance with 6 mm gauge length and 2.1 ± 0.01% gauge factor, were attached to the central portion of each tensile coupon, one in the longitudinal and another in the transverse centreline direction. For bonding the strain gauges to the coupon's surface, a standard procedure followed by Turvey and Zhang (2018) was adopted. The surface at the gauge locations were first abraded with emery paper for exposing the fibres from the polyester coating. An M-Bond neutralizer was then used to clean the surface, after which the strain gauges were attached to the surface using an epoxy adhesive.

Before testing, the cross sectional area of each coupon was measured with a digital Vernier calliper (up to a precision of 0.01 mm) at three different locations along the gauge length. The mean width and thicknesses were used to determine each coupon's mean cross-sectional area. All the tensile tests were carried out in the Universal Testing Machine (UTM) or loading frame (make: Bangalore Integrated System Solutions (BISS), India) of 250 kN load capacity (see Figure 3.7a). Before testing each sample, utmost care was taken to ensure the alignment of the longitudinal axis of the gripped specimen with the test direction. The load was then applied in a displacement control mode with a speed of 1mm/min. Specimens were loaded up to failure while recording the load and strain data simultaneously from the load cell and the extensometer. Data recording was carried out at 0.1 s intervals. A data acquisition system was used to record the strain data generated from the strain gauges. After completion of each test, the specimen was examined carefully to identify its failure modes.

3.3.2 Compression test

The in-plane compressive properties of the GFRP profiles were determined according to the specifications given in ASTM D3410. This test procedure applies the compressive force into the specimen by shear at the wedge grip interfaces. Specimens were prepared according to the specifications given in the standard with overall length of 140 mm, grip length 60 mm and a gauge length of 20 mm (see Figure 3.6b). The widths of the specimens were kept at 25 mm. In the selection of the gauge length, particular attention was given to avoid buckling and minimizing the effect of transverse end restraint at the grips and on the application of uniform compressive stress throughout the gauge section. In case of H1 profile, coupon specimens were prepared in the transverse direction with overall length 69 mm, width 25 mm, grip length 25 mm and gauge length 19 mm. To prevent gripping damage, aluminium tabs of 2 mm thickness were bonded to the grips using an epoxy adhesive. All the compression tests were conducted in a UTM of 100 kN capacity (make: Instron, UK). The cross-section dimensions of the compression coupons were measured before they were clamped between the grips and their alignment were checked. The load was then applied in a displacement control mode with a speed of 1mm/min. A compression coupon test is shown in Figure 3.7b.

3.3.3 10^{o} off-axis tension test

For characterizing the in-plane shear properties of the GFRP profiles, 10^{o} *off-axis* tension tests were performed according to the recommendations given in Hodgkinson (2000). Specimens were prepared to align their load axis with an angle of 10° to the unidirectional roving direction. However, coupons could only be prepared for the H1 profile from its flanges due to unavailability of required lengths its web and also in other profiles. The plan dimensions of the coupons are 200 mm × 25 mm with grip length of 50 mm (see Figure 3.6c). The gauge length was so selected to apply a state of uniform shear stress across the central cross-section of the coupon specimen while minimizing errors in obtaining shear modulus that might occur due to the end constraints. For measuring independent strain data in the structural axes, three unidirectional strain gauges were attached to the central portion of each coupon with angle of 0^{o}, 45^{o} and 90^{o}, respectively, to the loading axis. All the strain gauges had resistance of 350 Ω with gauge length 6 mm and gauge factor 2.1 ± 0.01%. For bonding the strain gauges to the coupon's face, similar procedure described in Section 3.3.1 was followed.

A total of seven specimens were tested from both flanges of the wide flange (WF or H1) section. Before testing, utmost care was taken to ensure the alignment of the loading axis of the specimen with the test direction, as small errors in the orientation could lead to erroneous measurement of shear stress and strain data. All the tensile tests were performed in a 250 kN load capacity UTM (make: BISS, see Figure 3.7c). The load was applied with a speed of 1mm/min. Specimens were loaded up to failure while recording the load and strain data simultaneously from the load cell and strain gauges at 0.1 s intervals. Strain data were recorded with a data acquisition system. After completion of each test, specimen was examined carefully to identify its failure modes.

3.3.4 Interlaminar shear test

The interlaminar shear strengths of the GFRP profiles were determined in accordance with the procedure given in ASTM D2344. According to this method, the load is being applied by means of a three point loading where the ratio of loading span length to specimen thickness is restricted to 4.0 with a minimum specimen thickness of 2.0 mm (see Figure 3.6d). For the present study, specimens were prepared for each profile with length = thickness × 6.0 mm and width = thickness × 2.0 mm as specified in the code. All the tests were conducted in a UTM of 100 kN capacity (make: Instron, UK, see Figure 3.7d). For each test, the load was applied in a displacement control mode with a speed of 1mm/min.

3.4 DISCUSSION ON COUPON FAILURE PATTERNS AND TEST RESULTS

In the following paragraphs, a thorough description on the analysis procedure of the experimental data has been presented. This is followed by a brief report on the coupon failure patterns observed during the tests. Finally, detailed test results are reported which include the mean values, standard deviations and coefficient of variations of different GFRP properties.

3.4.1 Data analysis

Based on the tensile coupon tests, the ultimate tensile strength, ultimate tensile strain, tensile chord modulus of elasticity and Poisson’s ratio of the corresponding specimens have been evaluated. The ultimate tensile stresses have been obtained by dividing the ultimate loads, taken from the load-strain curve with their corresponding mean cross sectional areas. The longitudinal strain values were obtained from strain gauges (also verified with extensometer results). Ultimate tensile strains are considered as the strain values corresponding to the ultimate loads in the load-strain curves. For each coupon, the elastic tensile modulus has been calculated in the strain range of 1000 to 3000 με. For the same range, coupon's Poisson's ratios have also been calculated from the ratios of strain values obtained by the transverse and longitudinal strain gauges.

In a similar manner, the ultimate compressive strength and compressive modulus of elasticity of the compression coupon specimens are evaluated. Additionally, strain data were recorded for some of the specimens.

The in-plane shear stress (τ_{12}) and shear strain (γ_{12}) produced within the specimen along the 10° plane without end constraints are obtained from Equation 3.1 and Equation 3.2, respectively, as specified in Hodgkinson (2000). Here, σ_{xx} is the stress value in the loading direction obtained by dividing the applied load with the cross-sectional area of the coupon. The in-plane strain along the 10° plane (γ_{12}) is determined from the respective equations by substituting ε_1, ε_2 and ε_3, that are obtained from the strain gauges 1(0°), 2(45°) and 3(90°), respectively. The in-plane shear modulus (G_{LT}) values for the GFRP profile are then measured from the initial slope of the shear stress versus shear strain plot within a strain range of 500 to 2500 με.

$$\tau_{12} = 0.171\sigma_{xx} \tag{3.1}$$

$$\gamma_{12} = 1.879\varepsilon_2 - 1.282\varepsilon_1 - 0.598\varepsilon_3 \tag{3.2}$$

In case of interlaminar shear tests, the short beam strength is determined according to Equation 3.3. In Equation 3.3, F^{sbs} is the short-beam strength in MPa; P_{mi} is the maximum load observed during the test in N; b is the measured specimen width in mm and s is the measured specimen thickness in mm. The details of the interlaminar shear strength obtained for all the specimens are reported in Table 3.2.

$$\mathrm{F}^{sbs} = 0.75 \times \frac{P_{mi}}{b \times s} \tag{3.3}$$

3.4.2 Failure patterns

In case of tensile coupons, failure occurred mostly at the gauge length region by delamination (see Figure 3.8a). In most cases, failure took place in a brittle manner while emitting a clear cracking sound. Delamination occurred mainly between the roving layers and fibre mats followed by glass fibre fracture along the gauge length. Some of the coupons failed at the grips by crushing, whereas, in some cases, debonding of aluminium tabs occurred before failure could be initiated at the gauge length portion. Where coupon specimens failed at grips or otherwise unexpectedly, such test results are discarded and only successful tests results are considered for the present study.

In most of the cases, the compression coupons failed in the mid portion of the gauge length by either delamination or longitudinal splitting (see Figure 3.8b). The middle portion of the gauge section is the most favourable failure area as the effect of gripping or tabbing is less in this area. Some of the coupons failed at the grip portion. Such test results were discarded and not included in the report.

In Figure 3.9a, longitudinal tensile stresses and corresponding strain values of representative coupon samples of the various GFRP profiles have been plotted. It can be seen that all tensile coupons exhibited linear elastic behaviour up to failure. In case of longitudinal compression coupon, the behaviour was elastic but with a combination of linear and nonlinear pattern as shown in Figure 3.9b. The longitudinal tensile response was mainly influenced by the presence of stiffer roving layers. However, in compression, the response was also influenced by the presence of fibre mats and the polyester matrix. The observations made herein are in good agreement with other literatures e.g. Turvey and Zhang (2018), Zhang *et al*. (2018), Guades *et al*. (2014), Quadrino *et al*. (2018) and Correia *et al*. (2013).

In case of 10° *off-axis* tensile test, failure started with a distinct straight crack parallel to the fibre direction, propagating in a quick manner through the gauge section and splitting the specimen into two parts (see Figure 3.8c). Similar failure patterns have also been reported by Zhang *et al*. (2018), Quadrino *et al*. (2018) and Khashaba (2004). According to Hodgkinson (2000), failure in this particular test is caused by a combination of shear and transverse tensile stresses. Consequently, it may underestimate the actual value of the ultimate shear strength and strain. However, to minimize this error, use of long specimens with aspect ratios larger than 10 are recommended (Hodgkinson, 2000).

With regard to the failure patterns in the interlaminar shear specimens, early cracks appeared under the loading nose at the mid-span section followed by longitudinal cracks propagating to the end sections of the specimens (see Figure 3.8d).

3.4.3 Test results

For all GFRP profiles, the mean values, standard deviations and coefficient of variations are determined for tensile and compressive loads, stresses and strains; interlaminar shear and in-plane shear stresses; major Poisson's ratios; along with their corresponding elastic moduli values. As mentioned earlier, no transverse coupon could be obtained due to limitations in profile sizes (except for the H1 profile) and only properties in the profiles' longitudinal direction are obtained. However, variations in their material properties are observed. In Table 3.2, detailed report on the test results obtained is furnished. The transverse compressive strength (not presented in Table 3.2) in case of WF or H1 profile were found to be 37.39 MPa with a standard deviation of 0.57 and COV 1.52. In Table 3.2, the symbols F and W specify about coupons obtained from flange and web, respectively, whereas, F+W indicates values obtained from both web and flanges in combination. Symbols T, C and I designate specimens tested in tensile, compression and interlaminar shear tests, respectively. The number of samples tested for each set of test is also presented. In the following sub-sections, discussion on the test results is presented.

3.4.3.1 Channel profile – C1

From Table 2, it can be seen that the mean tensile load value obtained in case of web specimens exceeds those of flange by 33.7%, whereas, in case of mean tensile stress this difference is about 21.5%. The mean ultimate tensile strain in case of web is greater than the flange by almost 18%. However, the difference in the mean elastic modulus values of the web and flange is only 2.5%. Also, the mean major Poisson's ratio values are found to be almost similar. The mean compressive ultimate load and stress values in case of web are lower by almost 11–12% as can be seen in Table 3.2. The strains values in compression tests could not be measured; hence compression modulus values are not determined for C1 profile. However, the mean value of the interlaminar shear strengths in case of web is found to be greater by 14.4% than that of flange.

3.4.3.2 Channel profile – C2

In case of C2, the mean tensile properties in web cannot be obtained as only one coupon test could be successfully tested. Interlaminar shear test also could not be performed for flange parts. The mean compressive load value obtained in case of flange is lower by 4.1% than the web, whereas, similar difference of almost 4.4% can be seen in case of mean compressive stress values. In a similar way, mean compressive ultimate strain and elastic modulus values in flanges are found to be lower by 24.8 and 2.4%, respectively, than the web. On the other hand, the difference in mean values for tension and compressive load for the flange part is around 53.2% and corresponding difference in mean stress values is around 50.2%. Similarly, the difference in mean ultimate tension and compression strain is 24.7% and corresponding difference in mean elastic moduli values is around 3.4%.

3.4.3.3 Channel profile – C3

In case of C3, compression and interlaminar shear tests could not be performed for the flanges due to limited material available. Also, only one interlaminar test for the web could be successfully conducted. Nevertheless, other tests were carried out accordingly. From Table 2, it can be seen that the mean tensile load value in case of web exceeds that of flange by 20.3%, whereas, the difference in mean tensile stress is about 24.9%. The mean ultimate tensile strain in web is found to be greater than the flange by 26.1%. However, the difference in the mean elastic modulus values of the flange and web is almost negligible (0.7%). Also, the mean major Poisson’s ratio in web is lower by 18.7% than the flange.

3.4.3.4 Wide flange profile – H1

From Table 3.2, the mean tensile load value obtained in the flange of H1 profile is found to be 3.7% higher than the web. Also, mean ultimate tensile stress value for the flange exceeds the value of web by 6.8%. Similarly, difference in the mean ultimate strain in tension is found to be approximately 7%. The major Poisson’s ratio value in flange exceeds the value of web by almost 8%. On the other hand, small differences in the mean elastic moduli values (approximately 1%) and mean interlaminar shear strength values (approximately 0.6%) can be observed. In case of compression tests, strain data could not be recorded for the flange specimens. Nevertheless, the ultimate load and stress values are determined. It can be seen that the difference in mean values of ultimate loads obtained for the web and flange is around 3.9%, whereas, this difference in case of mean ultimate stresses is almost 2.7%. In Table 3.2, the mean, standard deviation and coefficient of variation in in-plane shear strength and shear modulus values for the flange of H1 profile are presented.

3.4.3.5 Rectangular hollow profiles – RH1and RH2

In case of RH1 and RH2 profiles, compression tests could not be performed due to unavailability of required material. In Table 3.2, other test results such as mean ultimate tensile loads, ultimate stresses and corresponding ultimate strains, major Poisson's ratio and interlaminar shear strengths are shown.

From the above observations, it can be understood that there are differences in the mean values obtained from the flanges and webs of the profiles. The differences in compression and tensile test results are found to be in the range of 0.7–33.7% (differences for channel sections (i.e. C1, and C3) are particularly more than ~10%). Similar observations have been reported by Turvey and Zhang (2018), where, differences up to 9.2% can be seen in the mean values obtained from flanges and webs of the GFRP profiles. These differences are possibly due to the uneven distribution of the voids and cracks present in the webs and flanges that arise due to various imperfections in the manufacturing process. As a result of these irregularities, micro-cracks and subsequent failures may have taken place at different time intervals during loading.

3.5 DETERMINATION OF MATERIAL CHARACTERISTIC VALUES

Derivation of characteristic values for obtaining the design material properties are carried out in accordance with the procedure described in Annex D of EN 1990:2002 + A1:2005. This procedure is based on the 5% fractile value of the scatter in the experimental data. The characteristic values are obtained from Equation 3.4, where, X_k, X_m, k_n and X_{SD} are the characteristic value, mean value, characteristic fractile factor and their standard deviation, respectively. The value of characteristic fractile factor k_n depends upon the number of experiments performed for each set of test. The value of k_n reduces with the increase in number of tests. For example, k_n for RH1 profile with two successful tensile tests will be 2.01, whereas, for H1 profile with fourteen successful tensile tests, it will be 1.70.

$$X_k = X_m - k_n X_{SD} \tag{3.4}$$

For all GFRP profiles, the characteristic values for tensile, compression, interlaminar shear and in-plane shear stresses; tensile and compression strains; major Poisson's ratio; tensile, compression and shear moduli are obtained accordingly and presented in Table 3.3. For most of the cases, minimum of three to four specimens have been tested. However, all specimens could not be failed in the desired failure modes and such test results are discarded. In some cases, only one coupon test is successful and characteristic values cannot be determined for them. For the present study, characteristic values are derived for a minimum of two successful test data. The characteristic values for the flanges and webs of the profiles are obtained separately and also, in combination (F+W) wherever possible. The design stress values for the profiles are then evaluated by considering the characteristic values in combination. In certain situations, where combined material characteristic values cannot be obtained (e.g. for profiles RH1, RH2 etc.), the characteristic values of the individual flanges or webs are considered in determining the design values.

3.6 DESIGN ULTIMATE STRESSES AND ELASTIC MODULI FOR NORMAL ENVIRONMENT CONDITION

In recent years, several design manuals and guidelines have come up for the design of GFRP structures. These mainly include the Italian Guideline (2007), ASCE (2010), EUROCOMP Design Code and Handbook (1996), and the EU's CEN Technical Committee 250 (Ascione *et al*., 2016) etc. Nevertheless, there is no uniform guideline for recommending the partial safety factors and these factors in various design guidelines differ. Subsequently, these differences on material reduction factors have consequences on the structural behaviour of GFRPs, their design and costing. Therefore, in order to identify these differences and their effects on the material design values for limit state design purpose, a comparative study has been performed by considering the abovementioned four design guidelines. The characteristic values obtained in Table 3.3 are fitted with the relevant partial safety factors and conversion factors recommended in the guidelines, for deriving the material design values (ultimate stresses and elastic moduli) to be used for limit state design considering normal environmental condition. In the following paragraphs, detailed discussion on the material partial safety factors and conversion factors and subsequent design values obtained are reported.

3.6.1 Italian Guideline (2007)

The material design values (X_d) as per the Italian guideline (2007) can be derived from Equation 3.5, where, X_k , η and γ_m are the characteristic value, conversion factor and partial safety coefficient of the material, respectively.

$$X_d = \eta \frac{X_k}{\gamma_m} \tag{3.5}$$

The conversion factor, η is the product of two sub-factors η_a *and* η_l associated with the environmental effects and long term effects, respectively. A reduced value of η_a = 0.81 (taken from EUROCOMP, 1996) is considered to incorporate the unavailability of adequate protective systems against environmental degradation. For ultimate limit states, the conversion factor η_l = 1.00 which accounts for the failure of the GFRP profiles due to long term stresses caused by the rheological phenomena such as viscosity, relaxation and fatigue. The material partial safety factor γ_m is the product of two sub-factors γ_{f1} *and* γ_{f2}. Here, γ_{f1} is related to the uncertainty level of determining the properties of the GFRPs depending on the coefficient of variation (V_x). If V_x is less than 10%, value of γ_{f1} will be 1.10 and if V_x is in between 10–20 %, a value of 1.15 can be attributed to it. The value of γ_{f2} is taken to be 1.30 to account for the fragile behaviour of the GFRPs.

3.6.2 ASCE Guideline (2010)

The ASCE (2010) design guide has expressed the material design values (X_d) by Equation 3.6, where, X_k has been modified by two adjustment factors C_M and C_T. Moisture condition factor, C_M for polyester material will be 0.80 and 0.95 for obtaining the design strength and elastic moduli values, respectively. The temperature factor is derived for an average temperature of 35°C and its values for obtaining the design strength and elastic moduli are 0.95 and 0.94, respectively. Therefore, the combined value of C_MC_T for a temperature of 35°C will be 0.76 and 0.89 for calculating the design stress and elastic moduli values, respectively.

$$X_d = X_k C_M C_T \tag{3.6}$$

3.6.3 EUROCOMP Design Code and Handbook (1996)

In EUROCOMP (1996) design guide, the required material design values (X_d) are obtained from Equation 3.7, where, X_k and γ_m are the characteristic value and partial safety factor, respectively.

$$X_d = \frac{X_k}{\gamma_m} \tag{3.7}$$

The partial safety factor, γ_m is the product of three partial safety coefficients, $\gamma_{m,1}$, $\gamma_{m,2}$ and $\gamma_{m,3}$. The partial safety coefficient, $\gamma_{m,1}$ is associated with the uncertainty level in obtaining the properties of the profiles. If the properties of the GFRP profiles are obtained from experimental data, the value of $\gamma_{m,1}$ is taken to be 1.15. The partial safety coefficient, $\gamma_{m,2}$ is related with the production process and curing of the GFRP profiles. The manufacturer produced the GFRP profiles by pultrusion and are assumed to be fully cured at the production site and hence, $\gamma_{m,2}$ is taken as 1.1. The coefficient $\gamma_{m,3}$ accounts for the environmental effects and duration of loading on the structure. For the present case, for long term loading with an operating temperature range of 25–50°C and a heat distortion temperature range of 80–90°C, $\gamma_{m,3}$ will be 2.8. Therefore, the value of the partial safety factor, γ_m will become 3.54. On the other hand, a minimum value of γ_m = 1.5 is specified in the design guide for using in building structures which is considered in evaluating the design values for the present study.

3.6.4 EU's CEN Technical Committee 250 (2016)

In this design guide by Ascione *et al*. (2016), conversion factor η_c and partial safety factor γ_M are applied to the characteristic value X_k for obtaining the design values (X_d) in Equation 3.8, where, η_c is associated with the affects of environmental degradation and duration of loads and γ_m is related to the uncertainty level in determining the properties of the material.

$$X_d = \eta_c \frac{X_k}{\gamma_M} \tag{3.8}$$

The conversion factor, η_c is the product of other conversion sub-factors such as temperature effects (η_{ct}) and humidity effects (η_{cm}) etc. The value of η_{ct} in normal temperature condition is given by 0.9 for strength and elastic modulus verification. For outdoor climate with a service temperature of less than 30°C, the conversion sub-factor η_{cm} will be 0.9. The material partial safety factor γ_M is obtained by multiplying two sub-factors γ_{M1} and γ_{M2}, where, γ_{M1} is based on the uncertainty level of determining the properties of the material and γ_{M2} is associated with the production process and curing of the GFRPs. Where material properties are derived from experiments, a value of 1.15 will be attributed to γ_{M1}. For a fully cured GFRP profile, if coefficient of variation (V_x) is less than 10%, γ_{M2} will be 1.35 for both strength and global stability verification and if V_x is in between 10–17%, this value will be 1.6 and 1.5, respectively.

The partial safety factors and the subsequent conversion factors are applied to the characteristic values and the design stresses and moduli values obtained are presented in Table 3.4 considering the four design guidelines. It can be seen that due to the differences in the factors considered in the guidelines, there has been a considerable variation in the design stresses and moduli values obtained for the various GFRP profiles. To get a clear understanding on these differences, detailed material design stresses and elastic moduli values are plotted and representative bar diagrams are shown in Figures 3.10a and 3.10b, respectively.

From Figure 3.10a, it is observed that the longitudinal tensile design stress values for C1 profile obtained according to ASCE (2010) exceed Ascione *et al*. (2016) by almost 73%, whereas, Italian guideline (2007) and EUROCOMP (1996) differ by ~23.1 and 51.5%, respectively. In the same way, for C3 and H1 profiles similar differences can be obtained. However, the longitudinal compressive design stresses and interlaminar shear strengths for C1, C3 and H1 profiles as per Italian guideline (2007), ASCE (2010) and EUROCOMP (1996) exceed Ascione *et al*. (2016) by ~8.6, 45.7 and 27.8%, respectively. Similar differences can be found in case of the longitudinal design tensile and interlaminar shear stress values for profiles C2, RH1 and RH2; and compressive design stress for profile C2. The design tensile elastic moduli values for C1, C2, C3 and RH1; and the compression moduli for C2 and H1 derived according to Italian guideline (2007), ASCE (2010) and EUROCOMP (1996) differ Ascione *et al*. (2016) by ~8.6, 70.6 and 27.8%, respectively. However, the differences in the design tensile elastic modulus values obtained for H1 and RH2 profile, as per Italian guideline (2007), ASCE (2010) and EUROCOMP (1996) with Ascione *et al*. (2016) are ~15.4, 89.6 and 42%, respectively. Representative bar diagram for tensile and compression design moduli values for C2 profile is shown in Figure 3.10b.

3.7 CONCLUSION

This chapter reports an extensive study on the mechanical behaviour and material properties of GFRP channel, wide flange and rectangular hollow profiles of different sizes. Experimental investigations mainly include tensile, compression, interlaminar shear and 10° *off-axis* tensile tests performed on coupons obtained from flanges and webs of the profiles. The following conclusions can be drawn based on the present investigation:

1) From burn-off tests, it is observed that the manufacturer have used mainly three forms of E-glass fibre architectures, namely, combined mat, unidirectional roving and continuous strand mat, where, the unidirectional roving layers are sandwiched between adjacent layers of combined mats and continuous strand mats. The average fibre content in each profile is found to be around 71.6%.
2) From the hardness tests, the HR numbers of the profiles have been found to be in the range of 98–104 in *L-scale*.
3) Based on SEM image analysis, it is found that the H1 profile exhibits a continuous defect at the web-flange junction which continues throughout the length of the profile, whereas, discontinuous voids can be seen in other profiles.
4) All tensile specimens have exhibited linear elastic behaviour up to failure. In case of longitudinal compression coupons, the behaviour is elastic but with a combination of linear and nonlinear patterns.
5) Differences in mean compression and tensile values obtained from the flanges and webs of the profiles are found to be in the range of 0.7–33.7%.
6) Considerable variations in the design stresses and moduli values are observed which are due to the differences in the partial safety factors and conversion factors considered in the various guidelines.
7) The longitudinal tensile design stress values for C1, C3 and H1 profiles obtained according to ASCE (2010) exceed Ascione *et al*. (2016) by almost 73%, whereas, Italian guideline (2007) and EUROCOMP (1996) differ Ascione *et al*. (2016) by ~23.1 and 51.5%, respectively. The longitudinal compressive design stresses and interlaminar shear strengths as per Italian guideline (2007), ASCE (2010) and EUROCOMP (1996) differ Ascione *et al*. (2016) by ~8.6, 45.7 and 27.8%, respectively.

Table 3.1: Dimensions of the GFRP profiles and their respective fibre contents.

GFRP profiles	Symbol	Cross-sectional dimensions (mm)	Average fibre content (wt %)
Wide flange	H1	69 × 100 × 5	70.39
Channel	C1	69 × 29 × 5	73.78
	C2	48 × 29 × 3	72.98
	C3	79 × 29 × 3	71.53
Rectangular hollow	RH1	40 × 20 × 3	72.10
	RH2	15 × 106.5 × 2.9	68.84

Table 3.2: Mean, standard deviation and coefficient of variation of different material properties obtained from tensile, compression, interlaminar shear and in-plane shear tests conducted on longitudinal coupons cut out from flanges and webs of the GFRP profiles.

GFRP profiles	Coupon location	Coupons successfully failed	Ultimate load (kN)		Ultimate stress (MPa)		Ultimate strain (με)		Elastic modulus (GPa)		Major Poisson's ratio	Interlaminar shear strength (MPa)	In-plane shear strength (MPa)	Shear modulus (GPa)
			T	C	T	C	T	C	T	C				
		T(2)	**45.91**	**40.22**	**381.5**	**321.6**	**10161**	–	**37.6**	–	**0.308**	**41.2**	–	–
	F	C(2)	*2.42*	*0.81*	*28.89*	*1.18*	*1004*	–	*1.51*	–	*0.004*	*0.61*	–	–
		I(2)	5.27	2.00	7.57	0.37	9.88	–	4.02	–	1.14	1.47	–	–
		T(2)	**61.42**	**35.93**	**463.4**	**288.8**	**11984**	–	**38.6**	–	**0.311**	**36.0**	–	–
C1	**W**	C(2)	*1.11*	*4.98*	*31.95*	*31.99*	*375*	–	*1.46*	–	*0.008*	*3.79*	–	–
		I(2)	1.80	13.85	6.90	11.07	3.13	–	3.78	–	2.42	10.53	–	–
		T(4)	**53.67**	**38.08**	**422.4**	**305.2**	**11072**	–	**38.1**	–	**0.309**	**38.6**	–	–
	F + W	C(4)	*7.98*	*4.16*	*51.02*	*27.94*	*1185*	–	*1.56*	–	*0.006*	*3.75*	–	–
		I(4)	14.87	10.92	12.08	9.15	10.70	–	4.09	–	1.955	9.72	–	–
		T(3)	**30.94**	**20.20**	**408.9**	**272.3**	**11885**	**9525**	**36.6**	**37.8**	**0.354**	–	–	–
	F	C(4)	*0.49*	*0.46*	*0.32*	*7.52*	*1100*	*228*	*0.43*	*0.66*	*0.005*	–	–	–
		–	1.57	2.27	0.08	2.76	9.25	2.39	1.18	1.74	1.499	–	–	–
		T(1)	**30.83**	**21.03**	**391.2**	**284.4**	**10679**	**11890**	**36.6**	**38.7**	**0.353**	**37.3**	–	–
C2	**W**	C(2)	–	*0.23*	–	*3.43*	–	*1920*	–	*0.45*	–	*0.41*	–	–
		I(2)	–	1.08	–	1.21	–	16.15	–	1.15	–	1.1	–	–
		T(4)	**30.91**	**20.48**	**404.4**	**276.2**	**11584**	**10313**	**36.6**	**38.1**	**0.354**	–	–	–
	F + W	C(6)	*0.42*	*0.56*	*7.67*	*8.61*	*1086*	*1583*	*0.38*	*0.73*	*0.005*	–	–	–
		I(2)	1.37	2.72	1.90	3.12	9.38	15.35	1.03	1.93	1.310	–	–	–
		T(2)	**24.83**	–	**335.5**	–	**10818**	–	**31.0**	–	**0.260**	–	–	–
	F	–	*1.23*	–	*12.26*	–	*265*	–	*0.37*	–	*0.009*	–	–	–
		–	4.93	–	3.65	–	2.45	–	1.21	–	3.462	–	–	–
		T(2)	**29.86**	**19.21**	**419.2**	**265.1**	**13642**	–	**30.7**	–	**0.219**	**36.5**	–	–
C3	**W**	C(4)	*0.69*	*1.12*	*1.58*	*17.89*	*447*	–	*0.89*	–	*0.024*	–	–	–
		I(1)	2.32	5.84	0.38	6.75	3.27	–	2.89	–	10.959	–	–	–
		T(4)	**27.34**	–	**377.4**	–	**12230**	–	**30.8**	–	**0.240**	–	–	–
	F + W	C(4)	*2.70*	–	*42.76*	–	*1459*	–	*0.69*	–	*0.027*	–	–	–
		I(1)	9.89	–	11.33	–	11.93	–	2.25	–	11.425	–	–	–

Table 3.2: Mean, standard deviation and coefficient of variation of different material properties obtained from tensile, compression, interlaminar shear and in-plane shear tests conducted on longitudinal coupons cut out from flanges and webs of the GFRP profiles. (Continued)

GFRP profiles	Coupon location	Coupons successfully failed	Ultimate load (kN)		Ultimate stress (MPa)		Ultimate strain (με)		Elastic modulus (GPa)		Major Poisson's ratio	Interlaminar shear strength (MPa)	In-plane shear strength (MPa)	Shear modulus (GPa)
			T	**C**	T	C	T	C	T	C				
H1	**F**	T(5)	**40.39**	**26.63**	**345.2**	**217.7**	**10973**	–	**32.8**	–	**0.306**	**38.1**	**21.6**	**3.5**
		C(3)	*3.49*	*1.96*	*38.97*	*19.44*	*382*	–	*4.23*	–	*0.004*	*3.68*	*1.52*	*0.39*
		I(2)	8.64	7.37	11.29	8.93	3.48	–	12.89	–	1.146	9.67	7.05	11.12
	W	T(9)	**38.96**	**25.62**	**323.2**	**212.1**	**10259**	**9309**	**32.5**	**31.5**	**0.283**	**38.3**	–	–
		C(4)	*4.93*	*1.14*	*33.35*	*1.60*	*1244*	*1263*	*3.09*	*1.55*	*0.015*	*2.01*	–	–
		I(2)	12.66	4.44	10.32	0.75	12.13	13.57	9.50	4.90	5.336	5.24	–	–
	F + W	T(14)	**39.47**	**26.06**	**331.0**	**214.5**	**10514**	–	**32.6**	–	**0.292**	**37.9**	–	–
		C(7)	*4.52*	*1.62*	*36.98*	*13.08*	*1079*	–	*3.54*	–	*0.029*	*3.27*	–	–
		I(4)	11.46	6.23	11.17	6.10	10.26	–	10.86	–	9.878	8.6	–	–
RH1	**W**	T(2)	**27.84**	–	**382.7**	–	**12031**	–	**31.9**	–	**0.267**	**31.9**	–	–
		–	*0.02*	–	*9.49*	–	*779*	–	*1.28*	–	*0.004*	*0.01*	–	–
		I(2)	0.06	–	2.48	–	6.47	–	4.00	–	1.498	0.02	–	–
RH2	**F**	T(3)	**23.07**	–	**368.4**	–	**12482**	–	**29.8**	–	**0.360**	**39.8**	–	–
		–	*1.87*	–	*32.11*	–	*1263*	–	*4.00*	–	*0.004*	*2.93*	–	–
		I(3)	8.11	–	8.72	–	10.12	–	13.42	–	1.071	7.37	–	–

Notes: T(5), C(2) and I(4) indicate five coupons successfully tested in tension; two in compression; and four in interlaminar shear tests, respectively. The numbers written in **bold** are mean values and numbers written in ***Italic*** are standard deviations. The numbers written without **bold** and ***Italic*** are coefficient of variations.

Table 3.3: Characteristic values for tensile, compression, interlaminar shear and in-plane shear properties of the GFRP profiles.

GFRP profiles	Coupon location	Characteristic stress (MPa)		Characteristic strain (με)		Characteristic modulus (GPa)		Characteristic major Poisson's ratio	Interlaminar shear strength (MPa)	In-plane shear strength (MPa)	Shear modulus (GPa)
		T	C	T	C	T	C	T			
C1	F	323.4	319.2	8143	–	34.6	–	0.300	40.0	–	–
	W	399.1	224.5	11231	–	35.7	–	0.295	28.4	–	–
	F + W	329.1	254.1	8903	–	35.3	–	0.298	31.7	–	–
C2	F	408.3	258.5	9807	9108	35.8	36.7	0.344	–	–	–
	W	–	277.5	–	8030	–	37.9	–	36.5	–	–
	F + W	390.4	261.0	9596	7511	35.9	36.9	0.346	–	–	–
C3	F	310.9	–	10285	–	30.3	–	0.242	–	–	–
	W	416.1	232.4	12744	–	29.1	–	0.171	–	–	–
	F + W	299.1	–	9560	–	29.6	–	0.189	–	–	–
H1	F	275.0	181.0	10285	–	25.2	–	0.299	30.7	18.9	2.8
	W	265.5	209.2	8107	6997	27.2	28.7	0.257	34.3	–	–
	F + W	268.0	191.5	8676	–	26.6	–	0.243	32.0	–	–
RH1	F	363.7	–	10466	–	29.3	–	0.259	31.8	–	–
RH2	F	307.8	–	10095	–	22.3	–	0.353	34.2	–	–

Table 3.4: Comparison of design ultimate stresses and design elastic moduli values for the GFRP profiles obtained according to various design guidelines.

GFRP profiles	Design Guidelines	Tensile design stress (MPa)	Compressive design stress (MPa)	Tensile design elastic modulus (GPa)	Compressive design elastic modulus (GPa)	Interlaminar shear strength (MPa)	In-plane shear strength (MPa)	Shear modulus (GPa)
C1	Italian	178.3	144.0	20.0	–	18.0	–	–
	ASCE	250.1	193.1	31.4	–	24.1	–	–
	Eurocomp	219.4	169.4	23.5	–	21.2	–	–
	CEN	144.8	132.5	18.4	–	16.6	–	–
C2	Italian	221.2	147.9	20.4	20.9	20.7	–	–
	ASCE	296.7	198.4	32.0	32.8	27.7	–	–
	Eurocomp	260.3	174.0	23.9	24.6	24.3	–	–
	CEN	203.7	136.2	18.7	19.2	19.0	–	–
C3	Italian	162.0	131.7	16.8	–	–	–	–
	ASCE	227.3	176.6	26.4	–	–	–	–
	Eurocomp	199.4	154.9	19.7	–	–	–	–
	CEN	131.7	121.2	15.4	–	–	–	–
H1	Italian	145.2	108.5	14.4	16.3	18.1	10.7	1.5
	ASCE	203.7	145.6	23.7	25.6	24.3	14.4	2.5
	Eurocomp	178.7	127.7	17.7	19.2	21.3	12.6	1.9
	CEN	118.0	99.9	12.5	15.0	16.7	9.9	1.3
RH1	Italian	206.0	–	16.6	–	18.0	–	–
	ASCE	276.4	–	26.1	–	24.2	–	–
	Eurocomp	242.4	–	19.6	–	21.2	–	–
	CEN	189.7	–	15.3	–	16.6	–	–
RH2	Italian	174.4	–	12.1	–	19.4	–	–
	ASCE	233.9	–	19.8	–	26.0	–	–
	Eurocomp	205.2	–	14.8	–	22.8	–	–
	CEN	160.5	–	10.5	–	17.8	–	–

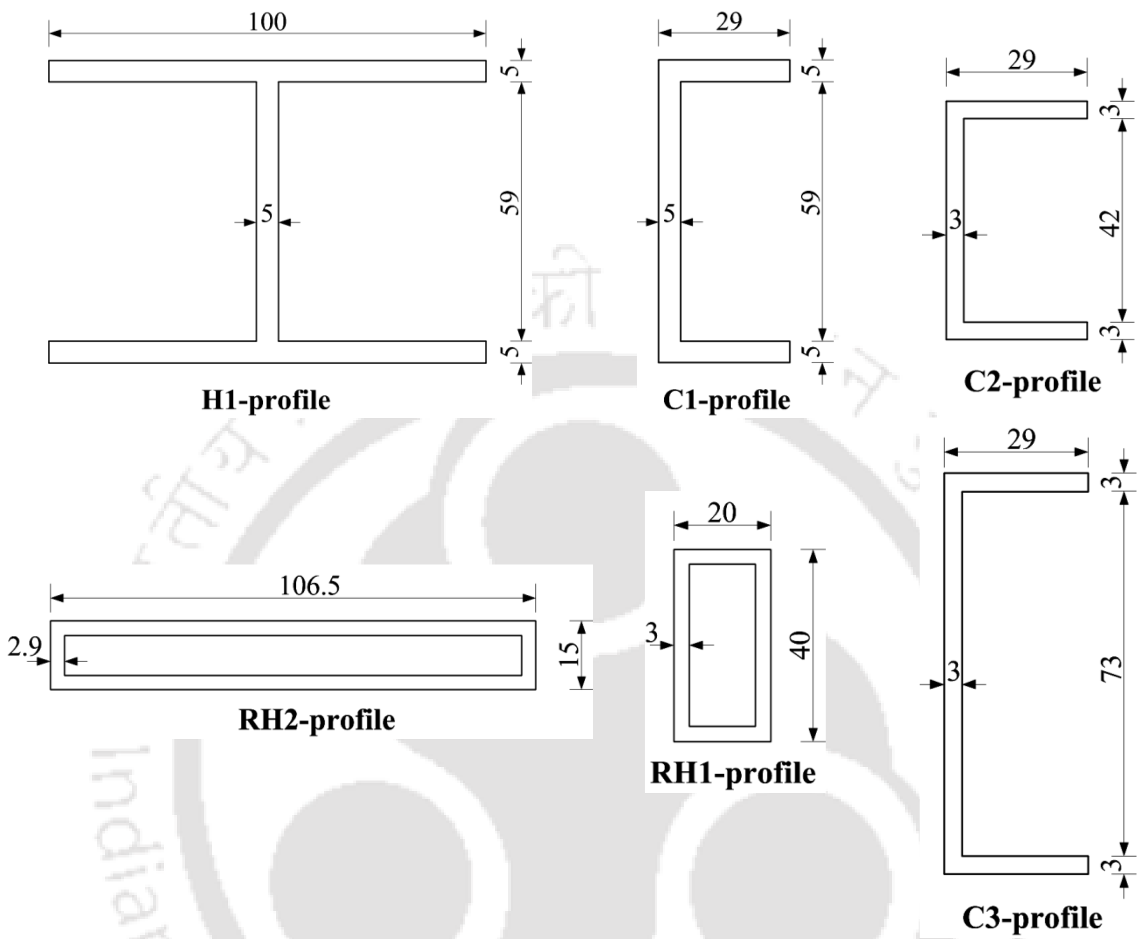

Figure 3.1: Cross-sectional sketches of the GFRP profiles with dimensions in mm.

Figure 3.2: Muffle furnace with specimens.

a) Combined mat b) Unidirectional fibre c) Continuous strand mat

Figure 3.3: Fibre architectures used in the GFRP profiles, obtained after burn-off test.

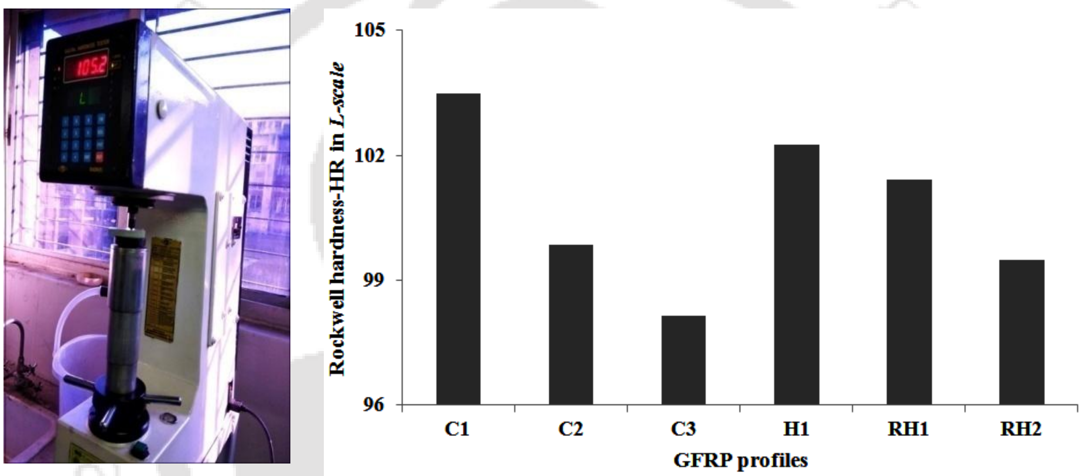

Figure 3.4: a) Rockwell hardness testing machine; b) hardness values for the GFRP profiles in *L-scale*.

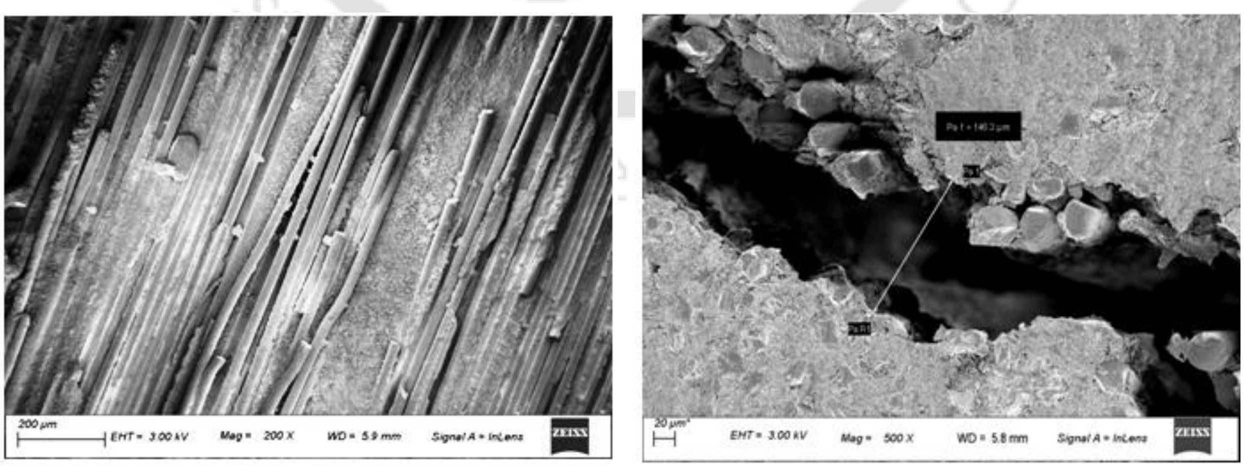

a) Longitudinal fibres at magnification of 200x b) Cross-sectional view of a discontinuous defect with 500x magnification

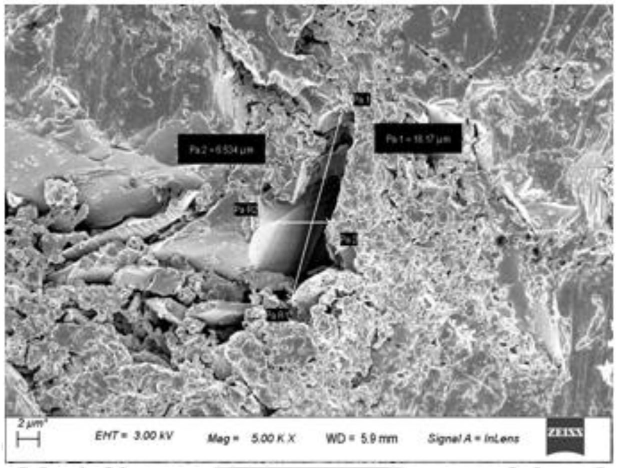

c) Discontinuous voids at 5000x magnification

Figure 3.5: SEM image of different GFRP profiles.

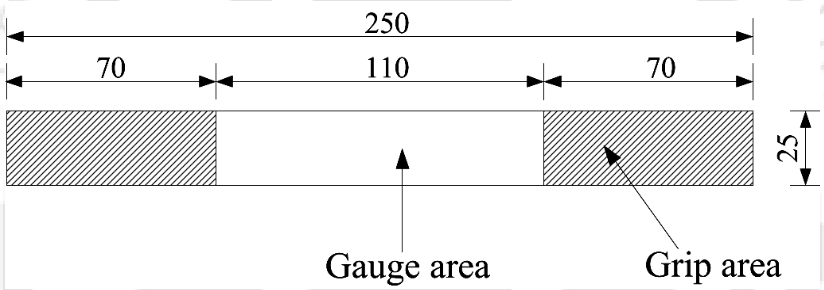

a) Longitudinal tension coupon

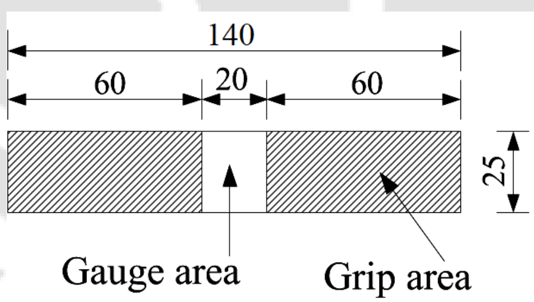

b) Longitudinal compression coupon

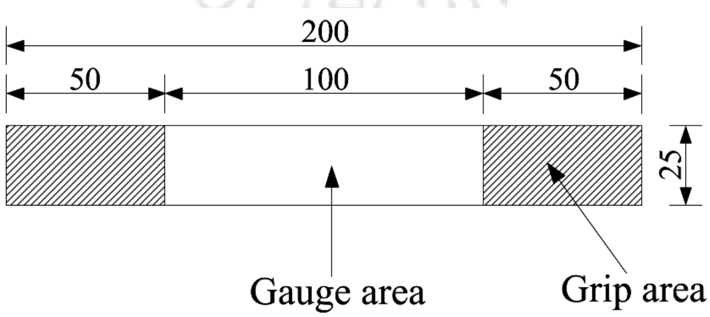

c) 10° *off-axis* coupon

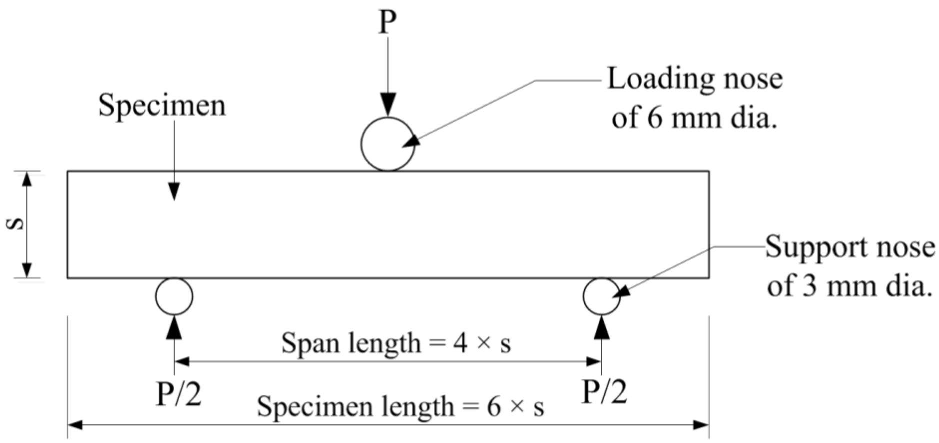

d) Horizontal shear load diagram for interlaminar shear test

Figure 3.6: Detailed dimensions of the coupons tested.

a) Tensile test

b) Compression coupon test

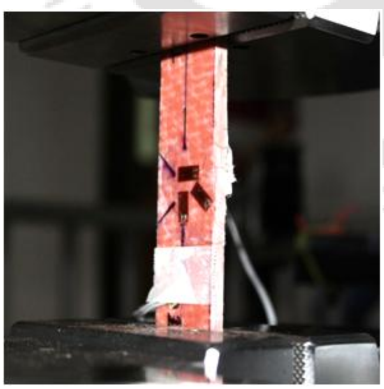

c) 10° *off-axis* tensile test

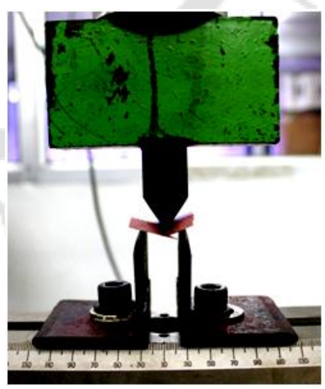

d) Interlaminar shear test

Figure 3.7: Coupon tests and their failure modes

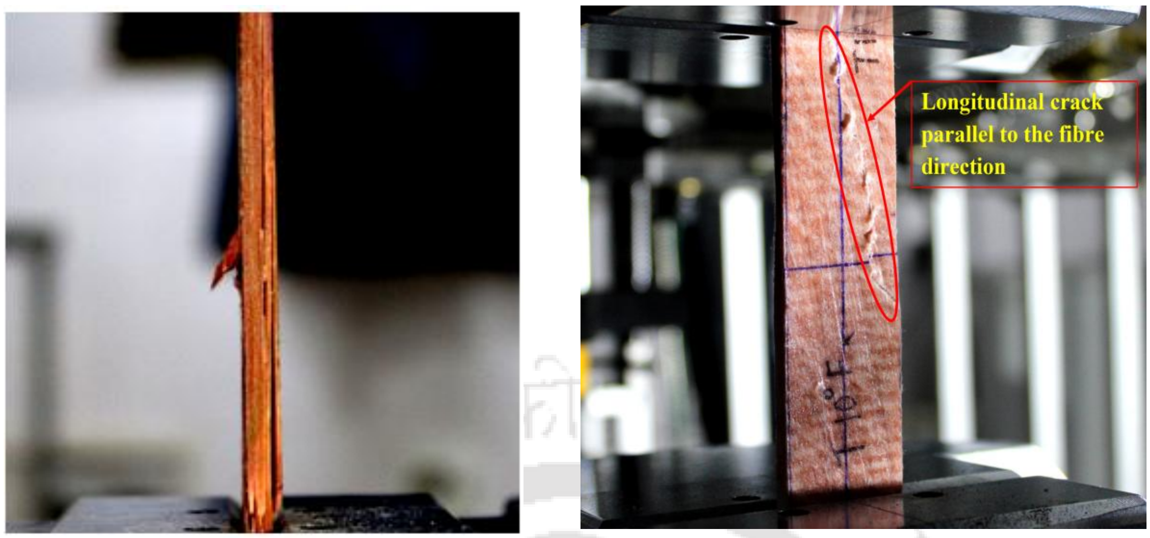

a) Edge view of a tensile coupon

c) 10^{o} *off-axis* tensile specimen

b) Edge view of compression coupons

d) Interlaminar shear specimen

Figure 3.8: Failure modes of coupon specimens.

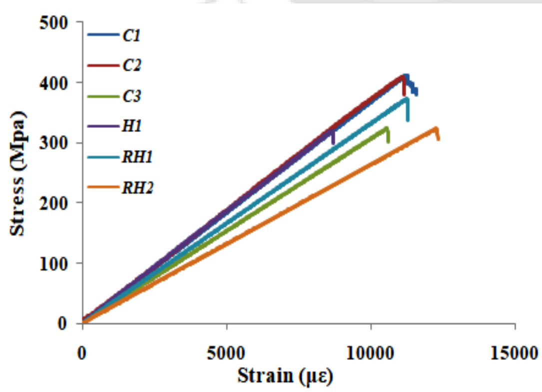

a) Tensile coupons of various GFRP profiles

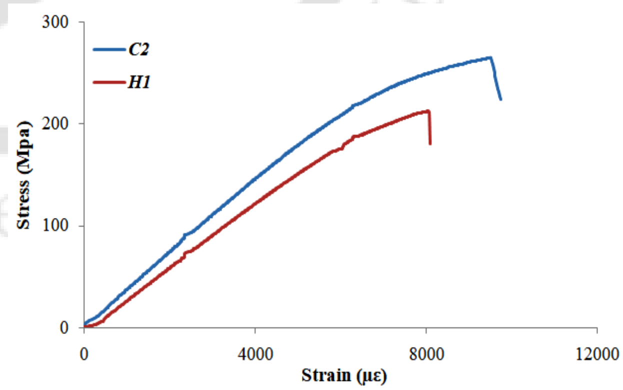

b) Compression coupons of C2 and H1 profiles

Figure 3.9: Stress-strain plots of representative longitudinal coupons of GFRP profiles.

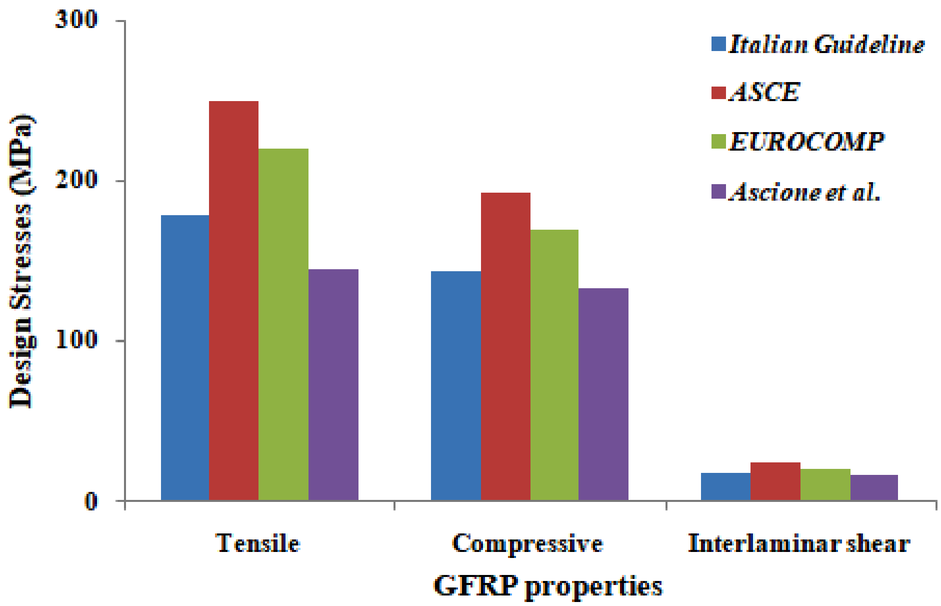

a) C1-profile

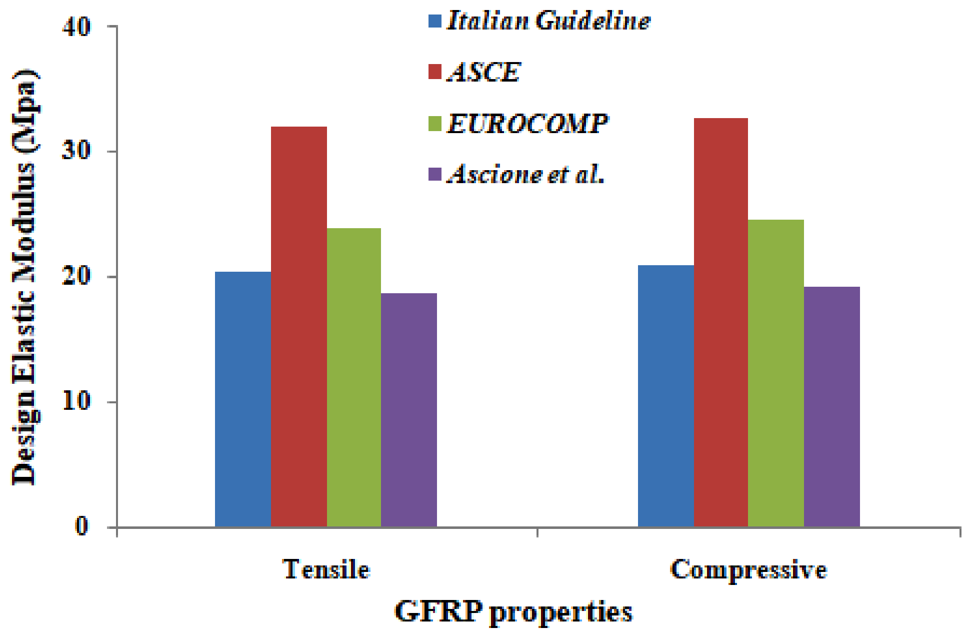

b) C2-profile

Figure 3.10: Comparison of the design stresses and moduli values obtained as per various design guidelines for C1 and C2 profiles, respectively.

This page is intentionally left blank.

CHAPTER 4

WEB CRIPPLING BEHAVIOUR OF UNPERFORATED GFRP WIDE FLANGE–SECTION PROFILES

4.1 INTRODUCTION

In the previous chapter (**Chapter 3**), investigation on the mechanical behaviour of pultruded GFRP profiles considering six different section sizes has been presented. In similar lines, this chapter will investigate extensively the web crippling behaviour of the GFRP wide flange (WF) section profile (due to time constraint, web crippling of other GFRP sections are not considered for the present research effort). As discussed previously, the web crippling failure in GFRP members is a major concern for the designers due to their weak mechanical properties in the transverse direction. However, limited research has been reported on the web-crippling phenomenon of GFRP profiles. Researchers have primarily investigated the effects of plate thickness (e.g. Borowicz and Bank, 2010), bearing length (e.g. Borowicz and Bank, 2010; Chen and Wang, 2015; Fernandes et al., 2015; Chen and Wang, 2015; Zhang and Chen, 2017) slenderness ratio (e.g. Borowicz and Bank, 2010; Wu and Bai, 2014; Fernandes et al., 2015; Wu et al., 2019) and loading (e.g. end two flanges (ETF) and interior two flanges (ITF)) and support boundary conditions (specimens seated on bearing plate or on the ground) (e.g. Wu and Bai, 2014; Chen and Wang, 2015; Fernandes et al., 2015; Chen and Wang, 2015; Zhang and Chen, 2017; Wu et al., 2019), on the web crippling behaviour of GFRP profiles. In the case of bearing length effect on web crippling strength, Borowicz and Bank (2010) and Fernandes et al. (2015) observed an enhancement in the ultimate crippling capacity with increasing bearing length. Fernandes et al. (2015) also concluded that by increasing the bearing length, failure pattern of the GFRP profiles changed from web-crushing to web-buckling. On the other hand, Chen and Wang (2015), Chen and Wang (2015) and Zhang and Chen (2017) reported that increasing the bearing length did not increase the ultimate crippling strength of the GFRP profiles, but rather resulted in decreased ultimate load. Hence, given the limited experimental data and inconsistency in the effect of plate bearing length, it is believed that, additional experimental data would be beneficial for the scientific community, to gain more insight on the web crippling behavior of GFRP profiles. Further, based on the experimental tests on GFRP I–sections of various sizes, e.g. overall height of 152.4 to 304.8 mm (Borowicz and Bank, 2010); 100 to 400 mm (Fernandes et al., 2015); 99.50 mm (Chen and Wang, 2015), web crippling design equations were proposed in the literature, as functions of bearing length, slenderness ratio, plate thickness etc. In this context, it may be worthwhile to assess their suitability, as more experimental data are made available.

The present experimental study investigates systematically the effects of bearing lengths on web crippling behaviour of smaller sized (overall height = 69 mm) GFRP pultruded wide flange (WF) profile, manufactured by an Indian pultruder (details are given in **Chapter 3**), under ITF and ETF loading conditions. It may be noted that the currently available experimental database in the literature covers I-sections of overall height in the range of 99.50 mm to 400 mm, and hence, the current study would add additional experimental data to the limited literature database. The investigation also examines the effects of loading conditions and thickness of loading (or support) plates on web crippling phenomena. Finite element (FE) analyses were performed in order to check the effectiveness of conventional FE numerical methods for simulating the web crippling behaviour in GFRP profiles and reproducing the experimental test results. The outcomes of the study are presented in the form of load–displacement curves, failure modes and ultimate web crippling strength values. Applicability of the existing crippling load design formulae for GFRP profiles are checked by comparing with those of present experimental results. Following the comparison, improved design equations are proposed based on data from present experimental campaign and from literature. The suitability of the proposed design rules for web crippling of GFRP WF or I–section is then assessed by using reliability analysis.

4.2 EXPERIMENTAL INVESTIGATION

4.2.1 General

The present experimental campaign mainly includes web crippling experiments conducted on a GFRP wide flange (WF)–section profile under ITF and ETF loading conditions. Detailed dimensions of the GFRP WF–section profile is given in Figure 4.1. Details of the web crippling tests and their results are presented in the following sections.

4.2.2 Web crippling test specimens

The test programme was conducted by considering 53 specimens tested under web crippling. All specimens were obtained by cutting the same GFRP wide flange section. The length of the specimens (L) for both ETF and ITF loading conditions were determined according to the specifications given in North American Specification (2007). The bearing plates used for the tests were mild steel plates which were machined to specified dimensions. For each loading condition (except for the "*N120* series"), two different plate thicknesses (t_{plate}), namely, 8 and 10 mm; and five bearing lengths (N): 25, 50, 70, 100 and 120 mm, were used. Three specimens were tested for each type of test condition i.e. each load configuration, bearing length and plate thickness. Details of the test specimens and bearing plates are listed in Tables 4.1 and 4.2.

4.2.3 Specimen labelling

Test specimens were labeled in such a way that the loading condition, thickness of bearing plate, length of bearing and test sequence number could be easily recognized from their label. For instance, the label ''ETF–N25–tp08–1" can be referred as: first notation "ETF" stands for the loading type which indicates end-two-flange loading (ITF for interior-two-flange loading); second notation "N25" specifies the length of bearing i.e. 25 mm; "tp08" indicates the thickness of bearing plate as 8 mm; and the last notation defines the test sequence number, where, "1" is the first completed test, respectively.

4.2.4 Test setup and procedure

The web crippling experiments were performed under the end-two-flange (ETF) and interior-two-flange (ITF) loading conditions according to the specifications given in the NAS (2007) (see Figures 4.2a–c). Two similar bearing plates were placed at the mid-length and end of each specimen to generate ITF and ETF loading conditions, respectively. Application of load or reaction forces was through the steel bearing plates. The lengths of the bearing plates (200 mm) were such that it could act across the full flange width of the wide flange–section profile. Two half rounds (mild steel) were used to simulate the hinge supports at the loading points. All web crippling tests were carried out in a UTM of 250 kN load capacity (see Figures 4.3a–b). Load was applied in a displacement control mode with a speed of 1mm/min. Specimens were loaded up to failure while recording the load and its cross-head displacement data simultaneously at 0.1 s interval. Each specimen was examined carefully to identify its failure modes during and after completion of each test.

4.3 NUMERICAL INVESTIGATION

4.3.1 General

Finite element (FE) analyses were performed in order to check the effectiveness of conventional FE numerical methods for simulating the web crippling behaviour in GFRP profiles and reproducing the experimental test results. The investigation was mainly carried out to evaluate the failure patterns and ultimate load in two series of tests, namely; “ITF_N50_tp10” and “ETF_N50_tp10”. For validating the FE models, both numerical and experimental results were compared. All finite element models for simulating the web-crippling experiments were modelled using the standard commercial finite element software, Abaqus (2009) by following similar modelling procedure adopted in different literature (e.g. Fernandes et al., 2015; Nunes et al., 2017).

4.3.2 Geometrical properties and mesh

The geometry and dimensions of the GFRP profile and steel load bearing plates used in the experimental tests were specified according to their measured values. The midline dimensions of the web and flanges were taken into consideration while fixing the cross-section geometry of the GFRP profile and its thickness. The flanges and web of the GFRP WF profile were meshed using four-node shell elements with reduced integration (S4R), while the steel load bearing plates were meshed using eight-node solid elements with reduced integration (C3D8R).

In order to choose an appropriate element size in the numerical models, mesh convergence study was carried out. Linear buckling analysis was performed by considering different mesh sizes (2 mm to 10 mm) for ETF specimen. The first or critical Eigen value for each mesh size was obtained and subsequently plotted against the ratio of web height to element sizes in Figure 4.4. Thus, the number of elements in the web across the specimen's height was varied in the range of 15–25 and along the length this number was kept in a range of 57–102 for "ITF_N50_tp10" specimen and 31–62 for "ETF_N50_tp10" specimen, respectively. In the flange, the number of elements across its width was in the range of 22–40. An average aspect ratio of ~1 was maintained for all elements. In Figures 4.5a and 4.5b, numerical models developed for specimen series "ITF_N50_tp10" and "ETF_N50_tp10" are shown alongside their axes definition, respectively.

4.3.3 Material properties and failure criteria

For simulating the material behaviour, the steel plates were defined as linear elastic with a Young's modulus value of 210 GPa and a Poisson's ratio of 0.3. GFRP was defined as a composite, elastic and laminated material. The strength and elastic properties obtained from the mechanical characterization tests, as given in **Chapter 3**, were utilized to assign the GFRP material properties in the FE models. In the present study, geometrically non-linear effects of the GFRP are considered, while, physically non-linear effects are not included in the FE models. This is particularly done owing to the fact that GFRP is a brittle material and it needs to utilize highly complicated crack propagation methods for simulating its progressive failure. In this study, the Hashin damage initiation criterion (Hashin, 1980; Barbero et al., 2013) was used to predict the initial failure of the GFRP profiles. This damage criterion involves four independent damage initiation criteria which are: (a) fibre tension, F_f^t; (b) fibre compression, F_f^c; (c) matrix tension, F_m^t; and (d) matrix compression, F_m^c and described in detail in Section 2.5.1. In the present study, as the fibre tension criteria does not dominate the material damage, the α_i value considered is not relevant. Hence, a default value of α_i = 0.0 is adopted as given in the ABAQUS (2009) built-in solver.

The fracture toughness properties for the GFRP material were evaluated based on the procedure given in Nunes et al. (2016) and subsequently adopted in the numerical models. In Nunes et al. (2016), the fracture energy has been defined as the area under the stress-strain curves obtained from the mechanical characterization tests. In the present study, the longitudinal tensile fracture energy (G_{ft}) and longitudinal compressive fracture energy (G_{fc}) values were obtained using this procedure. In the absence of strain data, the transverse tensile fracture energy (G_{mt}) and transverse compressive fracture energy (G_{mc}) values were directly adopted from Nunes et al. (2016) and used in the Hashin damage evolution suboption in Abaqus (2009). The fracture energy values used in the models are as follows:

Longitudinal tensile fracture energy (G_{ft}) = 1.4875 N/mm

Longitudinal compressive fracture energy (G_{fc}) = 0.9872 N/mm

Transverse tensile fracture energy (G_{mt}) = 0.424 N/mm (Nunes et al., 2016)

Transverse compressive fracture energy (G_{mc}) = 0.948 N/mm (Nunes et al., 2016)

4.3.4 Boundary conditions

In the FE models, the loading boundary conditions were employed to the steel bearing plates. For applying boundary conditions, two reference points were positioned each at the middle of bottom surface of the bottom plate (RP–1) and top surface of the top plate (RP–2) to which the degrees of freedom were coupled with kinematic coupling. All degrees of freedom were restrained at the bottom surface of the bottom plate while vertical displacement degree of freedom along y axis was released at the top surface of the top steel plate. In both cases of linear buckling analysis and non linear analysis, application of load was through imposed displacement to the top steel bearing plate (through RP–2) in the y–direction.

4.3.5 Contact formation

In all FE models, the contact pair formulation was adopted for employing contact between different parts of the models. Different surfaces were defined that were to undergo contact. Surface–to–surface interactions were employed between the GFRP profiles and the steel bearing plates. The steel bearing plates were positioned with an offset distance equal to half the flange thickness of the GFRP profile. In defining the interaction, the normal behaviour was considered to be ‘‘hard’’ contact. Regarding the tangential behaviour, it was deemed to be only due to friction and a friction coefficient value of 0.4 was adopted as reported in Fernandes et al. (2015). Several numerical analyses were performed with a range of friction coefficient values (0.2–0.4) and results were found to be non sensitive to this parameter.

4.3.6 Finite element (FE) analysis

For each series, initially, linear buckling analysis was carried out for estimating the eigenvalue of the critical buckling load and the deformed shape of corresponding buckling mode (see Figures 4.6a–b). The results of the linear buckling analyses were then used in the non-linear models by incorporating the initial geometrical imperfections with the first buckling mode shape. In the absence of experimental data, the value of initial geometric imperfections was taken to be $h_w/2000$, as reported in Fernandes et al. (2015). The FE models were also verified with different initial geometric imperfection values such as $h_w/1500$, $h_w/1800$, $h_w/2200$ and $h_w/2500$. However, no significant change in the initial failure loads was observed. Non-linear analyses were then carried out using the static Riks method for determining the initial failure loads and distributions of the stress fields for various load levels. The analyses were carried out using a maximum number of 100 increments.

4.3.7 Verification of FE models

Verification of the finite element models against the experimental results was necessary to check the accuracy of the models. The finite element models developed in this study were checked and verified against the experimental results with regard to the failure patterns, ultimate strength and load–displacement behaviour of the GFRP WF-section profiles. Detailed discussion is provided in the following sections.

4.4 RESULTS AND DISCUSSION

4.4.1 General

In the experimental programme, 26 specimens were tested under ITF loading condition and 27 specimens were tested under ETF loading condition. The experimental ultimate web crippling loads per web (P_{EXP}) are given in Tables 4.1 and 4.2. For validation purpose, finite element analyses were carried out and compared with the experimental result of specimen series "ITF_N50_tp10" and "ETF_N50_tp10" and discussed in detail. In the following subsections, detailed discussions on the failure patterns, load-displacement behaviour and ultimate loads are presented.

4.4.2 Failure patterns

4.4.2.1 ITF load configuration

In case of specimens with ITF loading, failure mainly occurred at the web with longitudinal cracking or material wrinkling in the vicinity of the bearing plates (see Figures 4.7a–c). All specimens in the "ITF–N100" series showed multiple longitudinal cracks under the loading plates near the web-flange junction as well as at the mid height of the web (see Figure 4.7a). In case of series "ITF–N70", longitudinal cracks appeared at the web and near both web-flange junctions (see Figure 4.7b). Specimens in the series "ITF–N50" showed initial failure at the centre of the web with longitudinal cracking accompanied by web-flange junction failure (see Figure 4.7c). In a similar pattern, "ITF–N25" series specimens also exhibited longitudinal cracks under the loading plates near the web-flange junctions.

It is clear that most of the specimens failed by crushing of web and web-flange junction separation. In some specimens, only web crushing could be observed. No specimen showed out of plane web deformation or web buckling. In both ETF and ITF loading configurations, failure was in the vicinity of the loading region. However, in some cases e.g. for "ITF–N50–tp10–1" (see Figure 4.7c), web-flange junction separation extended to the end of the specimens. After the initial web-flange junction separation, the web was able to continue carrying load until failure by crushing. Other specimens in the "ITF– N50–tp10" series showed multiple longitudinal cracks under the loading plates near the web-flange junction as well as at the mid height of the web (see Figure 4.7d). For obtaining a clear understanding of the failure patterns, "ITF– N50–tp10–2" specimen was cut at the middle and its cross sectional view is presented in Figure 4.7e. Shear failure could be observed in the web which propagated towards the end and web-flange junction of the specimens. In all cases, initial cracking sound was heard which increased with the increase of load. This continued until the load reached its ultimate value with the emission of a larger cracking sound.

In order to have a better understanding of the web crippling failure patterns; the longitudinal, transverse and shear stress fields in the numerical model for "ITF– N50–tp10" specimen were evaluated and analysed. The stress distributions were assessed for two different load levels as shown in the numerical load–displacement curve: at the commencement of failure (L1) and at ultimate failure (L2) (see Figure 4.8). From Figures 4.9a–f, it can be seen that the shear stress initiates the failure and reaches its maximum value correspondingly. Initial stress concentration can be observed in some of the finite elements in both the web-flange junctions near the edges of the bearing plates (see Figure 4.9a) after which it spreads towards the middle of the web (see Figure 4.9b). On the other hand, the transverse and longitudinal stresses could not reach their ultimate values (see Figures 4.9c–f). The failure modes obtained from the FE predictions can be compared with the experimental failure patterns (see Figures 4.7d–e). It can be concluded that the FE models could predict well the failure modes in the GFRP specimens. The shear stress distribution in the web of the specimen was observed mainly in the vicinity of the bearing plates. No out of plane web deformation or web buckling could be seen similar to the experimental findings. It can be concluded that shear stresses played the most influential part in failure initiation than the longitudinal and transverse stresses in the GFRP specimens. Similar observation was also reported by Fernandes et al. (2015) and Nunes et al. (2017).

4.4.2.2 ETF load configuration

In regard to the ETF loading, specimens failed suddenly with a clearly audible cracking sound on the onset of failure. All specimens showed steep sloped “shear-wedge” at their cross sections that extended from end to interior (see Figures 4.10a–c). Specimens in the “ETF–N100” series exhibited longitudinal crack in the web under the loading plates near the web-flange junction. Similar kind of failure patterns were observed in case of series “ETF–N70”, where, web-flange junction failure was accompanied by longitudinal cracks that started from a steep sloped “shear-wedge” at their cross sections and extended from end to interior (see Figure 4.10a). Specimens in both “ETF–N50” and “ETF–N25”series showed longitudinal cracks with steep sloped “shear-wedge” at their cross sections that extended from end to interior of web (see Figures 4.10b–c).
From the above observations, it is clear that all specimens under ETF loading configuration failed by shearing or crushing of web. Similar to ITF specimens, no specimen showed out of plane web deformation or web buckling. In all cases, initial cracking sound was heard which increased with the increase of load. This continued until the load reached its ultimate value with the emission of a larger cracking sound.

The longitudinal, transverse and shear stress fields in the numerical model for “ETF– N50–tp10” specimen were assessed. The stress distributions were evaluated for two different load levels as shown in the numerical load–displacement curves (see Figure 4.11): at the commencement of failure (P1) and at ultimate failure (P2). From Figures 4.12a–f, it can be seen that the shear stress initiates the failure in the GFRP specimen and reaches its maximum value correspondingly. The shear stress distribution was observed mainly in the vicinity of the bearing plates. Initial stress concentration can be observed in some of the finite elements in both the web-flange junctions near the edges of the bearing plates (see Figure 4.12a) after which it spreads towards the middle of the web (see Figure 4.12b). On the other hand, the transverse and longitudinal stresses could not reach their ultimate values (see Figures 4.12c–f). The failure modes obtained from the FE prediction can be compared with the experimental failure patterns (see Figure 4.10b). It can be concluded that the FE models could predict well the failure modes in the GFRP specimen. Similar to the experimental findings, there was no out of plane web deformation or web buckling in the specimen. It is clear that shear stresses played the most critical part in failure initiation than the longitudinal and transverse stresses in the GFRP specimens.

4.4.3 Load–displacement behaviour

The load–displacement plots of the GFRP specimens for both ITF and ETF loading conditions are shown in Figures 4.13a–b and Figures 4.14a–b. As the results of all tested specimens in a series (i.e. for a particular load configuration, bearing length and plate thickness) are very consistent, a single representative curve of each series is shown in the figures. It can be clearly observed that all specimens exhibited linear behaviour up to a peak point which was followed by a sudden fall in the load–displacement response. In some specimens, this peak point in the load–displacement curve can be linked to the initial web-flange junction failure and for others it can be the initial web crushing failure. The continuation of the load–displacement curve after the initial peak load demonstrates that the web continued to carry the load upto a point where the ultimate failure would occur by crushing or shearing of the web.

The numerical load–displacement curves of the GFRP specimens for both ITF and ETF loading condition are presented in Figures 4.8 and 4.11 and compared with the respective experimental curves. Linear elastic behaviour can be seen up to a point which was followed by a sudden drop in the load–displacement response. It can be said that though the numerical results were not exactly matching with the experimental results but were close (P_{EXP}/P_{FEA} = 1.01 and 0.92 for ITF and ETF loading, respectively). The differences in the ultimate loads and behaviour after ultimate loads may be due to the shortcomings of the Hashin damage initiation criteria (available in Abaqus, 2009) used in the numerical models. Also, compared to their numerical counterparts, the experimental load–displacement curves are found to have lower elastic stiffness. The reduced stiffness in the experimental curves may arise due to the fact that the experimental displacements are plotted from the cross-head displacement data which includes the effects of clearances and initial adjustments of the test fixtures; and could not be simulated by the FE models. In literature (Nunes et al., 2017) also some differences could be observed between the experimental and numerical load–displacement curves due to similar reasons. From the above observations, it can be understood that the FE models could simulate the experimental results closely (though not exactly).

4.4.4 Ultimate crippling loads

In Tables 4.1 and 4.2, the web-crippling tests results *viz*. ultimate loads, failure patterns etc. for both ITF and ETF load configurations are presented. The load–displacement curves of specimens with the two different loading conditions are plotted in Figures 4.13a–b. From these figures and Tables 4.1 and 4.2, it can be observed that change in loading condition greatly influences the ultimate load of the specimens. As for example, shifting the loading condition from ETF to ITF in case of specimens with bearing length 25 mm and thickness 8 mm (series "N25–tp08") increased the ultimate load by +68.9%. Similarly, other tested series also showed increase in ultimate load that ranged from +16.1% (series "N100–tp08") to +66.9% (series "N25–tp10"). In a similar manner, increasing the bearing length from 25 mm to 120 mm (or N/t_w = 5 to 24) with a plate thickness of 8 mm increased the ultimate load by upto +280.9% in case of ETF loading, whereas, in the case of ITF loading, this increase was +85.5% when the bearing length was increased from 25 mm to 100 mm (see Figures 4.14a–b). For the case of bearing plates with 10 mm thickness, when the bearing length was increased from 25 mm to 100 mm (or N/t_w = 5 to 20), the ultimate load increased by upto +95.1% (ITF) and +161.7% (ETF), respectively. It is evident that for a particular loading condition and plate thickness, specimens tested with the largest bearing length exhibited the highest load carrying capacity while those with the shortest bearing length presented the lowest load carrying capacity. However, while assessing the effects of plate thickness on the ultimate load, it was found that increasing plate thickness from 8 mm to 10 mm (or t_{plate}/t_w = 1.6 to 2.0) did not considerably change the ultimate loads and for almost all cases it was insignificant. Hence, it was decided not to consider the effects of plate thickness in calculating the average ultimate load in a series with same bearing length values for further analysis.

4.4.5 Effect of loading conditions, bearing length and plate thickness on web crippling behaviour

From the above experimental observations, it can be concluded that loading condition and bearing length have direct influence on the web crippling strength and behavior of GFRP WF–sections. For a particular loading condition and plate thickness, load carrying capacity was increased with the increase in bearing length. This observation agrees well with those reported by Borowicz and Bank (2010) and Fernandes et al. (2015), but contrasts with that of Chen and Wang (2015), Chen and Wang (2015) and Zhang and Chen (2017). Another conclusion is that changing the loading condition from ETF to ITF increased the ultimate load of the specimens which is similar to the observations made by Wu and Bai (2014), Fernandes et al. (2015), Chen and Wang (2015), Zhang and Chen (2017) and Wu et al. (2019). On the other hand, variation in plate thickness from 8 mm to 10 mm (or t_{plate}/t_w = 1.6 to 2.0) did not have significant effect on the ultimate loads in almost all cases. In this regard, further investigation considering a wide range of plate thickness to web thickness ratio is required to bring a conclusion.

4.5 COMPARISON OF RESULTS WITH DESIGN METHODS

4.5.1 General

Development of design equations for GFRP profiles by previous researchers were based on the formulations developed for hot-rolled and cold-formed steel sections (e.g. NAS, 2007; AISC, 2005; Eurocode3, 2006). However, it may be noted that, in contrast to metallic members, owing to their material anisotropy, GFRP profiles exhibit completely different and complex failure patterns that mainly include web crushing, web buckling and web–flange junction separation. In the following sections, applicability of various design equations proposed in the literature and newly proposed design rules for the estimation of crippling load capacity of GFRP profiles are briefly highlighted.

4.5.2 Design methods for GFRP profiles

As discussed previously, limited number of studies has been reported on the web crippling behaviour of GFRP profiles. Design formulae for GFRP profiles have been proposed in the literature by Borowicz and Bank (2010), Wu and Bai (2014), Fernandes et al. (2015), Wu et al. (2019) and Chen and Wang (2015). In Section 2.4.2, a brief discussion on these design formulations is presented. It is worth mentioning that the design formulae for GFRP profiles (Equations 2.1 to 2.18) developed in the above literatures were calibrated using their own experimental data. In this context, to check their applicability with the results of the present experimental campaign, comparisons are made between the results obtained by these analytical formulae with the present experimental results and are presented in Tables 4.3 and 4.4 for both ETF and ITF loading conditions, respectively. For the present study, the value of k in Equation 2.1 is taken to be 1.5 times the flange thickness as given in Borowicz and Bank (2010). In Equation 2.16, the values of the empirical coefficients C, C_r, C_{Lh}, C_χ are 0.0688, 0.5757, 0.0037 and 0.0647 for the ETF loading, and 0.1489, 0.5492, 0.0015 and 0.0634 for the ITF loading, respectively (as reported in Fernandes et al., 2015). The value of buckling reduction factor, χ_F has been calculated using formulae given in the EC3: 1–5 (2006) and found to be in the range of 0.56–0.87. Use of GFRPs' yield stress is very misleading as these are brittle material. However, for calculation purpose, the f_y value in Equations 2.17 and 2.18 are taken to be the longitudinal tensile strength of the web. From Tables 4.3 and 4.4, it can be observed that none of these analytical formulae gives accurate prediction of the experimental web crippling loads. The design formulae proposed by Borowicz and Bank (2010), Fernandes et al. (2015) and Chen and Wang (2015) overestimated the web crippling capacity; whereas, Wu and Bai (2014) gave very arbitrary prediction. Hence, new design equations are necessary for reliable prediction of the web-crippling capacity for GFRP WF or I–section profiles under ETF and ITF loading conditions.

4.5.3 Proposed design methods for GFRP WF or I–section profiles

Development of new design equations for the present study is based on the formulations given in Eurocode3 (2006) (Equations 2.19–2.20); NAS (2007) (Equation 2.21); Wu et al. (2019) (Equations 2.5–2.15); and Fernandes et al. (2015) (Equation 2.16). In deriving new design equations, combined test data from the current experimental campaign and experimental data from Fernandes et al. (2015) have been used.

As already discussed, GFRP members are highly orthotropic in nature with very low mechanical properties in their transverse direction than the pultruded direction. As such, it will not be appropriate to use an average yield stress value which is generally measured in the longitudinal or pultruded direction. According to Bank (2006), the critical crushing stress for resisting transverse forces is equal to the transverse compressive strength of the web ($f_{cu,T}$). As discussed earlier, Fernandes et al. (2015) adopted transverse compression strength ($f_{cu,T}$) and replaced the the yield strength of steel (f_y) in the NAS (2007) equation in deriving their equation. According to Bai and Keller (2009); Bai et al. (2009); and Yu and Bai (2014), under transverse compressive load, GFRP sections are prone to fail in interlaminar shear. Borowicz and Bank (2010) and Wu and Bai (2014) considers that the web crippling load at failure is a function of the interlaminar shear strength (f_s). This was based on the failure modes observed during their experimental investigation. Wu and Bai (2014) reported Mode III shear failure at the web flange junction of the GFRP square hollow sections, whereas, Borowicz and Bank (2010) observed that the development of bulge under the load-head caused by the penetration of the shear wedge material from the web-flange junction into the web of the FRP I-beams led to interlaminar shear failure. Wu et al. (2019) proposed design equations separately for specimens with initial web flange junction failure and specimens with initial web buckling failure. The equation for specimens with initial web flange junction failure considered the web crippling load to be a function of the interlaminar shear strength (f_s). On the other hand, the design equation proposed for web buckling failure used transverse compressive strength of the web to calculate the web crippling capacity of GFRP channel sections.

From the above discussions, it is convinced that the researchers have used mainly two strength parameters to derive the design equations for GFRP sections viz. interlaminar shear strength (f_s) for specimens with initial web flange-junction failure and transverse compression strength ($f_{cu,T}$) for specimens with initial web crushing or web buckling. In the present investigation, given the nature of failure patterns in the GFRP specimens, the predominant failure mode is the web crushing or web shear failure which mainly occurs in the web region of the GFRPs, although some specimens also showed web-flange junction failure. Therefore, the current study will use transverse compression strength ($f_{cu,T}$) parameter in deriving the design equations which will be based on the Fernandes et al. (2015), Wu et al. (2019), Eurocode3 (2006) and NAS (2007) design equations. The yield strength of steel (f_y) in the Eurocode3 (2006) and NAS (2007) equations will be replaced by the transverse compression strength ($f_{cu,T}$) in the web of the GFRP profiles. Also, the coefficients in the design equation in Fernandes et al. (2015) are modified to fit into the new test data set.

Multiple regression analyses have been carried out and new design formulae are developed and calibrated for GFRP WF or I–shaped section profiles loaded under ETF and ITF loading conditions. The proposed design formulae for estimating web crippling strength of GFRP WF or I–section under ETF and ITF loading conditions are as follows:

A) **Modified Eurocode3 (2006) formulae**:

$$P_{EC3,ETF} = 0.252\left[12 - \frac{h_w / t_w}{4.8}\right]\left[1 + 0.33 \times \frac{N}{t_w}\right] t_w^2 f_{cu,T} \tag{4.1}$$

$$P_{EC3,ITF} = 0.31\left[17 - \frac{h_w / t_w}{8}\right]\left[1 + 0.158 \times \frac{N}{t_w}\right] t_w^2 f_{cu,T} \tag{4.2}$$

B) **Modified NAS (2007) formula**:

$$P_{NAS,ETF} = 0.164 t_w^2 f_{cu,T}\left(1 - 0.03 \times \sqrt{\frac{r}{t_w}}\right)\left(1 + 36.5 \times \sqrt{\frac{N}{t_w}}\right)\left(1 - 0.14 \times \sqrt{\frac{h_w}{t_w}}\right) \tag{4.3}$$

$$P_{NAS,ITF} = 1.23 t_w^2 f_{cu,T}\left(1 - 0.002 \times \sqrt{\frac{r}{t_w}}\right)\left(1 + 4.0 \times \sqrt{\frac{N}{t_w}}\right)\left(1 - 0.67 \times \sqrt{\frac{h_w}{t_w}}\right) \tag{4.4}$$

C) **Modified Fernandes et al. (2015)**:

$$P_{ETF} = 0.0474 f_{cu,T} h_w^2\left(1 - 0.58 \times \sqrt{\frac{r}{t_w}}\right)\left(1 + 0.0036 \times \frac{h_w^2 N}{t_w^3}\right)\left(1 - 0.0634 \times \frac{h_w}{t_w}(1 - \chi_F)\right) \tag{4.5}$$

$$P_{ITF} = 0.136 f_{cu,T} h_w^2\left(1 - 0.5642 \times \sqrt{\frac{r}{t_w}}\right)\left(1 + 0.0013 \times \frac{h_w^2 N}{t_w^3}\right)\left(1 - 0.0606 \times \frac{h_w}{t_w}(1 - \chi_F)\right) \tag{4.6}$$

Here, h_w, t_f, t_w, N and $f_{cu,T}$ are the web height; flange thickness; web thickness; bearing length; and transverse compression strength of GFRP member, respectively. r is inside bend radius which is taken as the sum of the web-flange junction radius and the thickness of the profile as given in Fernandes et al. (2015); and χ_F is the buckling reduction factor as given in EC3: 1–5.

D) **Equivalent force based design equation (after Wu et al., 2019)**:

As discussed in Section 2.4.1, Wu et al. (2019) proposed design equations based on the principles given in AS 4100 (1998) for steel web buckling (Equations 2.5–2.15). AS 4100 (1998) considers the dispersion of stress from the bearing plate to the web flange junction and to the mid height of web with two different constant angles (α_d and β_d), as shown in Figures 4.15a–b. In order to assess the dispersion angles in the case of GFRP profile under consideration, shear stress contour and their variations at the onset of failure along specimen distance through the web-flange junction and mid height of web are plotted for both ITF and ETF specimens. For this purpose, stress paths were defined at the nodes along the web-flange junction and mid height of the web for the specimens considered. Typical stress plots are shown in Figures 4.16a–b and 4.17a–b. Two bearing lengths *viz.* 50 mm and 120 mm are considered for this purpose. To see the effect of thickness of specimens on the dispersion angles α_d and β_d, thicknesses of the specimens (t_w or t_f) have been varied between 3 to 20 mm. For each case, the stress plots are obtained and the area under each curve has been transformed into equivalent rectangular area ($F_{eqv} = d_{shear} \times B_{eff}$) (see Figure 4.18). Following this, the effective lengths (B_{eff}) of stress dispersion are calculated at the web-flange junction and mid height of web and subsequently, the dispersion angles α_d and β_d are measured.

In Figure 4.19, the dispersion angles α_d (alpha) and β_d (beta) are plotted against the specimens' thickness for both 50 mm and 120 mm bearing plates. It can be seen that the effect of bearing length (N) and section thickness (t_f or t_w) on angle α_d is almost negligible. However, a new value of angle α_d equal to ~84.41° is proposed which is obtained by averaging the α_d values for different thicknesses and bearing lengths. On the other hand, it can be seen that, angle β_d is significantly influenced by the thickness of section irrespective of the bearing lengths (see Figure 4.19). As, thickness increases, the angle of dispersion (β_d) becomes steeper. Henceforth, in defining angle, β_d, the thickness effect is considered and a new equation (Equation 4.13) has been proposed considering the effects of t_f (R^2 = 0.91).

The proposed equivalent force based design equations are as follows:

$$P_{n,ITF} = 1.13\alpha_c A f_{cu,T} \tag{4.7}$$

$$P_{n,ETF} = 1.06\alpha_c A f_{cu,T} \tag{4.8}$$

where, (4.9)

$$A = Kt_w$$

$$K = \min\{B_{eff}, L\} \tag{4.10}$$

$$B_{eff,ETF} = N + \frac{h_w}{2\tan\alpha_d} + \frac{t_f}{\tan\beta_d} \tag{4.11}$$

$$B_{eff,ITF} = N + \frac{h_w}{\tan\alpha_d} + \frac{2t_f}{\tan\beta_d} \tag{4.12}$$

$$\beta_d = 33.19 + 1.48t_f \tag{4.13}$$

Here, α_c is the member slenderness reduction factor as given in Wu et al. (2019) (for details see Section 2.4.1).

Using the newly proposed design equations (Equations 4.1–4.13), web crippling strengths are predicted and compared with the combined test data from the current experimental campaign and data from Fernandes et al. (2015) (see Tables 4.5 and 4.6). To get a clear understanding, comparisons are shown for the web crippling strengths from current test results and proposed equations for both loading in Figures 4.20a–b. In the following section, applicability of the newly proposed design equations is evaluated through reliability analysis.

4.6 RELIABILITY ANALYSIS

In this section, the suitability of the proposed design rules for web crippling of GFRP WF or I–section is assessed by using reliability analysis. In reliability analysis, reliability index (β) is used to quantify the relative safety of a given design. If the β value for a given design is greater than another design, then the relative safety or reliability of the design is assumed to be more. In the present study, the reliability analysis is carried out following the methods described in the Commentary section of the ASCE Specifications for the design of cold-formed stainless steel structural members (ASCE 8–02, 2002). However, as the GFRP members show very little ductility, the target reliability index (β_o) values for the member limit states need to be larger than the target reliabilities generally considered for the existing LRFD specifications for cold-formed steel (NAS, 2007) and stainless steel (ASCE 8–02, 2002) members. In that case, a target reliability range of 3.5–4.0 is recommended for material strength limit states by the Pre-standard for LRFD of FRP structures (ASCE, 2010). For the present analysis, the lower bound value of 3.5 is chosen as the target reliability index (β_o) to establish the suitability of the proposed design formulae. The resistance factor or ϕ–factor to be applied to web crippling resistance is taken to be 0.70 as given in the specification. In the analysis, a load combination of 1.2DL + 1.6LL is considered as specified in the ASCE (ASCE/SEI 7-10, 2013) Standard. Here, DL and LL indicate dead load and live load, respectively. The dead load to live load ratio is considered to be 0.2 as recommended in the NAS (2007) specification. For the current experimental campaign and test data obtained from Fernandes et al. (2015), comparisons are made between the experimental web crippling strengths and predicted strengths obtained using the proposed design equations and are presented in Tables 4.5 and 4.6. From these comparisons, the mean (P_m) and coefficients of variation (COV) (V_p) of load ratio are calculated. From Table F1 of the NAS (2007), other statistical parameters are obtained which include the mean value of material (M_m = 1.10) and fabrication factor (F_m = 1.0) and their corresponding coefficients of variations V_M = 0.10 and V_F = 0.05, respectively, for web crippling strength.

The mean values (P_m), coefficients of variation (V_p) and reliability index (β) values of the ratio of experimental to the predicted values for both current experimental data and test data obtained from Fernandes et al. (2015) are evaluated and summarized in Tables 4.5 and 4.6. The Eurocode3 (2006) based formula (Equation 4.1) for ETF loading gives a mean of 1.10 with a standard deviation (SD) of 0.15 and coefficient of variation (COV) of 0.14, whereas, for ITF loading (Equation 4.2) the mean is 1.13 with a SD of 0.17 and a COV of 0.15. The NAS (2007) based design formula for ETF loading (Equation 4.3) yields a mean of 1.25 with a SD of 0.26 and a COV of 0.21, whereas, for ITF loading (Equation 4.4) the mean is 1.13 with a SD of 0.18 and COV of 0.16. Also, the modified Fernandes et al. (2015) in case of ETF loading (Equation 4.5) yields a mean of 1.21 with a SD of 0.23 and a COV of 0.19, whereas, for ITF loading (Equation 4.6) the mean is 1.08 with a SD of 0.12 and COV of 0.11. On the other hand, the modified Wu et al. (2019) in case of ETF loading (Equation 4.8) gives a mean of 1.12 with a SD of 0.17 and a COV of 0.15, whereas, for ITF loading (Equation 4.7) the mean is 1.22 with a SD of 0.22 and COV of 0.18. From Tables 4.5 and 4.6, it is observed that the reliability index values

(β) for all proposed design equations are ≥ 3.5 and hence, it can be said that the proposed equations for determining web-crippling strengths of GFRP WF or I–shaped section profiles are reliable. In the present study, out of the proposed equations, the most economical design equations (based on target reliability, β_o = 3.50) are NAS (2007) based equations for both ETF (Equation 4.3, β = 3.50) and ITF (Equation 4.4, β = 3.51) loading conditions.

4.7 CONCLUSION

In this chapter, an extensive study on the web crippling behaviour of GFRP wide flange (WF) profile has been performed by utilising a GFRP WF–section manufactured by an Indian pultruder. Experimental investigations mainly include full scale web crippling experiments performed on 53 specimens under ETF and ITF loading configurations. Numerical investigations are also performed by considering the "N50–t10" series under both load conditions. The following conclusions are drawn based on the present investigation:

1) In case of specimens with ITF loading, failure mainly occurred at the web with longitudinal cracking or material wrinkling in the vicinity of the bearing plates. No specimen showed out of plane web deformation or web buckling. Shear failure could be observed in the web which propagated towards the end and web-flange junction of the specimens.
2) In regard to the ETF loading, specimens failed suddenly with a clearly audible cracking sound on the onset of failure. All specimens showed steep sloped "shear-wedge" at their cross sections that extended from end to interior.
3) All specimens exhibited linear behaviour up to a peak point which was followed by a sudden fall in the load–displacement response. In some specimens, this peak point in the load–displacement curve can be linked to the initial web-flange junction failure and for others it can be the web crushing failure initiation. The continuation of the load–displacement curve after the initial peak load demonstrates that the web continued to carry the load upto a point where the ultimate failure would occur by crushing or shearing of the web.
4) Change in loading condition greatly influences the ultimate load of the specimens. Shifting the loading condition from ETF to ITF in case of specimens with bearing

length 25 mm and thickness 8 mm (series “N25–t08”) increased the ultimate load by +68.9%.

5) Bearing lengths are found to have direct influence on the web crippling strength and behavior of GFRP WF–sections. It is evident that for a particular loading condition and plate thickness, specimens tested with the largest bearing length exhibited the highest load carrying capacity while those with the shortest bearing length presented the lowest load carrying capacity.

6) It was found that increasing plate thickness from 8 mm to 10 mm (or t_{plate}/t_w = 1.6 to 2.0) did not considerably change the ultimate loads and for almost all cases, it was insignificant.

7) FE models could simulate the experimental load–displacement curves of the GFRP specimens with satisfactory accuracy. However, compared to their numerical counterparts, the experimental load–displacement curves are found to have lower elastic stiffness.

8) From the experimental and numerical results, it is clear that shear stresses played the most significant part in failure initiation than the longitudinal and transverse stresses in the GFRP specimens.

9) Based on the combined test data from the current experimental campaign and data from literature, new design equations have been developed based on Eurocode3 (2006), NAS (2007), Fernandes et al. (2015) and Wu et al. (2019), for both ETF and ITF loading configurations.

Table 4.1: Specimen details and experimental results for ETF loading

Specimen name	b_{plate} (mm)	t_{plate} (mm)	L (mm)	Failure modes	Ultimate Load, P_{exp} (kN)	Average P_{exp} (kN)	STD	COV
ETF-N120-tp08-1	120	8	225	Web crushing	26.10			
ETF-N120-tp08-2	120	8	225	Web crushing	24.67	24.80	1.02	0.04
ETF-N120-tp08-3	120	8	225	Web crushing	23.62			
ETF-N100-tp10-1	100	10	205	Web crushing	17.11			
ETF-N100-tp10-2	100	10	205	Web crushing	14.90	17.01	1.68	0.10
ETF-N100-tp10-3	100	10	205	Web crushing	19.02			
ETF-N100-tp08-1	100	8	205	Web crushing	16.75			
ETF-N100-tp08-2	100	8	205	Web crushing	17.20	17.56	0.85	0.05
ETF-N100-tp08-3	100	8	205	Web crushing	18.73			
ETF-N70-tp10-1	70	10	175	Web crushing	16.25			
ETF-N70-tp10-2	70	10	175	Web crushing	15.66	15.66	0.48	0.03
ETF-N70-tp10-3	70	10	175	Web crushing	15.08			
ETF-N70-tp08-1	70	8	175	Web crushing	14.86			
ETF-N70-tp08-2	70	8	175	Web crushing	14.85	15.02	0.23	0.02
ETF-N70-tp08-3	70	8	175	Web crushing	15.35			
ETF-N50-tp10-1	50	10	155	Web crushing	11.66			
ETF-N50-tp10-2	50	10	155	Web crushing	11.01	11.35	0.27	0.02
ETF-N50-tp10-3	50	10	155	Web crushing	11.40			
ETF-N50-tp08-1	50	8	155	Web crushing	11.06			
ETF-N50-tp08-2	50	8	155	Web crushing	10.79	11.18	0.38	0.03
ETF-N50-tp08-3	50	8	155	Web crushing	11.70			
ETF-N25-tp10-1	25	10	130	Web crushing	6.62			
ETF-N25-tp10-2	25	10	130	Web crushing	7.42	6.90	0.37	0.05
ETF-N25-tp10-3	25	10	130	Web crushing	6.66			
ETF-N25-tp08-1	25	8	130	Web crushing	6.61			
ETF-N25-tp08-2	25	8	130	Web crushing	6.56	6.51	0.11	0.02
ETF-N25-tp08-3	25	8	130	Web crushing	6.36			

Table 4.2: Specimen details and experimental results for ITF loading

Specimen name	b_{plate} (mm)	t_{plate} (mm)	L (mm)	Failure modes	Ultimate Load, P_{exp} (kN)	Average P_{exp} (kN)	STD	COV
ITF-N100-tp10-1	100	10	310	Web crushing	19.53			
ITF-N100-tp10-2	100	10	310	Web crushing	24.27	22.47	2.10	0.09
ITF-N100-tp10-3	100	10	310	Web crushing	23.62			
ITF-N100-tp08-1	100	8	310	Web crushing	20.92			
ITF-N100-tp08-2	100	8	310	Web crushing	19.95	20.39	0.40	0.02
ITF-N100-tp08-3	100	8	310	Web crushing	20.30			
ITF-N70-tp10-1	70	10	280	Web crushing	18.39			
ITF-N70-tp10-2	70	10	280	Web crushing	18.43	18.70	0.41	0.02
ITF-N70-tp10-3	70	10	280	Web crushing	19.27			
ITF-N70-tp08-1	70	8	280	Web crushing	18.64			
ITF-N70-tp08-2	70	8	280	Web crushing	17.73	17.93	0.52	0.03
ITF-N70-tp08-3	70	8	280	Web crushing	17.42			
ITF-N50-tp10-1	50	10	260	Web crushing	15.70			
ITF-N50-tp10-2	50	10	260	Web crushing	17.25	16.15	0.78	0.05
ITF-N50-tp10-3	50	10	260	Web crushing	15.50			
ITF-N50-tp08-1	50	8	260	Web crushing	15.63			
ITF-N50-tp08-2	50	8	260	Web crushing	16.85	15.47	1.19	0.08
ITF-N50-tp08-3	50	8	260	Web crushing	13.94			
ITF-N25-tp10-1	25	10	232	Web crushing	12.49			
ITF-N25-tp10-2	25	10	232	Web crushing	11.55	11.52	0.81	0.07
ITF-N25-tp10-3	25	10	232	Web crushing	10.51			
ITF-N25-tp08-1	25	8	232	Web crushing	10.93			
ITF-N25-tp08-2	25	8	232	Web crushing	11.93	10.99	0.74	0.07
ITF-N25-tp08-3	25	8	232	Web crushing	10.12			

Table 4.3: Comparison of experimental results with existing design formulae for ETF loading

Specimen series	P_{exp} (kN)	Borrowicz and Bank (2011)		Fernandes et al. (2015)		Chen and Wang (2015)		Wu and Bai (2014)	
		P_{pred} (kN)	P_{pred}/P_{exp}	P_{pred} (kN)	P_{pred}/P_{exp}	P_{pred} (kN)	P_{pred}/P_{exp}	P_{pred} (kN)	P_{pred}/P_{exp}
ETF-N120-tp08	24.80	33.78	1.36	80.41	3.24	54.03	2.18	18.77	0.76
ETF-N100-tp10	17.01	32.71	1.92	70.90	4.17	56.87	3.34	15.64	0.92
ETF-N100-tp08	17.56	31.10	1.77	70.90	4.04	56.87	3.24	15.64	0.89
ETF-N70-tp10	15.66	28.69	1.83	55.63	3.55	61.13	3.90	10.95	0.70
ETF-N70-tp08	15.02	27.08	1.80	55.63	3.70	61.13	4.07	10.95	0.73
ETF-N50-tp10	11.35	26.01	2.29	44.47	3.92	63.98	5.64	7.82	0.69
ETF-N50-tp08	11.18	24.40	2.18	44.47	3.98	63.98	5.72	7.82	0.70
ETF-N25-tp10	6.90	22.65	3.28	28.76	4.17	67.53	9.79	3.91	0.57
ETF-N25-tp08	6.51	21.05	3.23	28.76	4.42	67.53	10.38	3.91	0.60
Average			2.19		3.91		5.36		0.73
St. dev.			0.62		0.34		2.74		0.11
COV			0.29		0.09		0.51		0.15

Table 4.4: Comparison of experimental results with existing design formulae for ITF loading

Specimen series	P_{exp} (kN)	Borrowicz and Bank (2011)		Fernandes et al. (2015)		Chen and Wang (2015)		Wu and Bai (2014)	
		P_{pred} (kN)	P_{pred}/P_{exp}	P_{pred} (kN)	P_{pred}/P_{exp}	P_{pred} (kN)	P_{pred}/P_{exp}	P_{pred} (kN)	P_{pred}/P_{exp}
ITF-N100-tp10	22.47	32.71	1.46	70.30	3.13	72.76	3.24	28.86	1.28
ITF-N100-tp08	20.39	31.10	1.53	70.30	3.45	72.76	3.57	28.86	1.42
ITF-N70-tp10	18.70	28.69	1.53	57.17	3.06	78.21	4.18	20.20	1.08
ITF-N70-tp08	17.93	27.08	1.51	57.17	3.19	78.21	4.36	20.20	1.13
ITF-N50-tp10	16.15	26.01	1.61	47.72	2.95	81.85	5.07	14.43	0.89
ITF-N50-tp08	15.47	24.40	1.58	47.72	3.08	81.85	5.29	14.43	0.93
ITF-N25-tp10	11.52	22.65	1.97	34.73	3.02	86.40	7.50	7.21	0.63
ITF-N25-tp08	10.99	21.05	1.91	34.73	3.16	86.40	7.86	7.21	0.66
Average			1.64		3.13		5.13		1.00
St. dev.			0.18		0.14		1.61		0.26
COV			0.11		0.04		0.31		0.26

Table 4.5: Comparison of experimental results with proposed design predictions for ETF loading

Specimen series	P_{exp} (kN)	Modified Eurocode3 (2006)		Modified NAS (2007)		Modified Fernandes et al. (2015)		Modified Wu et al. (2019)	
		P_{pred} (kN)	P_{exp}/P_{pred}	P_{pred} (kN)	P_{exp}/P_{pred}	P_{pred} (kN)	P_{exp}/P_{pred}	P_{pred} (kN)	P_{exp}/P_{pred}
Current study:									
ETF–N120	24.79	20.05	1.24	13.88	1.79	18.91	1.31	21.93	1.13
ETF–N100	17.28	17.08	1.01	12.68	1.36	16.58	1.04	18.52	0.93
ETF–N70	15.34	12.63	1.21	10.62	1.44	12.88	1.19	13.41	1.14
ETF–N50	11.27	9.66	1.17	8.99	1.25	10.22	1.10	10.01	1.13
ETF–N25	6.70	5.96	1.12	6.38	1.05	6.55	1.02	5.75	1.17
Fernandes et al. (2015):									
I100–ETF–15	16.77	18.75	0.89	20.68	0.81	12.40	1.35	14.87	1.13
I100–ETF–50	38.24	35.48	1.08	37.42	1.02	21.99	1.74	34.08	1.12
I100–ETF–100	45.48	59.37	0.77	52.76	0.86	33.94	1.34	61.51	0.74
I120–ETF–15	19.66	16.53	1.19	16.26	1.21	14.72	1.34	15.15	1.30
I120–ETF–50	38.88	33.96	1.14	29.46	1.32	30.12	1.29	34.84	1.12
I120–ETF–100	64.86	58.86	1.10	41.55	1.56	42.13	1.54	62.96	1.03
I200–ETF–15	37.15	32.98	1.13	30.92	1.20	40.96	0.91	26.98	1.38
I200–ETF–50	78.17	58.45	1.34	55.89	1.40	84.03	0.93	55.75	1.40
I200–ETF–100	115.33	94.85	1.22	78.76	1.46	125.24	0.92	96.85	1.19
I400–ETF–100	73.99	87.64	0.84	72.46	1.02	64.36	1.15	82.83	0.89
Average			1.10		1.25		1.21		1.12
St. dev.			0.15		0.26		0.23		0.17
COV			0.14		0.21		0.19		0.15
Resistance factor (φ)			0.70		0.70		0.70		0.70
Reliability index (β)			3.53		3.50		3.52		3.52

Table 4.6: Comparison of experimental results with proposed design predictions for ITF loading

Specimen series	P_{exp} (kN)	Modified Eurocode3 (2006)		Modified NAS (2007)		Modified Fernandes et al. (2015)		Modified Wu et al. (2019)	
		P_{pred} (kN)	P_{exp}/P_{pred}	P_{pred} (kN)	P_{exp}/P_{pred}	P_{pred} (kN)	P_{exp}/P_{pred}	P_{pred} (kN)	P_{exp}/P_{pred}
Current study:									
ITF–N120									
ITF–N100	21.43	18.71	1.15	16.69	1.28	21.20	1.01	21.33	1.00
ITF–N70	18.31	14.45	1.27	14.10	1.30	17.18	1.07	15.88	1.15
ITF–N50	15.81	11.61	1.36	12.06	1.31	14.34	1.10	12.25	1.29
ITF–N25	11.25	8.05	1.40	8.78	1.28	10.52	1.07	7.71	1.46
Fernandes et al. (2015):									
I100–ITF–15	29.81	29.53	1.01	29.16	1.02	26.70	1.12	22.93	1.30
I100–ITF–50	41.11	45.28	0.91	49.51	0.83	36.09	1.14	43.41	0.95
I100–ITF–100	56.50	67.78	0.83	68.16	0.83	48.55	1.16	72.65	0.78
I120–ITF–15	32.17	27.79	1.16	28.00	1.15	25.84	1.24	23.30	1.38
I120–ITF–50	51.96	46.14	1.13	47.97	1.08	44.65	1.16	44.29	1.17
I120–ITF–100	76.97	72.37	1.06	66.26	1.16	61.92	1.24	74.27	1.04
I200–ITF–15	67.83	60.01	1.13	54.94	1.23	76.04	0.89	44.37	1.53
I200–ITF–50	109.09	86.84	1.26	92.62	1.18	123.23	0.89	75.04	1.45
I200–ITF–100	161.34	125.17	1.29	127.13	1.27	172.68	0.93	118.86	1.36
I400–ITF–100	127.26	140.32	0.91	146.88	0.87	120.26	1.06	107.87	1.18
Average			1.13		1.13		1.08		1.22
St. dev.			0.17		0.18		0.12		0.22
COV			0.15		0.16		0.11		0.18
Resistance factor (φ)			0.70		0.70		0.70		0.70
Reliability index (β)			3.54		3.51		3.66		3.60

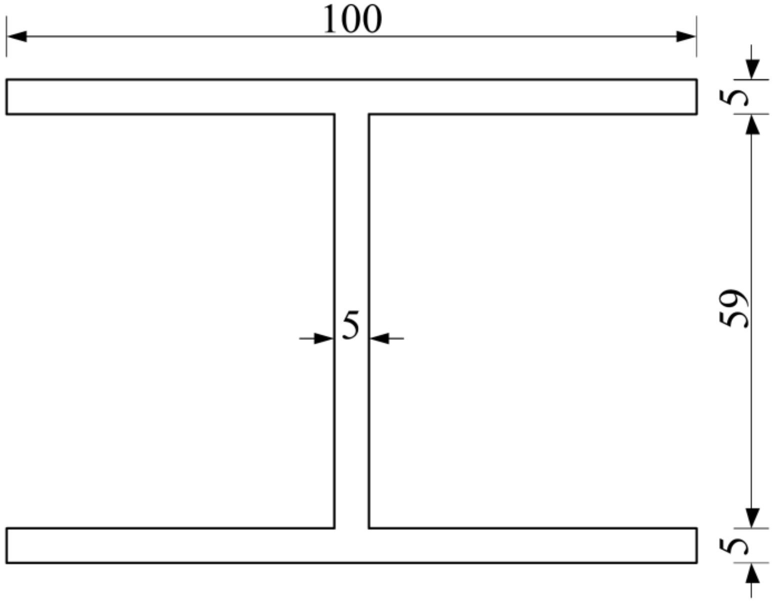

Figure 4.1: Dimensional sketch of the wide flange profile.

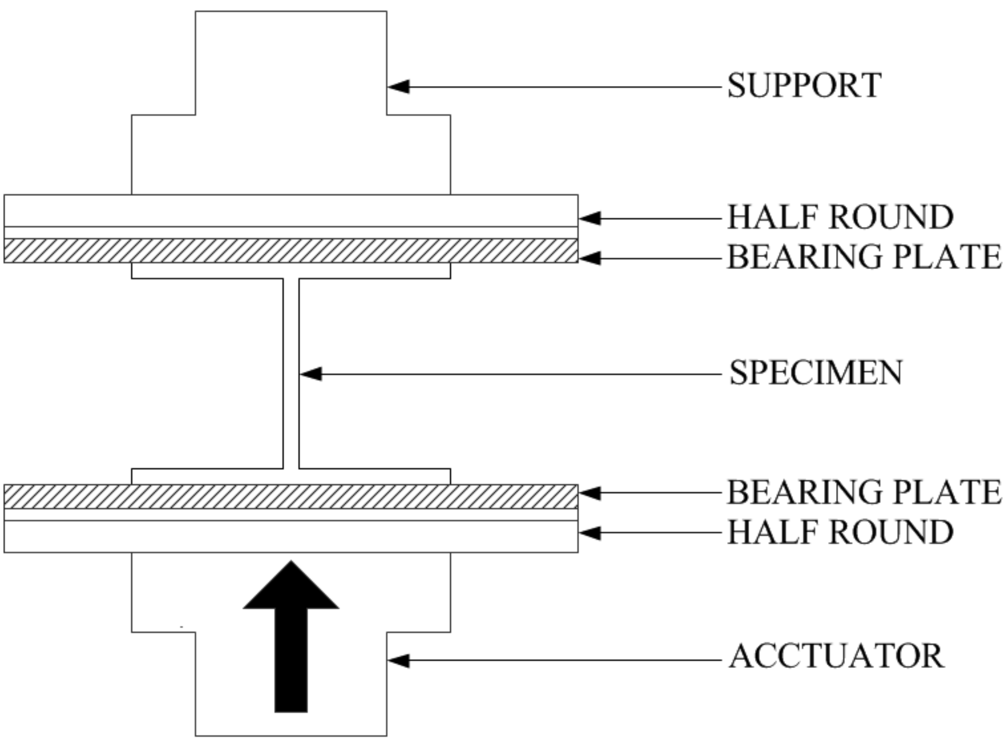

Figure 4.2(a): Loading arrangement for web crippling test.

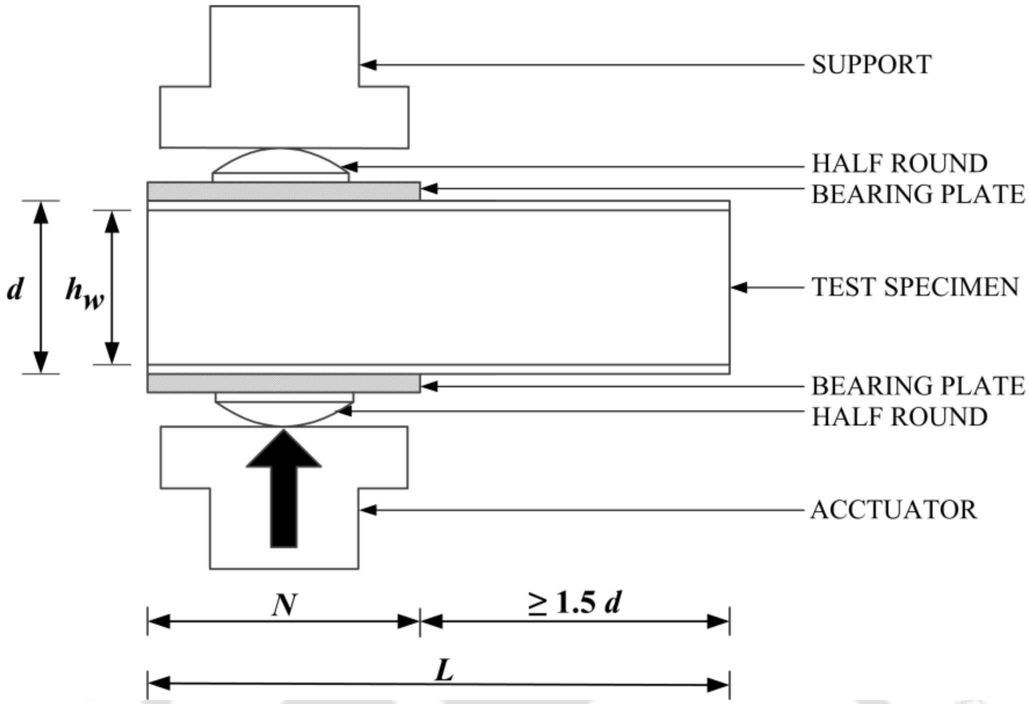

Figure 4.2(b): ETF loading setup.

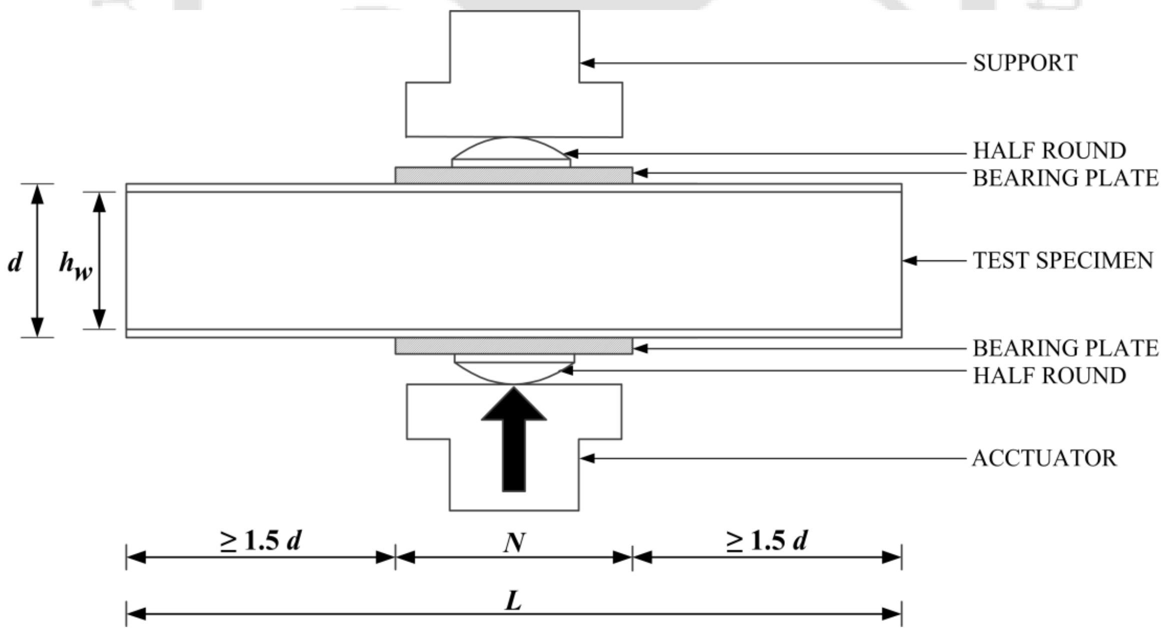

Figure 4.2(c): ITF loading setup.

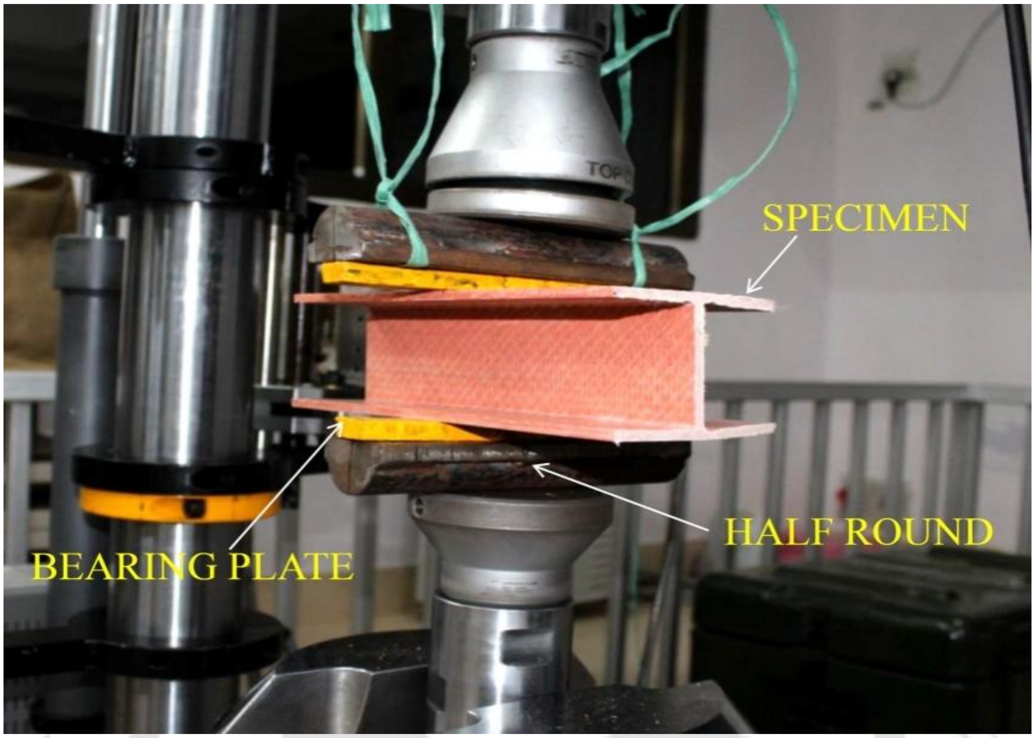

Figure 4.3(a): ITF load configuration.

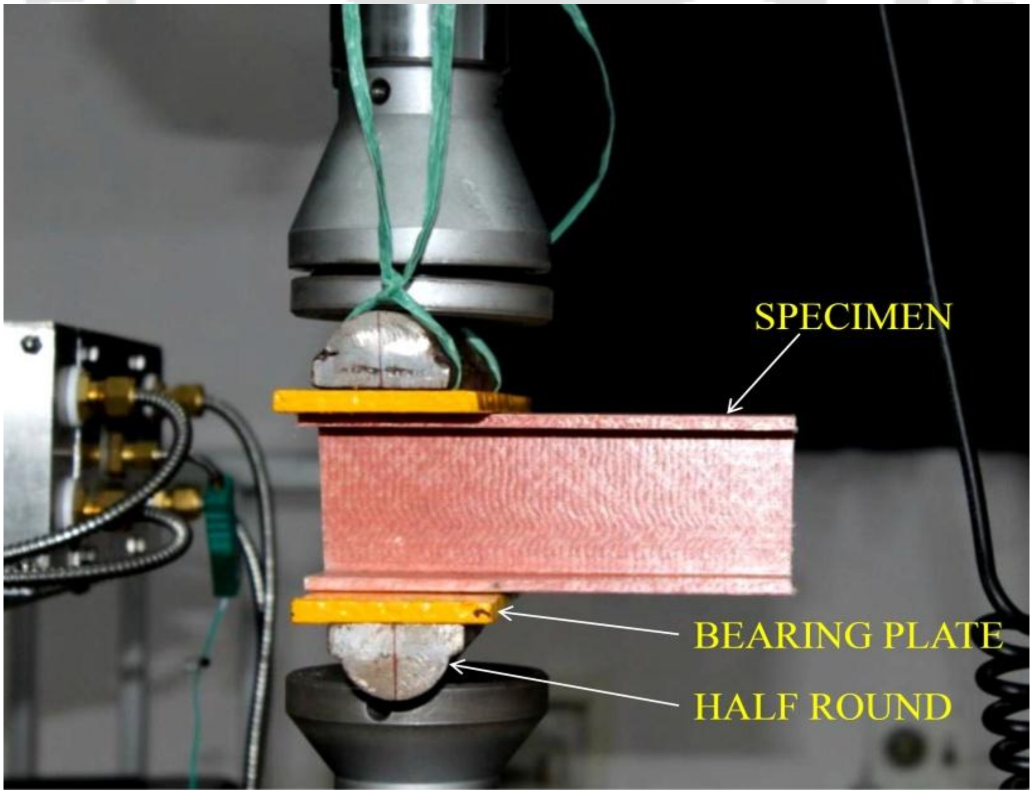

Figure 4.3(b): ETF load configuration.

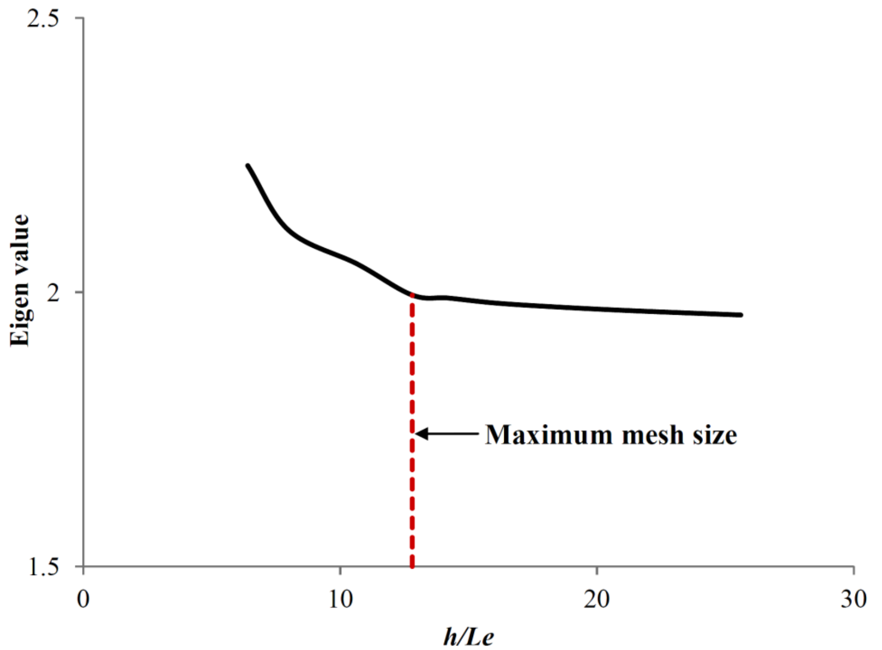

Figure 4.4: Mesh convergence study.

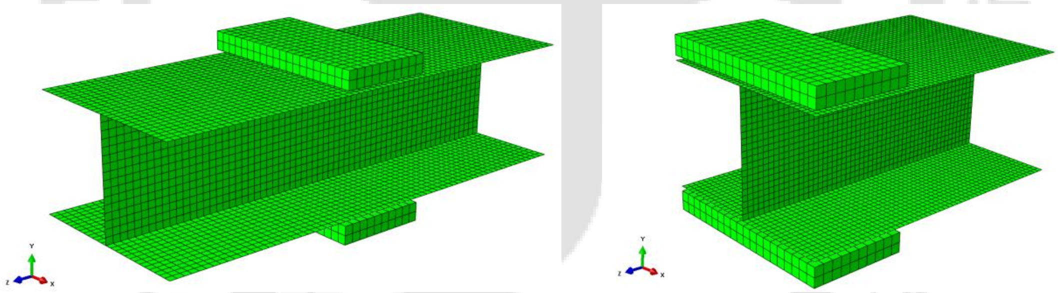

a) b)

Figure 4.5: Numerical model for a) ITF and b) ETF specimens.

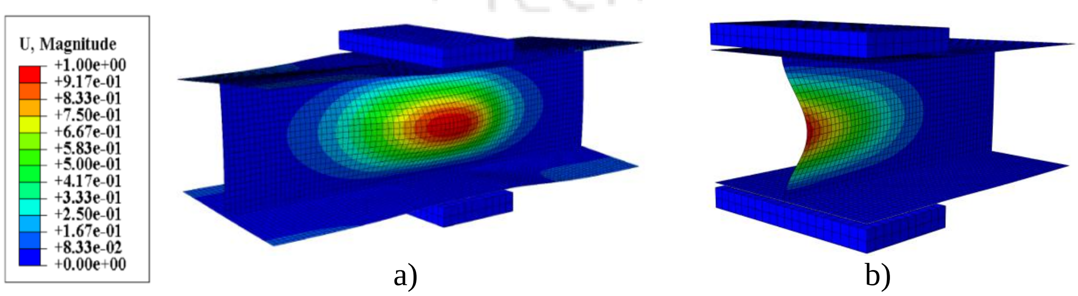

a) b)

Figure 4.6: First buckling mode shape for a) ITF and b) ETF specimens.

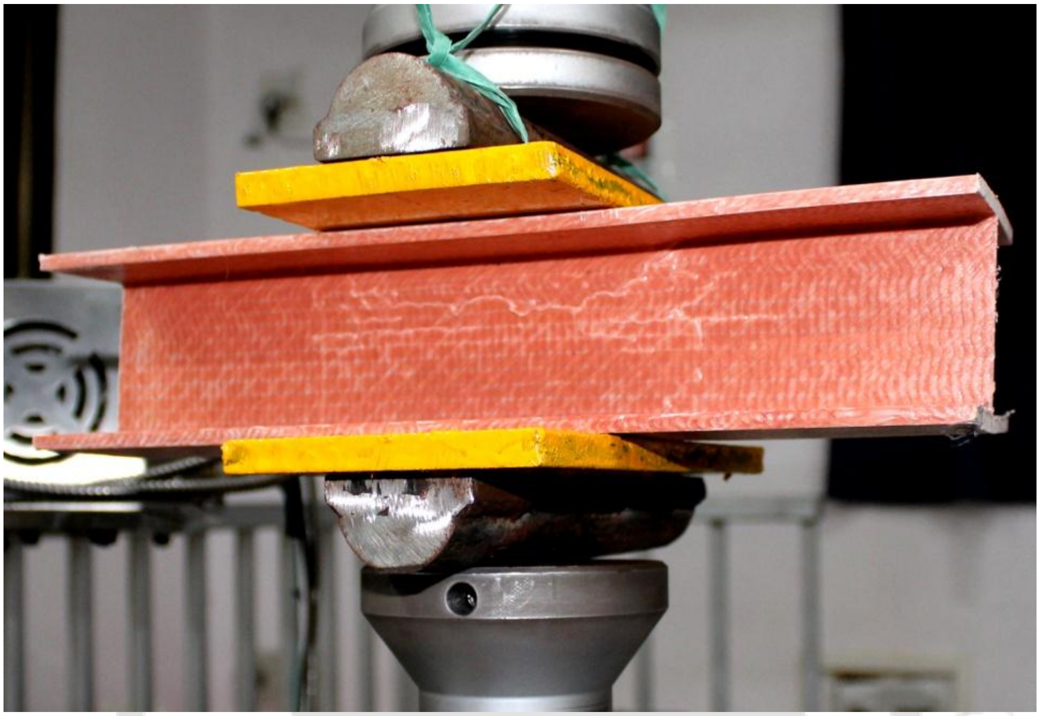

Figure 4.7(a): Failure modes of ITF–N100-tp10-2.

Figure 4.7(b): Failure modes of ITF–N70-tp10-1.

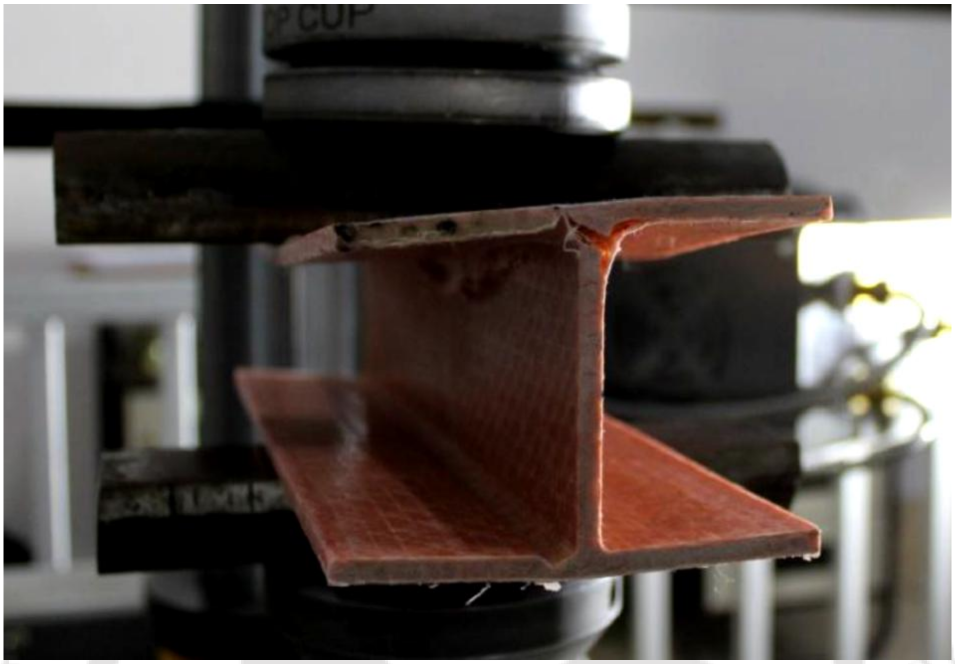

Figure 4.7(c): Failure modes of ITF–N50-tp10-1

d)

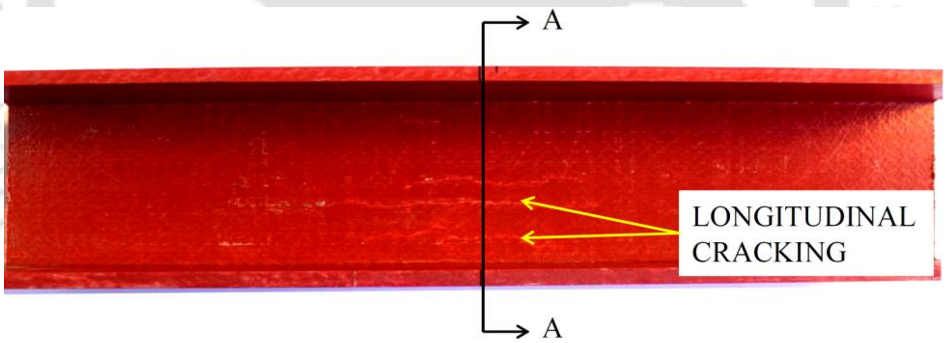

e)

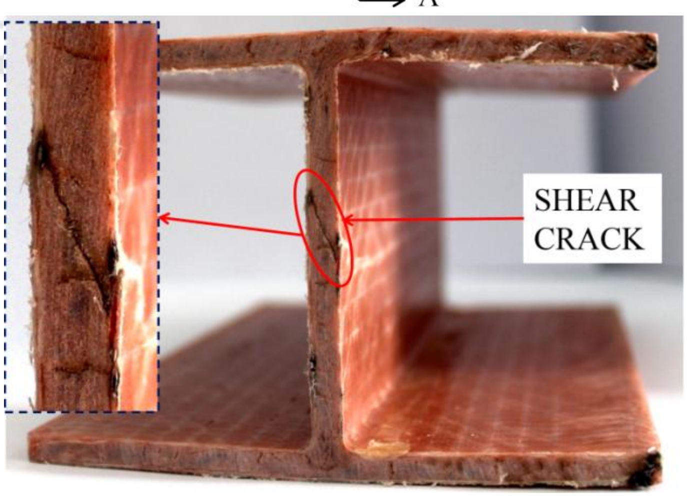

Figure 4.7: Failure modes in d) “ITF–N50-tp10-2” e) through A–A.

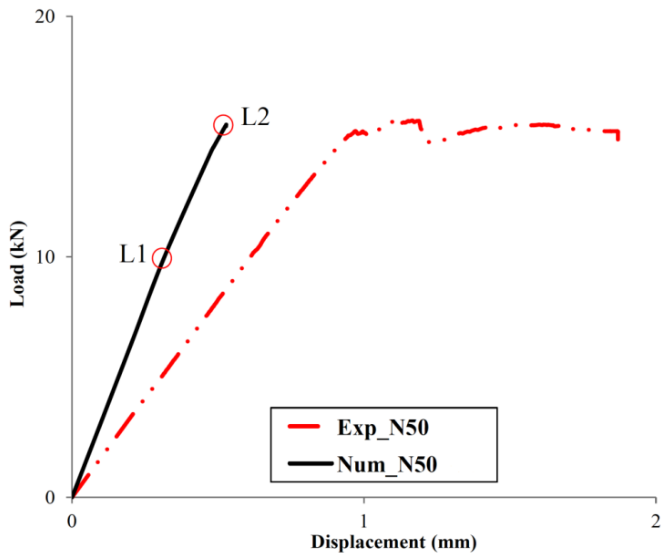

Figure 4.8: Comparison of experimental and numerical load-displacement curves for ITF loading.

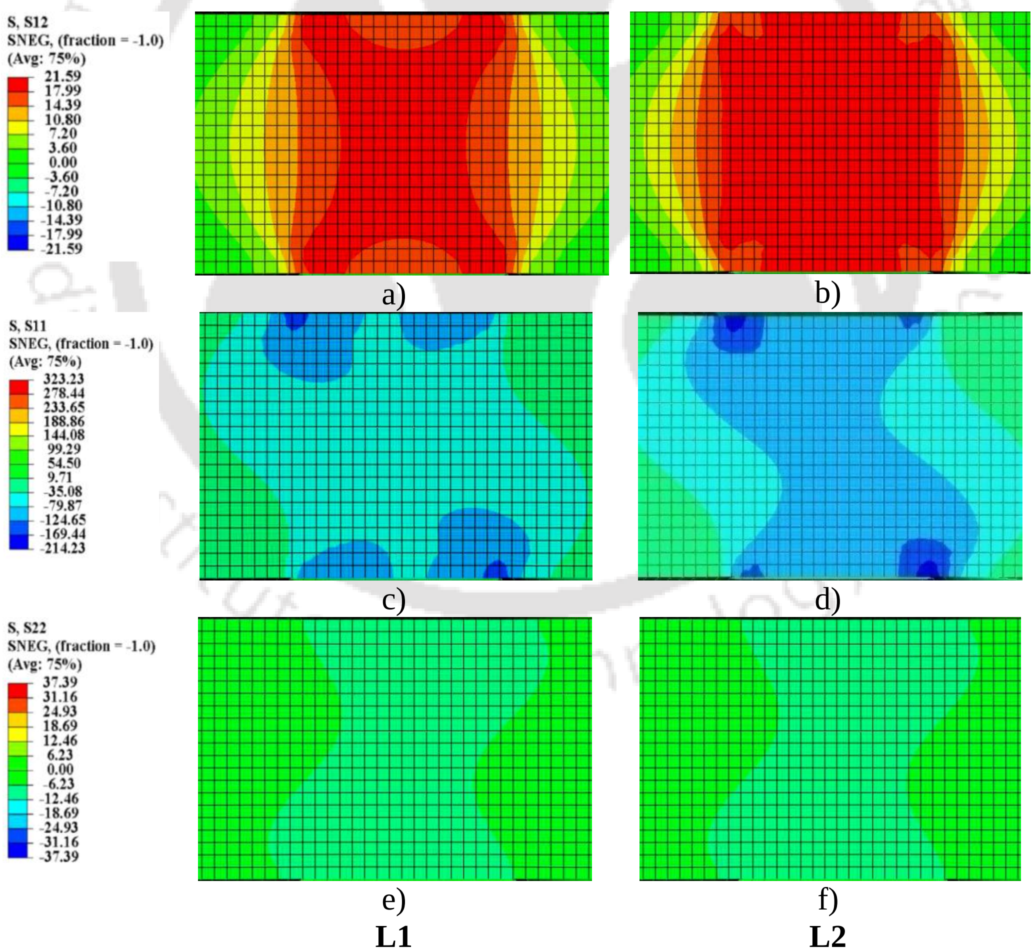

Figure 4.9: Shear stress (a, b), longitudinal tensile stress (c, d) and transverse compressive stress (e, f) distributions at different load levels for ITF specimen.

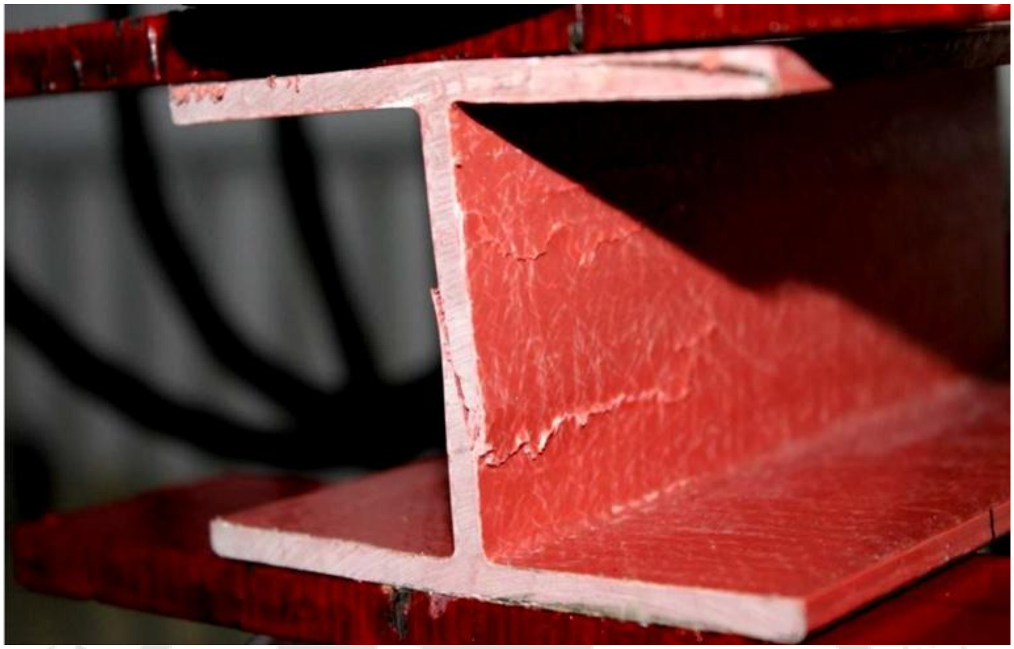

Figure 4.10(a): Failure modes of ETF–N70-tp10-2.

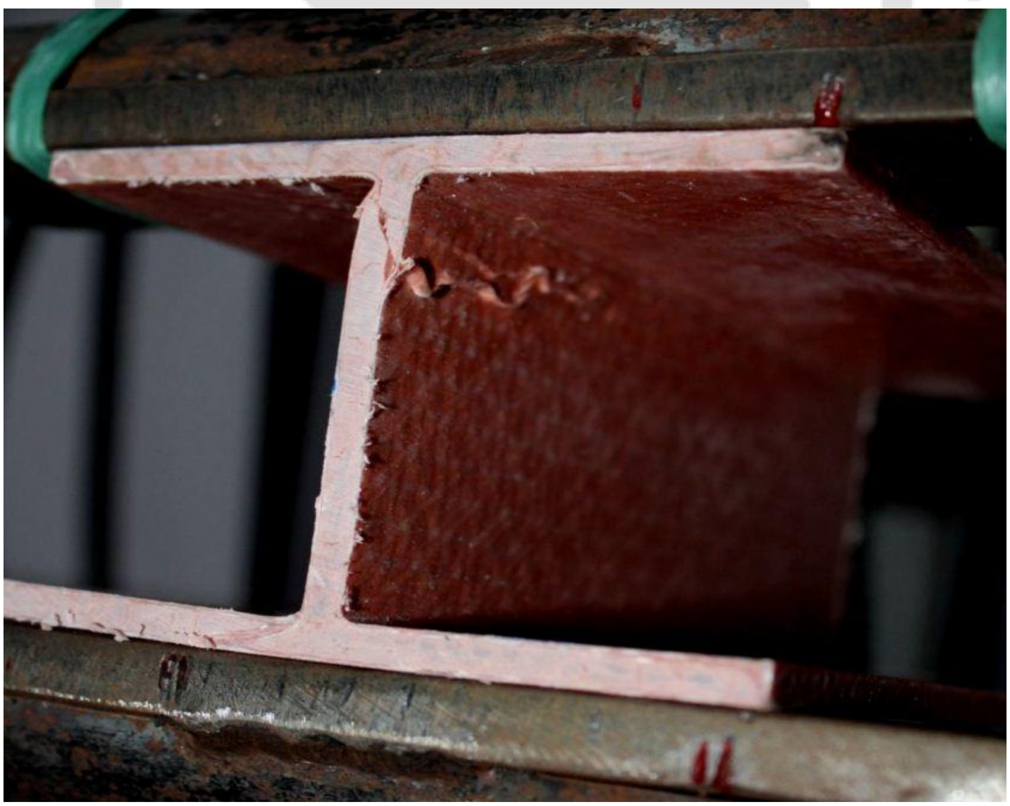

Figure 4.10(b): Failure modes of ETF–N50-tp10-1.

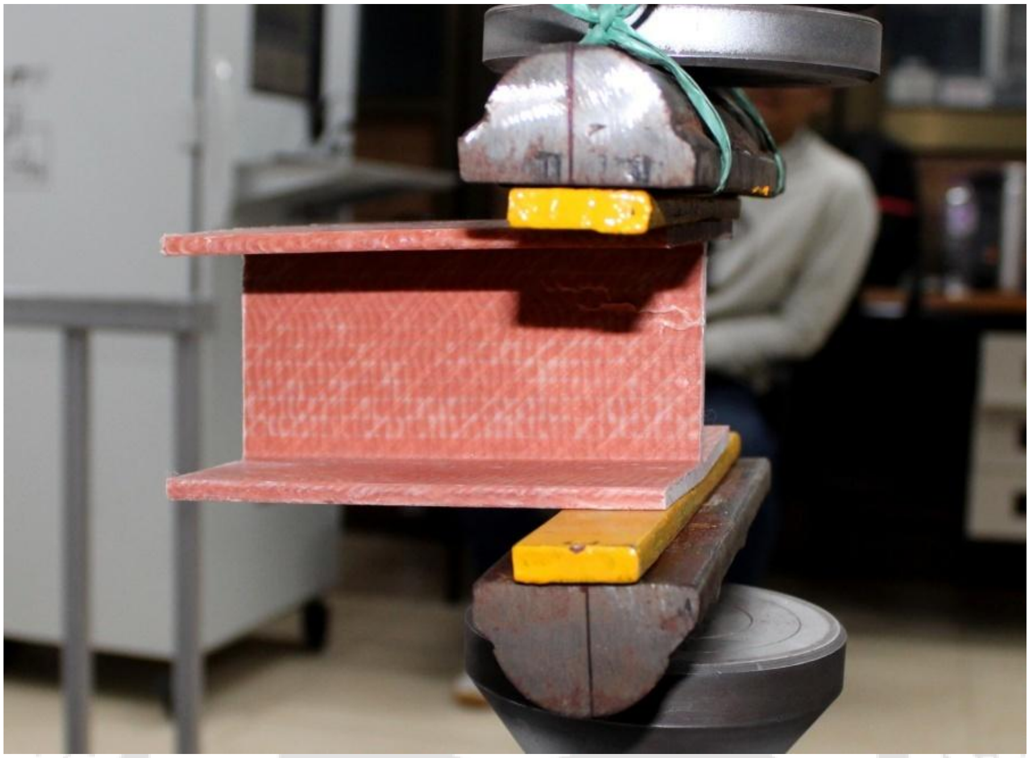

Figure 4.10(c): Failure modes of ETF–N25-tp10-2.

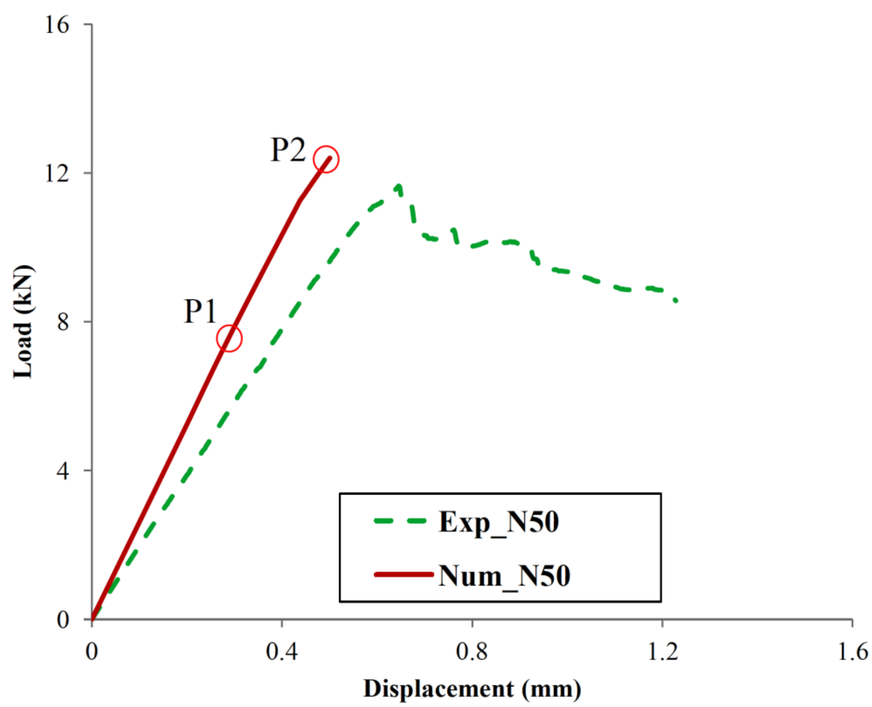

Figure 4.11: Comparison of experimental and numerical load-displacement curves for ETF loading.

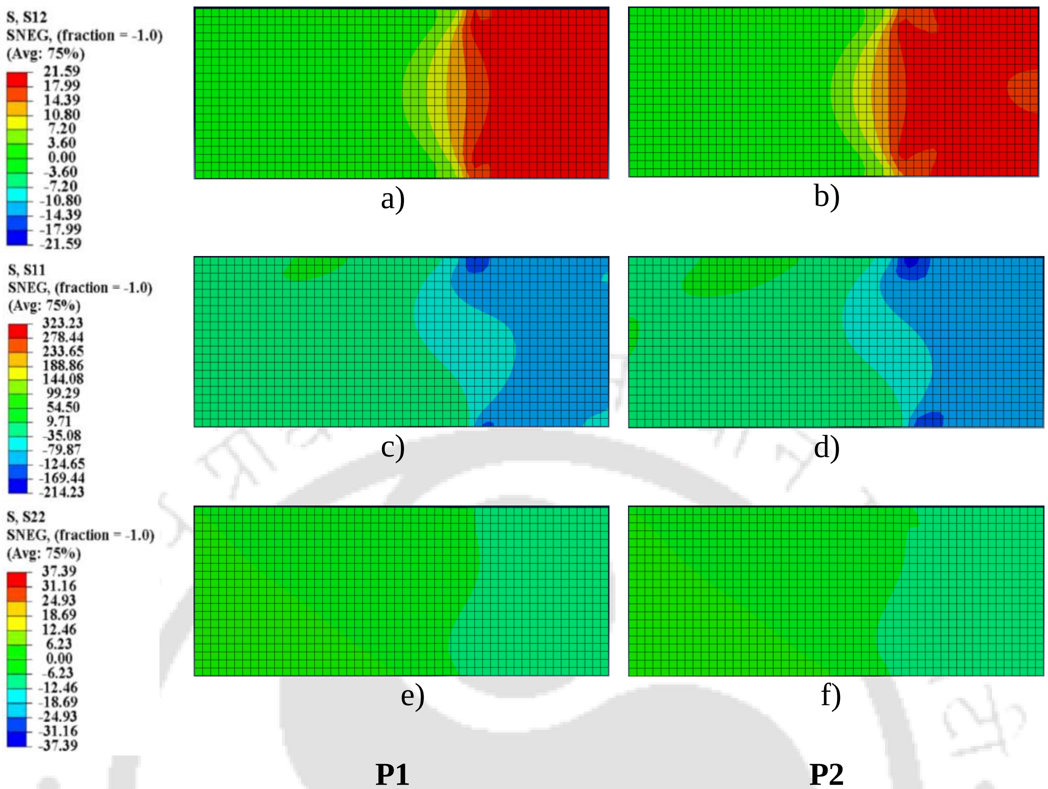

Figure 4.12: Shear stress (a, b), longitudinal tensile stress (c, d) and transverse compressive stress (e, f) distributions at different load levels for ETF specimen.

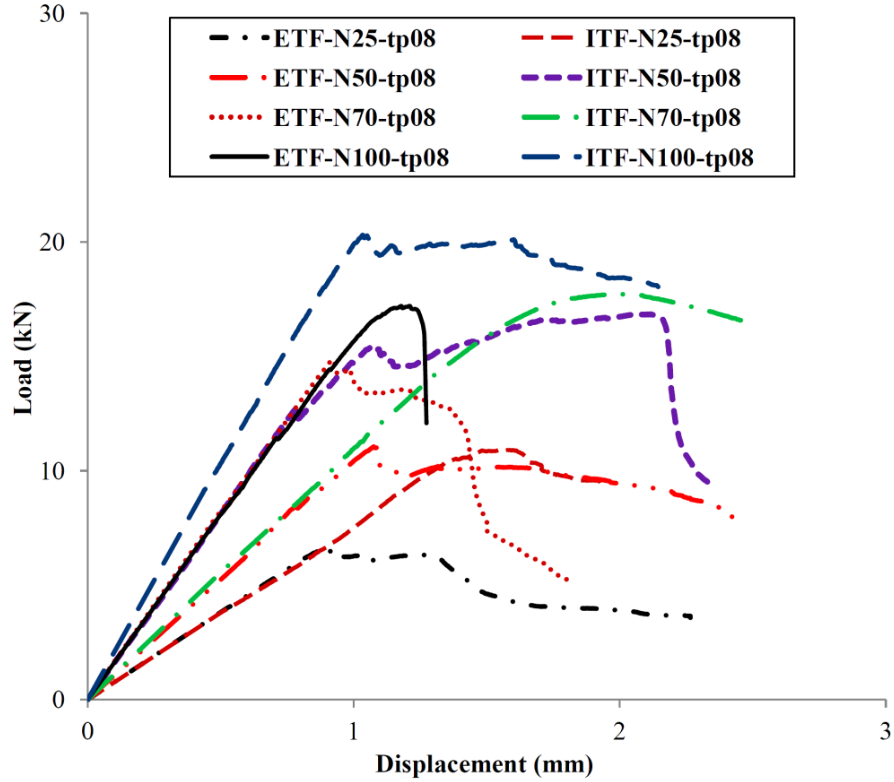

Figure 4.13(a): Effects of loading conditions on ultimate strength for thickness t_{plate}=8 mm.

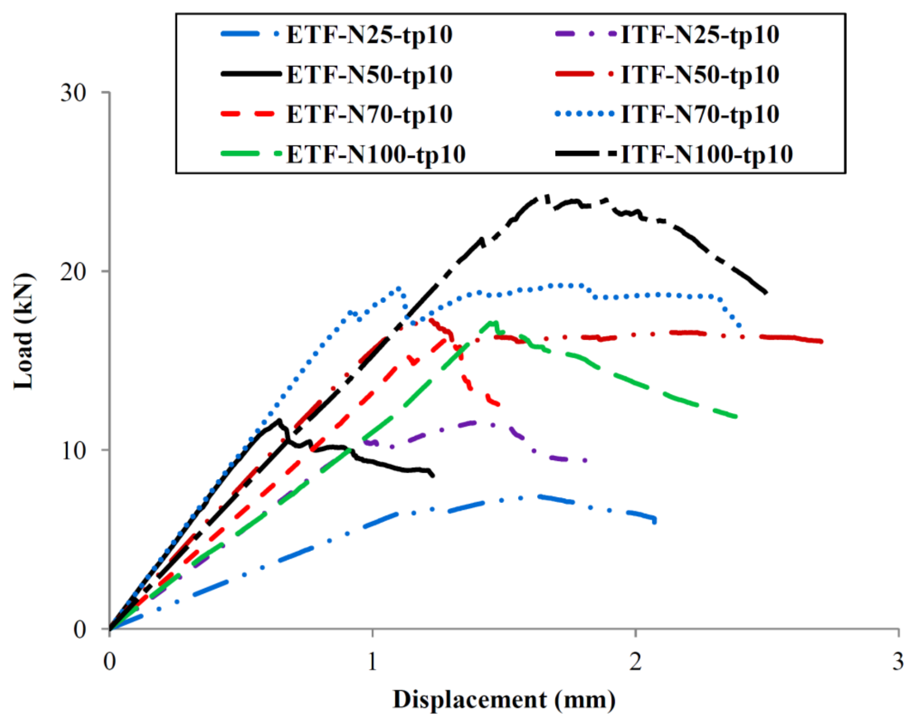

Figure 4.13(b): Effects of loading conditions on ultimate strength for thickness t_{plate}=10 mm.

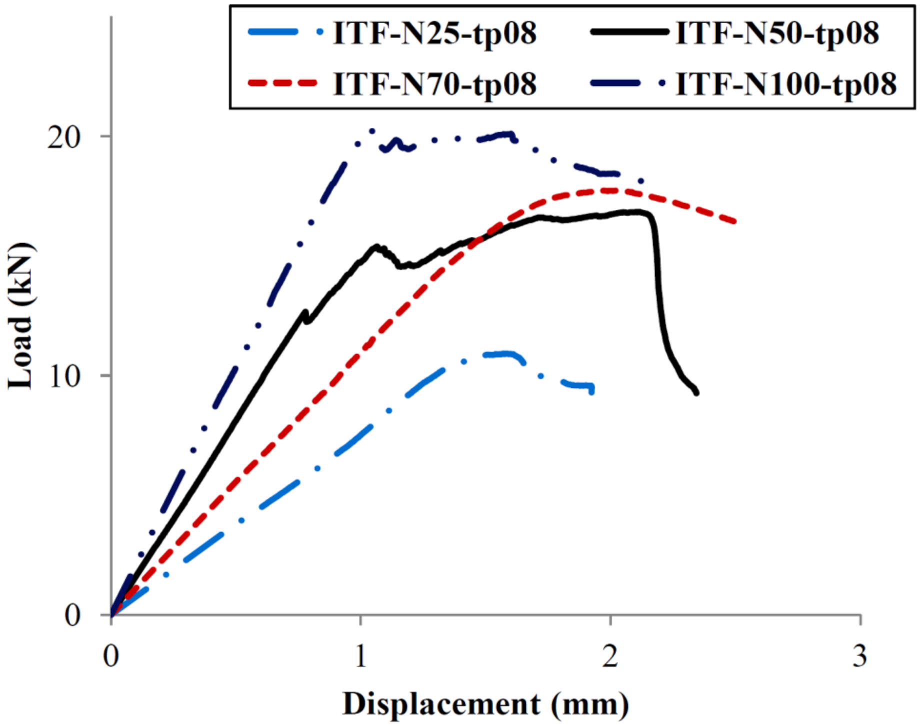

Figure 4.14(a): Effects of bearing lengths on ultimate strength for ITF loading with t_{plate}=8 mm.

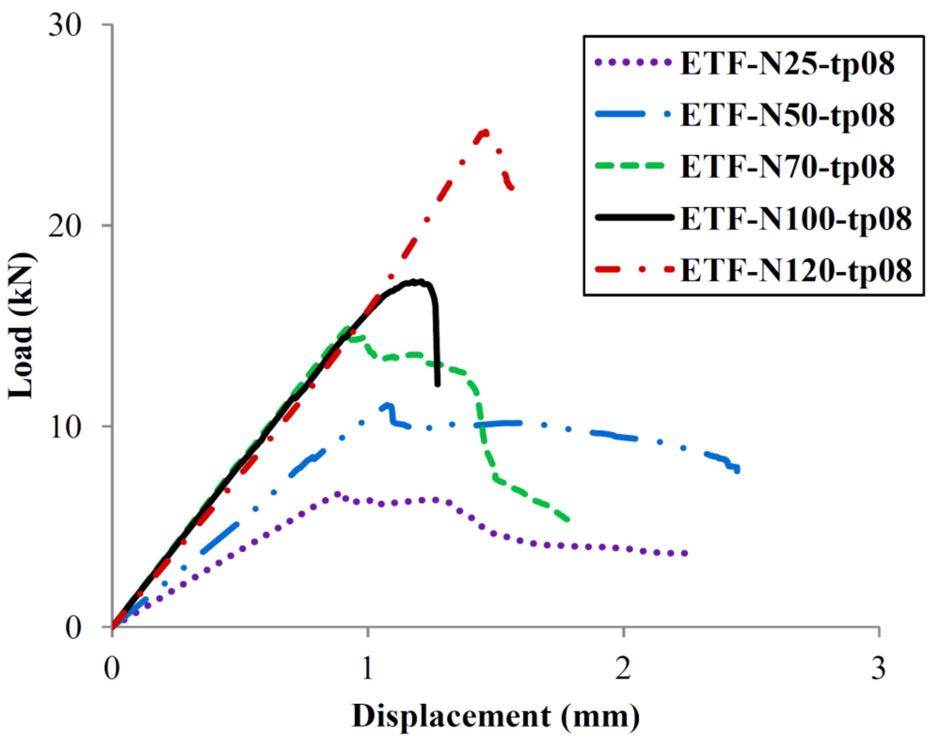

Figure 4.14(b): Effects of bearing lengths on ultimate strength for ETF loading with t_{plate}=8 mm.

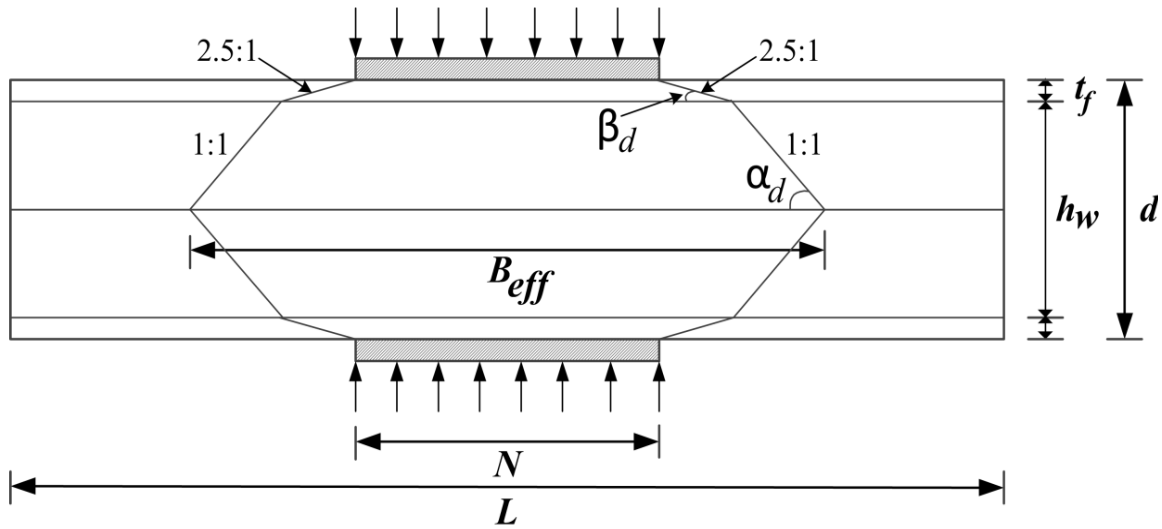

Figure 4.15(a): Stress dispersion under ITF loading.

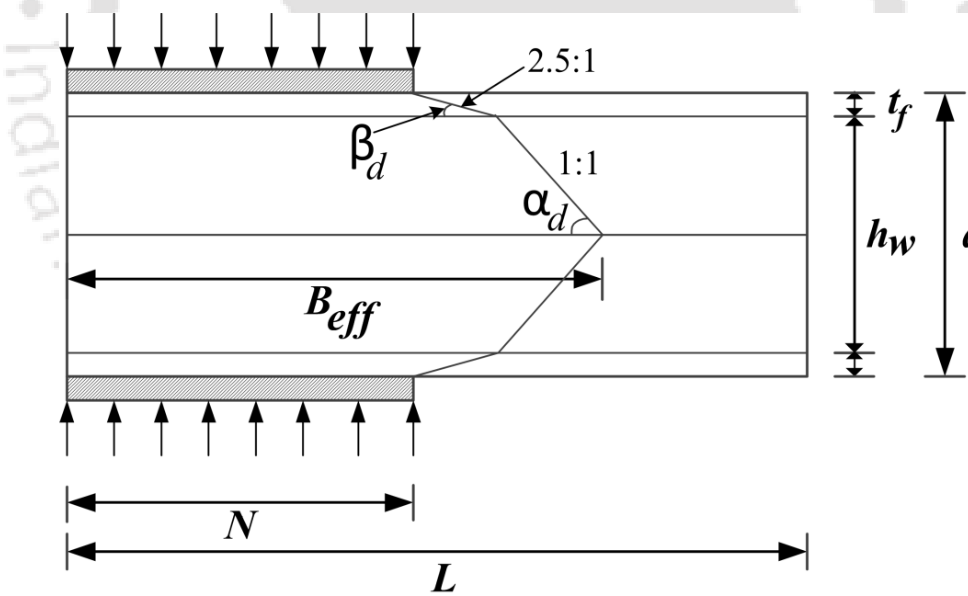

Figure 4.15(b): Stress dispersion under ETF loading.

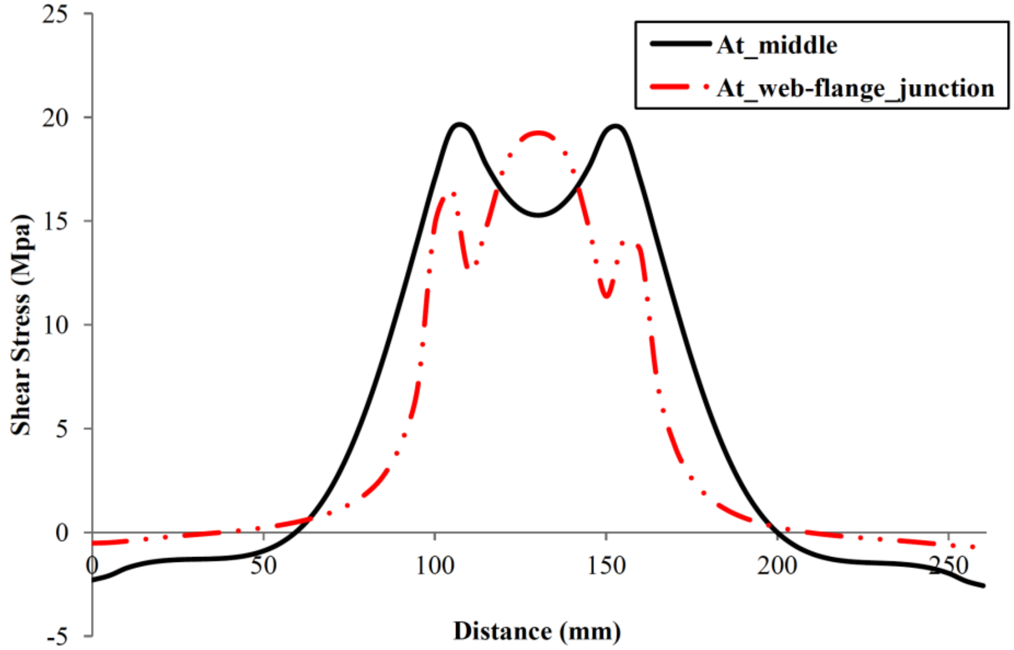

Figure 4.16(a): Shear stress plot for “ITF_N50” series with t_f = 5 mm.

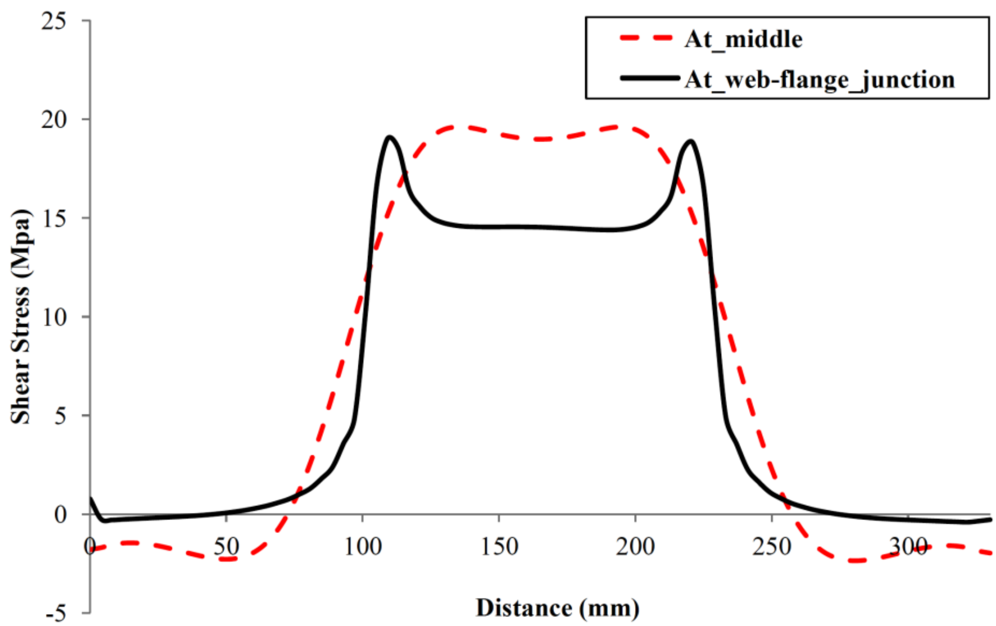

Figure 4.16(b): Shear stress plot for “ITF_N120” series with t_f = 3 mm.

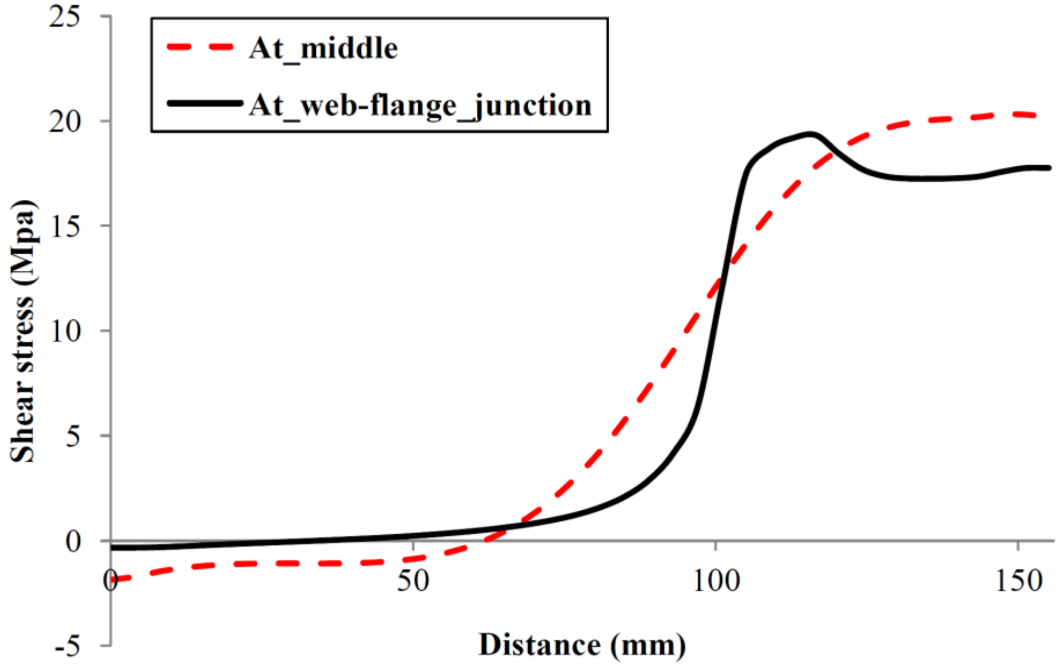

Figures 4.17(a): Shear stress plot for “ETF_N50” series with t_f = 5 mm.

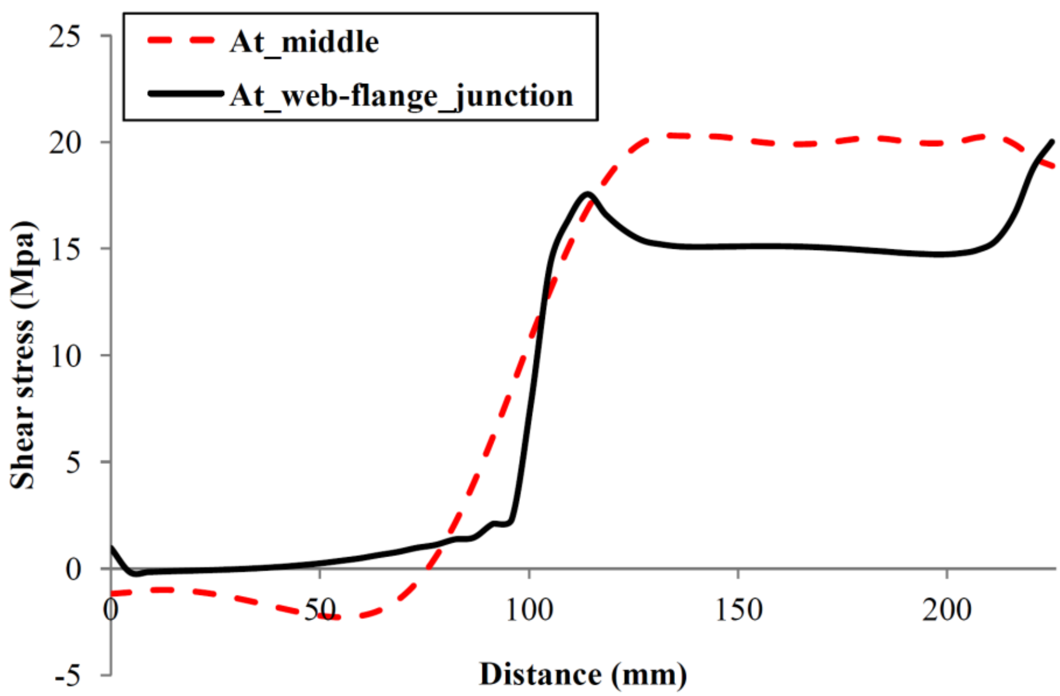

Figures 4.17(b): Shear stress plot for “ITF_N120” series with t_f = 3 mm.

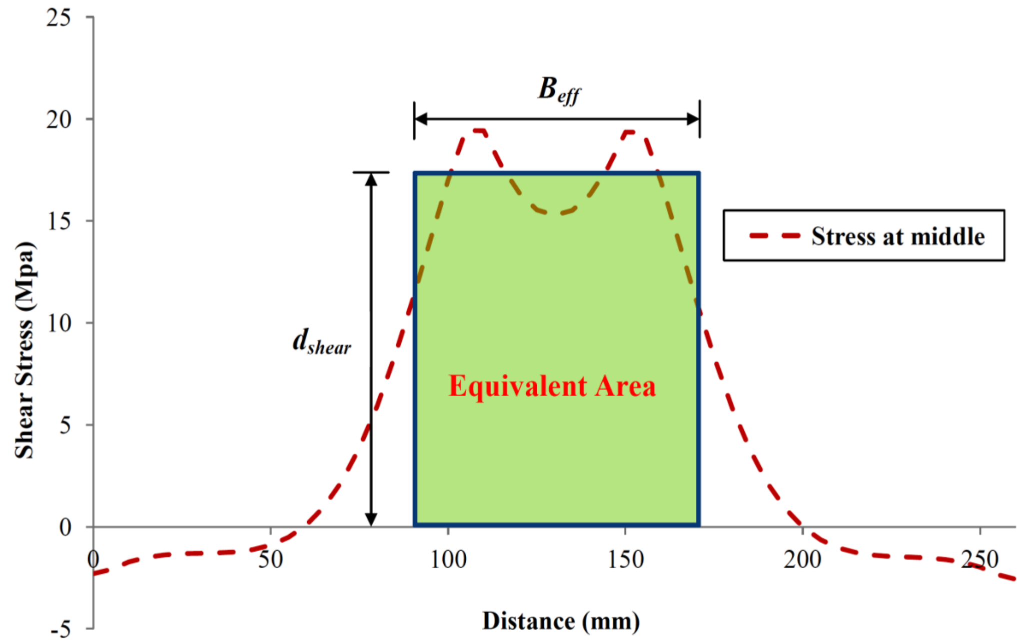

Figure 4.18: Representative stress plot and equivalent area under the curve.

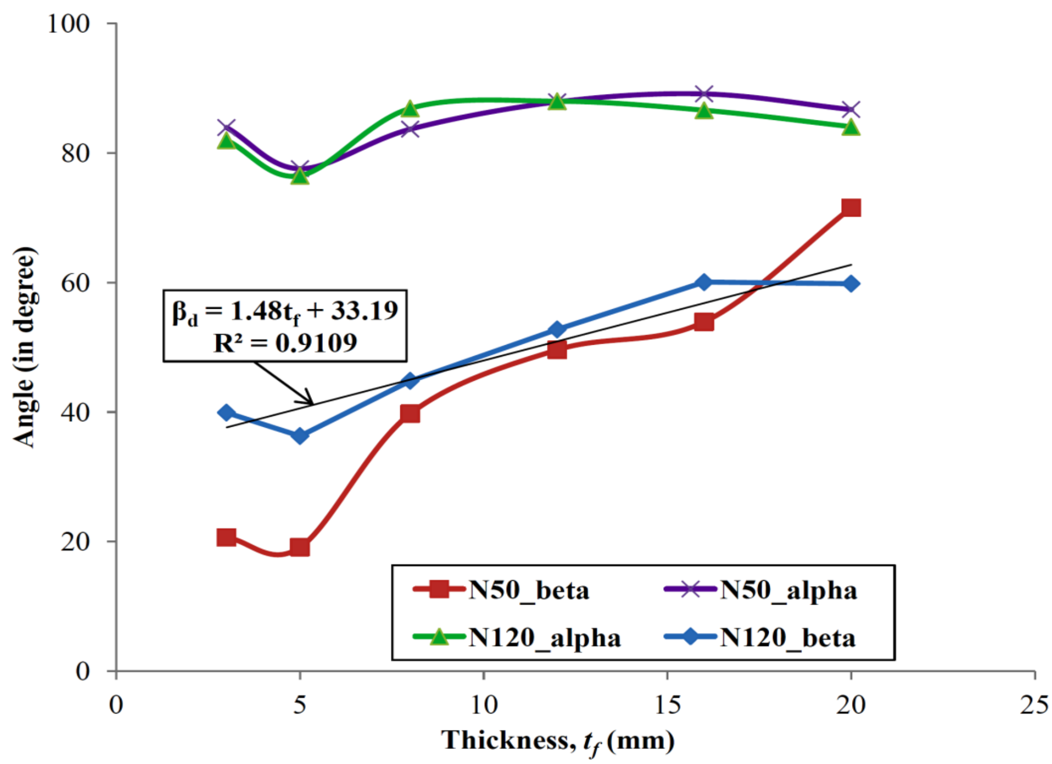

Figure 4.19: Plot of angles α_d and β_d with respect to t_f.

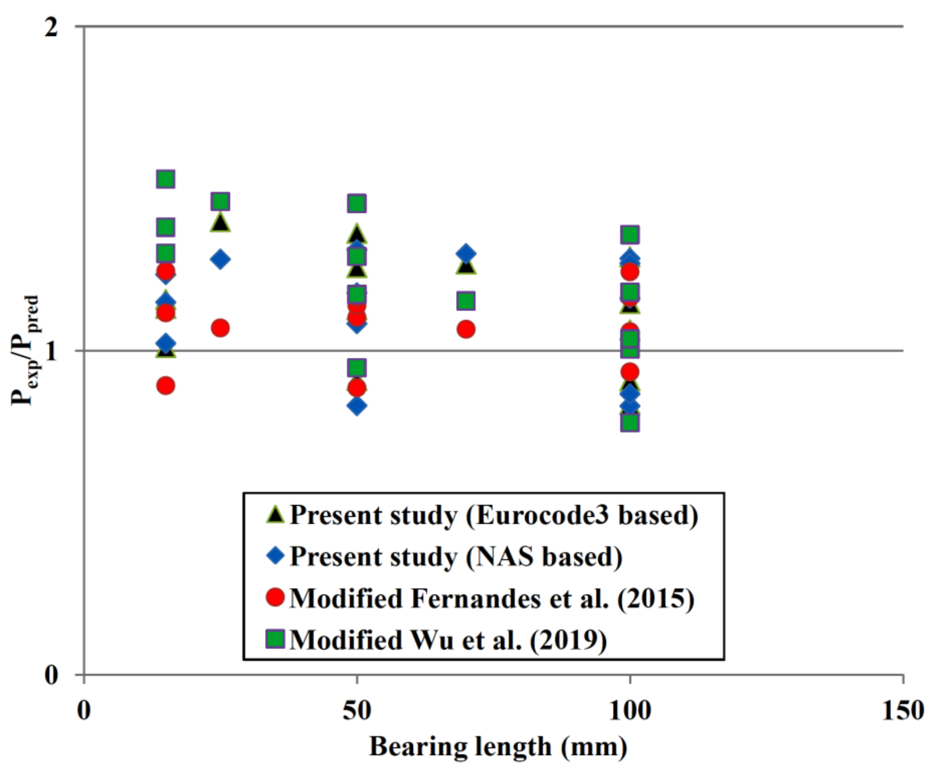

Figure 4.20(a): Experimental web crippling strengths (current and Fernandes et al., 2015) normalised with respect to the predicted strengths for ITF loading.

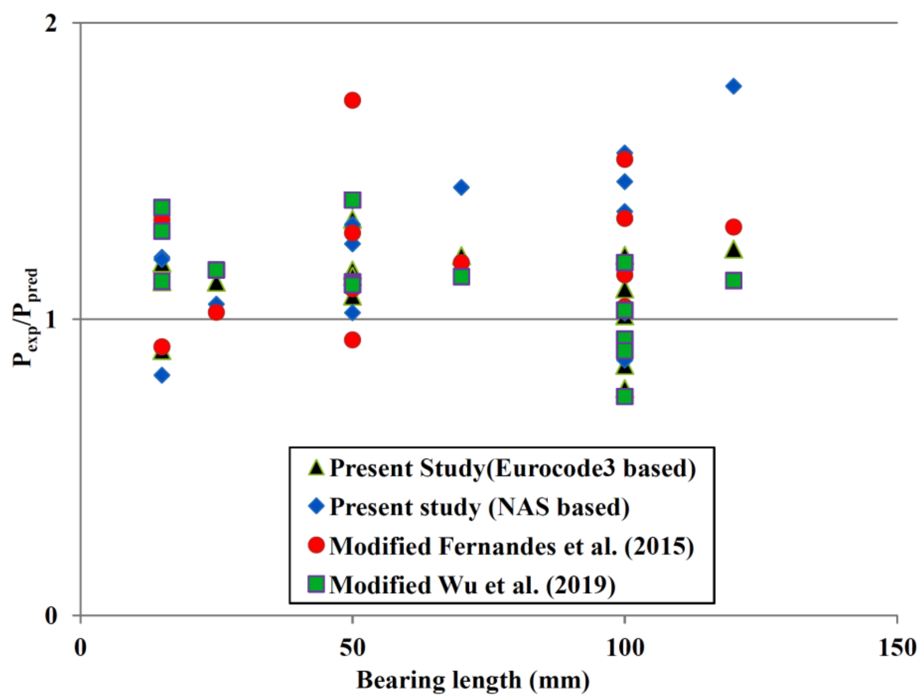

Figure 4.20(b): Experimental web crippling strengths (current and Fernandes et al., 2015) normalised with respect to the predicted strengths for ETF loading.

CHAPTER 5

WEB CRIPPLING BEHAVIOUR OF WEB PERFORATED GFRP WIDE FLANGE–SECTION PROFILES

5.1 INTRODUCTION

The web crippling behaviour of the GFRP wide flange section profiles studied in Chapter 4, has been extended in this chapter, by considering circular perforation in the centre of web. As discussed in the literature review, past investigations on the web crippling failure in GFRP profiles have focused mainly on unperforated web profiles (e.g. Borowicz and Bank, 2010; Wu and Bai, 2014; Chen and Wang, 2015a; Fernandes *et al*., 2015; Chen and Wang, 2015b; Zhang and Chen, 2017; Fernandes *et al*., 2015; Wu *et al*., 2019). However, studies relating to the effects of web perforations (or holes or cut-outs or openings) on the web crippling behaviour of GFRP section profiles have been hardly reported. Perforations in the web may be required for various purposes such as to pass services through the web and for ease of connections in built-up members etc. Under concentrated loading, high stresses may develop around the openings which can reduce the web crippling resistance of the members. To the best of authors' knowledge, in case of GFRP profiles, Gand *et al*. (2020) conducted web crippling experiments on I–beams considering rectangular and circular web perforation with different loading conditions and reported a reduction of 20% and 25% in the load-carrying capacity with circular (a/h = 0.72; a being the perforation size and h being the web height) and rectangular web perforation (a/h = 0.54), respectively. However, the investigation was done considering only a particular perforation size (a/h = 0.72) and did not include the effect of varying perforation sizes (or perforation size to web height ratios).

Henceforth, the present study investigates systematically the effects of centred circular web perforations of different sizes on the web crippling behaviour of GFRP wide flange (WF) profile, under two-flange loading conditions (both ETF and ITF). The investigation comprises experimental tests conducted on full scale specimens extracted from the GFRP profile. Numerical investigations are also carried out using the finite element (FE) program Abaqus (2009), and with the validated FE models; parametric studies have been performed to study the effect of different perforation sizes. The outcomes of the experimental and numerical investigations are presented in the form of load–displacement curves, failure modes and ultimate web crippling strength values. Based on the test and numerical results, web crippling strength reduction factor equations are proposed. The suitability of the proposed design rules are then assessed by using reliability analysis.

5.2 EXPERIMENTAL INVESTIGATION

5.2.1 General

The present experimental campaign mainly includes web crippling experiments conducted on a GFRP WF–section profile under ETF and ITF loading conditions. Details of the web crippling experiments are presented in the following sections.

5.2.2 Web crippling test specimens

The experimental programme was performed by considering 29 specimens tested under two flange loading conditions, out of which 14 tests were conducted under ITF loading and 15 tests were performed under ETF loading. Specimens were obtained from the same GFRP WF–section profile (for detailed dimension see Figure 5.1). For investigating the effect of web perforations, perforation diameter sizes were varied between 11.8 mm (0.2h) and 47.2 mm (0.8h). Perforations were made by drilling at the mid height and central portion of the web for ITF specimens; and centred to bearing length at the end for ETF specimens (see Figures 5.2 and 5.3) for four different perforation diameter sizes: 11.8 mm (0.2*h*), 23.6 mm (0.4*h*), 35.4 mm (0.6*h*) and 47.2 mm (0.8*h*). The thickness of the bearing plates (mild steel plates) were 10 mm. Details of the test specimens and bearing plates are listed in Tables 5.1 and 5.2.

5.2.3 Specimen labelling

Test specimens were labeled in order to recognize easily the loading condition, specimen's cross sectional sizes, web perforation size, perforation position, length of bearing and test sequence number for each test series. For example, the label "ITF–69x100–t5.0–A0.2–C–N50–1" can be referred as: first notation "ITF" stands for the loading type which indicates interior-two-flange loading (ETF for end-two-flange loading); second notation "69x100" specifies the overall section depth (d = 69 mm) and flange width (b_f = 100 mm); "t5.0" is the web thickness (t_w) of 5 mm; "A0.2" indicates the perforation size (a) equal to 0.2 times the web height, h (or h_w); "C" stands for perforation located at the centre of web; "N50" indicates the length of bearing (N) i.e. 50 mm; and the last notation "1" indicates the test sequence number, respectively.

5.2.4 Test setup and procedure

The web crippling experiments were performed under the two-flange loading condition according to the specifications given in the NAS (see Figures 5.2–5.5), similar to the procedures described in Section 4.2.4. Two half rounds (mild steel) were welded to the steel bearing plates (lengths of the bearing plates = 200 mm) in order to simulate the hinge supports at the loading points. All web crippling tests were performed in a displacement control manner (speed 1mm/min) using a UTM of 250 kN load capacity. Specimens were examined carefully to identify their failure patterns (see Figures 5.6a–f and Figures 5.7a–j) during and after completion of the tests.

5.3 NUMERICAL INVESTIGATION

5.3.1 General

Finite element analyses were carried out in order to assess the effectiveness of conventional FE numerical methods for simulating the web crippling behaviour in GFRP profiles with perforations and reproducing the experimental test results. Validations of the FE models were done by comparing both numerical and experimental results. All FE models were modelled using the standard commercial finite element software, Abaqus (2009) by following similar modelling procedure adopted in Section 4.3. The material properties, failure criteria, boundary conditions, contact formation for all FE models were assigned in a similar procedure.

5.3.2 Geometrical properties and mesh

Similar procedures as given in Section 4.3.2 for assigning geometrical properties and mesh sizes were adopted herein. For the specimens with web perforations, perforations were made at the mid height of web centred to the bearing plate. In all cases, finer local mesh was used around the perforations in order to capture stress localisation and stress distribution properly. In Figures 5.8a and 5.9a, numerical models developed for ITF and ETF specimens with '0.6*h*' diameter perforation size are shown alongside their axes definition. In Figures 5.8b and 5.9b, typical fan type meshing used around '0.6*h*' diameter perforation size are shown.

5.3.3 Finite element (FE) analysis

For each series, similar analysis procedure was followed as discussed in Section 4.3.6. Initially linear buckling analysis was performed and the eigenvalue of the critical buckling load and the deformed shape of corresponding buckling mode (see Figures 5.10a–b and 5.11a–b) were estimated. Following this, non-linear analyses were carried out using the static Riks method by incorporating the initial geometrical imperfections with the first buckling mode shapes of Eigen buckling analyses (as discussed in Section 4.3.6).

5.3.4 Verification of FE models

Verification of the finite element models developed in this study were done by comparing with the experimental failure patterns, ultimate strength and load–displacement behaviour of the GFRP WF or I-section profiles. Detailed discussion is presented in the following sections.

5.4 RESULTS AND DISCUSSION

5.4.1 ITF load configuration

A total of 14 specimens were tested under ITF loading condition, out of which 11 specimens were for centred web perforation and 3 specimens were without web perforations. The experimental ultimate web crippling loads obtained (P_{EXP}) are presented in Table 5.1. For each series of test, finite element analysis was also carried out and compared with the experimental results.

5.4.1.1 Failure patterns

In case of specimens tested without web perforations, failure mainly occurred at the web with longitudinal cracking or material wrinkling near the web-flange junction. All specimens in the "ITF–69x100–t5.0–A0.0–C–N50" series showed multiple longitudinal cracks under the loading plates near the web-flange junction as well as at the mid height of the web (see Figure 5.6a). In case of specimens with centred web perforations, failure started with the initiation of cracks around the perforations due to the development of local stress concentration which propagated to the web. Specimens in the series "ITF–69x100–t5.0–A0.2–C–N50" showed horizontal crack formation around the perforation at the mid height of the web which extended towards the web accompanied by web-flange junction failure under the bearing plates (see Figure 5.6b). In series "ITF–69x100–t5.0–A0.6–C–N50", horizontal longitudinal cracking around the perforations could be seen along with the formation of diagonal shear cracks which propagated towards the web-flange junction (see Figure 5.6d). Similar failure patterns could be observed in case of series "ITF–69x100–t5.0–A0.4–C–N50" and "ITF–69x100–t5.0–A0.8–C–N50" (see Figures 5.6c and 5.6e). For obtaining a clear understanding of the failure patterns, specimen in series "ITF–69x100–t5.0–A0.6–C–N50" was cut at the mid length and the cross sectional view is shown in Figure 5.6f. Shear failure can be observed in the web which propagated towards away from the perforation and web-flange junction of the specimens.

From the above observations, it can be said that specimens without perforation failed by web-flange junction separation and shearing or crushing of web. Specimens with centred web perforation exhibited longitudinal and shear cracks around the perforation which propagated diagonally towards the web and web-flange junction, respectively. In some cases, web-flange junction failure was seen. No specimen showed out of plane web deformation or web buckling. In all cases, initial cracking sound was heard which increased with the increase of load. This continued until the load reached its ultimate value with the emission of a larger cracking sound.

In order to have a better understanding of the web crippling failure patterns; the longitudinal, transverse and shear stress fields in the GFRP specimens were evaluated and analysed. The stress distributions were assessed for two different load levels as shown in the numerical load–displacement curves: at the commencement of failure (L1, M1 and N1) and at ultimate failure (L2, M2 and N2) (see Figure 5.12). Three different series were considered for the study namely: ITF–69x100–t5.0–A0.0–C–N50 (L1, L2), ITF–69x100–t5.0–A0.2–C–N50 (M1, M2) and ITF–69x100–t5.0–A0.6–C–N50 (N1, N2). From Figures 5.13a–f, it can be seen that the shear stress initiates the failure in all models and attains its maximum value correspondingly. For the series "ITF–69x100–t5.0–A0.0–C–N50", initial stress concentration can be observed in some of the finite elements in both the web-flange junctions near the edges of the bearing plates (see Figure 5.13a) after which it spreads towards the middle of the web (see Figure 5.13b). For the series "ITF–69x100–t5.0–A0.2–C–N50" and "ITF–69x100–t5.0–A0.6–C–N50", failure started with the initiation of stress concentration around the perforations and extended towards the web-flange junctions near the edges of the bearing plates (see Figure 5.13c–f). On the other hand, the transverse and longitudinal stresses could not reach their ultimate values (see Figures 5.14a–f and 5.15a–f). The failure modes obtained from the FE predictions (Figures 5.13–5.15) can be compared with the experimental failure patterns (see Figures 5.6a, 5.6b, 5.6d). It can be concluded that the FE models could predict well the failure modes in the GFRP specimens. The shear stress distribution in the web of each specimen was observed mainly in the vicinity of the bearing plates. No out of plane web deformation or web buckling could be seen in any of the specimens. It can be concluded that shear stresses played the most influential part in failure initiation than the longitudinal and transverse stresses regardless of the web perforation size. Similar observation was also reported by Fernandes *et al*. (2015) and Nunes *et al*. (2017).

5.4.1.2 Load–displacement behaviour

Typical load–displacement plots of the tested GFRP specimens for both with and without perforations under ITF loading condition are presented in Figure 5.12. As the results of all tested specimens in a series are very consistent, a single representative curve of each series is shown in the figure. It can be seen that all specimens exhibited linear behaviour up to a point after which a sudden drop in the load–displacement response could be observed. This point in the load–displacement curve can be linked to the initial web-flange junction failure or crushing at web, in case of intact specimens. For specimens in series "ITF–69x100–t5.0–A0.2–C–N50", this can be linked to the initial crack formation around the perforation and the initiation of web-flange junction failure under the bearing plates. In case of series

“ITF–69x100–t5.0–A0.6–C–N50”, this failure point indicates the initial crack formation around the perforations. The continuation of the load–displacement curve after the initial peak load demonstrates that the web continued to carry the load upto a point where the ultimate failure would occur by crushing of the web.

The numerical load–displacement curves of the GFRP specimens for both with and without perforations under ITF loading condition are presented in Figure 5.12 and compared with the experimental curves. Linear elastic behaviour can be seen up to a point which was followed by a sudden drop in the load–displacement response. It can be said that the FE models could simulate the experimental load–displacement curves of the GFRP specimens closely (although not exactly). As discussed in Section 4.4.3, the differences in the ultimate loads and behaviour after ultimate loads may be due to the shortcomings of the Hashin damage initiation criteria (available in Abaqus, 2009) used in the numerical models. In addition, compared to their numerical counterparts, the experimental load–displacement curves are found to have lower elastic stiffness. The reduced stiffness in the experimental curves may arise due to the fact that the experimental displacements are plotted from the cross-head displacement data which includes the effects of clearances and initial adjustments of the test fixtures; and could not be simulated by the FE models. For comparison purpose, the ultimate loads obtained from the experiments and finite element analysis are compared and presented in Table 5.1. From the ratios of the experimental ultimate loads and numerical loads (mean of P_{EXP}/P_{FEA} = 1.15, COV = 0.09), it can be understood that the FE results agree well with the experimental results.

5.4.1.3 Effect of perforation diameter

The present investigation evaluates the effect of perforation diameter by drilling 11.8 mm, 23.6 mm, 35.4 mm and 47.2 mm diameter perforations while other parameters are kept constant. In Table 5.1, the web-crippling ultimate loads (both experimental and numerical) are presented. In Figures 5.16a–b, the web crippling ultimate loads and strength reduction factors obtained from the numerical study are plotted against *a/h* ratios. From Figures 5.12, 5.16a–b and Table 5.1, significant decrease in web crippling strength could be observed due to web perforations. Also, variations in the ultimate load and failure patterns of the specimens could be seen with the change in web perforation diameter. In case of experimental specimens, compared to the intact specimens, the average web crippling strength for perforated specimens in series

“ITF–69x100–t5.0–A0.2–C–N50” (11.8 mm perforation), “ITF–69x100–t5.0–A0.4–C–N50” (23.6 mm perforation), “ITF–69x100–t5.0–A0.6–C–N50” (35.4 mm perforation) and “ITF–69x100–t5.0–A0.8–C–N50” (47.2 mm perforation) was reduced by 14.7%, 22.2%, 24.2% and 41.1%, respectively. Also, as the diameter of the perforation was increased from 11.8 mm to 47.2 mm, the reduction in crippling strength was increased by about 30.9%. Another observation from these findings is that significant reduction in stiffness could be noticed for the specimens with larger diameter perforations. In a similar manner, significant reduction in strength and stiffness could be observed from the numerical load–displacement response for specimens with larger diameter perforations. It can be concluded that specimens with the largest web perforation showed maximum reduction in strength and stiffness while those with the least diameter web perforation exhibited the lowest reduction. Hence, by reducing the perforation diameter, the web crippling strength and stiffness could be significantly increased.

5.4.2 ETF load configuration

A total of 15 specimens were tested under ETF loading condition, out of which 12 specimens were for centred web perforation and 3 specimens were without web perforation. The experimental ultimate web crippling loads obtained (P_{EXP}) are summarised in Table 5.2. For each series of test, finite element analysis was also carried out and compared with the experimental results.

5.4.2.1 Failure patterns

In case of specimens without web perforations, failure mainly occurred at the web with longitudinal cracking or material crushing in the vicinity of the bearing area. For specimens in series “ETF–69x100–t5.0–A0.0–C–N50”, single or multiple longitudinal cracks could be observed under the loading plates near the web-flange junction as well as at the mid height of the web (see Figure 5.7a). From Figure 5.7b, shear failure could be observed in the web which propagated towards the interior of the specimen. In case of perforated specimens, failure started with the development of cracks around the perforations due to the initiation of local stress concentration in the vicinity of the perforations which subsequently propagated to the webs. Specimens in the series “ETF–69x100–t5.0–A0.2–C–N50” showed horizontal crack formation around the perforation at the web (see Figure 5.7c). From Figure 5.7d, shear dominant failure pattern could be observed which started from the perforation edge and propagated towards the end and interior of the web. Similar failure patterns could be observed in series "ETF–69x100–t5.0–A0.4–C–N50" (see Figures 5.7e–f). In case of series "ETF–69x100–t5.0–A0.6–C–N50", horizontal longitudinal cracking around the perforations could be seen along with the formation of diagonal shear cracks that propagated towards the web-flange junction (see Figure 5.7g). Formation of wedge type shear failure could be seen near the perforation edge (see Figure 5.7h). Similar failure patterns were also observed in case of series "ETF–69x100–t5.0–A0.8–C–N50" (see Figures 5.7i–j).

From the above observations, it can be seen that specimens without perforation failed by shearing or crushing of web. Specimens with relatively smaller perforation sizes (a = 0.2h–0.4h) exhibited horizontal cracks around the perforation which propagated towards the end and interior of the web. Specimens with relatively larger perforation sizes (a = 0.6h–0.8h) exhibited horizontal cracks around the perforation as well as diagonal shear cracks propagating diagonally towards the web and web-flange junction, respectively. Out of plane web deformation or web buckling was not visible for any specimen. Similar to ITF specimens, initial cracking sound was heard in all specimens and increased with the increase of load, and continued until the load reached its ultimate value with the release of a larger cracking sound.

In order to enhance the understanding of the failure patterns; the longitudinal, transverse and shear stress fields in the GFRP specimens were assessed and analysed. The stress distributions were evaluated for two different load levels as shown in the numerical load–displacement curves: at the commencement of failure (P1, Q1 and R1) and at ultimate failure (P2, Q2 and R2) (see Figure 5.17). Three different series were considered for the study viz., ETF–69x100–t5.0–A0.0–C–N50 (P1, P2), ETF–69x100–t5.0–A0.2–C–N50 (Q1, Q2) and ETF–69x100–t5.0–A0.6–C–N50 (R1, R2). From Figures 5.18a–f, it can be observed that the shear stress initiates the failure in all models and reaches its ultimate value correspondingly. In case of series "ETF–69x100–t5.0–A0.0–C–N50", initial stress concentration can be seen in some of the finite elements near both the web-flange junctions and the edges of the bearing plates after which it propagates towards the mid of the web (see Figures 5.18a–b). In series "ETF–69x100–t5.0–A0.2–C–N50" and "ETF–69x100–t5.0–A0.6–C–N50", failure commenced with the initiation of stress concentration around the perforations and propagated towards the web-flange junctions near the inner edges of the bearing plates and towards the end of web (see

Figures 5.18c–f). In contrast, the transverse and longitudinal stresses did not reach their maximum values (see Figures 5.19a–f and 5.20a–f). The failure patterns observed in the FE analyses (Figures 5.18–5.20) can be compared with the experimental failure modes (see Figures 5.7a–j). It can be said that the FE models predicted well the experimental failure modes in the GFRP specimens. The stress distributions in the web of each specimen were mainly in the vicinity of the loading plates. No web buckling could be observed in any specimen. It can be said that regardless of the perforation diameter sizes, shear stresses played the most dominating role in initiation of failure than the longitudinal and transverse stresses.

5.4.2.2 Load–displacement behaviour

Load–displacement plots of the GFRP specimens tested for both with and without perforations under ETF loading condition are shown in Figure 5.17. Due to consistency in the test results, a single representative curve for each series is shown in the figure. Linear behaviour can be observed in each specimen up to a point after which a sudden drop occurred in the load–displacement curve. In case of intact specimens, the sudden drop in the load–displacement curve can be linked to the initiation of material or shear cracking in the web. For specimens in series "ETF–69x100–t5.0–A0.2–C–N50", the sudden drop in the load–displacement curve can be related to the initial crack formation around the perforation and the initiation of web-flange junction failure under the bearing plates. In case of series "ETF–69x100–t5.0–A0.6–C–N50", this failure point signifies the initiation of crack formation around the perforations. After the initial peak load, the web would continue to carry the load up to a certain point after which the web would fail by crushing at the ultimate failure.

In Figure 5.17, numerical/FE load–displacement curves of the GFRP specimens are plotted for both with and without perforations under ETF loading condition and compared with the experimental curves. In all cases, linear elastic behaviour can be observed up to a point which was followed by a sudden drop in the load–displacement curve. It can be concluded that the FE models could predict the experimental load–displacement curves of the GFRP specimens closely (however not matching exactly). Also, the experimental load–displacement curves are found to have lower elastic stiffness compared to their numerical counterparts. The probable causes for the differences between the experimental and numerical curves are described in Section 5.4.1.2. In Table 5.2, the ultimate loads obtained from the experimental programme and finite element analyses are compared and can be concluded that the FE results agree with the experimental results closely.

5.4.2.3 Effect of perforation diameter

In the present investigation, the effect of perforation diameter on the web crippling of GFRP section profiles is evaluated by considering 11.8 mm, 23.6 mm, 35.4 mm and 47.2 mm diameter perforations while other parameters are kept constant. The experimental and numerical web-crippling ultimate loads for ETF loading are presented in Table 5.2. To investigate the effect of perforation sizes, the web crippling ultimate loads and strength reduction factors obtained from the numerical study are plotted against *a/h* ratios in Figures 5.21a–b. From Figures 5.17, 5.21a–b and Table 5.2, considerable reduction in the web crippling strength could be seen due to web perforations, along with variations in the ultimate load and failure patterns of the specimens with change in perforation diameters. In case of experimental specimens, compared to the intact specimens, the average web crippling strength for perforated specimens in series "ETF–69x100–t5.0–A0.2–C–N50", "ETF–69x100–t5.0–A0.4–C–N50" (23.6 mm perforation), "ETF–69x100–t5.0–A0.6–C–N50" and "ETF–69x100–t5.0–A0.8–C–N50" was reduced by ~26.0%, 43.2%, 61.6% and 78.3%, respectively. In addition, as the perforation size was increased from 11.8 mm to 47.2 mm, the reduction in crippling strength was increased by around ~73.8%. Another observation from these findings is that the specimens with larger diameter perforations exhibited significant reduction in stiffness. Also, from the load–displacement curves, considerable reduction in strength and stiffness could be seen in specimens with larger diameter perforations. It may be said that specimens with lowest diameter web perforation showed the least reduction, while specimens with largest web perforation exhibited maximum reduction in strength and stiffness. Therefore, the web crippling strength and stiffness could be considerably increased by reducing the perforation diameter.

5.5 Parametric Study

The experimental web crippling behaviour of the GFRP WF–sections with and without circular web perforations under ETF and ITF loading conditions were closely predicted by the FE models developed in the previous section. Based on these FE models, parametric studies were performed in order to investigate the effects of web perforations, bearing lengths and cross-section sizes on the web crippling strengths of the WF–sections.

In case of metallic sections with perforations, the web crippling strength was mainly influenced by the ratio of the web perforation diameter to the web height (*a/h*) and the ratio of the bearing length to web height (*N/h*) (Uzzaman *et al*., 2012; Uzzaman *et al*., 2013; Lian *et al*., 2016; Lian *et al*., 2017; Lian *et al*., 2017; Yousefi *et al*., 2017; Yousefi *et al*., 2017; Yousefi *et al*.; 2018). In case of GFRPs, it is reported that bearing length has significant influence on the web crippling strength of GFRP profiles (Borowicz and Bank, 2011; and Fernandes *et al*., 2015). Also, from the present experimental and numerical investigations, it is understood that the main parameters influencing the web crippling behaviour of the perforated GFRP sections are *a/h* and *N/h* ratios. In the parametric study, effects of these two parameters were studied extensively by considering different web perforation sizes, different bearing plate lengths and different cross-section sizes. Specimens with three different section sizes were considered by varying their thicknesses (t_w) from 3 mm to 8 mm (web slenderness values, h/t_w varied from 7.0 to 20.33). The lengths of the bearing plates considered were 50 mm, 70 mm, 100 mm and 120 mm. The ratios of the web perforation diameter to the web height (*a/h*) considered were 0.2, 0.4, 0.6 and 0.8. The ratios of the bearing plate length to the web height (*N/h*) were varied in the range of 0.82 to 2.14. All the web perforations were positioned at the mid-depth of the webs and centreed to the bearing plates. The labeling of specimens were done in such a way that their dimensions, length of the bearing plates (*N*) and web perforation diameter to the web depth ratios (*a/h*) could be easily identified from their labels (for details see Section 5.2.4). In each series, the web crippling strengths of the specimens were obtained for sections with and without web perforations. Accordingly, strength reduction factors (*R*, defined as the ratio of web crippling strengths for sections with web perforations to those corresponding sections without web perforations) were used for computing the degrading effect of web perforations on the web crippling strengths of the GFRP sections.

In the parametric study, a total of 120 specimens was analysed out of which 60 specimens were under ITF loading condition and 60 specimens were for ETF loading condition. The parametric study mainly investigates the effects of *a/h* and *N/h* ratios. Details of the cross-section dimensions, bearing lengths used for the specimens and their corresponding web crippling strengths (P_{FEA}) predicted for both ETF and ITF loading are presented in Tables 5.3 and 5.4.

In Figures 5.22a–d, the web crippling strengths and reduction factors for specimens under ITF loading condition are plotted against the ratios *a/h* and *N/h*, respectively. It can be seen that the ultimate strength or the reduction factor is decreased as *a/h* increases from 0.2 to 0.8 (see Figures 5.22a and 5.22b). Another interesting observation is that the reduction rate is higher when *a/h* ratio increases from 0.0 to 0.2 compared to the range of 0.2 to 0.8. From Figures 5.22c and 5.22d, it can be understood that the ultimate strength or the reduction factor is significantly influenced by the bearing plate length to web height ratio (*N/h*). As the ratio *N/h* is increased, the ultimate strength of the specimens also increases. In case of specimens with relatively thicker section (t_w = 8 mm), increasing the *N/h* ratio from 0.89 to 2.14 increases the strength by an average of around ~108.2%, whereas, for specimens with thinner sections (t_w = 3 to 5 mm), the average strength increase is found to be around ~122.1% to ~106.7%, respectively.

In Figures 5.23a–d, the web crippling strengths and reduction factors for specimens under ETF loading are plotted against the ratios *a/h* and *N/h*, respectively. It is observed that the ultimate strength or the reduction factor is decreased as *a/h* increases from 0.2 to 0.8 (see Figures 5.23a and 5.23b). Another interesting observation is that the reduction rate is higher when *a/h* ratio increases from 0.0 to 0.2 compared to the range of 0.2 to 0.8. From Figures 5.23c and 5.23d, it can be seen that the ultimate strength or the reduction factor is significantly influenced by the bearing plate length to web height ratio (*N/h*). As the ratio *N/h* is increased, the ultimate strength of the specimens also increases. In case of specimens with thicker section (t_w = 8 mm), increasing the *N/h* ratio from 0.89 to 2.14 increases the strength by an average of around ~251.5%. For specimens with thinner sections with t_w = 3 mm and 5 mm, the average strength increase is found to be around ~239.3% (*N/h* ratio from 0.82 to 1.97) and ~285.1% (*N/h* ratio from 0.85 to 2.03), respectively.

5.6 Proposed strength reduction factors

From the experimental and numerical investigations, it has been readily observed that the web crippling behaviour of GFRP sections with centred web perforations are mainly influenced by *a/h* and *N/h* ratios. Henceforth, in order to compute the degrading effect of web perforations on the web crippling strengths of the GFRP sections with centred web perforation under ITF and ETF loading conditions, strength reduction factor (R_p = ratio of web crippling strengths for sections with web perforations to those without web perforations) equations are proposed based on the experimental and numerical results using bivariate linear regression analysis. The equations are given as follows:

For centred perforation under ITF loading:

$$R_P = 0.81 - 0.40\left(\frac{a}{h}\right) + 0.02\left(\frac{N}{h}\right) \leq 1 \tag{5.1}$$

For centred perforation under ETF loading:

$$R_P = 0.66 - 0.59\left(\frac{a}{h}\right) + 0.13\left(\frac{N}{h}\right) \leq 1 \tag{5.2}$$

It may be noted that the above equations have been arrived at, for the conditions:

$a/h \leq 0.8$, $N/h \leq 2.14$, and $h/t_w \leq 20.33$.

5.7 Reliability Analysis

The suitability of the proposed strength reduction factor equation for web crippling of GFRP WF or I–section with web perforation is assessed by using reliability analysis. The reliability analysis for the present investigation is performed following similar procedures described in Section 4.6 which is according to the methods described in the Commentary section of the ASCE Specifications for the design of cold-formed stainless steel structural members (ASCE 8–02). A target reliability value of 3.5 is chosen as the target reliability index (β_o) to establish the suitability of the proposed reduction formulae with a resistance factor or ϕ–factor of 0.70 as detailed in Section 4.6.

5.8 Comparison of experimental and numerical results with the proposed strength reduction factors

Comparisons are made between the strength reduction factor (R) values obtained from the experimental and numerical results with the proposed strength reduction factor (R_P) values and plotted with respect to a/h and h/t_w ratios for both ITF and ETF loading conditions in Figures 5.24a–b and Figures 5.25a–b, respectively. Also, their mean values, coefficients of variation and reliability index (β) values are evaluated. It can be observed that the proposed strength reduction factors are slightly conservative and in good agreement with the experimental and numerical results for centreed web perforation under both ITF and ETF loading conditions.

Equations 5.1 and 5.2 resulted in a mean of 1.08 and 1.17 with standard deviation (SD) of 0.11 and 0.2, and coefficient of variation (COV) of 0.10 and 0.17, respectively. From reliability analyses, the reliability index (β) values for the proposed strength reduction factor equations are found to be 3.71 (> β_o = 3.5) and 3.54 (> β_o = 3.5) for ITF and ETF loading conditions, respectively. Hence, it can be said that the proposed strength reduction equations are reliable.

5.9 CONCLUSION

In this chapter, both experimental and numerical investigation on the web crippling behaviour of GFRP WF–section profile with centred web perforation has been performed by utilising a GFRP WF–section profile. Experimental investigations included full scale web crippling experiments performed on 29 specimens under ITF and ETF loading configurations. The outcomes of the experimental and numerical investigations are presented in the form of load–displacement curves, failure modes and ultimate web crippling strength values. The following conclusions are drawn based on the present investigation:

1) In case of ITF loading, specimens without perforation showed multiple longitudinal cracks under the loading plates near the web-flange junction as well as at the mid height of the web. Specimens with centred web perforation exhibited longitudinal and shear cracks around the perforation which propagated diagonally towards the web and web-flange junction, respectively.
2) For ETF loading, specimens without perforation showed multiple longitudinal cracks under the loading plates near the web-flange junction as well as at the mid height of the web. For specimens with centred web perforation, failure started with the initiation of cracks around the perforations due to the development of local stress concentration which propagated to the web.
3) All web crippling specimens under ITF and ETF loading conditions exhibited linear elastic behaviour up to the initial failure point after which a sudden drop was observed in the load–displacement curves. The FE models could simulate the experimental load–displacement curves of the GFRP specimens with satisfactory accuracy.
4) Significant decrease in web crippling strength could be observed due to web perforations. Compared to the intact specimens, under ITF loading, the average web crippling strength for perforated specimens with web perforation sizes 0.2h, 0.4h, 0.6h *and* 0.8h was reduced by

14.7%, 22.2%, 24.2% and 41.1%, respectively. In case of ETF loading, compared to the intact specimens, the average web crippling strength for perforated specimens with web perforation sizes 0.2*h*, 0.4*h*, 0.6*h and* 0.8*h* was reduced by 26.0%, 43.2%, 61.6% and 78.3%, respectively.

5) Based on the parametric study, reliable web crippling strength reduction factors are proposed for GFRP WF–section under ITF and ETF loading configurations. It was observed that the web crippling strength reduction factors are influenced by both *a/h* and *N/h* ratios.

Table 5.1: Specimen details with experimental and numerical ultimate loads for ITF loading.

Specimen	Web depth, *d* (mm)	Flange width, b_f (mm)	Thickness, t_w (mm)	Perforation diameter, *a* (mm)	Ultimate Load, P_{EXP} (kN)	Average P_{EXP} (kN)	Numerical web crippling strength, P_{FEA} (kN)	Comparison P_{EXP}/P_{FEA}
ITF–69x100–t5.0–A0.0–C–N50–1	69	100	5	0.0	15.70			
ITF–69x100–t5.0–A0.0–C–N50–2	69	100	5	0.0	17.25	16.15	15.93	1.01
ITF–69x100–t5.0–A0.0–C–N50–3	69	100	5	0.0	15.50			
ITF–69x100–t5.0–A0.2–C–N50–1	69	100	5	11.8	12.14	13.77	11.49	1.20
ITF–69x100–t5.0–A0.2–C–N50–3	69	100	5	11.8	15.40			
ITF–69x100–t5.0–A0.4–C–N50–1	69	100	5	23.6	12.70			
ITF–69x100–t5.0–A0.4–C–N50–2	69	100	5	23.6	12.14	12.56	10.73	1.17
ITF–69x100–t5.0–A0.4–C–N50–3	69	100	5	23.6	12.85			
ITF–69x100–t5.0–A0.6–C–N50–1	69	100	5	35.4	12.74			
ITF–69x100–t5.0–A0.6–C–N50–2	69	100	5	35.4	12.43	12.24	9.68	1.26
ITF–69x100–t5.0–A0.6–C–N50–3	69	100	5	35.4	11.56			
ITF–69x100–t5.0–A0.8–C–N50–1	69	100	5	47.2	9.72			
ITF–69x100–t5.0–A0.8–C–N50–2	69	100	5	47.2	10.32	9.52	8.77	1.09
ITF–69x100–t5.0–A0.8–C–N50–3	69	100	5	47.2	8.53			
Mean								1.15
COV								0.09

Table 5.2: Specimen details with experimental and numerical ultimate loads for ETF loading.

Specimen	Web depth, d (mm)	Flange width, b_f (mm)	Thickness, t_w (mm)	Perforation diameter, a (mm)	Ultimate Load, P_{EXP} (kN)	Average P_{EXP} (kN)	Numerical web crippling strength, P_{FEA} (kN)	Comparison P_{EXP}/P_{FEA}
ETF–69x100–t5.0–A0.0–C–N50–1	69	100	5	0.0	11.66			
ETF–69x100–t5.0–A0.0–C–N50–2	69	100	5	0.0	11.01	11.35	12.40	0.92
ETF–69x100–t5.0–A0.0–C–N50–3	69	100	5	0.0	11.40			
ETF–69x100–t5.0–A0.2–C–N50–1	69	100	5	11.8	8.06			
ETF–69x100–t5.0–A0.2–C–N50–2	69	100	5	11.8	8.56	8.40	8.63	0.97
ETF–69x100–t5.0–A0.2–C–N50–3	69	100	5	11.8	8.56			
ETF–69x100–t5.0–A0.4–C–N50–1	69	100	5	23.6	6.56			
ETF–69x100–t5.0–A0.4–C–N50–2	69	100	5	23.6	6.56	6.45	6.86	0.94
ETF–69x100–t5.0–A0.4–C–N50–3	69	100	5	23.6	6.24			
ETF–69x100–t5.0–A0.6–C–N50–1	69	100	5	35.4	4.71			
ETF–69x100–t5.0–A0.6–C–N50–2	69	100	5	35.4	4.54	4.36	4.84	1.10
ETF–69x100–t5.0–A0.6–C–N50–3	69	100	5	35.4	5.38			
ETF–69x100–t5.0–A0.8–C–N50–1	69	100	5	47.2	2.39			
ETF–69x100–t5.0–A0.8–C–N50–2	69	100	5	47.2	4.78	2.47	2.26	0.92
ETF–69x100–t5.0–A0.8–C–N50–3	69	100	5	47.2	2.54			
Mean								0.97
COV								0.08

Table 5.3: Specimen details and web crippling strengths for ITF loading predicted from parametric study.

Specimen	Web depth	Flange width	Thickness	Bearing length	N/h	Slenderness	FEA load, P_{FEA} (kN)				
	d (mm)	b_f (mm)	t_w (mm)	N (mm)		h/t_w	A0	A0.2	A0.4	A0.6	A0.8
ITF–67×100–t3.0–C–N50	67	100	3	50	0.82	20.33	10.48	8.11	7.64	7.05	6.15
ITF–67×100–t3.0–C–N70	67	100	3	70	1.15	20.33	13.78	10.42	9.58	8.99	8.16
ITF–67×100–t3.0–C–N100	67	100	3	100	1.64	20.33	18.14	13.6	13.48	12.25	11.94
ITF–67×100–t3.0–C–N120	67	100	3	120	1.97	20.33	23.31	16.77	16.45	15.74	14.94
ITF–69×100–t5.0–C–N50	69	100	5	50	0.85	11.8	15.93	11.48	10.73	9.87	8.77
ITF–69×100–t5.0–C–N70	69	100	5	70	1.19	11.8	20.10	13.29	12.99	12.50	11.42
ITF–69×100–t5.0–C–N100	69	100	5	100	1.69	11.8	26.17	18.22	17.88	17.33	16.43
ITF–69×100–t5.0–C–N120	69	100	5	120	2.03	11.8	30.61	22.47	21.39	21.38	20.16
ITF–72×100–t8.0–C–N50	72	100	8	50	0.89	7.0	32.80	22.64	21.49	20.09	18.01
ITF–72×100–t8.0–C–N70	72	100	8	70	1.25	7.0	41.49	27.39	26.27	25.03	22.9
ITF–72×100–t8.0–C–N100	72	100	8	100	1.79	7.0	56.57	36.95	36.48	35.56	33.25
ITF–72×100–t8.0–C–N120	72	100	8	120	2.14	7.0	63.17	44.46	44.43	43.85	40.91

Table 5.4: Specimen details and web crippling strengths for ETF loading predicted from parametric study.

Specimen	Web depth	Flange width	Thickness	Bearing length	N/h	Slenderness	FEA load, P_{FEA} (kN)				
	d (mm)	b_f (mm)	t_w (mm)	N (mm)		h/t_w	A0	A0.2	A0.4	A0.6	A0.8
ETF–67×100–t3.0–C–N50	67	100	3	50	0.82	20.33	7.58	6.55	5.39	4.04	1.88
ETF–67×100–t3.0–C–N70	67	100	3	70	1.15	20.33	10.49	8.95	7.68	6.94	5.33
ETF–67×100–t3.0–C–N100	67	100	3	100	1.64	20.33	13.96	12.17	11.58	10.38	8.64
ETF–67×100–t3.0–C–N120	67	100	3	120	1.97	20.33	17.23	15.56	14.8	13.52	11.70
ETF–69×100–t5.0–C–N50	69	100	5	50	0.85	11.8	12.40	8.63	6.86	4.84	2.26
ETF–69×100–t5.0–C–N70	69	100	5	70	1.19	11.8	17.11	11.53	10.76	9.25	7.21
ETF–69×100–t5.0–C–N100	69	100	5	100	1.69	11.8	22.68	16.79	16.22	15.70	13.97
ETF–69×100–t5.0–C–N120	69	100	5	120	2.03	11.8	28.12	19.66	19.65	19.25	17.78
ETF–72×100–t8.0–C–N50	72	100	8	50	0.89	7.0	26.14	17.73	14.73	10.85	5.33
ETF–72×100–t8.0–C–N70	72	100	8	70	1.25	7.0	33.89	23.59	21.79	19.24	15.37
ETF–72×100–t8.0–C–N100	72	100	8	100	1.79	7.0	46.75	35.2	32.56	30.92	26.97
ETF–72×100–t8.0–C–N120	72	100	8	120	2.14	7.0	58.37	40.44	39.96	38.9	36.08

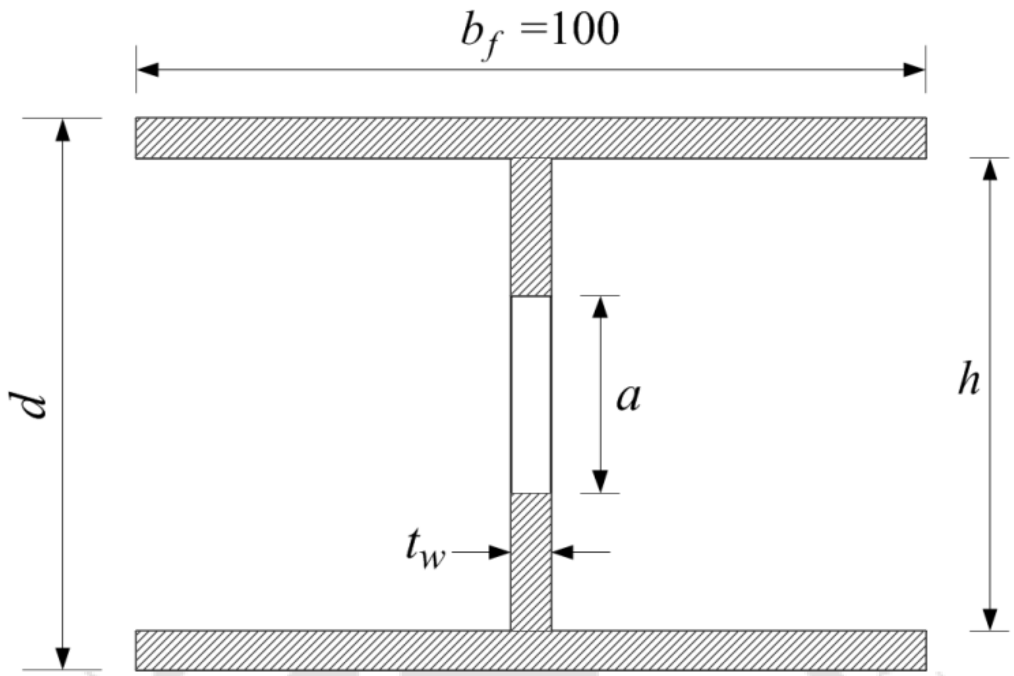

Figure 5.1: Dimensional sketch of the wide flange profile (in mm).

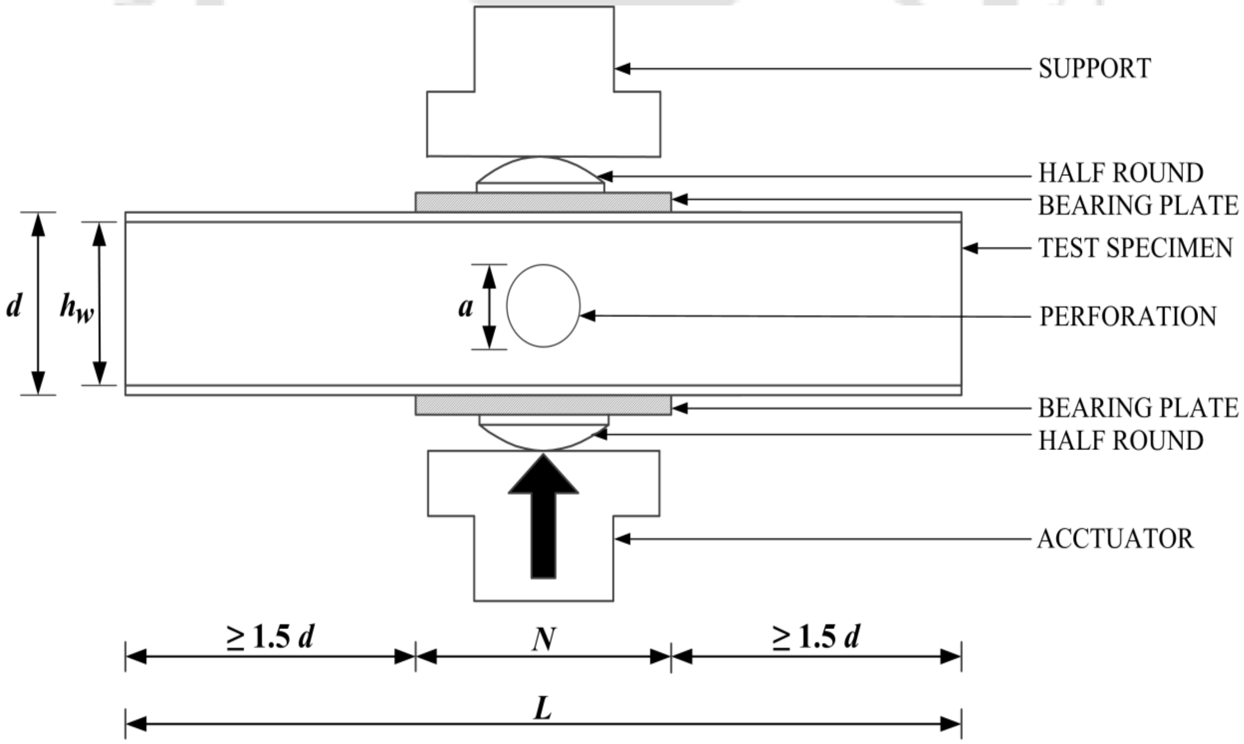

Figure 5.2: ITF loading arrangement for specimens with centred perforation (front view).

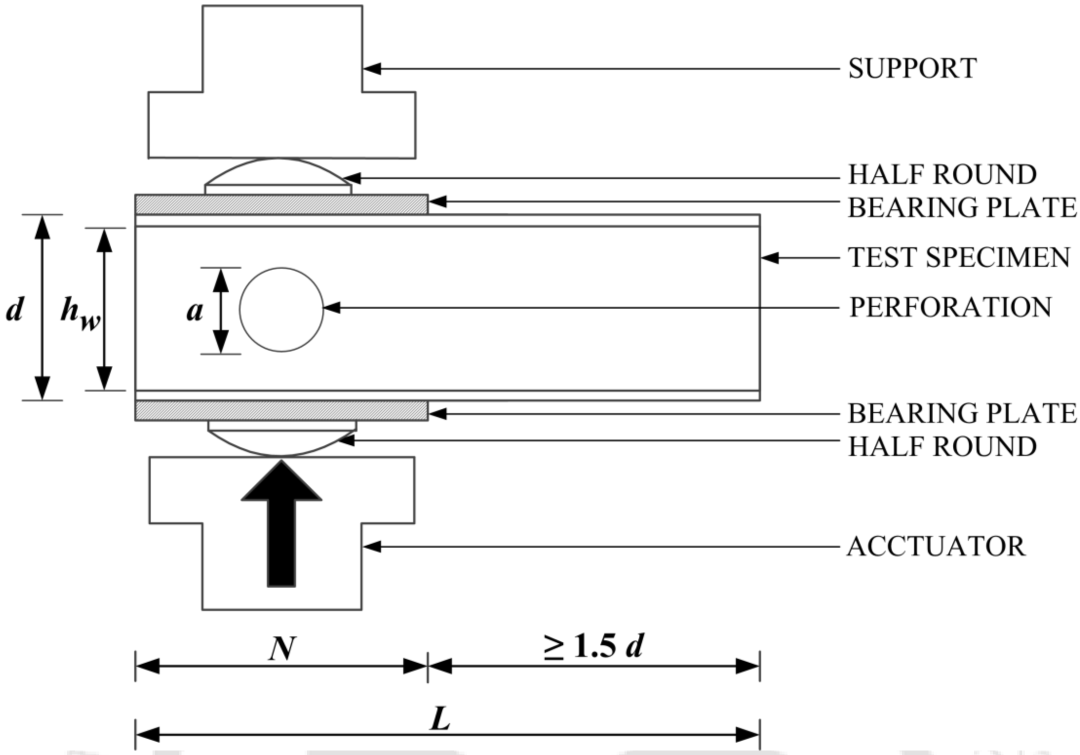

Figure 5.3: ETF loading arrangement for specimens with centred perforation (front view).

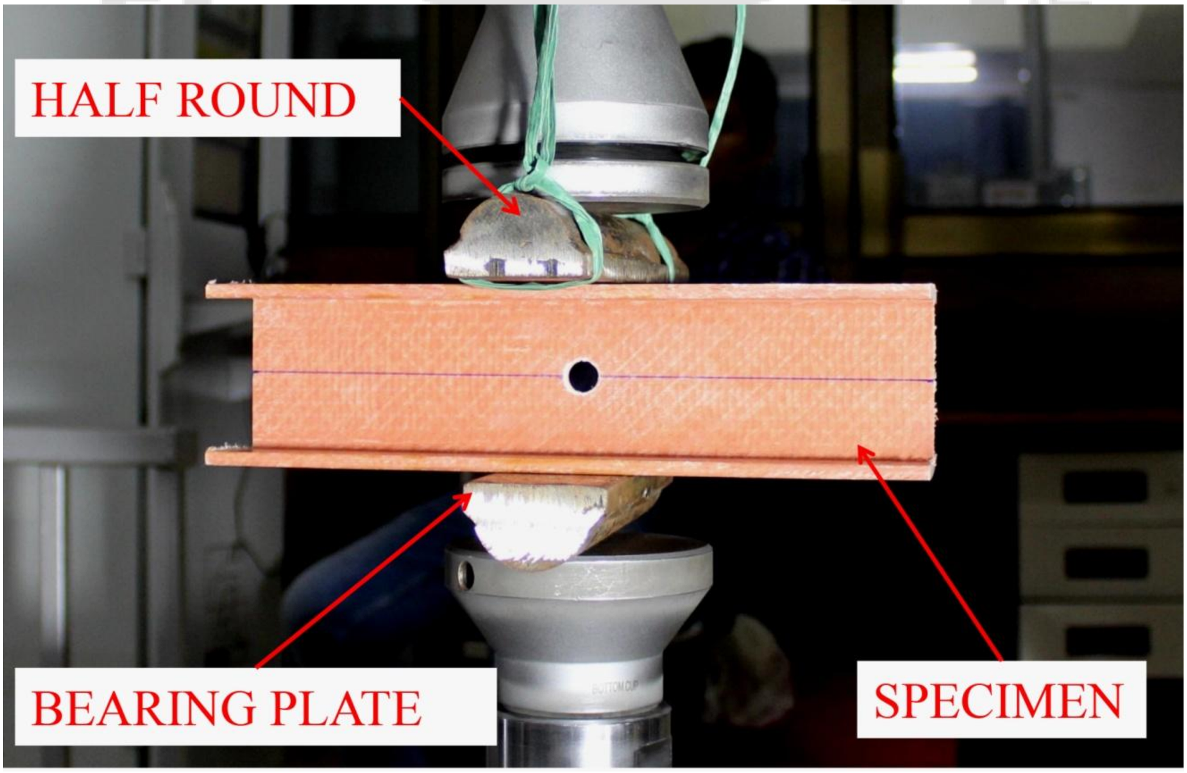

Figure 5.4: ITF load configuration with centred perforation.

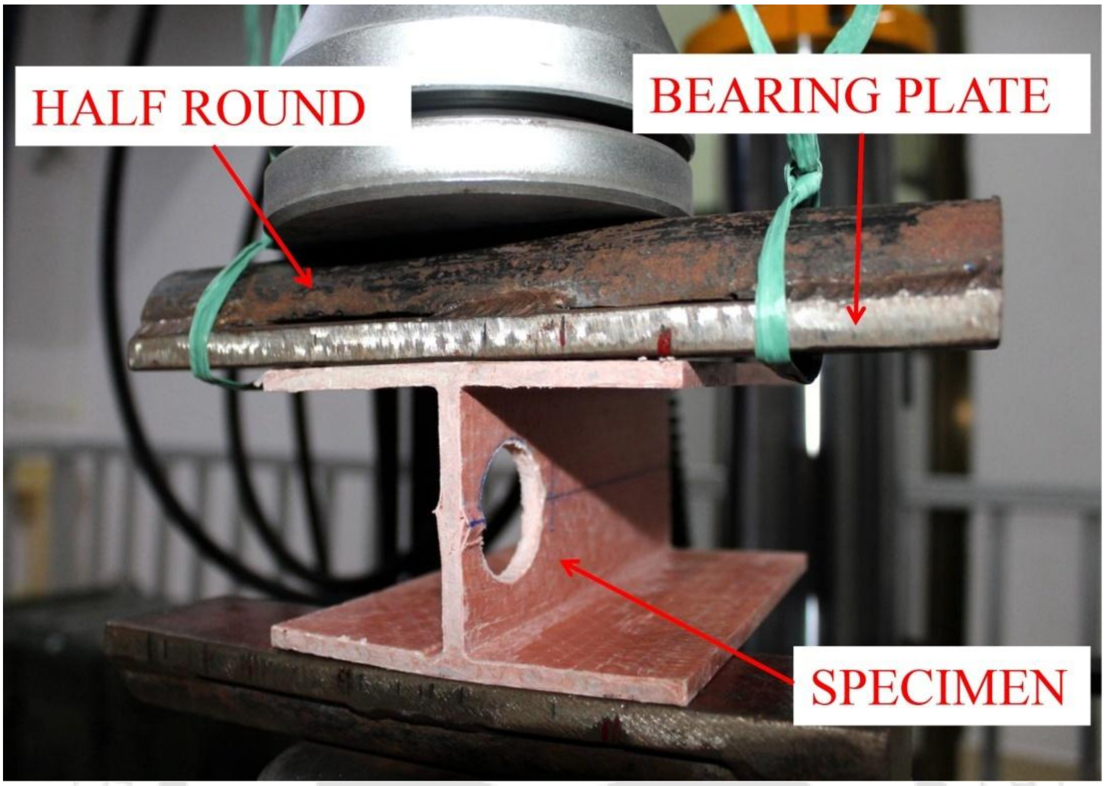

Figure 5.5: ETF load configuration with centred perforation.

a)

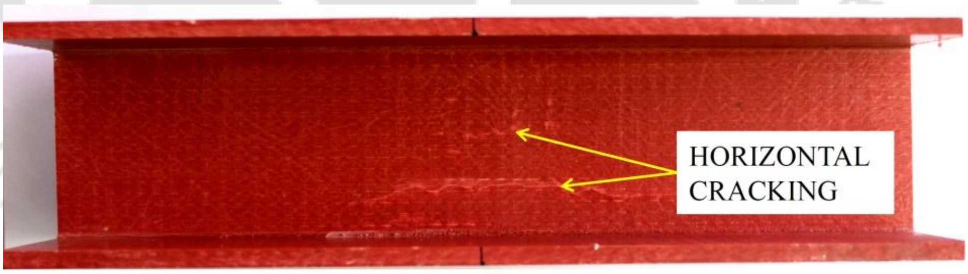

b)

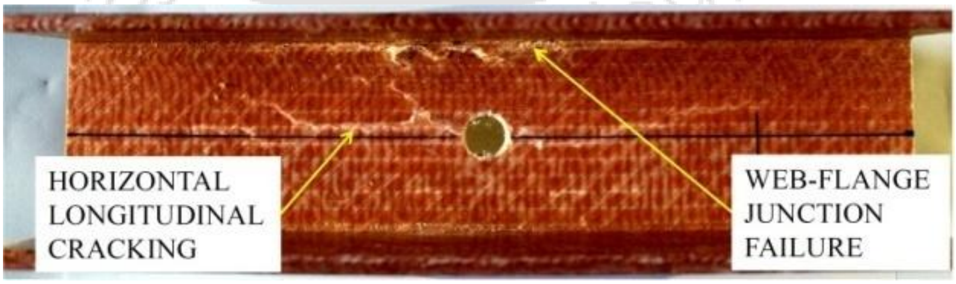

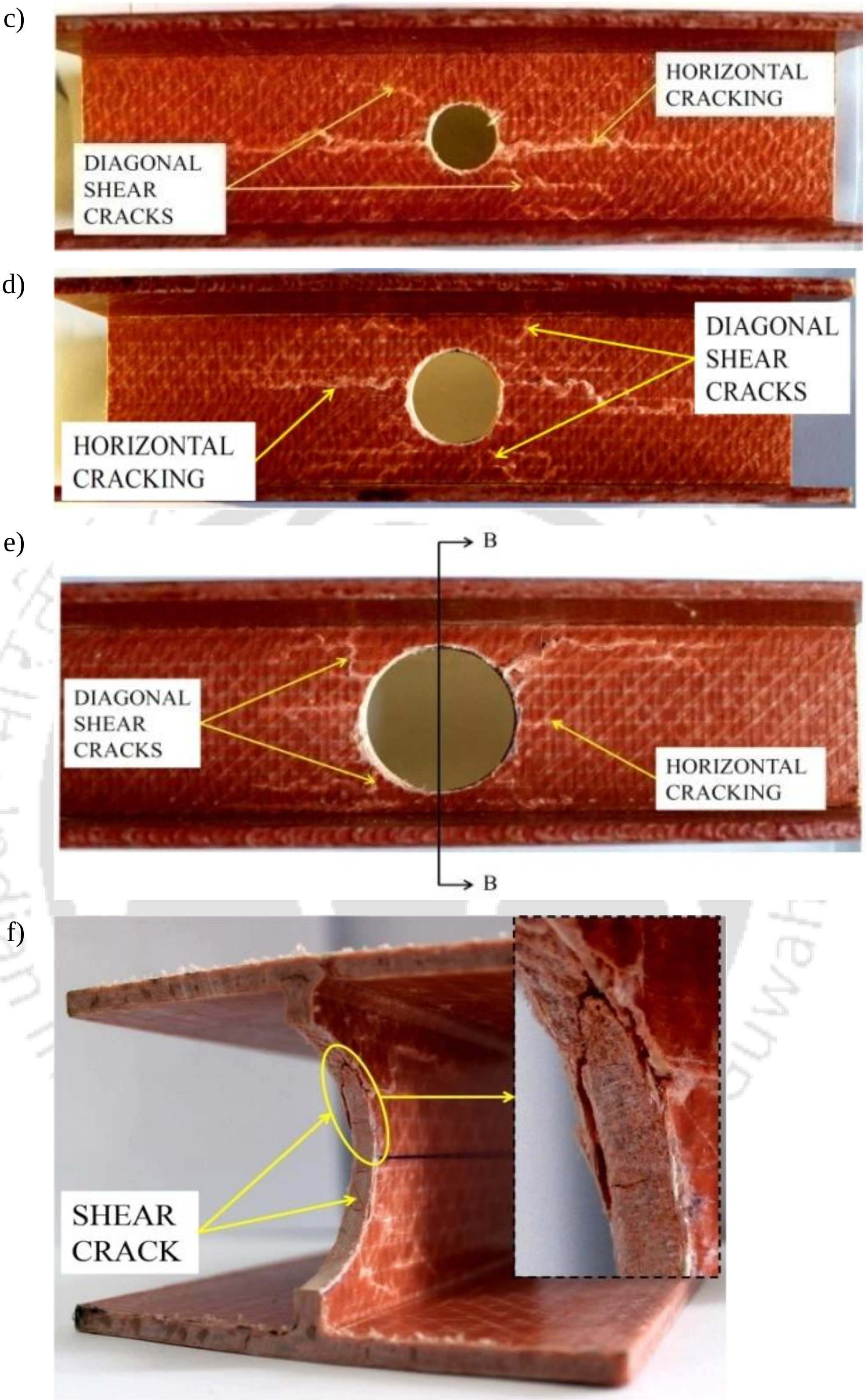

Figure 5.6: Failure modes in series a) ITF–69x100–t5.0–A0.0–N50; b) ITF–69x100–t5.0–A0.2–C–N50; c) ITF–69x100–t5.0–A0.4–C–N50; d) ITF–69x100–t5.0–A0.6–C–N50; e) ITF–69x100–t5.0–A0.8–C–N50; f) through B–B.

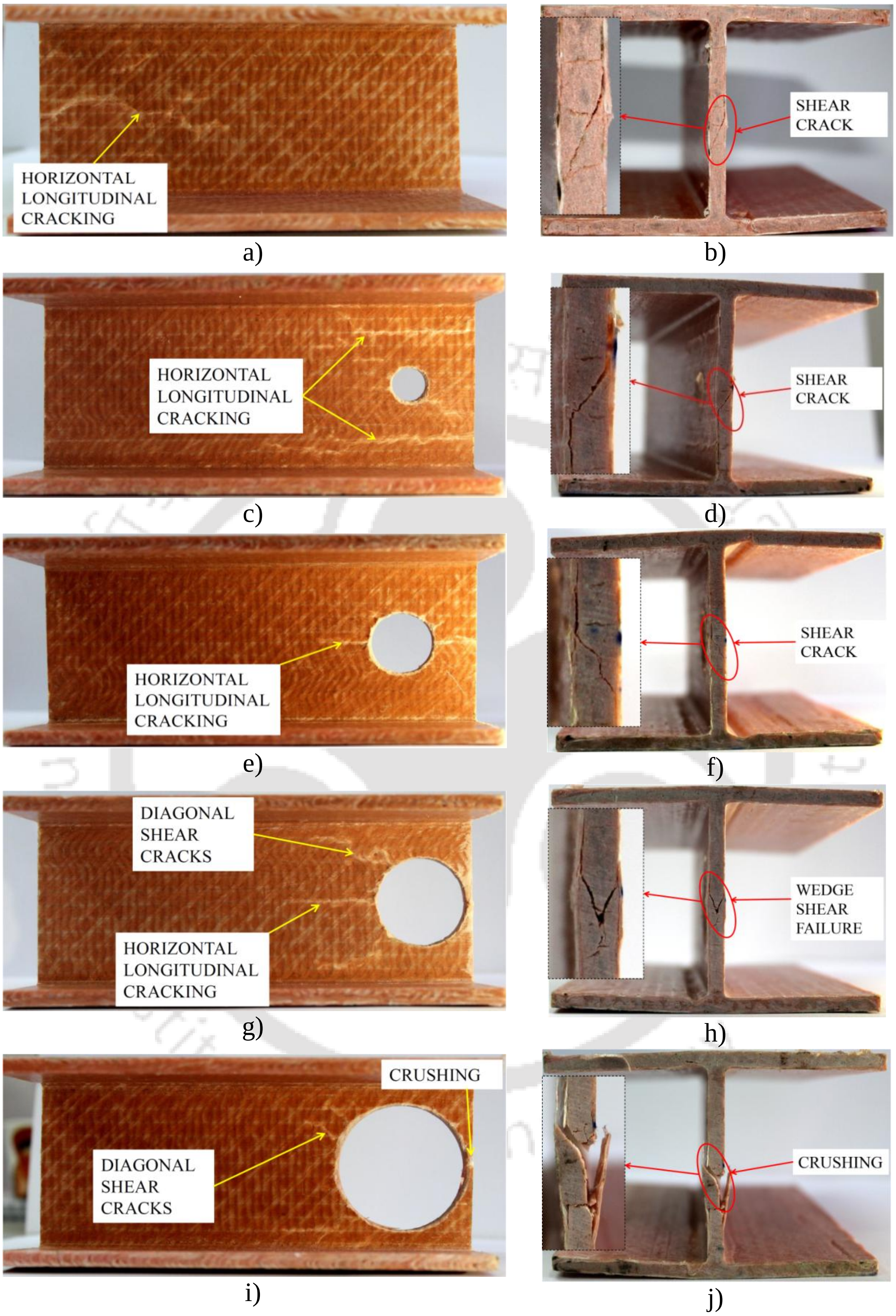

FRONT VIEW **SIDE VIEW**

Figure 5.7: Failure modes in series ETF–69x100–t5.0–A0.0–N50 (a, b); ETF–69x100–t5.0–A0.2–C–N50 (c, d); ETF–69x100–t5.0–A0.4–C–N50 (e, f); ETF–69x100–t5.0–A0.6–C–N50 (g, h); and ETF–69x100–t5.0–A0.8–C–N50 (i, j).

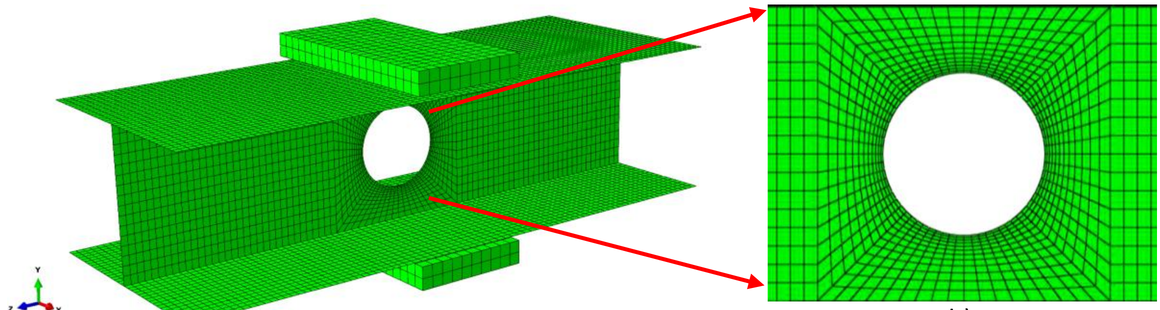

b)

a)

Figure 5.8: a) Finite element model for ITF specimen with perforation size 0.6*h*; and b) corresponding Fan type meshing.

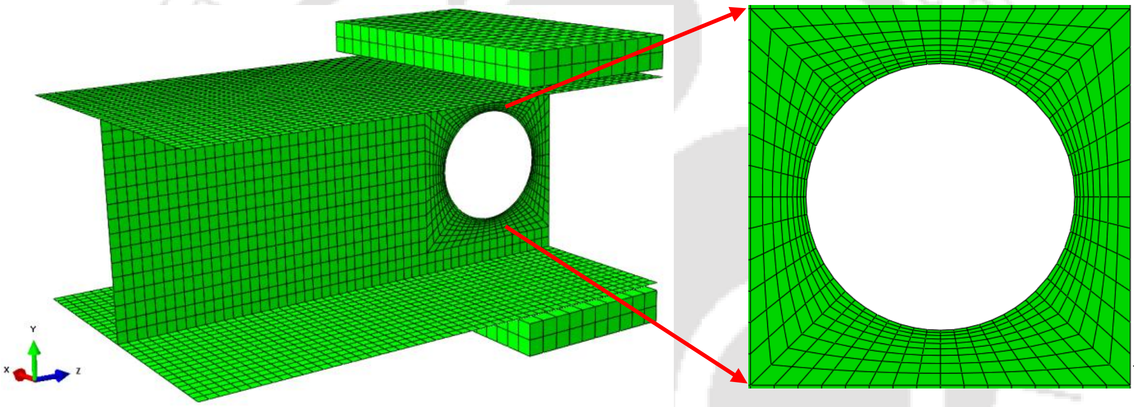

b)

a)

Figure 5.9: a) Finite element model for ETF specimen with perforation size 0.6*h*; and b) corresponding Fan type meshing.

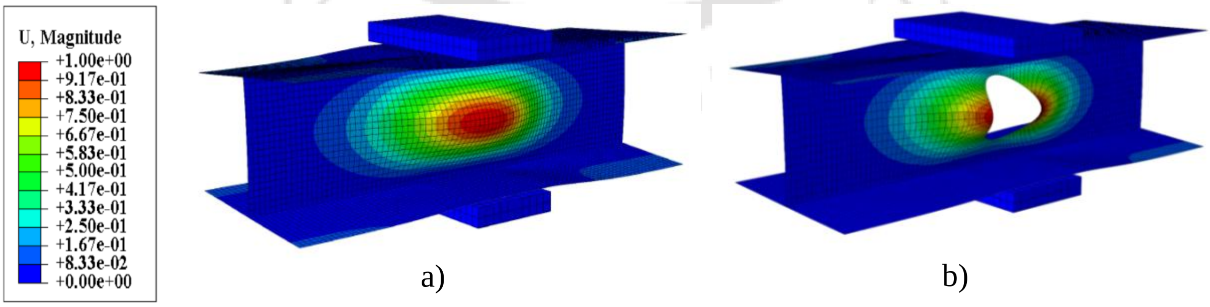

Figure 5.10: First buckling mode shape for ITF specimens a) without perforation; and b) with perforation size 0.6*h*.

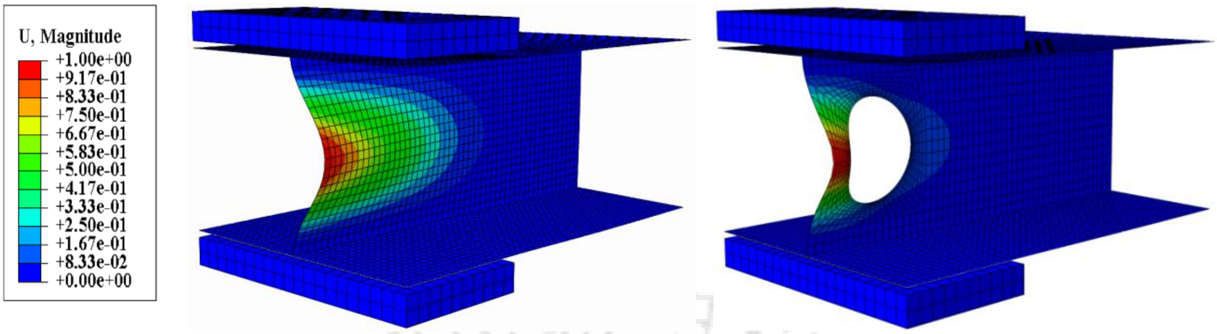

Figure 5.11: First buckling mode shape for ETF specimens a) without perforation; and b) with perforation size 0.6*h*.

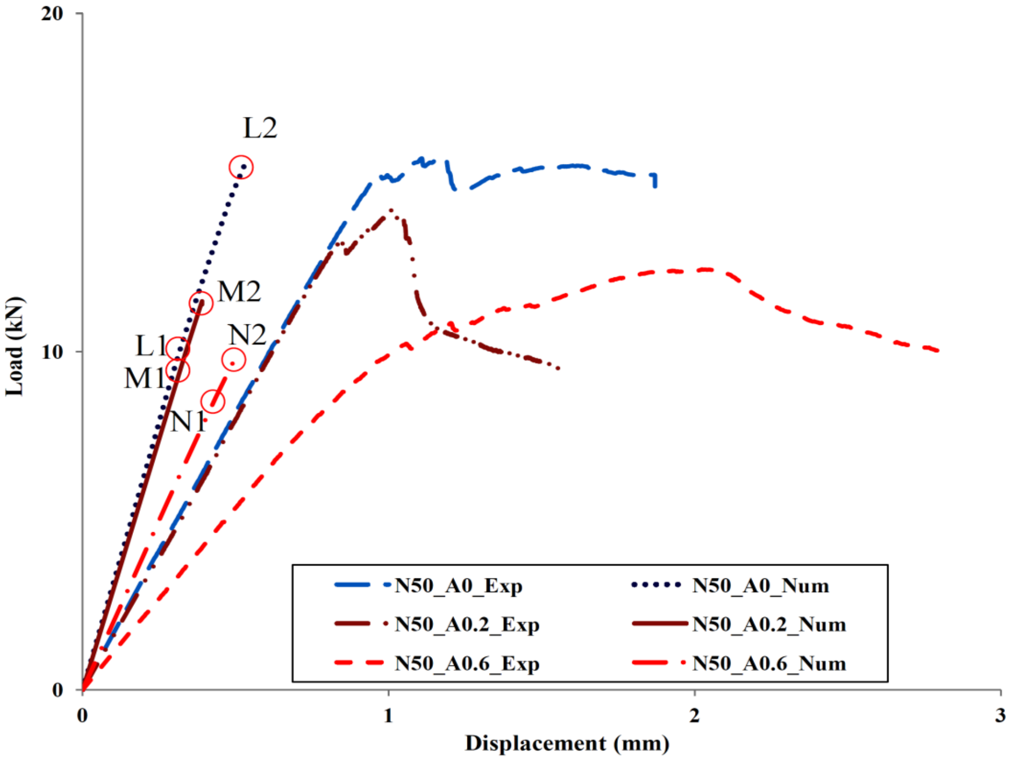

Figure 5.12: Experimental and numerical load-displacement curves for ITF specimens with varying web perforations.

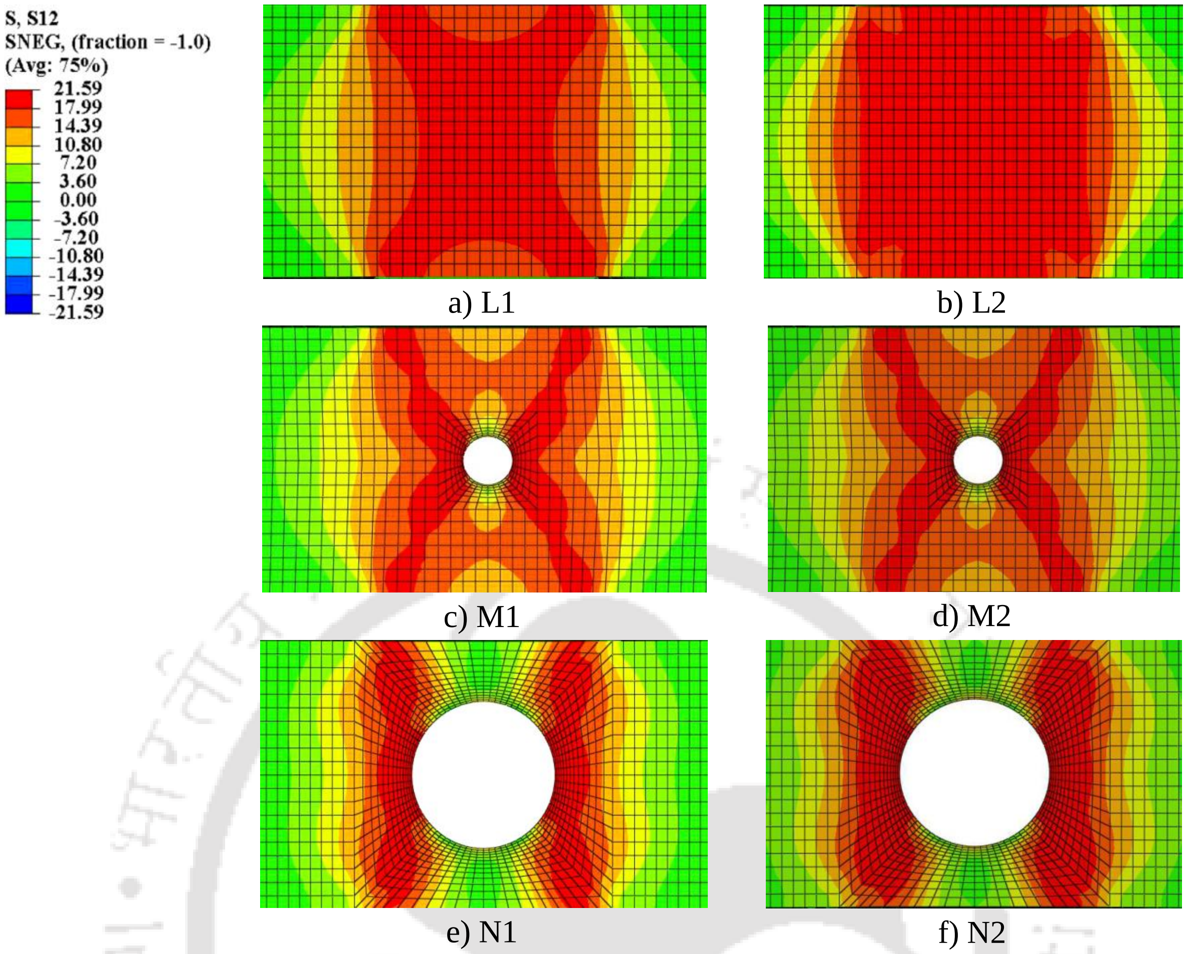

Figure 5.13: Shear stress distributions at different load levels in series ITF–I69–N50–A0.0 (a, b); ITF–I69–N50–A0.2–C (c, d); and c) ITF–I69–N50–A0.6–C (e, f).

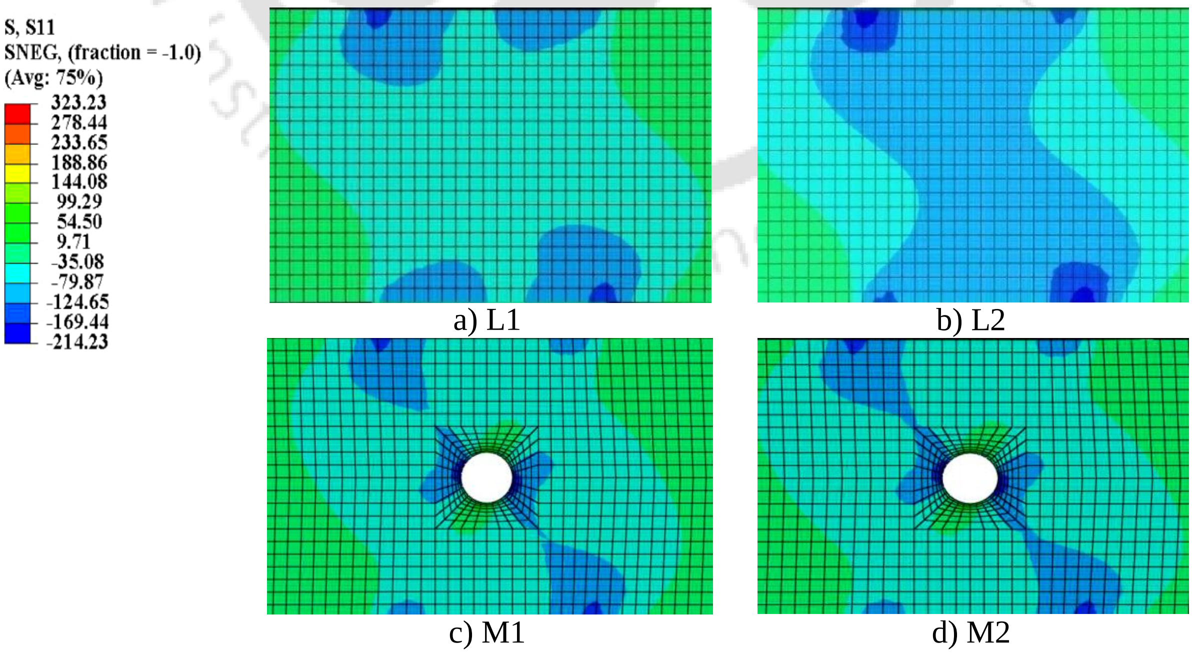

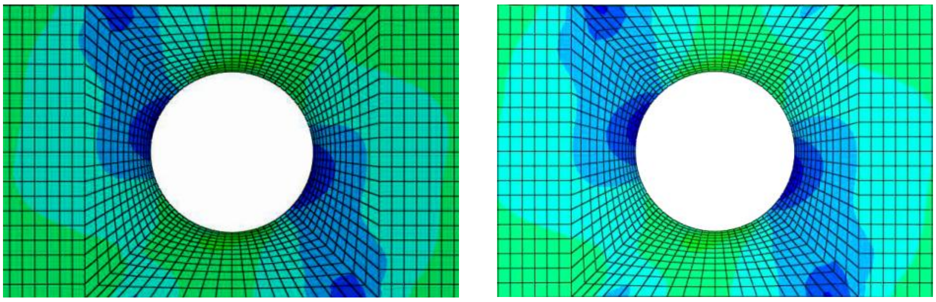

e) N1 f) N2

Figure 5.14: Longitudinal stress distributions at different load levels in series ITF–I69–N50–A0.0 (a, b); ITF–I69–N50–A0.2–C (c, d); and ITF–I69–N50–A0.6–C (e, f).

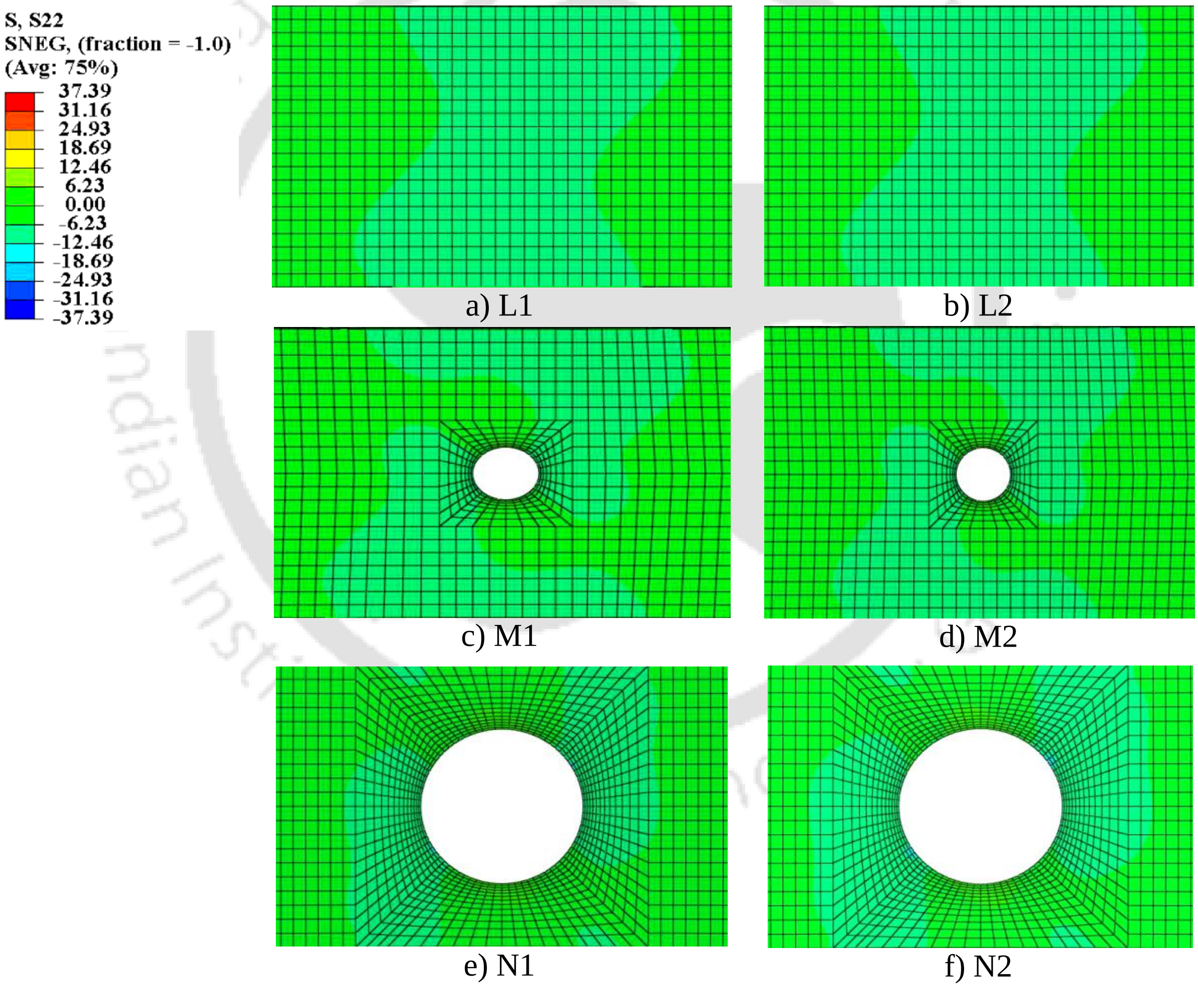

Figure 5.15: Transverse compressive stress distributions at different load levels in series ITF–I69–N50–A0.0 (a, b); ITF–I69–N50–A0.2–C (c, d); and ITF–I69–N50–A0.6–C (e, f).

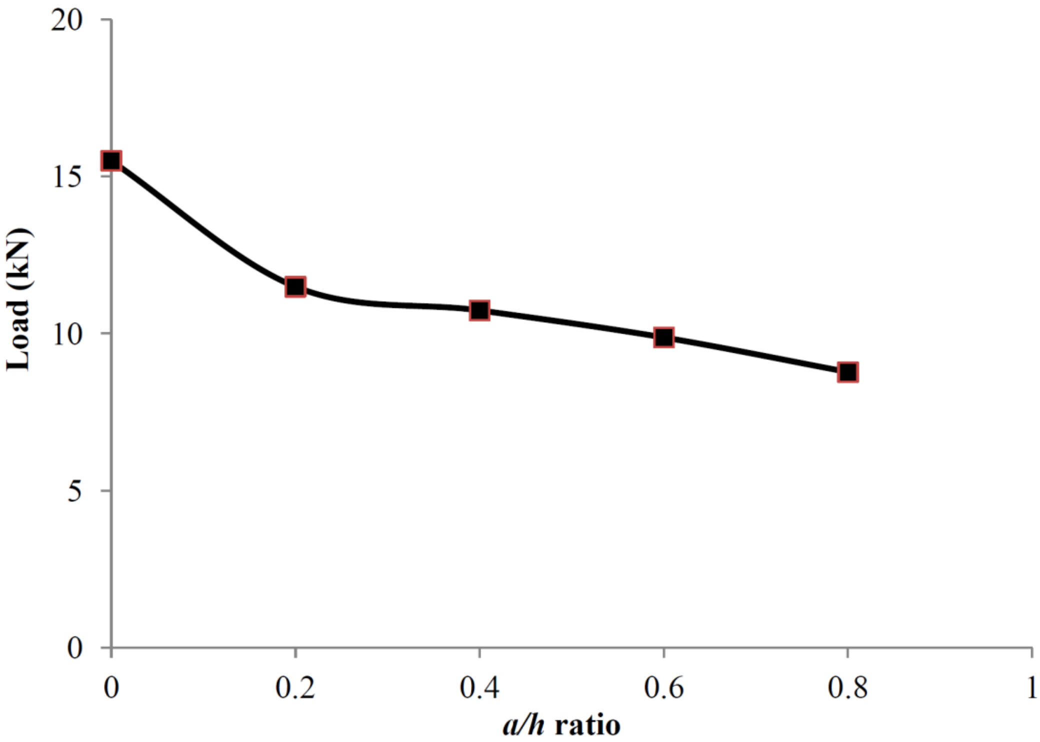

a)

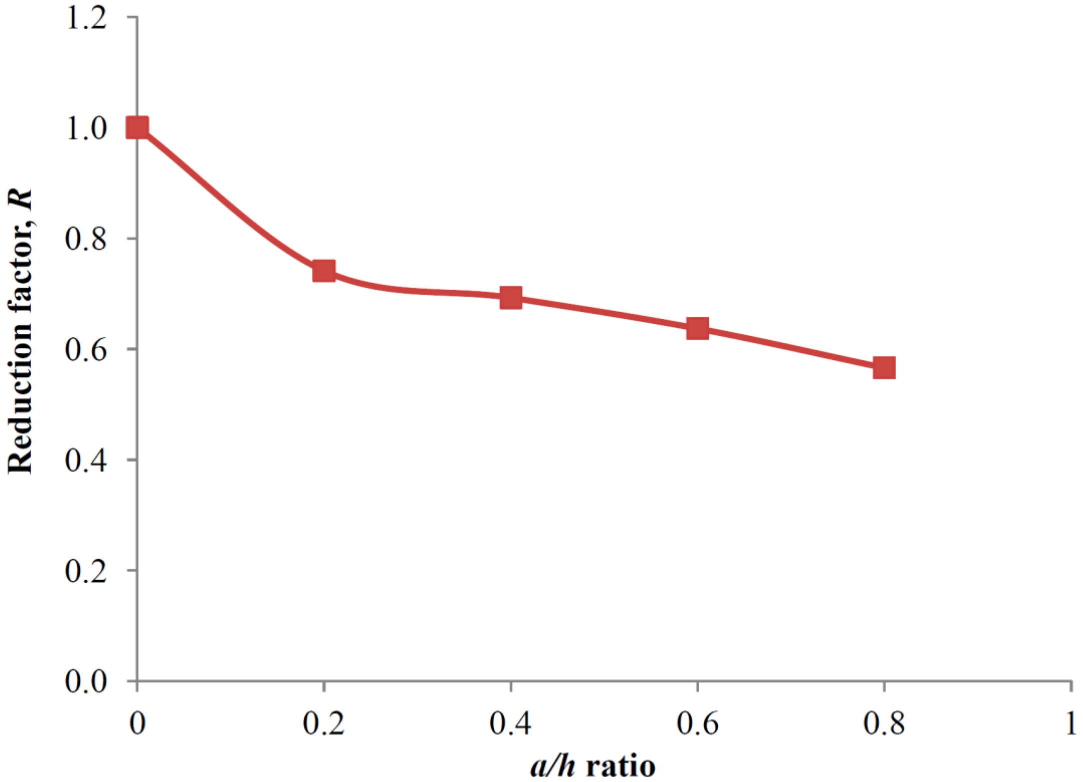

b)

Figure 5.16: Reduction in a) numerical web crippling strength; and b) normalized load with varying web perforation sizes for ITF specimens.

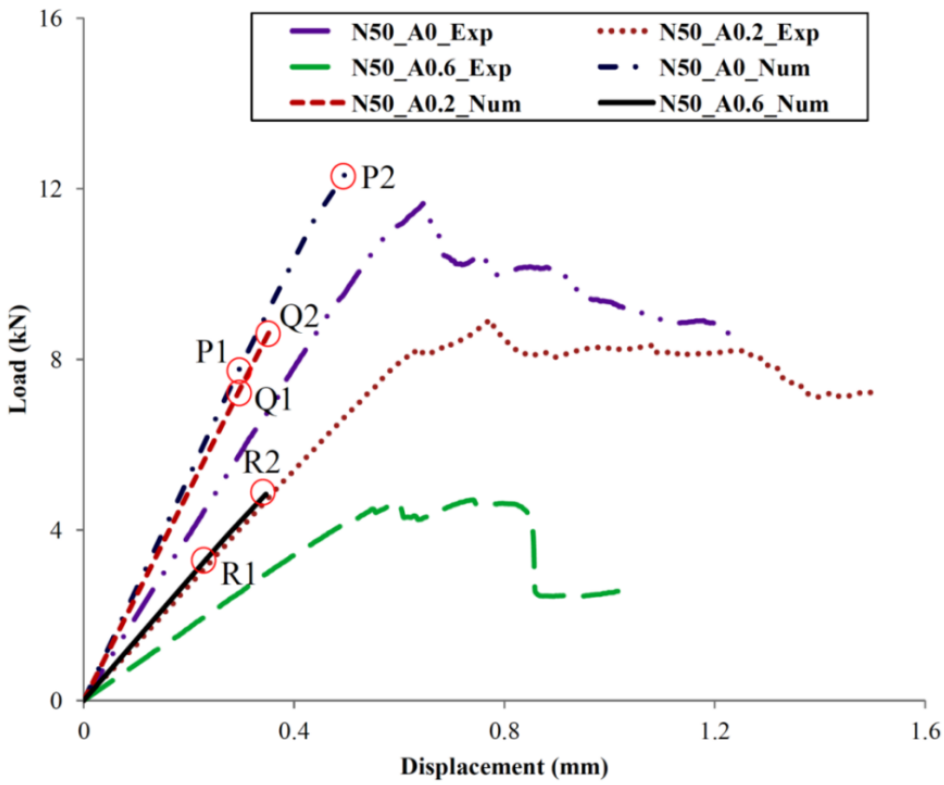

Figure 5.17: Experimental and numerical load-displacement curves for ETF specimens with varying web perforations.

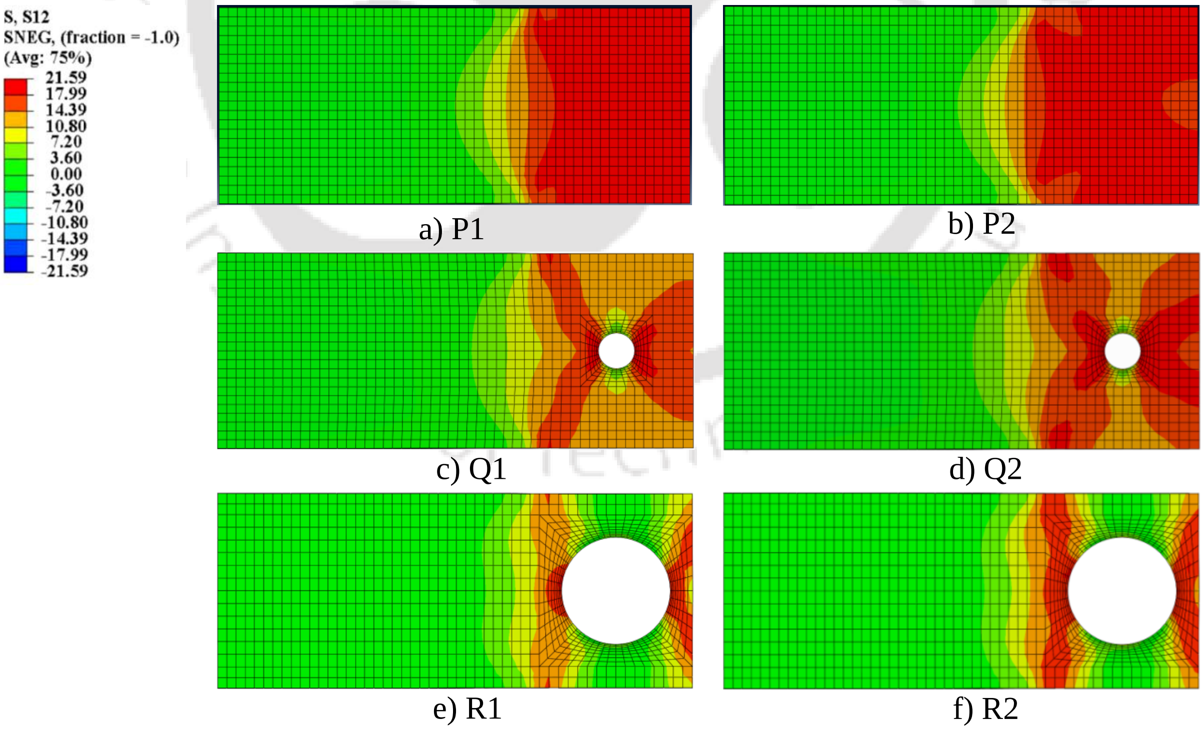

Figure 5.18: Shear stress distributions at different load levels in series ETF–I69–N50–A0.0 (a, b); ETF–I69–N50–A0.2–C (c, d); and c) ETF–I69–N50–A0.6–C (e, f).

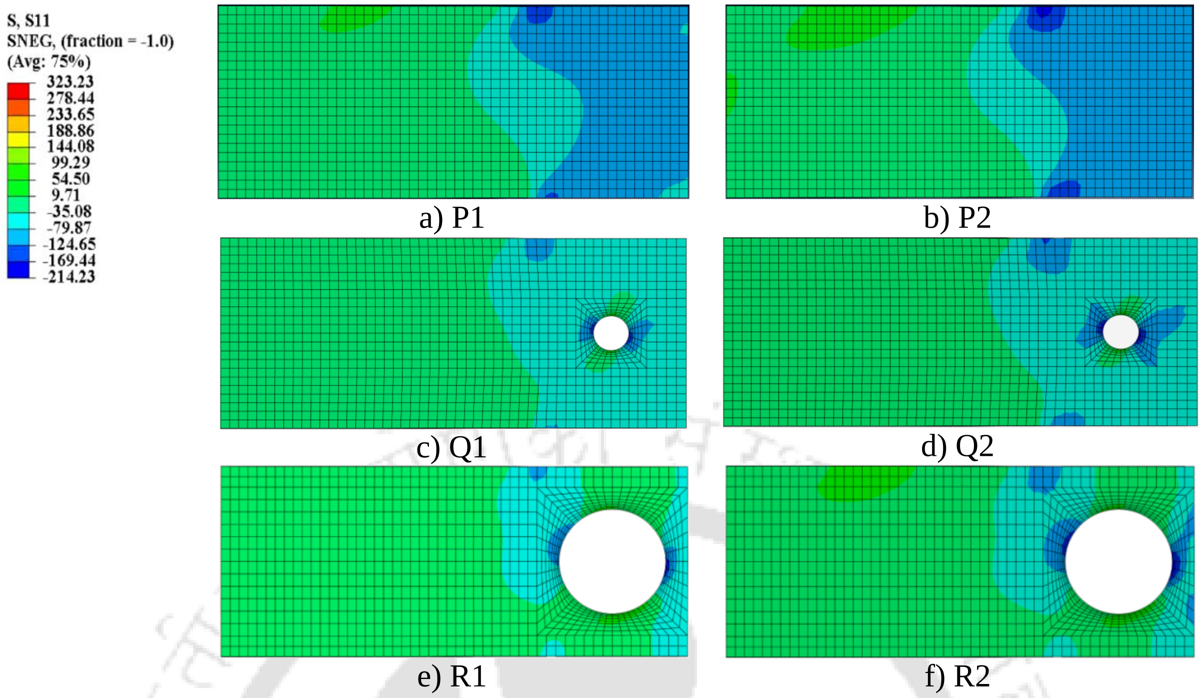

Figure 5.19: Longitudinal stress distributions at different load levels in series ETF–I69–N50–A0.0 (a, b); ETF–I69–N50–A0.2–C (c, d); and ETF–I69–N50–A0.6–C (e, f).

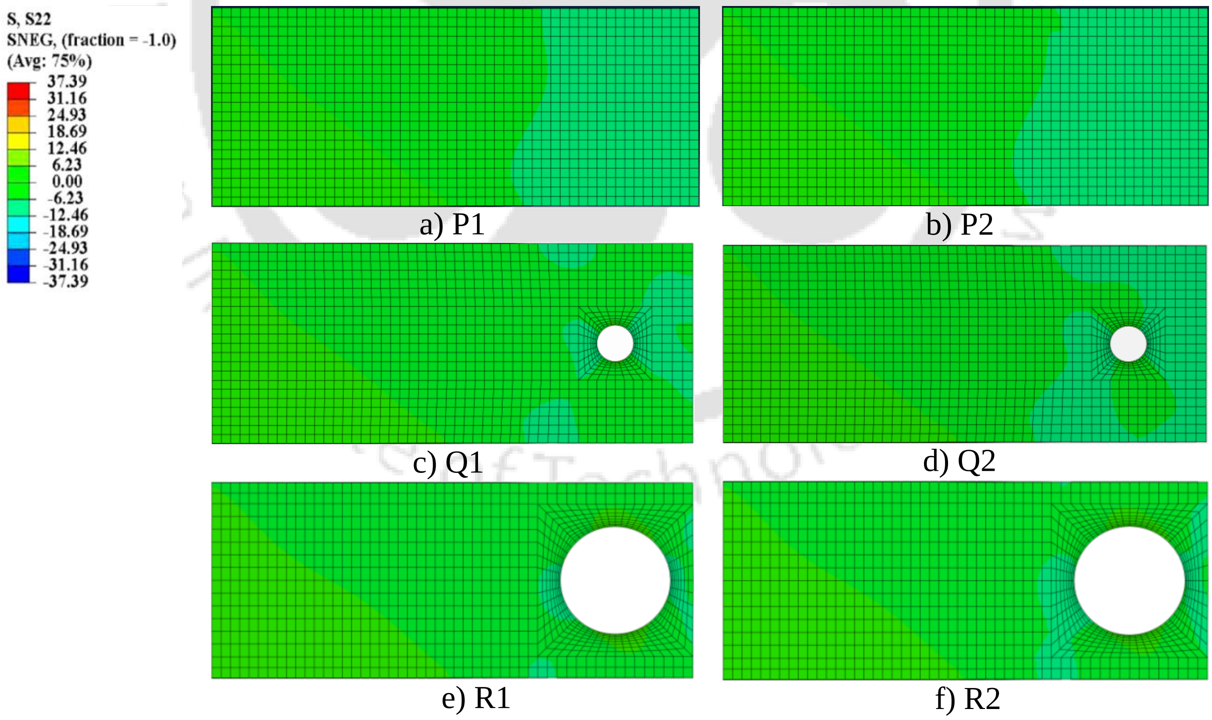

Figure 5.20: Transverse compressive stress distributions at different load levels in series ETF–I69–N50–A0.0 (a, b); ETF–I69–N50–A0.2–C (c, d); and ETF–I69–N50–A0.6–C (e, f).

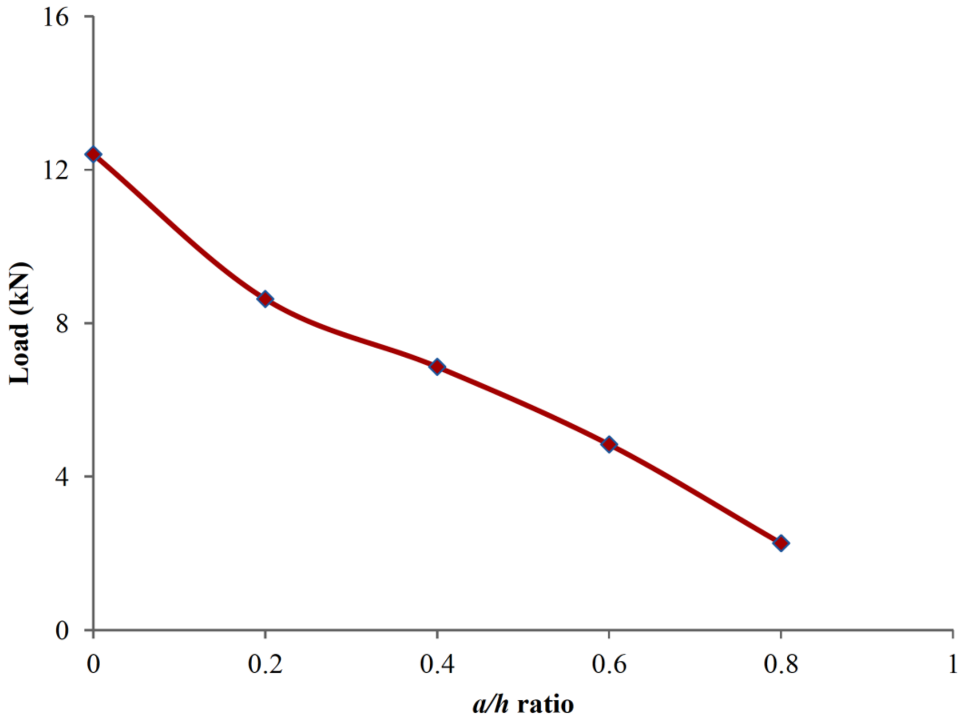

a)

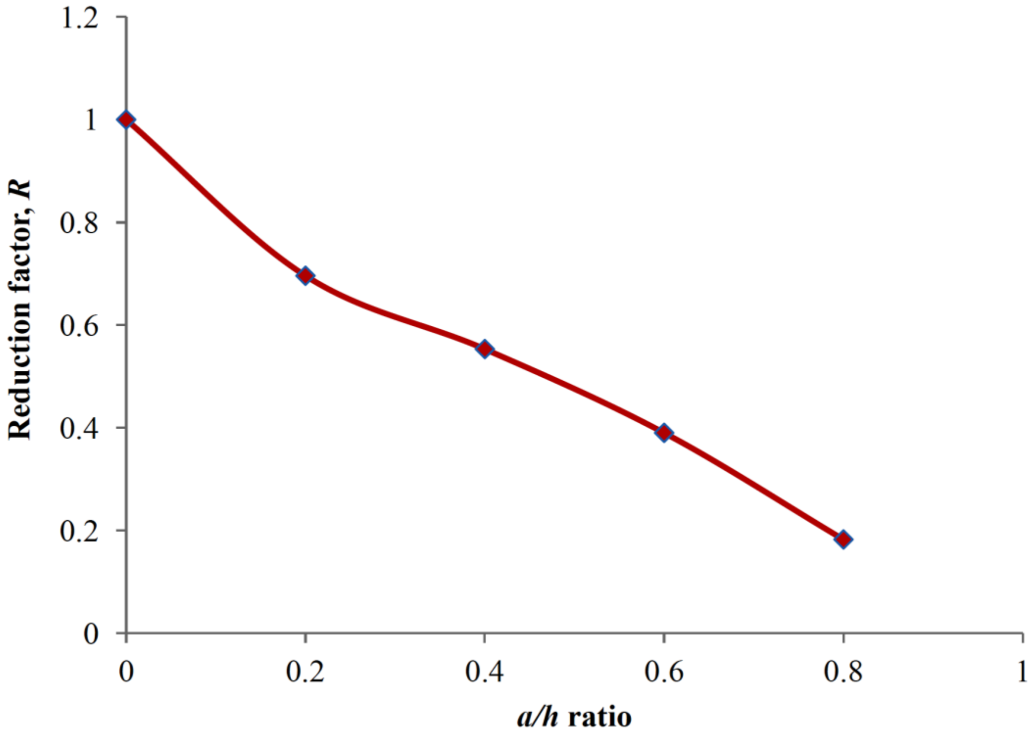

b)

Figure 5.21: Reduction in a) numerical web crippling strength; and b) normalized load with varying web perforation sizes for ETF specimens.

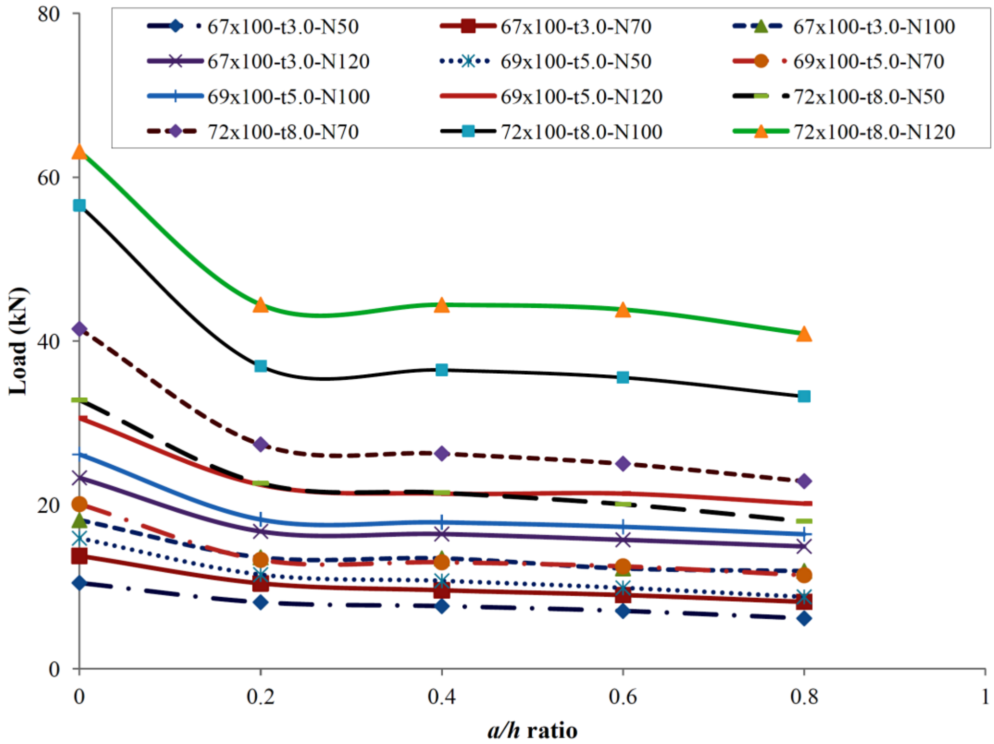

Figure 5.22 (a): Variation in web crippling strengths with *a/h* ratio for centred web perforation for ITF specimens.

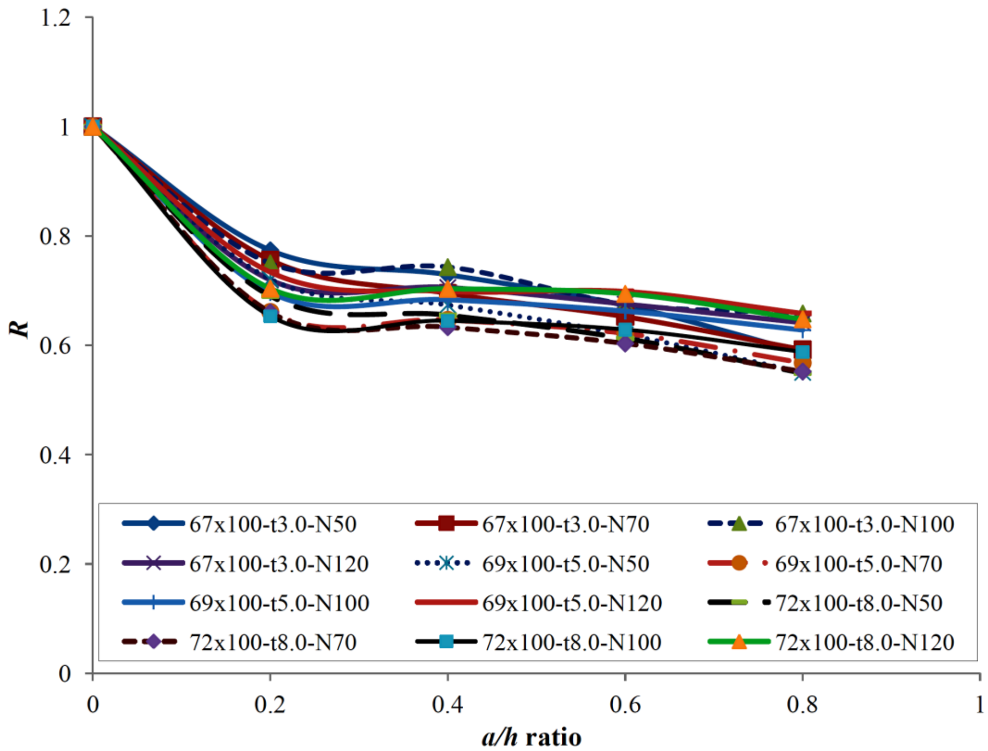

Figure 5.22 (b): Variation in strength reduction factors with *a/h* ratio for centred web perforation for ITF specimens.

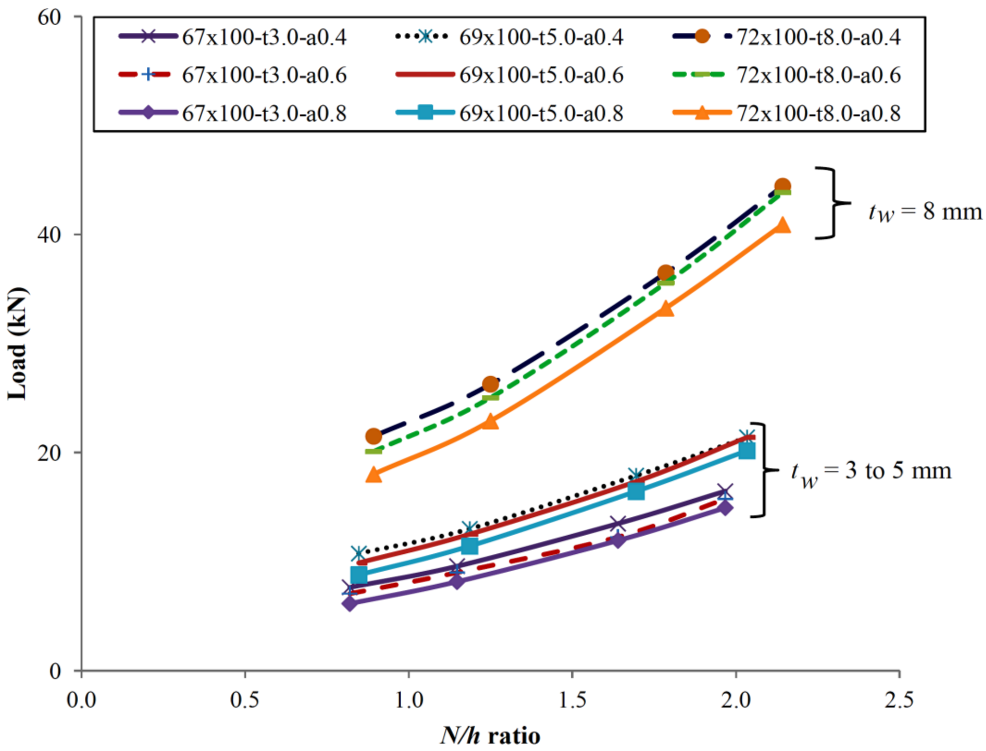

Figure 5.22 (c): Variation in web crippling strengths with *N/h* ratio for centred web perforation for ITF specimens.

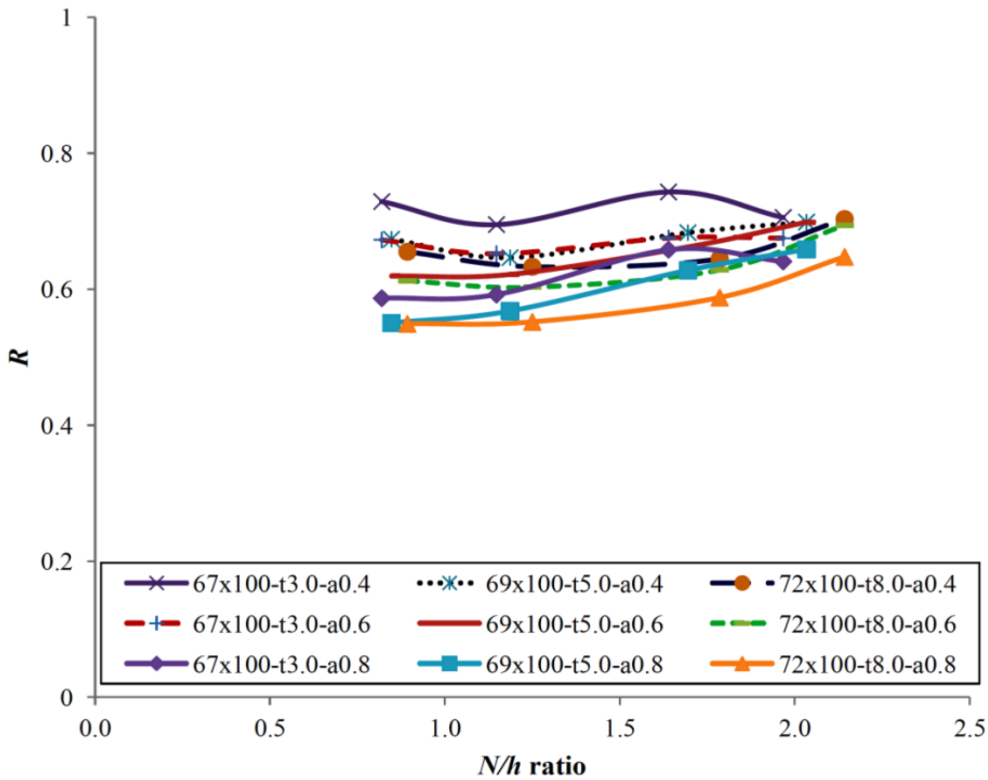

Figure 5.22 (d): Variation in strength reduction factors with *N/h* ratio for centred web perforation for ITF specimens.

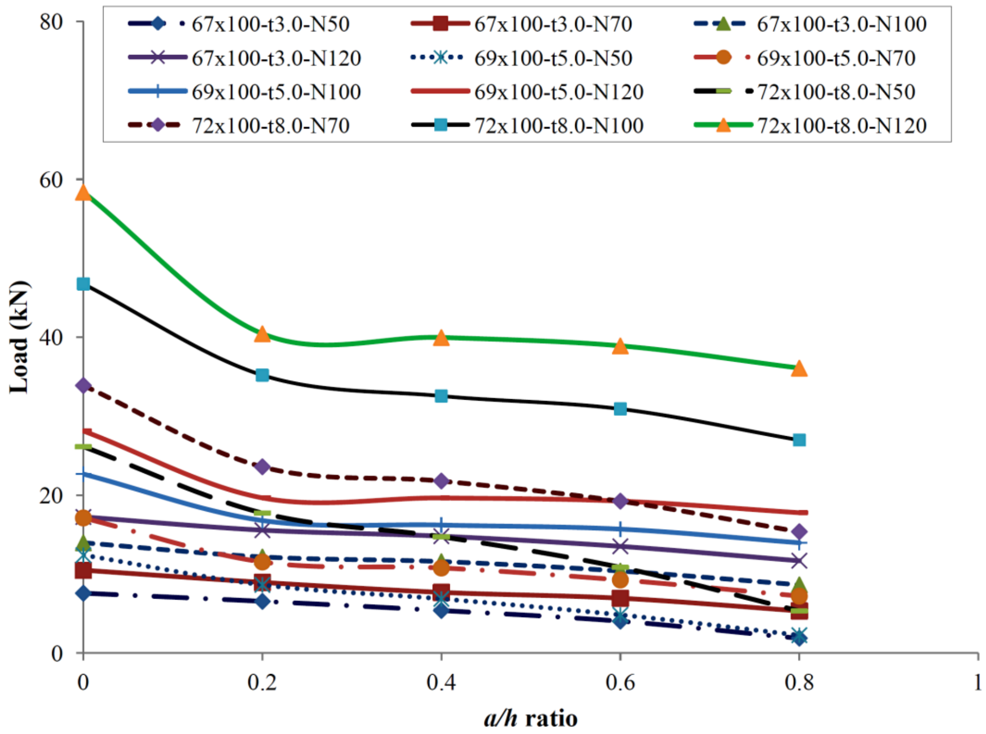

Figure 5.23 (a): Variation in web crippling strengths with *a/h* ratio for centred web perforation for ETF specimens.

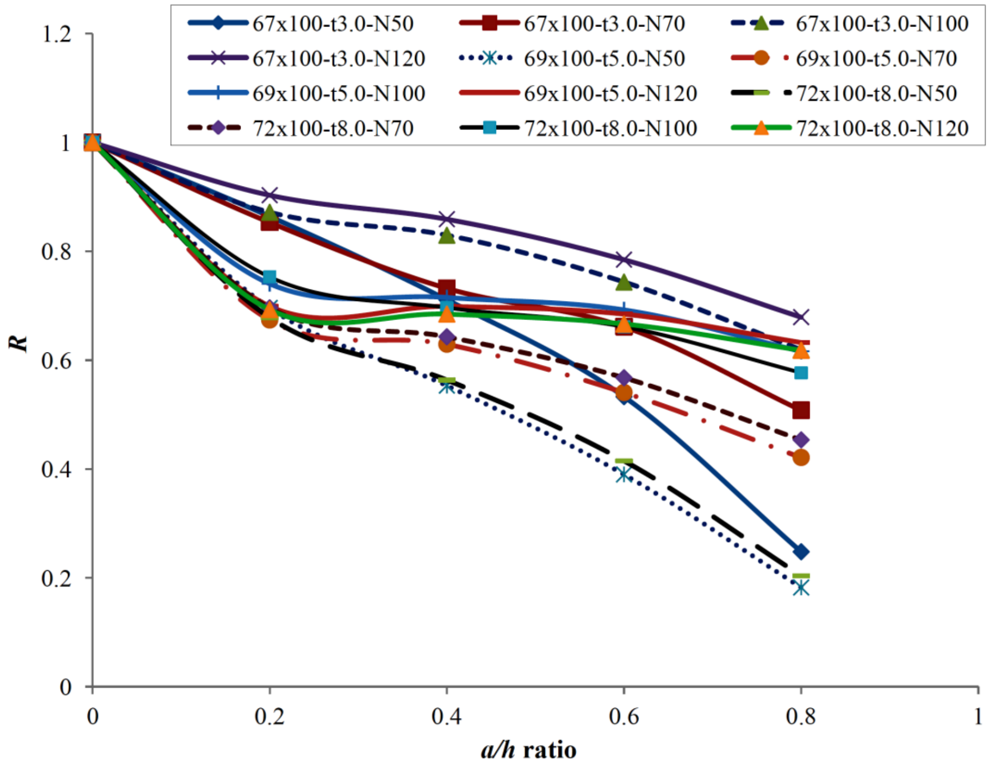

Figure 5.23 (b): Variation in strength reduction factors with *a/h* ratio for centred web perforation for ETF specimens.

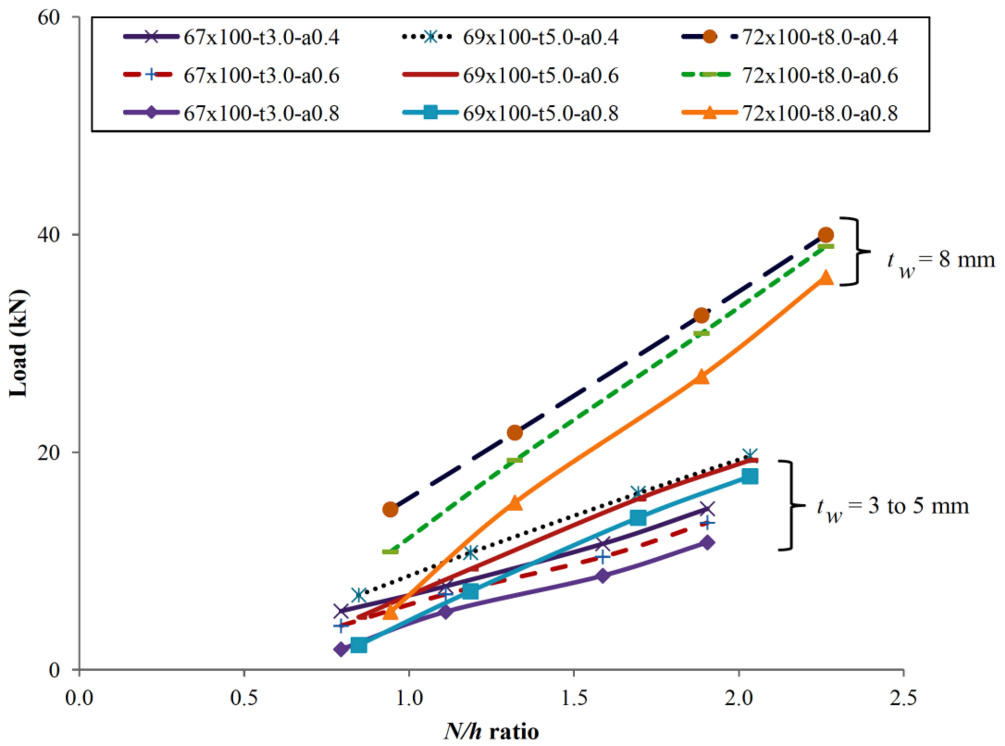

Figure 5.23 (c): Variation in web crippling strengths with *N/h* ratio for centred web perforation for ETF specimens.

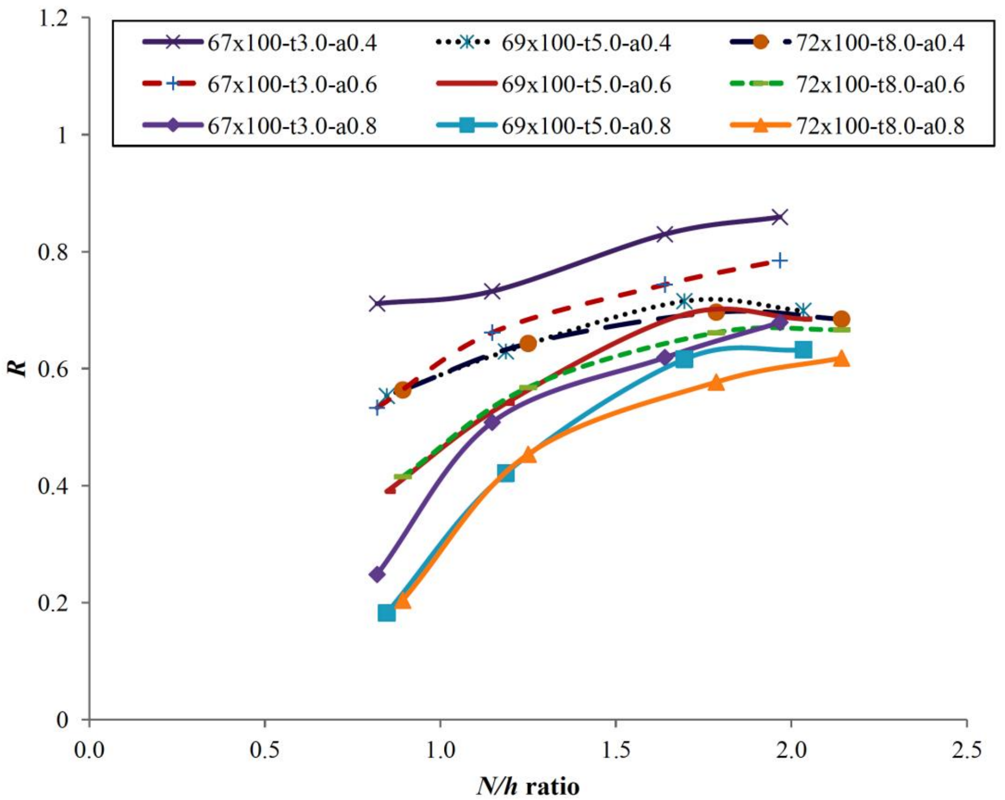

Figure 5.23 (d): Variation in strength reduction factors with *N/h* ratio for centred web perforation for ETF specimens.

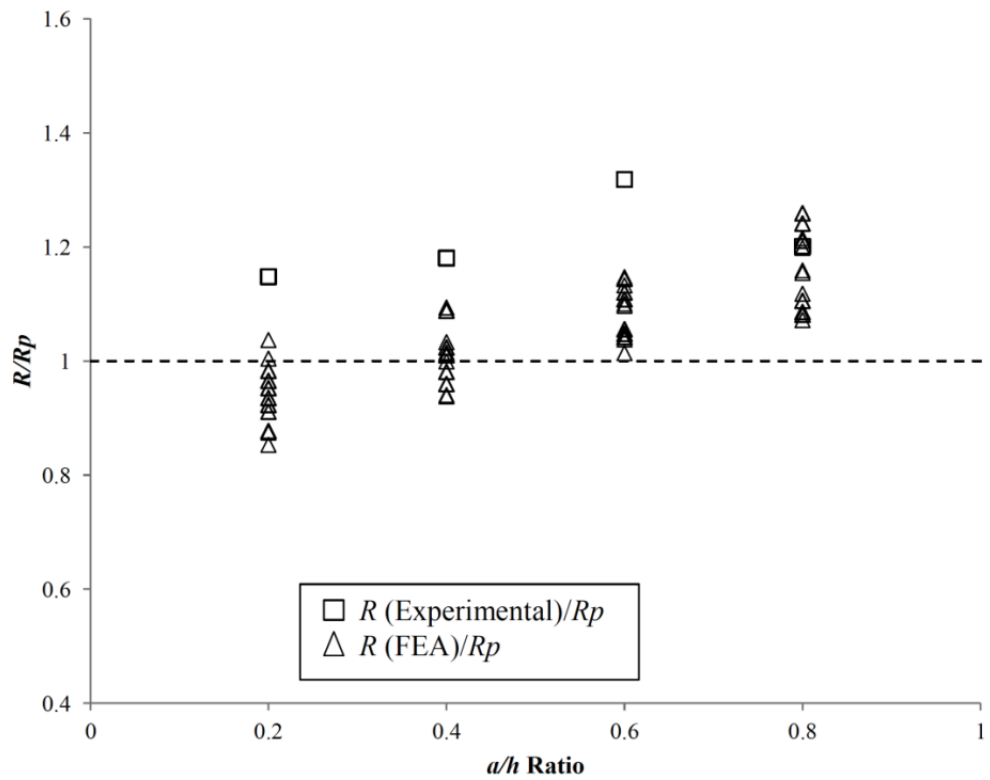

Figure 5.24 (a): Comparison of strength reduction factors with respect to *a/h* ratio for ITF specimens.

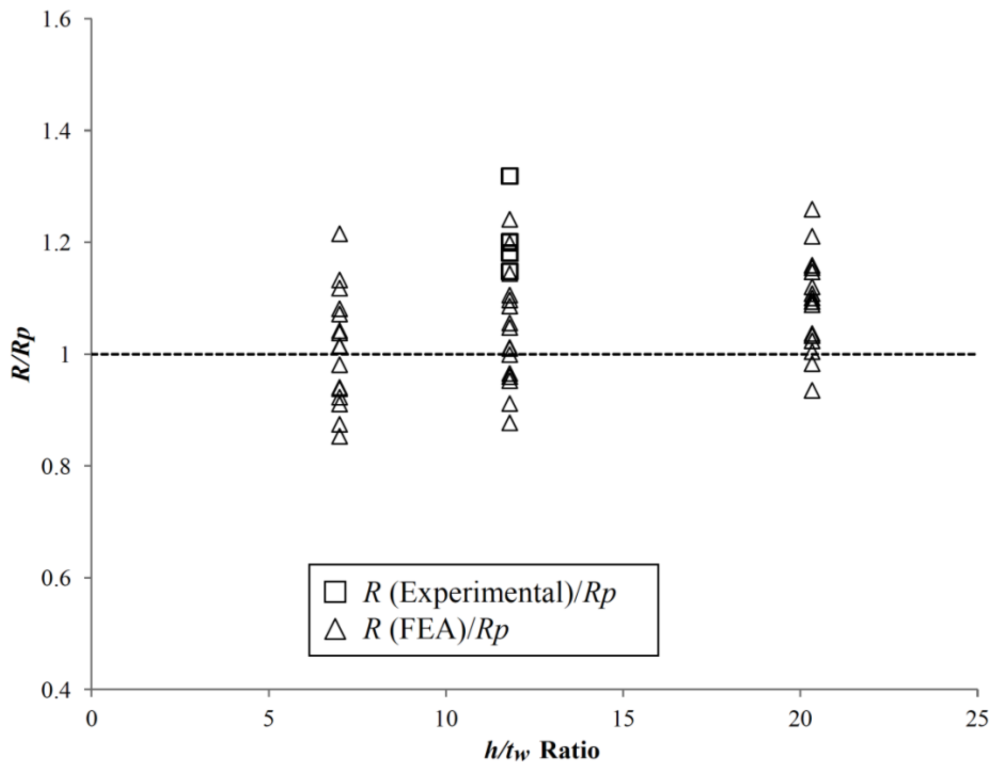

Figure 5.24 (b): Comparison of strength reduction factors with respect to h/t_w ratio for ITF specimens.

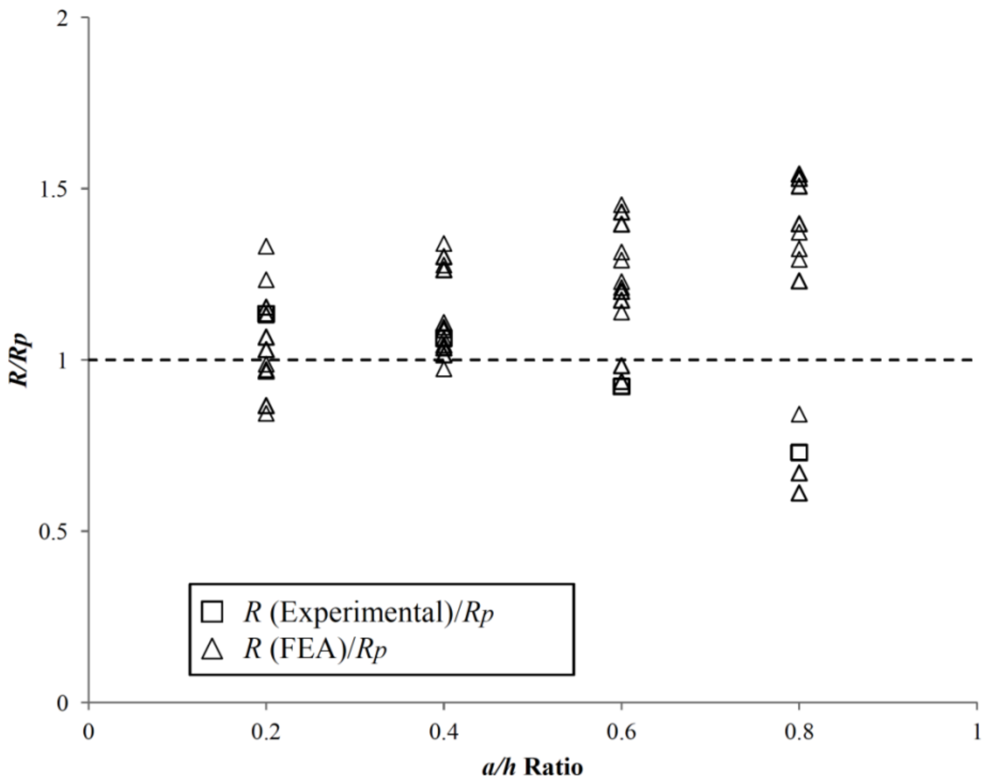

Figure 5.25 (a): Comparison of strength reduction factors with respect to *a/h* ratio for ETF specimens.

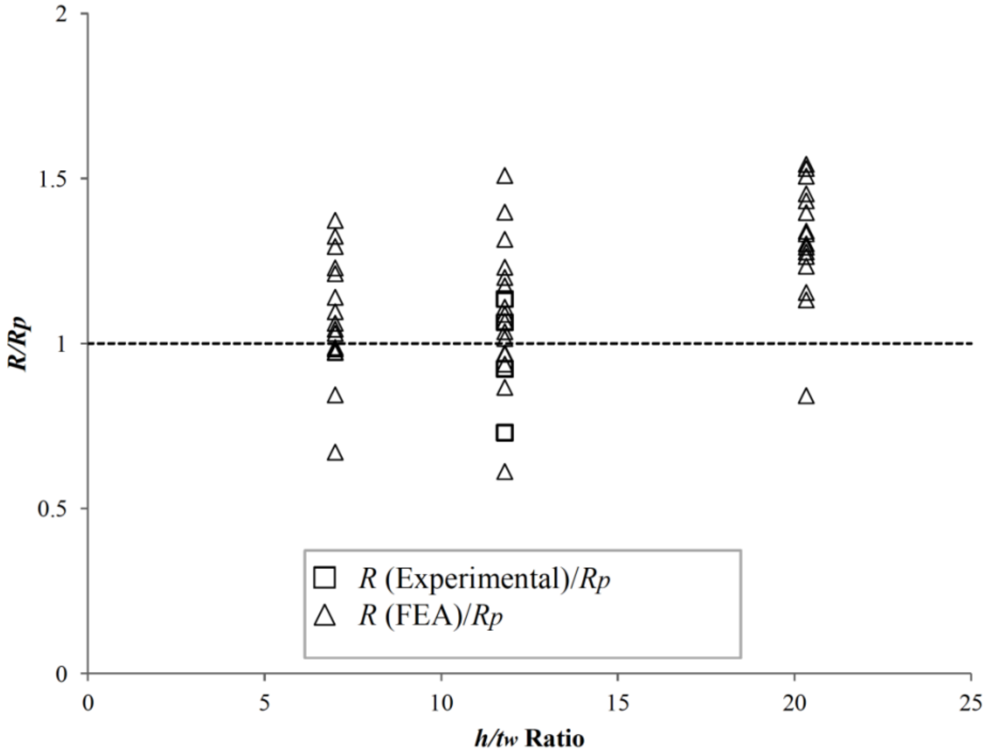

Figure 5.25 (b): Comparison of strength reduction factors with respect to h/t_w ratio for ETF specimens.

This page is intentionally left blank.

CHAPTER 6

CONCLUSIONS AND SUGGESTIONS FOR FURTHER WORK

6.1 INTRODUCTION

Over the last few decades, numerous braced framed structures and truss structures have been constructed using the GFRP members due to various advantages over the traditional steel and concrete materials such as high strength to weight ratio, durability, quick and easy installation process. However, due to the lower mechanical properties in the transverse direction of the GFRP profiles than the pultruded direction, these profile sections often encounter web crippling failure when loaded in the transverse direction (e.g. Borowicz and Bank, 2011; Fernandes *et al*., 2015; Wu and Bai, 2014; Chen and Wang, 2015; Wu *et al.*, 2019). However, very limited research is available on the web crippling behaviour of GFRP profiles and in addition to that the effect of web perforations on the web crippling behaviour has been rarely reported. Hence, in the present thesis, an attempt has been made to systematically investigate the web crippling behaviour of GFRP WF-sections with and without perforations. The study also includes the effect of varying perforation diameters on the web crippling behaviour of GFRP profiles. In this chapter, key conclusions based on the current investigation are summarized along with suggestions for potential extension of the present work.

6.2 CONCLUSIONS

6.2.1 Mechanical properties and behaviour of GFRP profiles

An investigation on the mechanical properties and behaviour of GFRP profiles of various shapes and sizes is performed. The experimental investigations mainly comprises tensile, compression, interlaminar shear and 10° *off-axis* tensile tests performed on coupons obtained from flanges and webs of the profiles. Based on the data obtained, design stresses and moduli values are obtained considering four design guidelines, namely, the Italian guideline (2007), ASCE (2010), EUROCOMP (1996) and EU's CEN Technical Committee 250 (2016). Based on the present investigation, the following conclusions can be obtained:

1) From burn-off tests, it is observed that the manufacturer have used mainly three forms of E-glass fibre architectures, namely, combined mat, unidirectional roving and continuous strand mat, where, the unidirectional roving layers are sandwiched between adjacent layers of combined mats and continuous strand mats. The average fibre content in each profile is found to be around 71.6%.

2) From the hardness tests, the HR numbers of the profiles have been found to be in the range of 98–104 in *L-scale*.

3) Based on SEM image analysis, it is found that the H1 profile exhibits a continuous defect at the web-flange junction which continues throughout the length of the profile, whereas, discontinues voids can be seen in other profiles.

4) All tensile specimens have exhibited linear elastic behaviour up to failure. In case of longitudinal compression coupons, the behaviour is elastic but with a combination of linear and nonlinear patterns.

5) Differences in mean compression and tensile values obtained from the flanges and webs of the profiles are found to be in the range of 0.7–33.7%.

6) Considerable variations in the design stresses and moduli values are observed which are due to the differences in the partial safety factors and conversion factors considered in the various guidelines. As for example, the longitudinal tensile design stress values for C1, C3 and H1 profiles obtained according to ASCE (2010) exceed Ascione *et al*. (2016) by almost 73%, whereas, Italian guideline (2007) and EUROCOMP (1996) differ Ascione *et al*. (2016) by 23.1 and 51.5%, respectively.

6.2.2 Web crippling behaviour of unperforated GFRP wide flange–section profiles

Both experimental and numerical investigations are performed to study the web crippling behaviour of GFRP wide flange (WF) profile without perforation. The experimental investigations mainly include full scale web crippling experiments performed on 53 specimens without perforation under ETF and ITF loading configurations. The following conclusions can be drawn based on the investigation.

1) For specimens with ITF loading, failure mainly occurred at the web with longitudinal cracking or material wrinkling in the vicinity of the bearing plates. No specimen showed out of plane web deformation or web buckling. Shear failure could be observed in the web which propagated towards the end and web-flange junction of the specimens.

2) For specimens with ETF loading conditions, failure occurred suddenly with a clearly audible cracking sound on the onset of failure. All ETF specimens showed steep sloped "shear-wedge" at their cross sections that extended from end to interior.

3) All specimens exhibited linear behaviour up to a peak point which was followed by a sudden fall in the load–displacement response. In some specimens, this peak point in the load–displacement curve can be linked to the initial web-flange junction failure. The continuation of the load–displacement curve after the initial peak load demonstrates that the web continued to carry the load upto a point where the ultimate failure would occur by crushing or shearing of the web.

4) Change in loading condition greatly influences the ultimate load of the specimens. Shifting the loading condition from ETF to ITF in case of specimens with bearing length 25 mm and thickness 8 mm (series "N25–t08") increased the ultimate load by +68.9%.

5) Bearing lengths are found to have direct influence on the web crippling strength and behavior of GFRP WF–sections. It is evident that for a particular loading condition and plate thickness, specimens tested with the largest bearing length exhibited the highest load carrying capacity while those with the shortest bearing length presented the lowest load carrying capacity.

6) Increasing plate thickness from 8 mm to 10 mm (or t_{plate}/t_w = 1.6 to 2.0) did not considerably change the ultimate loads and for almost all cases it was insignificant.

7) FE models could simulate the experimental load–displacement curves of the GFRP specimens with satisfactory accuracy. However, compared to their numerical counterparts, the experimental load–displacement curves are found to have lower elastic stiffness.

8) From the experimental and numerical results, it is clear that shear stresses played the most significant part in failure initiation than the longitudinal and transverse stresses in the GFRP specimens.

9) Based on the combined test data from the current experimental campaign and data from literature, new design equations have been developed based on Eurocode3 (2006), NAS (2007), Fernandes *et al*. (2015) and Wu *et al*. (2019), for both ETF and ITF loading configurations.

6.2.3 Web crippling behaviour of web perforated GFRP wide flange–section profiles

The effect of perforation diameter on web crippling behaviour of perforated GFRP WF–section profile has been investigated by utilising a GFRP WF–section profile. The experimental study includes full scale web crippling experiments performed on 29 specimens with and without web perforations under ITF and ETF loading configurations. Numerical investigations have also been carried out using the finite element (FE) program Abaqus (2009). Main conclusions are presented below.

1) In case of ITF loading, specimens without perforation showed multiple longitudinal cracks under the loading plates near the web-flange junction as well as at the mid height of the web. Specimens with centred web perforation exhibited longitudinal and shear cracks around the perforation which propagated diagonally towards the web and web-flange junction, respectively.

2) For specimens with ETF loading, specimens without perforation showed multiple longitudinal cracks under the loading plates near the web-flange junction as well as at the mid height of the web. For specimens with centred web perforation, failure started with the initiation of cracks around the perforations due to the development of local stress concentration which propagated to the web.

3) All web crippling specimens under ITF and ETF loading conditions exhibited linear elastic behaviour up to the initial failure point after which a sudden drop was observed in the load–displacement curves. The FE models could simulate the experimental load–displacement curves of the GFRP specimens with satisfactory accuracy.

4) Significant decrease in web crippling strength could be observed due to web perforations. Compared to the intact specimens, under ITF loading, the average web crippling strength for

perforated specimens with web perforation sizes 0.2*h*, 0.4*h*, 0.6*h and* 0.8*h* was reduced by 14.7%, 22.2%, 24.2% and 41.1%, respectively.

5) In case of ETF loading, compared to the intact specimens, the average web crippling strength for perforated specimens with web perforation sizes 0.2*h*, 0.4*h*, 0.6*h and* 0.8*h* was reduced by 26.0%, 43.2%, 61.6% and 78.3%, respectively.

6) Based on the parametric study, reliable web crippling strength reduction factors are proposed for GFRP WF–section under ITF and ETF loading configurations. It was observed that the web crippling strength reduction factors are influenced by both *a/h* and *N/h* ratios.

6.3 SUGGESTION FOR FUTURE WORK

In this thesis, a comprehensive study considering both experimental and numerical investigations is performed on the web crippling behaviour of GFRP WF–section profiles with and without perforation. The study identifies the failure modes, load displacement patterns and ultimate loads of the GFRP profiles and has proposed design expressions for web crippling of GFRP WF section profiles with and without perforation. Although it appears that a considerable amount of work (large number of experimental studies and close to 120 FE models) has been undertaken on the web crippling of GFRP profiles, significant work can be identified and can be counted to develop the understanding of these behaviour. Some of the future extensions can be summarized herein.

6.3.1 Loading conditions

In the current study, the web crippling study is limited to two loading configurations viz., ETF and ITF loadings. Therefore, the present study can be extended by considering other loading configurations such as end-one-flange (EOF), interior-one-flange (IOF), interior-ground (IG) and end-ground (EG). In addition to the above loadings, effect of other loadings such as impact and blast on the web crippling behaviour may also be studied.

6.3.2 Offset web perforation

The current study only investigates the web crippling behaviour of GFRP profiles with centred web perforation. However, the effect of offset web perforation on the web crippling can also be studied including the effect of distance from the bearing plate edge and changing diameters.

6.3.2 Types of perforation

In the present study, only the effect of circular web perforation is investigated. Therefore, the investigation can be expanded to include various perforation shapes such as elliptical, rectangular, oval, square, rhombus etc. In addition, effect of multiple perforations can also be studied to examine the interaction effects.

6.3.4 Use of stiffeners

The web crippling strength of the GFRP members are reduced owing to the presence of perforations. However, in order to compensate the reduction in strength of the members, the use of stiffening elements (around the perforations) can be investigated. The study can be carried out using different types of stiffening elements and different cross sectional dimensions of the stiffeners.

6.4 OTHER SUGGESTIONS

In addition to the suggested topics, the current research work can also be extended to incorporate the following topics.

1) Perforation effects on other GFRP sections such as open section types e.g. channel sections
2) Perforation effects on closed section shapes such as rectangular hollow or square hollow sections.

REFERENCES

ABAQUS, (2009). User's manual and theory manual', Hibbitt, Karlsson and Sorensen. *Inc., Providence, RI, USA.*

AISI (2007). North American specification for the design of cold-formed steel structural members. AISI S100-2007, *American Iron and Steel Institute*, Washington.

ASCE 8-02 (2002). Specification for the design of cold-formed stainless steel Structural members. *American Society of Civil Engineers*. New York.

AS 4100-1998. Steel Structures. Australian Standard AS4100-1998. Sydney, Australia: Standards Association of Australia; 1998.

American Institute of Steel Construction. Steel construction manual. 2005.

ASCE, 2010. Pre-standard for load and resistance factor design (LRFD) of pultruded fibre reinforced polymer (FRP) structures.

American Society of Civil Engineers, 2013. Minimum Design Loads for Buildings and Other Structures (ASCE/SEI 7-10).

ApaTech. http://www.apatech.ru/foto/20071014-32ca41e4381b54196d280f64844df5e1.jpg [Accessed on 26 March, 2021]

Ascione, L., Caron, J. F., Godonou, P., van IJselmuijden, K., Knippers, J., Mottram, T., ... & Tromp, L. (2016). *Prospect for new guidance in the design of FRP: Support to the implementation, harmonization and further development of the Eurocodes*. Publications Office of the European Union.

ASTM D785-08. Standard test method for Rockwell hardness of plastics and electrical insulating materials. West Conshohocken, PA: ASTM.

ASTM D2344-16. Standard test method for short-beam strength of polymer matrix composite materials and their laminates. ASTM International; 2016.

ASTM D2584-18. Standard test method for ignition loss of cured reinforced resins. In American Society for Testing and Materials.

ASTM D3039-17. Standard test method for tensile properties of polymer matrix composite materials. ASTM International; 2017.

ASTM D 3410. Standard test method for compressive properties of polymer matrix composite materials with unsupported gage section by shear loading. West Conshohocken, Pennsylvania, USA: ASTM International; 2006.

Bakis, C. E., Bank, L. C., Brown, V., Cosenza, E., Davalos, J. F., Lesko, J. J., ... & Triantafillou, T. C. (2002). Fibre-reinforced polymer composites for construction—State-of-the-art review. *Journal of composites for construction*, *6*(2), 73-87.

Bai, Y., & Keller, T. (2009). Shear failure of pultruded fibre-reinforced polymer composites under axial compression. *Journal of Composites for Construction*, *13*(3), 234-242.

Bai, Y., Vallée, T., & Keller, T. (2009). Delamination of pultruded glass fibre-reinforced polymer composites subjected to axial compression. *Composite structures*, *91*(1), 66-73.

Bank, L. C. (2006). *Composites for construction: structural design with FRP materials*. John Wiley & Sons.

Barbero, E. J., Cosso, F. A., Roman, R., & Weadon, T. L. (2013). Determination of material parameters for Abaqus progressive damage analysis of E-glass epoxy laminates. *Composites Part B: Engineering*, *46*, 211-220.

Borowicz, D. T., & Bank, L. C. (2010). Behavior of pultruded fibre-reinforced polymer beams subjected to concentrated loads in the plane of the web. *Journal of Composites for Construction*, *15*(2), 229-238.

BS EN 1990:2002 + A1:2005 Annexe D, Design assisted by testing. London. British Standards Institution: 1990. p. 101-16.

Cardoso, D. C., & Togashi, B. S. (2018). Experimental investigation on the flexural-torsional buckling behavior of pultruded GFRP angle columns. *Thin-Walled Structures*, *125*, 269-280.

Chambers, R. E. (1997). ASCE design standard for pultruded fibre-reinforced-plastic (FRP) structures. *Journal of Composites for Construction*, *1*(1), 26-38.

Chawla, H., & Singh, S. B. (2019). Stability and failure characterization of fibre reinforced pultruded beams with different stiffening elements, part 2: Analytical and numerical studies. *Thin-Walled Structures*, *141*, 606-626.

Chen, Y., & Wang, C. (2015). Test on pultruded GFRP I–section under web crippling. *Composites Part B: Engineering*, 77:27-37.

Chen, Y., & Wang, C. (2015). Web crippling behaviour of pultruded GFRP rectangular hollow sections. *Composites Part B: Engineering*, 77:112-21.

Clarke, J. L. (1996). EUROCOMP design code and handbook: Structural design of polymer composites. *E & FN Spon, London*.

Correia, J. R., Branco, F. A., Silva, N. M. F., Camotim, D., & Silvestre, N. (2011). First-order, buckling and post-buckling behaviour of GFRP pultruded beams. Part 1: Experimental study. *Computers & Structures*, *89*(21-22), 2052-2064.

Correia, M. M. (2012). Structural behavior of pultruded GFRP profiles experimental study and numerical modeling. *Technical University of Lisbon, Av. Rovisco Pais*, 1001-1049.

Correia, M. M., Nunes, F., Correia, J. R. & Silvestre, N. (2012). Buckling behaviour and failure of hybrid fibre-reinforced polymer pultruded short columns. *Journal of Composites for Construction*;17(4):463-75.

EN 1993-1-3. Eurocode 3: Design of steel structures-Part 1-3: General rules-Supplementary rules for cold-formed members and sheeting. European Committee for Standardization, Brussels. 2005.

EN 1993-1-3. Eurocode 3: Design of steel structures-Part 1-3: General rules-Supplementary rules for cold-formed members and sheeting. European Committee for Standardization, Brussels. 2006.

EN 1993-1-5. Eurocode 3-Part 1-5: plated structural elements. European Committee for Standardization, Brussels. 2006.

Fernandes, L. A., Gonilha, J., Correia, J. R., Silvestre, N., & Nunes, F. (2015). Web-crippling of GFRP pultruded profiles. Part 1: Experimental study. *Composite Structures*, *120*, 565-577.

Fernandes, L. A., Nunes, F., Silvestre, N., Correia, J. R., & Gonilha, J. (2015). Web-crippling of GFRP pultruded profiles. Part 2: Numerical analysis and design. *Composite Structures*, *120*, 578-590.

Gand, A., Mohammed, M., & Jarrouj, S. (2020). Performance of perforated FRP stub beams subject to static transverse actions. *Engineering Solid Mechanics*, *8*(2), 105-118.

Guades, E., Aravinthan, T., & Islam, M. M. (2014). Characterisation of the mechanical properties of pultruded fibre-reinforced polymer tube. *Materials & Design*, *63*, 305-315.

Guermazi, N., Tarjem, A. B., Ksouri, I., & Ayedi, H. F. (2016). On the durability of FRP composites for aircraft structures in hygrothermal conditioning. *Composites Part B: Engineering*, *85*, 294-304.

Hashin, Z. (1980). Failure criteria for unidirectional fibre composites.

Hashin, Z., & Rotem, A. (1973). A fatigue failure criterion for fibre reinforced materials. *Journal of composite materials*, *7*(4), 448-464.

Hashem, Z. A., & Yuan, R. L. (2001). Short vs. long column behavior of pultruded glass-fibre reinforced polymer composites. *Construction and Building Materials*, *15*(8), 369-378.

Hodgkinson, J. M. (Ed.). (2000). Mechanical testing of advanced fibre composites. Woodhead publishing.

Hota, G., Barker, W., & Manalo, A. (2020). Degradation mechanism of glass fibre/vinylester-based composite materials under accelerated and natural aging. *Construction and Building Materials*, *256*, 119462.

Insausti, A., Puente, I., & Azkune, M. (2009). Interaction between local and lateral buckling on pultruded I-beams. *Journal of Composites for Construction*, *13*(4), 315-324.

Jones, R. M. (1998). *Mechanics of composite materials*. CRC press.

Karmod. www.karmod.eu/blog/wp-content/uploads/2013/04/Fibreglass-Buildings-3.jpg [Accessed on 26 March, 2021]

Khashaba, U. A. (2004). In-plane shear properties of cross-ply composite laminates with different off-axis angles. *Composite structures*, *65*(2), 167-177.

Kulkarni, M. V., Elangovan, K., & Prakash, J. N. (2011). Flexural and Hardness Testing on ABS and Glass Fibre Reinforced Nylon6. *New Trends in Mechanical Engineering*, 44-46.

Lian, Y., Uzzaman, A., Lim, J. B., Abdelal, G., Nash, D., & Young, B. (2016). Effect of web holes on web crippling strength of cold-formed steel channel sections under end-one-flange loading condition–Part I: Tests and finite element analysis. *Thin-Walled Structures*, *107*, 443-452.

Lian, Y., Uzzaman, A., Lim, J. B., Abdelal, G., Nash, D., & Young, B. (2016). Effect of web holes on web crippling strength of cold-formed steel channel sections under end-one-flange loading condition-Part II: Parametric study and proposed design equations. *Thin-Walled Structures*, *107*, 489-501.

Lian, Y., Uzzaman, A., Lim, J.B., Abdelal, G., Nash, D. & Young, B. (2017). Web crippling behaviour of cold-formed steel channel sections with web perforations subjected to interior-one-flange loading condition–Part I: experimental and numerical investigation. *Thin-Walled Structures*, *111*, pp.103-112.

Lian, Y., Uzzaman, A., Lim, J. B., Abdelal, G., Nash, D., & Young, B. (2017). Web crippling behaviour of cold-formed steel channel sections with web holes subjected to interior-one-flange loading condition–Part II: parametric study and proposed design equations. *Thin-Walled Structures*, *114*, 92-106.

National Research Council. (2007). Guide for the design and construction of structures made of FRP pultruded elements. *CNR-DT*, *205*, 25-31.

Newsteelconstruction. https://www.newsteelconstruction.com/wp/wp-content/uploads/2018/09/ Deansgate1-1809.jpg [Accessed on 26 March, 2021]

Nunes, F., Correia, M., Correia, J. R., Silvestre, N., & Moreira, A. (2013). Experimental and numerical study on the structural behavior of eccentrically loaded GFRP columns. *Thin-Walled Structures*, *72*, 175-187.

Nunes, F., Correia, J. R., & Silvestre, N. (2016). Structural behavior of hybrid FRP pultruded beams: Experimental, numerical and analytical studies. *Thin-Walled Structures*, *106*, 201-217.

Nunes, F., Correia, J. R., & Silvestre, N. (2016). Structural behaviour of hybrid FRP pultruded columns. Part 1: Experimental study. *Composite Structures*, *139*, 291-303.

Nunes, F., Silvestre, N., & Correia, J. R. (2016). Structural behaviour of hybrid FRP pultruded columns. Part 2: Numerical study. *Composite Structures*, *139*, 304-319.

Nunes, F., Silvestre, N., & Correia, J. R. (2017). Progressive damage analysis of web crippling of GFRP pultruded I-sections. *Journal of Composites for Construction*, *21*(3), 04016104.

Nguyen, T. T. (2014). *Lateral-torsional buckling resistance of pultruded fibre reinforced polymer shapes* (Doctoral dissertation, University of Warwick).

Owenscorning. www.dcpd6wotaa0mb.cloudfront.net/owenscorning.com/assets/main/composites/applications/bridge-construction/bridge-elements/bridgedeck3fb0fc711bc6a9954daedce8e592fd7ac543c6a82c61ab0cdb11cbbab073c0ba.jpg [Accessed on March 26, 2021]

Packer, J. A. (1984). Web crippling of rectangular hollow sections. *Journal of Structural Engineering*, *110*(10), 2357-2373.

Potyrala, P. B. (2011). *Use of fibre reinforced polymerompsites in bridge construction. State of the art in hybrid and all-composite structures* (Master's thesis, Universitat Politècnica de Catalunya).

Pultrusion. www.bedfordreinforced.com/app/uploads/2018/07/pultrusion_process_CO_1200x 1044- 768x668.jpg [Accessed on 26 March, 2021]

Quadrino, A., Penna, R., Feo, L., & Nisticò, N. (2018). Mechanical characterization of pultruded elements: Fibre orientation influence vs web-flange junction local problem. Experimental and numerical tests. *Composites Part B: Engineering*, *142*, 68-84.

Razzaq, Z., Prabhakaran, R., & Sirjani, M. M. (1996). Load and resistance factor design (LRFD) approach for reinforced-plastic channel beam buckling. *Composites Part B: Engineering*, *27*(3-4), 361-369.

Shan, L., & Qiao, P. (2005). Flexural–torsional buckling of fibre-reinforced plastic composite open channel beams. *Composite Structures*, *68*(2), 211-224.

Singh, S. B., & Chawla, H. (2018). An investigation of material characterization of pultruded FRP H-and I-beams. *Mechanics of Advanced Materials and Structures*, *25*(2), 124-142.

Singh, S. B., & Chawla, H. (2019). Stability and failure characterization of fibre reinforced pultruded beams with different stiffening elements, Part I: Experimental investigation. *Thin-Walled Structures*, *141*, 593-605.

Silva, N. M. F., Camotim, D., Silvestre, N., Correia, J. R., & Branco, F. A. (2011). First-order, buckling and post-buckling behaviour of GFRP pultruded beams. Part 2: Numerical simulation. *Computers & structures*, *89*(21-22), 2065-2078.

Sirajudeen, R. S., & Sekar, R. (2020). Buckling Analysis of Pultruded Glass Fibre Reinforced Polymer (GFRP) Angle Sections. *Polymers*, *12*(11), 2532.

Specification for the design of cold-formed stainless steel structural members. Reston, VA: American Society of Civil Engineers; 2002. SEI/ASCE–8–02.

Tsai, S. W. (1968). Strength theories of filamentary structure. *Fundamental aspects of fibre reinforced plastic composites*.

Tsai, Y. I., Bosze, E. J., Barjasteh, E., & Nutt, S. R. (2009). Influence of hygrothermal environment on thermal and mechanical properties of carbon fibre/fibreglass hybrid composites. *Composites Science and Technology*, *69*(3-4), 432-437.

Turvey, G. J. (1996). Lateral buckling tests on rectangular crosssection pultruded GRP cantilever beams. *Composites Part B: Engineering*, *27*(1), 35-42.

Turvey, G. J., & Zhang, Y. (2018). Mechanical properties of pultruded GFRP WF, channel and angle profiles for limit state/permissible stress design. *Composites Part B: Engineering*, *148*, 260-271.

Uzzaman, A., Lim, J. B., Nash, D., Rhodes, J., & Young, B. (2012). Web crippling behaviour of cold-formed steel channel sections with offset web holes subjected to interior-two-flange loading. *Thin-Walled Structures*, *50*(1), 76-86.

Uzzaman, A., Lim, J. B., Nash, D., Rhodes, J., & Young, B. (2012). Cold-formed steel sections with web openings subjected to web crippling under two-flange loading conditions—part I: Tests and finite element analysis. *Thin-Walled Structures*, *56*, 38-48.

Uzzaman, A., Lim, J. B., Nash, D., Rhodes, J., & Young, B. (2012). Cold-formed steel sections with web openings subjected to web crippling under two-flange loading conditions—Part II: Parametric study and proposed design equations. *Thin-Walled Structures*, *56*, 79-87.

Uzzaman, A., Lim, J. B., Nash, D., Rhodes, J., & Young, B. (2013). Effect of offset web holes on web crippling strength of cold-formed steel channel sections under end-two-flange loading condition. *Thin-Walled Structures*, *65*, 34-48.

Wan, Y. Z., Wang, Y. L., Huang, Y., Luo, H. L., He, F., & Chen, G. C. (2006). Moisture absorption in a three-dimensional braided carbon/Kevlar/epoxy hybrid composite for orthopaedic usage and its influence on mechanical performance. *Composites Part A: Applied Science and Manufacturing*, *37*(9), 1480-1484.

Weland AB. https://www.weland.com/media/2562/fasta_laengder-aw00005021.jpg [Accessed on 26 March, 2021]

Wu, C., & Bai, Y. (2014). Web crippling behaviour of pultruded glass fibre reinforced polymer sections. *Composite Structures*, *108*, 789-800.

Wu, C., Zhang, L. T., Bai, Y., & Zhao, X. L. (2019). Web crippling behavior of pultruded GFRP channel sections under transverse bearing load. *Composite Structures*, *209*, 129-142.

Wu, C., Zhao, X. L., & Duan, W. H. (2011). Design rules for web crippling of CFRP strengthened aluminium rectangular hollow sections. *Thin-Walled Structures*, *49*(10), 1195-1207.

Young, B., & Hancock, G. J. (2001). Design of cold-formed channels subjected to web crippling. *Journal of Structural engineering*, *127*(10), 1137-1144.

Yousefi, A. M., Lim, J. B. & Clifton, G. C. (2017). Cold-formed ferritic stainless steel unlipped channels with web openings subjected to web crippling under interior-two-flange loading condition–Part I: Tests and finite element model verification. *Thin-Walled Structures*, *116*, pp.333-341.

Yousefi, A. M., Lim, J. B. & Clifton, G. C. (2017). Cold-formed ferritic stainless steel unlipped channels with web openings subjected to web crippling under interior-two-flange loading condition–Part II: Parametric study and design equations. *Thin-Walled Structures*, *116*, pp.342-356.

Yousefi, A. M., Lim, J. B. & Clifton, G. C. (2018). Cold-formed ferritic stainless steel unlipped channels with web perforations subject to web crippling under one-flange loadings. *Construction and Building Materials*, *191*, pp.713-725.

Zaman, A., Gutub, S. A., & Wafa, M. A. (2013). A review on FRP composites applications and durability concerns in the construction sector. *Journal of Reinforced Plastics and Composites*, *32*(24), 1966-1988.

Zhang, S., Caprani, C., & Heidarpour, A. (2018). Influence of fibre orientation on pultruded GFRP material properties. *Composite Structures*, *204*, 368-377.

Zhang, W., & Chen, Y. (2017). Tests on GFRP pultruded profiles with channel section subjected to web crippling. *Applied Composite Materials*, *24*(4), 849-862.

Zhong, Y., & Joshi, S. C. (2015). Impact behavior and damage characteristics of hygrothermally conditioned carbon epoxy composite laminates. *Materials & Design (1980-2015)*, *65*, 254-264.

APPENDIX A

SAMPLE DESIGN CALCULATION FOR WEB CRIPPLING STRENGTH OF UNPERFORATED GFRP WIDE FLANGE–SECTION PROFILE

A.1 GENERAL

In this appendix, calculation of web crippling strength of GFRP profile considering a typical wide flange–section member (b_f = 100 mm, h_w = 59 mm, t_f = 5 mm, t_w = 5 mm, see Figure A.1) with unperforated web under two-flange loading conditions (N = 50 mm, t_{plate} = 10 mm), using design proposals by Borowicz and Bank (2010), Fernandes *et al*. (2015), Chen and Wang (2015) and Wu and Bai (2014) are shown. Furthermore, calculations of web crippling capacities according to the newly proposed design equations are also presented. Related equations are presented again for ease of reading.

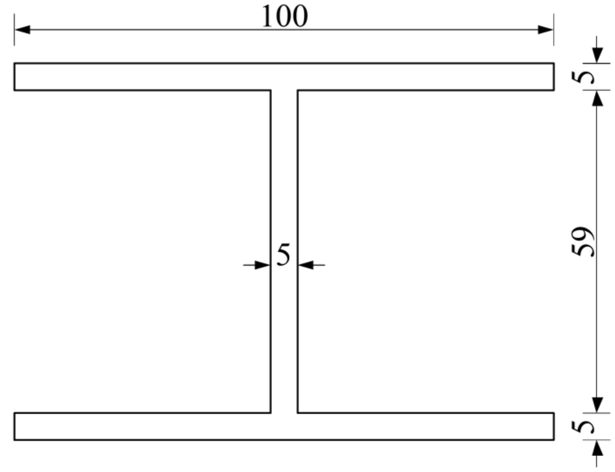

Figure A.1: Schematic diagram for the wide flange–section profile.

A.2 PREVIOUSLY PROPOSED DESIGN EQUATIONS

A.2.1 Borowicz and Bank (2010)

The nominal web crippling strength of the GFRP wide flange–section is given by the following equation:

$$P_n = 0.7 d t_w f_s \left(1 + \frac{2k + 6t_{plate} + b_{plate}}{d}\right) \tag{A.1}$$

Here,

d = 69 mm

t_w = 5 mm

f_s = 38.3 MPa

k = 1.5×t_f = 1.5×5 = 7.5

Hence,

P_n = 0.7×69×5×38.3×(1+(2×7.5+6×10+50)/69) = 26005.7 N = 26.01 kN

A.2.2 Fernandes *et al*. (2015)

The web crippling strength of the GFRP WF–section as per Fernandes *et al*. (2015) is given by the following equation:

$$P_n = C f_{cu,T} h_w^2 \left(1 - C_r \sqrt{\frac{r}{t_w}}\right)\left(1 + C_{Lh} \frac{h_w^2 N}{t_w^3}\right)\left(1 - C_\chi \frac{h_w}{t_w}(1 - \chi_F)\right) \tag{A.2}$$

Here,

h_w = 59 mm; t_w = 5 mm; r = 0; N = 50 mm;

$f_{cu,T}$ = 37.39 MPa

For ETF loading, C = 0.0688; C_r = 0.5757; C_{Lh} = 0.0037; C_χ = 0.0647

For ITF loading, C = 0.1489; C_r = 0.5492; C_{Lh} = 0.0015; C_χ = 0.0634

From, EC3: 1–5, the buckling reduction factor is obtained as χ_F = 0.75 and 0.73 for ETF and ITF loading, respectively.

Hence,

For ETF loading,

$$P_{n,ETF} = 0.0688\times37.39\times59^2\times\left(1-0.5757\times\sqrt{\frac{0}{5}}\right)\times$$

$$\left(1+0.0037\times\frac{59^2\times50}{5^3}\right)\times\left(1-.0647\times\frac{59}{5}(1-0.75)\right)=44.47\text{kN}$$

For ITF loading,

$$P_{n,ETF} = 0.1489\times37.39\times59^2\times\left(1-0.5492\times\sqrt{\frac{0}{5}}\right)\times$$

$$\left(1+0.0015\times\frac{59^2\times50}{5^3}\right)\times\left(1-.0634\times\frac{59}{5}(1-0.73)\right)=47.72\text{kN}$$

A.2.3 Chen and Wang (2015)

The web crippling strength for the GFRP WF–section member as per Chen and Wang (2015) can be obtained by the following equations:

$$P_{ETF} = \left[9-\frac{(H-2t_f)/t_w}{60}\right]\left[1-0.01\times\frac{N}{t_w}\right]t_w^2 f_y \tag{A.3}$$

$$P_{ITF} = \left[12-\frac{(H-2t_f)/t_w}{60}\right]\left[1-0.01\times\frac{N}{t_w}\right]t_w^2 f_y \tag{A.4}$$

Here,

H = 69 mm; t_w = 5 mm; t_f = 5 mm; N = 50 mm; f_y = 323.2 MPa

Hence,

$$P_{ETF} = \left[9-\frac{(69-2\times5)/5}{60}\right]\times\left[1-0.01\times\frac{50}{5}\right]\times5^2\times323.2/1000 = 63.98\text{ kN}$$

$$P_{ITF} = \left[12-\frac{(69-2\times5)/5}{60}\right]\times\left[1-0.01\times\frac{50}{5}\right]\times5^2\times323.2/1000 = 81.85\text{ kN}$$

A.2.4 Wu and Bai (2014)

The web crippling capacity for the GFRP WF–section member as per Chen and Wang (2015) can be obtained by the following equations:

$$P_{ETF} = a_e f_s A_{shear} \tag{A.5}$$

$$P_{ITF} = a_i f_s A_{shear} \tag{A.6}$$

Here,

a_e = 0.58; a_i = 1.07; f_s = 38.3 MPa

A_{shear} = shear area under the bearing plate

= $t_w \times b_{plate}$ / cos(45°)

Hence,

P_{ETF} = 0.001×0.58×38.3×5×50/cos(45°) = 7.82 kN

P_{ITF} = 0.001×1.07×38.3×5×50/cos(45°) = 14.43 kN

A.3 PROPOSED DESIGN EQUATIONS

Newly proposed design equations for the present study are based on the formulations given in Eurocode3 (2006); NAS (2007); Wu *et al*. (2019); and Fernandes *et al*. (2015).

A.3.1 Modified Eurocode3 (2006)

The web crippling capacity for the GFRP WF–section member as per modified Eurocode3 (2006) are obtained by the following equations:

$$P_{EC3,ETF} = 0.252\left[12 - \frac{h_w / t_w}{4.8}\right]\left[1 + 0.33 \times \frac{N}{t_w}\right] t_w^2 f_{cu,T} \tag{A.7}$$

$$P_{EC3,ITF} = 0.31\left[17 - \frac{h_w / t_w}{8}\right]\left[1 + 0.158 \times \frac{N}{t_w}\right] t_w^2 f_{cu,T} \tag{A.8}$$

Here,

h_w = 59 mm; t_w = 5 mm; N = 50 mm; $f_{cu,T}$ = 37.39 MPa

Hence,

$$P_{EC3,ETF} = 0.252 \times \left[12 - \frac{59/5}{4.8}\right] \times \left[1 + 0.33 \times \frac{50}{5}\right] \times 5^2 \times 37.39/1000 = 9.66\text{kN}$$

$$P_{EC3,ITF} = 0.31 \times \left[17 - \frac{59/5}{8}\right] \times \left[1 + 0.158 \times \frac{50}{5}\right] \times 5^2 \times 37.39/1000 = 11.61\text{kN}$$

A.3.2 Modified NAS (2007)

The web crippling strength for the GFRP WF–section member as per modified NAS (2007) can be obtained by the following equations:

$$P_{NAS,ETF} = 0.164 t_w^2 f_{cu,T}\left(1-0.03\times\sqrt{\frac{r}{t_w}}\right)\left(1+36.5\times\sqrt{\frac{N}{t_w}}\right)\left(1-0.14\times\sqrt{\frac{h_w}{t_w}}\right) \quad \text{(A.9)}$$

$$P_{NAS,ITF} = 1.23 t_w^2 f_{cu,T}\left(1-0.002\times\sqrt{\frac{r}{t_w}}\right)\left(1+4.0\times\sqrt{\frac{N}{t_w}}\right)\left(1-0.67\times\sqrt{\frac{h_w}{t_w}}\right) \quad \text{(A.10)}$$

Here,

$r = 0$; $h_w = 59$ mm; $t_w = 5$ mm; $N = 50$ mm; $f_{cu,T} = 37.39$ MPa

Hence,

$$P_{NAS,ETF} = 0.164\times 5^2\times 37.39(1-0.03\times 0)\left(1+36.5\times\sqrt{\frac{50}{5}}\right)\left(1-0.14\times\sqrt{\frac{59}{5}}\right) = 8.99\text{kN}$$

$$P_{NAS,ITF} = 1.23\times 5^2\times 37.39(1-0.002\times 0)\left(1+4.0\times\sqrt{\frac{50}{5}}\right)\left(1-0.67\times\sqrt{\frac{59}{5}}\right) = 12.06\text{kN}$$

A.3.3 Modified Fernandes *et al*. (2015)

The web crippling strength for the GFRP WF–section member as per modified Fernandes *et al*. (2015) is calculated by the following equations:

$$P_{ETF} = 0.0474 f_{cu,T} h_w^2\left(1-0.58\times\sqrt{\frac{r}{t_w}}\right)\left(1+0.0036\times\frac{h_w^2 N}{t_w^3}\right)\left(1-0.0634\times\frac{h_w}{t_w}(1-\chi_F)\right) \quad \text{(A.11)}$$

$$P_{ITF} = 0.136 f_{cu,T} h_w^2\left(1-0.5642\times\sqrt{\frac{r}{t_w}}\right)\left(1+0.0013\times\frac{h_w^2 N}{t_w^3}\right)\left(1-0.0606\times\frac{h_w}{t_w}(1-\chi_F)\right) \quad \text{(A.12)}$$

Here,

$h_w = 59$ mm; $t_w = 5$ mm; $r = 0$; $N = 50$ mm;
$f_{cu,T} = 37.39$ MPa

From, EC3: 1–5 (2006), the buckling reduction factor is obtained as $\chi_F = 0.75$ and 0.73 for ETF and ITF loading, respectively.

Hence,

$$P_{ETF} = 0.0474\times 37.39\times 5^2\times(1-0.58\times 0)\times$$
$$\left(1+0.0036\times\frac{59^2\times 50}{5^3}\right)\times\left(1-0.0634\times\frac{59}{5}\times(1-0.75)\right)/1000 = 10.22\text{kN}$$

$$P_{ITF} = 0.136\times37.39\times5^2\times(1-0.5642\times0)\times$$
$$\left(1+0.0013\times\frac{59^2\times50}{5^3}\right)\times\left(1-0.0606\times\frac{59}{5}(1-0.73)\right)/1000=14.34\text{kN}$$

A.3.4 Modified Wu *et al*. (2019)

The web crippling capacity for the GFRP WF–section member as per modified Wu *et al*. (2019) is calculated by the following equations:

$$P_{n,ITF} = 1.13\alpha_c \mathrm{A}\, f_{cu,T} \tag{A.13}$$

$$P_{n,ETF} = 1.06\alpha_c \mathrm{A}\, f_{cu,T} \tag{A.14}$$

$$A = Kt_w \tag{A.15}$$

$$K = \min\left\{B_{eff}, L\right\} \tag{A.16}$$

$$B_{eff,ETF} = N + \frac{h_w}{2\tan\alpha} + \frac{t_f}{\tan\beta} \tag{A.17}$$

$$B_{eff,ITF} = N + \frac{h_w}{\tan\alpha} + \frac{2t_f}{\tan\beta} \tag{A.18}$$

$$\beta = 33.19+1.48t_f \tag{A.19}$$

Here, α_c is the member slenderness reduction factor and is given by,

$$\alpha_c = \xi\left(1-\sqrt{\left[1-\left(\frac{90}{\xi\lambda}\right)^2\right]}\right) \tag{A.20}$$

$$\xi = \frac{(\lambda/90)^2+1+\eta}{2(\lambda/90)^2} \tag{A.21}$$

$$\lambda = \lambda_n + \alpha_a\alpha_b \tag{A.22}$$

$$\eta = 0.00326(\lambda-13.5)\geq 0 \tag{A.23}$$

$$\lambda_n = \frac{\sqrt{12}k_e(d-2t_w)}{t_w} \tag{A.24}$$

$$\alpha_a = \frac{2100\left(\lambda_n - 13.5\right)}{\lambda_n^2 - 15.3\lambda_n + 2050} \tag{A.25}$$

Here,

k_e = 1.0 for both ETF and ITF loading; α_b = 0.5

λ_n = 40.87

α_a = 18.57

λ = 50.155

η = 0.119

ξ = 2.3025

α_c = 0.86

β = 33.19+1.48×5 = 40.59°

α = 84.41°

$B_{eff,\,ETF}$ = 58.722 mm

$B_{eff,\,ITF}$ = 67.445 mm

Hence,

P_{ETF} = 1.06×0.86×58.722×5×37.39/1000 = 10.01 kN

P_{ITF} = 1.13×0.86×67.445×5×37.39/1000 = 12.25 kN.

This page is intentionally left blank.

APPENDIX B

SAMPLE DESIGN CALCULATION FOR WEB CRIPPLING STRENGTH OF PERFORATED GFRP WIDE FLANGE SECTION PROFILE

B.1 GENERAL

In this appendix, the calculation of web crippling strength of a typical GFRP wide flange–section member (b_f = 100 mm, h_w = 59 mm, t_f = 5 mm, t_w = 5 mm) with centred web perforation under two-flange loading conditions (N = 50 mm, t_{plate} = 10 mm), using the proposed reduction equations are shown. The proposed reduction equations are given as:

For perforation under ITF loading:

$$R_p = 0.81 - 0.40\left(\frac{a}{h}\right) + 0.02\left(\frac{N}{h}\right) \leq 1 \tag{B.1}$$

For perforation under ETF loading:

$$R_p = 0.66 - 0.59\left(\frac{a}{h}\right) + 0.13\left(\frac{N}{h}\right) \leq 1 \tag{B.2}$$

The limits in Equations B.1 and B.2 are: $a/h \leq 0.8$, $N/h \leq 2.14$, and $h/t_w \leq 20.33$.

Here,

h = 59 mm, N =50 mm

For perforation dia, $a = 0.4h$,

$R_p = 0.81 - 0.40\times0.4 + 0.02\times(50/59) = 0.67 < 1.0$, for ITF loading

$R_p = 0.66 - 0.59\times0.4 + 0.13\times(50/59) = 0.53 < 1.0$, for ETF loading

B.2 WEB CRIPPLING STRENGTH WITH 0.4*h* PERFORATION DIAMETER

B.2.1 Modified Eurocode3 (2006)

The reduced web crippling capacity for the GFRP WF–section with perforation size 0.4*h* as per modified Eurocode3 (2006) is obtained by the following equations:

$$P_{EC3,ETF} = 0.53 \times 0.252\left[12 - \frac{h_w / t_w}{4.8}\right]\left[1 + 0.33 \times \frac{N}{t_w}\right] t_w^2 f_{cu,T} \tag{B.3}$$

$$P_{EC3,ITF} = 0.67 \times 0.31\left[17 - \frac{h_w / t_w}{8}\right]\left[1 + 0.158 \times \frac{N}{t_w}\right] t_w^2 f_{cu,T} \tag{B.4}$$

Here,

h_w = 59 mm; t_w = 5 mm; N = 50 mm; $f_{cu,T}$ = 37.39 MPa

Hence,

$$P_{EC3,ETF} = 0.53 \times 0.252 \times \left[12 - \frac{59/5}{4.8}\right] \times \left[1 + 0.33 \times \frac{50}{5}\right] \times 5^2 \times 37.39/1000 = 5.12\text{kN}$$

$$P_{EC3,ITF} = 0.67 \times 0.31 \times \left[17 - \frac{59/5}{8}\right] \times \left[1 + 0.158 \times \frac{50}{5}\right] \times 5^2 \times 37.39/1000 = 7.78\text{kN}$$

B.2.2 Modified NAS (2007)

The web crippling strength for the perforated GFRP WF–section member as per modified NAS (2007) can be obtained by the following equations:

$$P_{NAS,ETF} = 0.53 \times 0.164 t_w^2 f_{cu,T}\left(1 - 0.03 \times \sqrt{\frac{r}{t_w}}\right)\left(1 + 36.5 \times \sqrt{\frac{N}{t_w}}\right)\left(1 - 0.14 \times \sqrt{\frac{h_w}{t_w}}\right) \tag{B.5}$$

$$P_{NAS,ITF} = 0.67 \times 1.23 t_w^2 f_{cu,T}\left(1 - 0.002 \times \sqrt{\frac{r}{t_w}}\right)\left(1 + 4.0 \times \sqrt{\frac{N}{t_w}}\right)\left(1 - 0.67 \times \sqrt{\frac{h_w}{t_w}}\right) \tag{B.6}$$

Here,

r = 0; h_w = 59 mm; t_w = 5 mm; N = 50 mm; $f_{cu,T}$ = 37.39 MPa

Hence,

$$P_{NAS,ETF} = 0.53 \times 0.164 \times 5^2 \times 37.39(1-0)\left(1 + 36.5 \times \sqrt{\frac{50}{5}}\right)\left(1 - 0.14 \times \sqrt{\frac{59}{5}}\right) = 4.76\text{kN}$$

$$P_{NAS,ITF} = 0.67 \times 1.23 \times 5^2 \times 37.39(1-0)\left(1 + 4.0 \times \sqrt{\frac{50}{5}}\right)\left(1 - 0.67 \times \sqrt{\frac{59}{5}}\right) = 8.08\text{kN}$$

B.2.3 Modified Fernandes *et al*. (2015)

The reduced web crippling strength for the GFRP WF–section member as per modified Fernandes *et al*. (2015) is calculated by the following equations:

$$P_{ETF} = 0.53 \times 0.0474\, f_{cu,T} h_w^2 \left(1 - 0.58 \times \sqrt{\frac{r}{t_w}}\right)\left(1 + 0.0036 \frac{h_w^2 N}{t_w^3}\right)\left(1 - 0.0634 \frac{h_w}{t_w}(1-\chi_F)\right) \tag{B.7}$$

$$P_{ITF} = 0.67 \times 0.136\, f_{cu,T} h_w^2 \left(1 - 0.5642 \times \sqrt{\frac{r}{t_w}}\right)\left(1 + 0.0013 \frac{h_w^2 N}{t_w^3}\right)\left(1 - 0.0606 \frac{h_w}{t_w}(1-\chi_F)\right) \tag{B.8}$$

Here,

h_w = 59 mm; t_w = 5 mm; r = 0; N = 50 mm;

$f_{cu,T}$ = 37.39 MPa

From, EC3: 1–5, the buckling reduction factor is obtained as χ_F = 0.75 and 0.73 for ETF and ITF loading, respectively.

Hence,

$$P_{ETF} = 0.53 \times 0.0474 \times 37.39 \times 5^2 \times (1 - 0.58 \times 0) \times \left(1 + 0.0036 \times \frac{59^2 \times 50}{5^3}\right) \times \left(1 - 0.0634 \times \frac{59}{5} \times (1 - 0.75)\right) / 1000 = 5.42\text{kN}$$

$$P_{ITF} = 0.67 \times 0.136 \times 37.39 \times 5^2 \times (1 - 0.5642 \times 0) \times \left(1 + 0.0013 \times \frac{59^2 \times 50}{5^3}\right) \times \left(1 - 0.0606 \times \frac{59}{5}(1 - 0.73)\right) / 1000 = 9.61\text{kN}$$

B.2.4 Modified Wu *et al*. (2019)

The web crippling capacity for the web perforated GFRP WF–section member as per modified Wu *et al*. (2019) is calculated by the following equations:

$$P_{ITF} = 0.67 \times 1.13 \alpha_c \mathrm{A}\, f_{cu,T} \tag{B.9}$$

$$P_{ETF} = 0.53 \times 1.06 \alpha_c \mathrm{A}\, f_{cu,T} \tag{B.10}$$

The values of A, α_c are derived in **Section A.3.4**.

α_c = 0.86; A_{ETF} = 58.722×5 mm^2; A_{ITF} = 67.445×5 mm^2; $f_{cu,T}$ = 37.39 MPa

Hence,

P_{ETF} = 0.53×1.06×0.86×58.722×5×37.39/1000 = 5.31 kN

P_{ITF} = 0.67×1.13×0.86×67.445×5×37.39/1000 = 8.21 kN

LIST OF PUBLICATIONS

A) Journals

1) **Haloi, J.,** Mushahary, S.K., Borsaikia, A.C. and Singh, K.D., 2021. Experimental investigation on the web crippling behaviour of pultruded GFRP wide-flange sections subjected to two-flange loading conditions. ***Composite Structures***, *259*, p.113469.

2) **Haloi, J.**, Borsaikia, A. C. and Singh, K. D., 2021. Web crippling behaviour of pultruded GFRP wide-flange sections with web perforations subjected to interior-two-flanges loading condition. ***Thin Walled Structures***, 166, p. 108072.

3) **Haloi, J.**, Borsaikia, A. C. and Singh, K. D., 2020. Mechanical properties of pultruded GFRP channel, wide flange and rectangular hollow profiles. ***Innovative Infrastructure Solutions*** (Accepted)

4) **Haloi, J.**, Borsaikia, A. C. and Singh, K. D., 2021. Web crippling behaviour of pultruded GFRP wide-flange sections with web perforations subjected to end-two-flanges loading condition. ***Engineering Structures*** (submitted)